

UC Merced

UC Merced Electronic Theses and Dissertations

Title

Promoting Energy Sustainability through Fundamental Study of Precious Metal Catalysts for Fuel Cells and Electrolyzers

Permalink

<https://escholarship.org/uc/item/0t1320cx>

Author

Labata, Marc Francis Maligsa

Publication Date

2022

Peer reviewed|Thesis/dissertation

UNIVERSITY OF CALIFORNIA, MERCED

**Promoting Energy Sustainability through Fundamental
Study of Precious Metal Catalysts for Fuel Cells and
Electrolyzers**

A dissertation submitted in partial satisfaction of the requirements for the degree
Doctor of Philosophy

in

Environmental Systems

by

Marc Francis M. Labata

Committee in charge:

Professor Po-Ya Abel Chuang, Chair

Professor Gerardo Diaz

Professor Peggy O'Day

Professor Min Hwan Lee

2022

© Marc Francis M. Labata, 2022
All rights reserved.

The thesis of Marc Francis M. Labata is approved, and it is acceptable in quality and form for any future publication on microfilm and electronically:

Professor Po-Ya Abel Chuang, Chair	Date
------------------------------------	------

Professor Gerardo Diaz	Date
------------------------	------

Professor Peggy O'Day	Date
-----------------------	------

Professor Min Hwan Lee	Date
------------------------	------

University of California, Merced
2022

*As I close this chapter of my life, may it lead me to know my true
purpose in this world.*

CURRICULUM VITAE

Marc Francis Labata

Environmental Systems Graduate Group
University of California, Merced
Mobile: +1-209-658-5828
Email: mlabata@ucmerced.edu

EDUCATION

Candidate, Doctor of Philosophy in Environmental Systems

(August 2017–Present)

University of California, Merced

Research Group: Thermal and Electrochemical Energy Laboratory

Research Advisor: Prof. Po-Ya Abel Chuang

Bachelor of Science in Chemical Engineering

(June 2011–June 2016)

University of the Philippines-Diliman

PUBLISHED WORKS

1. **Labata, M.F.**, Li, G.F. Altoe, M.V., & Chuang, P. Y. A (in preparation). *Establishing Structure-Function Relationship of Iridium-Cobalt Oxide as Oxygen Evolution Reaction (OER) Catalyst in Acidic and Alkaline Media.*
2. del Rosario, J. A. D., Li, G., **Labata, M. F.**, Ocon, J. D., & Chuang, P. Y. A (2021). *Unravelling the roles of alkali-metal cations for the enhanced oxygen evolution reaction in alkaline media.* Applied Catalysis B: Environmental.
3. **Labata, M. F.**, Li, G., Ocon, J. D., & Chuang, P. Y. A (2021). *Insights on Platinum-Carbon Catalyst Degradation Mechanism for Oxygen Reduction Reaction in Acidic and Alkaline Media.* Journal of Power Sources.

4. Li, G., Divinagracia, M., **Labata, M. F.**, Ocon, J. D., & Chuang, P. Y. A. (2019). *Electrolyte-depended oxygen evolution reactions in alkaline media: electrical double layer and interfacial interactions*. ACS Applied Materials & Interfaces.
 5. Musico, Y. L. F., Kakati, N., **Labata, M. F. M.**, Ocon, J. D., & Chuang, P. Y. A. (2019). *One-pot hydrothermal synthesis of heteroatom co-doped with fluorine on reduced graphene oxide for enhanced ORR activity and stability in alkaline media*. *Materials Chemistry and Physics*.
 6. Digol, J. L., **Labata, M. F. M.**, Divinagracia, M. F., & Ocon, J. D. (2017). *CoMn₂O₄ Anchored on N-Doped High-Dimensional Hierarchical Porous Carbon Derived from Biomass for Bifunctional Oxygen Electrocatalysis*. ECS Transactions.
-

ACCEPTED PROPOSALS TO USER FACILITIES

2021-2022 (ongoing). *STEM-EELS/EDS Characterization of Transition Metal Oxides for Electrochemical Energy Devices*. National Center for Electron Microscopy, Molecular Foundry, Lawrence Berkeley National Laboratory. PI: Abel Chuang; Primary Researcher: Marc Francis Labata; Co-researcher: Nitul Kakati, Peggy O'Day

2021-2022 (ongoing). *Investigation of Catalyst-Ionomer Interaction for Electrode Development in Fuel Cells and Electrolyzers*. Imaging and Manipulation of Nanostructures Facility, Molecular Foundry, Lawrence Berkeley National Laboratory. PI: Abel Chuang; Primary Researcher: Marc Francis Labata; Co-researcher: Nitul Kakati

2019-2020 (completed). *Synthesis and Characterization of Novel Electrode Materials for Fuel Cell Applications*. Imaging and Manipulation of Nanostructures Facility, Molecular Foundry, Lawrence Berkeley National Laboratory. PI: Abel Chuang; Primary Researcher: Marc Francis Labata; Co-researcher: Nitul Kakati

FELLOWSHIPS

Graduate Dean's Dissertation Fellowship – University of California, Merced (Spring 2022)

GradEXCEL Peer Mentor Fellowship – University of California, Merced (Academic Year 2021-2022)

Environmental Systems Graduate Student Summer Fellowship – UC Merced
(Summer 2019 and Summer 2018)

Environmental Systems Graduate Student Professional Development Fellowship – UC Merced
(Spring 2021, Spring 2019 and Spring 2018)

Philippine-California Advanced Research Institutes (PCARI) PhD Foreign Scholarship
(Academic Year 2017-Present)

Philippine-California Advanced Research Institutes (PCARI) MS Local Scholarship
(Academic Year 2016-2017)

Don Pablo K.T. Uy Foundation, Inc.
(2nd Semester, Academic Year 2013-2016)

Scholarship to Ensure Progress Foundation (STEPS), Inc.
(Academic Year 2013-2016)

University of the Philippines Alumni Association (UPAA) in British Columbia
(Academic Year 2012-2013)

CONFERENCES

2021 Molecular Foundry User Meeting Virtual Conference
(August 19-20, 2021)

Virtual Poster: *Property-function correlations of iridium-cobalt oxide nanoparticles as oxygen evolution reaction (OER) catalyst in acidic and alkaline media.*

239th Electrochemical Society Meeting
(May 30 – June 3, 2021)

Virtual Conference

Oral Presentation: *Establishing Structure-Function Relationship of Iridium-Cobalt Oxide as Oxygen Evolution Reaction (OER) Catalyst in Acidic and Alkaline Media*

2020 Molecular Foundry User Meeting Virtual Conference
(August 20-21, 2020) Virtual Posters:

- *Insights on Platinum-Carbon Catalyst Degradation Mechanism for Oxygen Reduction Reaction in Acidic and Alkaline Media.*

- Nanostructured Reduced Nickel Cobalt Tungstate on Ni Foam as Efficient Bifunctional Electrocatalyst for Urea Assisted Water Electrolysis.

235th Electrochemical Society Meeting

(May 26 – May 30, 2019)

Dallas, Texas, USA

Poster Presentation: *Study on the Stability and Durability of Dual Metal-Doped TiO₂ Catalyst Support for Pt*

Gordon Research Conference Fuel Cells

(July 29 – August 3, 2018) Bryant University, Smithfield RI, USA Poster Presentation: *Electrolyte-dependent Interfacial Interactions in Alkaline Oxygen Evolution Reaction*

231st Electrochemical Society Meeting

(May 28 – June 1, 2017)

New Orleans, Louisiana, USA

Poster Presentation: *CoMn₂O₄ Anchored on N-Doped High-Dimensional Hierarchical Porous Carbon Derived from Biomass for Bifunctional Oxygen Electrocatalysis*
Student Volunteer – Assisted the participants during the first day of the conference

AWARDS

2nd Place - University of California, Merced Grad Slam Competition

Competed with 10 finalists to pitch research in 3 minutes to the general public
April 2022

6th Place - Chemical Engineering Licensure Examination

534 successful examinees out of 918 test-takers

Professional Regulation Commission of the Philippines

November 2016

WORK EXPERIENCE

Teaching Assistant – Fluid Mechanics (ENGR 120)

(August 17 – December 31, 2021)

School of Engineering, University of California Merced

Teaching Assistant – Engineering Economic Analysis (ENGR 155)

(June 22 – August 14, 2020)

School of Engineering, University of California Merced

Intern – Philippine Batteries, Inc.

(June 4 – July 17, 2015)

Intern – Linde Philippines (South), Inc.

(May 2 – May 30, 2014)

AFFILIATIONS

Berkeley Lab Affiliate – Molecular Foundry

National Center for Electron Microscopy

Molecular Foundry, Lawrence Berkeley National Laboratory (LBNL)

(November 18, 2021 – May 13, 2022)

Berkeley Lab Affiliate – Molecular Foundry

Imaging and Manipulation of Nanostructures Facility

Molecular Foundry, Lawrence Berkeley National Laboratory (LBNL)

(August 9, 2019 – November 15, 2020)

Electrochemical Society (ECS) Student Member

(February 16, 2017 – Present)

Philippine Institute of Chemical Engineers (ID No: CHE0001058)

(December 20, 2017 – Present)

ACKNOWLEDGMENTS

This dissertation is a product of my collaboration with people from different walks of life. Without their help, I won't be able to accomplish all that is written here.

First, to my advisor and mentor, Prof. Abel Chuang, for guiding and supporting me in all my research endeavors. Thank you for constantly providing feedback and being patient with my growth. I will forever treasure my PhD experience throughout my life.

To our funding source, the Philippine-California Advanced Research Institutes (PCARI), the Department of Science and Technology-Science Education Institute (DOST-SEI), and the Graduate Dean's Dissertation Fellowship channeled through the Environmental Systems Program at UC Merced. Thank you for providing the means so I would be able to continuously work on these projects without worrying how to get by each day.

To all the lab members of my research group, Thermal and Electrochemical Energy Laboratory (TEEL), especially Dr. Nitul Kakati, Dr. Guangfu Li and Dr. Yvonne Musico for sharing their expertise with me and serving as my mentors and collaborators.

To the instrumental support from the Molecular Foundry and staff especially Dr. Jim Ciston, Dr. Karen Bustillo, Dr. Chengyu Song, Dr. Virginia Altoe and Mr. Rohan Dhall. Work at the Molecular Foundry was supported by the Office of Science, United States, Office of Basic Energy Sciences, United States, of the U.S. Department of Energy under Contract No. DE-AC02-05CH11231.

To Kennedy Nguyen at the Imaging and Microscopy Facility (IMF) and Dr. Liying Zhao of the Environmental Analytical Laboratory (EAL) at UC Merced, for helping me to collect data for my characterization results.

To my committee members: Prof. Peggy O'Day, Prof. Min Hwan Lee, and Prof. Gerardo Diaz, for providing feedback to improve this work.

To O'Day group, especially Edwin Rivas Meraz, for sharing their lab resources and extending help with the nitrogen gas adsorption instrument and other characterization needs.

To all hardworking and friendly staff at UC Merced in different offices.

To my early mentors in the Philippines, Prof. Joey Ocon and Prof. Julie Anne del Rosario of the Laboratory of Electrochemical Engineering (LEE), for encouraging me to do Ph.D. and helping me establish my academic footing.

To Desiree Sua-an and Reynaldo Geronia for providing me company during my first few months in Merced.

To Wernel Remolona and Amelyn Remolona for welcoming me to their home and making me feel a part of their family.

To all the friends and amazing people that I've met in Merced.

To all my extended family, friends and loved ones in the Philippines and in the US.

To my parents, Francisco and Corazon, and siblings Mary Anne, Marlon, and Mildred, for celebrating with my successes and comforting me when I am at my lowest points in my life.

To my faith community in the Central California, the Singles for Christ (SFC), for providing a space for me to grow spiritually and be a better Christian.

To the Almighty God who gives me strength to face every challenge and a new life each day.

My sincerest gratitude to all of your contributions for me to reach this milestone in my professional career.

ABSTRACT

Clean and efficient energy technologies are in high demand to resolve the issues related to limited fossil fuels and the climate crisis. Recently, electrochemical conversion devices, such as fuel cells and electrolyzers, demonstrate a viable option for a sustainable energy system. Electrolyzers can generate green hydrogen through water electrolysis, which can then be used in fuel cells to directly convert chemical energy to electricity. However, there are still technical barriers that need to be addressed before reaching full commercialization in these emerging technologies. For fuel cells, especially in heavy-duty vehicle applications, durability is a critical concern to be competitive with internal combustion engines. One of the key degradation losses in fuel cells comes from the catalyst layer made of platinum nanoparticles dispersed on carbon support (Pt/C). Here, a fundamental study was conducted to investigate the degradation mechanism of Pt/C using accelerated durability testing protocols in acidic and alkaline media. It was found that the generation of carboxyl functional groups due to carbon corrosion in acid poisons the Pt active sites during oxygen reduction reaction (ORR). In alkaline, carbon dissolution happens that triggers the formation of large Pt agglomerates. For electrolyzers, hydrogen generation relies on an expensive and scarce iridium metal as a catalyst for the oxygen evolution reaction (OER). To lower the cost of this device, alternative materials are developed to reduce the iridium (Ir) loading. We proposed to enhance Ir utilization by alloying with cobalt (Co), being a less expensive and more available metal. Surfactant-assisted Adam's fusion synthesis technique was developed as a scalable method to produce IrCo catalysts. The synthesized material outperforms commercial Ir baseline catalysts, in both acidic and alkaline media. In addition, the effects of the Ir/Co molar ratio, the use of surfactant, and acid etching were investigated to enhance OER performance. In this dissertation, the catalytic performance and degradation mechanisms of precious metals for ORR and OER in both acid and alkaline media were successfully studied using half-cell electrochemical set-up and physicochemical characterization tools. The new findings provide insights into developing more efficient and durable fuel cells and electrolyzers to promote energy sustainability toward a decarbonized society.

TABLE OF CONTENTS

CURRICULUM VITAE	ii
ACKNOWLEDGMENTS	vii
ABSTRACT	ix
LIST OF FIGURES	xiii
LIST OF TABLES	xxiv
LIST OF SYMBOLS	xxvii
1 INTRODUCTION	1
1.1 The Climate Crisis and the Role of Hydrogen	1
1.1.1 Climate Change	1
1.1.2 Sources of Greenhouse Gas Emissions	4
1.1.3 The Hydrogen Economy	6
1.2 Electrochemical Devices for Sustainable Energy	7
1.2.1 Fuel Cells	7
1.2.2 Electrolyzers	10
2 LITERATURE REVIEW	12
2.1 Catalyst Layer Degradation in Fuel Cells	12
2.2 Catalyst Development for Water Electrolyzers	15
3 EXPERIMENTAL TOOLS	19
3.1 Electrochemical Methods	19
3.1.1 Rotating Disk Electrode (RDE) and Rotating-Ring Disk Electrode (RRDE)	19

3.1.2	Linear Sweep Voltammetry (LSV))	22
3.1.3	Cyclic Voltammetry (CV)	24
3.1.4	Electrochemical Impedance Spectroscopy (EIS)	25
3.2	Material Characterization Techniques	28
3.2.1	Gas Adsorption Porosimetry	28
3.2.2	Inductively Coupled Plasma Mass Spectrometry (ICP-MS)	29
3.2.3	X-ray diffraction (XRD)	30
3.2.4	Electron Microscopy	31
3.2.4.1	Scanning Electron Microscopy (SEM)	33
3.2.4.2	Transmission Electron Microscopy (TEM) and Scanning Transmission Electron Microscopy (STEM)	34
3.2.5	Spectroscopy	36
3.2.6	Energy-dispersive X-ray spectroscopy (EDS)	36
3.2.6.1	Energy electron loss spectroscopy (EELS)	37
3.2.6.2	X-ray photoelectron spectroscopy (XPS)	38
4	DEGRADATION BEHAVIOR OF PLATINUM-CARBON CATALYST FOR OXYGEN REDUCTION REACTION (ORR) IN ACIDIC AND ALKALINE MEDIA	40
4.1	Abstract	40
4.2	Physicochemical, Performance and Durability Assessment Tools	40
4.2.1	Chemicals	40
4.2.2	Electrode Preparation and Electrochemical Tests	41
4.2.3	Physicochemical characterization	42
4.3	ORR Performance Loss	42
4.4	Catalyst utilization via Tafel analysis	43
4.5	Degradation of carbon support	49
4.6	Pt degradation and interfacial interactions with carbon support	54
4.7	Conclusion	56
4.8	Appendix	57
4.8.1	Particle Size and roughness factor (<i>rf</i>) in acid	58

4.8.2	Langmuir adsorption isotherm and the available Pt sites for HPC_Acid	59
5	DEVELOPMENT OF IRIIDIUM-COBALT OXIDE AS AN ALTERNATIVE CATALYST FOR OXYGEN EVOLUTION REACTION (OER)	66
5.1	Abstract	66
5.2	Catalyst Synthesis and Testing Protocols	66
5.2.1	Catalyst Synthesis	66
5.2.2	Physicochemical Characterization	67
5.2.3	Electrochemical Tests	68
5.2.4	Turnover Frequency	69
5.2.5	Mass Activity Conversion	69
5.3	Material Characterization	69
5.4	Electrochemical Performance	72
5.5	Stability Insights	76
5.6	Conclusions	78
5.7	Appendix	79
6	INVESTIGATING MATERIAL SYNTHESIS CONDITIONS OF IRIIDIUM-COBALT ALLOY	94
6.1	Abstract	94
6.2	Modification of the Adam's Fusion Method	94
6.3	Characterization with Energy Electron Loss Spectroscopy (EELS)	95
6.4	Effect of Iridium-Cobalt (Ir-Co) Ratio	96
6.5	Effect of Surfactant and Acid Etching	109
6.6	Catalyst Stability Under Half-Cell and Full-Cell Conditions	120
6.7	Possible Influence of Iridium Oxidation State on OER Activity	123
6.8	Conclusions	129
6.9	Appendix	132
6.9.1	XPS Fitting Details	132
6.9.2	Error Propagation for Oxidation State from XPS	133
7	CONCLUSIONS	135
8	FUTURE WORKS	137

LIST OF FIGURES

1.1	The Keeling Curve recording the CO ₂ concentration in the atmosphere in the last six decades [2].	2
1.2	(a) Projections of global carbon emissions and (b) CO ₂ concentration under different Representative Concentration Pathways (RCP). Image obtained from Smith and Myers [6].	3
1.3	Cost projection of renewable energy sources such as solar PV, concentrating solar power (CSP), offshore and onshore wind energy. Figure and data obtained in 2018 by International Renewable Energy Agency (IRENA).	4
1.4	Total greenhouse gas emissions from different economic sectors in the US. Data collected from 1990-2019 by US Environmental Protection Agency (2021) [10].	5
1.5	CO ₂ emissions from different modes of transportation. Data from BEIS/Defra Greenhouse Gas Conversion Factors 2019 [12]	5
1.6	An infographic of hard-to-decarbonize sectors where direct electrification using battery storage is not feasible with the current state-of-the-art technology. Image obtained from Energy Transitions Commission [13].	6
1.7	Schematics of the H2@Scale initiative of the US Department of Energy (DOE) demonstrating the future of hydrogen economy as a pathway to decarbonization [14]	7
1.8	A schematic diagram of a hydrogen fuel cell showing the major component of the device. Image provided by Setra Systems, Inc [17]	8

1.9	A more detailed illustration of the different components of the fuel cell, including the catalyst layer, which is critical to the performance and durability of the device. Image obtained from Prof. Chuang's ME 262 lecture slides at UC Merced.	9
1.10	Generation of hydrogen from water electrolysis. Image obtained from US Department of Energy (DOE).	10
3.1	(a) An illustration of the half-cell electrochemical set-up with the reference electrode (RE), working electrode (WE), and counter electrode (CE) with gas bubbling condition. (b) Rotating disk electrode (RDE) or rotating ring disk electrode (RRDE) typically used as working electrodes.	20
3.2	Illustration of the concentration profile of the oxidant near the electrode surface [121].	21
3.3	Linear sweep voltammetry technique (LSV) used to assess the electrochemical performance of the electrocatalysts.	22
3.4	A cyclic voltammetry (CV) curve for platinum on carbon support (Pt/C) showing the different redox reactions at varying potentials. Image taken from the lecture slide of Prof. Chuang's ME 262 class at UC Merced.	24
3.5	A Nyquist plot of an impedance data from an electrochemical system and the imaginary part (I_m) and real part (Re) are indicated as y- and x-axis, respectively. Frequency is labeled as f with the decreasing magnitude from right to left [128]	26
3.6	Schematics of an EIS measurement where the input and output signal have the same frequency, but a phase angle exists when both signals are overlapped [130]	27
3.7	An illustration of the gas adsorption process for the surface area and porosity measurement [133]	29
3.8	A schematic of the ICP-MS process where a sample is being ionized using a plasma source [136].	30

3.9	A depiction of the X-ray diffraction process to study crystallographic information of materials [138]	31
3.10	Electron beam-sample interaction with at different depths and different signals for analyzing surface properties of materials [141] .	32
3.11	Different parts of a scanning electron microscopy (SEM) to study the morphology of materials [142]	33
3.12	A breakdown of the components inside a transmission electron microscope (TEM) [142]	35
3.13	Ray path for the STEM and TEM mode [147]	36
3.14	An illustration of EDS and EELS signals obtained from TEM [152]	38
3.15	X-ray photoelectron spectroscopy (XPS) for quantification of surface composition and chemical states [154]	39
4.1	Electrochemical acid degradation data (0.1 M HClO ₄) for LPC_Acid (a,c,e) and HPC_Acid (b,d,f) recorded every 1,000 cycles: (a,b) CV recorded in N ₂ -purged electrolyte, (c,d) changes in roughness factor and normalized C_{dl} and (e,f) LSV results in O ₂ -saturated electrolyte at 1600 rpm.	43
4.2	Electrochemical impedance spectroscopy (EIS) data in O ₂ -saturated 0.1 M HClO ₄ at 0.85 V with 1600 rpm recorded at beginning-of-life (BOL) and end-of-life (EOL) for (a) LPC_Acid and (b) HPC_Acid. Symbols represent raw data and dashed lines are the fitting results. (c) Total resistance ($R_1 + R_2$) as a function of cycle number along with the equivalent circuit used in the simulation.	45
4.3	Electrochemical data for alkaline degradation (0.1 M KOH) collected every 1,000 cycles: (a) CV results in N ₂ -saturated electrolyte, (b) roughness factor and normalized C_{dl} change, and (c) LSV curve in O ₂ -saturated electrolyte at 1600 rpm.	46

4.4	(a) Analysis with the Tafel approximation showing the model predicted and experimental values for kinetic current (i_k) in LPC_Acid. (b) Comparison of the model and experimental values of rf in HPC_Acid. (c) Correlation of the effective Pt area utilization (model predicted rf divided by experimentally measured rf) with the normalized C_{dl} for HPC_Acid.	48
4.5	Electrochemical impedance spectroscopy (EIS) response and the corresponding capacitance plots in N_2 -saturated 0.1 M $HClO_4$ at 0.4 V for (a,c) LPC_Acid and (b,d) HPC_Acid.	50
4.6	XPS peak deconvolution of C $1s$ spectrum collected from glassy carbon electrode coated with catalyst layers for (a) fresh, (b) LPC_Acid, (c), HPC_Acid, and (d) HPC_Alkaline samples.	52
4.7	TEM images for (a) fresh samples, (b) LPC_Acid, (c) HPC_Acid, and (d) HPC_Alkaline showing the different Pt particle distribution and physical degradation. Illustration of Pt particle evolution from (e) well-dispersed fresh sample to (f) LPC_Acid demonstrating severe Ostwald ripening and (g) agglomerated Pt particles in HPC_Acid with significant Pt detachment due to carbon corrosion. (h) Particle size distribution based on (a-c) comparing fresh and acid degraded samples.	55
4.8	Schematic illustration of the degradation of both Pt and carbon support after being subjected to different potential cycling condition in acid and alkaline electrolyte. Major degradation mechanisms are also listed for each accelerated durability test (ADT) conditions. . .	56
4.9	Tafel plots for (a) LPC_Acid, (b) HPC_Acid, (c) and HPC_Alkaline every 1,000 cycles. Symbols represent raw data and solid lines are simulation results.	60
4.10	Tafel slopes and exchange current density, i_0 , for (a) LPC_Acid, (b) HPC_Acid and (c) HPC_Alkaline every 1,000 cycles.	61
4.11	HPC_Acid normalized kinetic current (i_k) and roughness factor obtained from the experiment.	61
4.12	Fractional coverage of CO_x (θ_{CO_x}) as a function of concentration approximated using Langmuir adsorption model.	62

4.13	Effective Pt area utilization in HPC_Alkaline estimated by dividing the model predicted rf obtained from Tafel equation model with the experimentally measured rf	62
4.14	(a) Electrochemical impedance spectra and (b) capacitance plot for HPC_Alkaline in N ₂ -saturated 0.1 M KOH recorded at 0.4 V.	63
4.15	XPS survey spectra for fresh and degraded Pt/C samples.	63
4.16	XPS peak deconvolution of Pt $4f$ spectrum, showing the different Pt chemical states present in (a) fresh sample, (b) HPC_Acid, and (c) HPC_Alkaline.	64
4.17	SEM images for (a) fresh sample, (b), HPC_Acid, and (c) HPC_Alkaline.	65
5.1	A general schematic for the surfactant-assisted Adam's fusion method developed in this study as illustrated by Dr. Guangfu Li of Thermal and Electrochemical Energy Laboratory (TEEL).	67
5.2	(a) X-ray diffractogram of the three catalysts being compared as well as reference patterns for standard materials, (b) X-ray photoelectron spectra for Ir $4f$ and the deconvoluted peaks of the Ir chemical states among the samples. Electron micrographs and Ir and Co chemical mapping from EDS for (c,d,) IrCo and (e,f) IrCo_ae.	70
5.3	Cyclic voltammetry curves of IrO _x -C, IrCo and IrCo_ae in (a) acid and (b) alkaline media collected at 50 mv/s. (c) Compiled overpotential at 10 mA/cm ² and Tafel slopes of the three different catalysts. Linear sweep voltammetry at 20 mV/s in (d) acid and (e) alkaline media. (f). Turnover frequency (TOF) was estimated from the LSV curves at an overpotential of 250 mV in acidic and alkaline media.	72

5.4	(a) Activity loss after degradation in half-cell for acidic and alkaline media determined from the area under the LSV curves before and after the stability tests. The change in (b) electrochemically active surface area (ECSA) and (c) total resistance, $R_{ct} + R_1$, both obtained from electrochemical impedance spectroscopy (EIS) before and after the stability tests. Full-cell stability tests in (d) 0.5 M H_2SO_4 and (e) 1.0 M KOH at a fixed current density of 50 mA/cm ² and the corresponding metal concentration in the electrolytes after the test detected using inductively coupled plasma mass spectrometry (ICP-MS).	76
5.5	Electron diffraction for (a) IrCo showing the patterns for Co_3O_4 and IrO_2 rutile (101) and (d) possibly a Co-substituted IrO_2 matrix and (e) IrO_2 (101) in IrCo_ae. Lattice fringes for (b,c) IrCo showing Co_3O_4 (311) and IrO_2 (10) rutile while a reduced d-spacing for (f) IrCo_ae also supports Co-substituted IrO_2 matrix.	80
5.6	Chemical mapping of iridium and cobalt using energy-dispersive X-ray spectroscopy (EDS) for (a) IrCo and (b) IrCo_ae. Overlap images for Ir (green) and Co (red) are shown for both catalysts where a strong spatial correlation between the nanoparticles, represented as bright spots, and Ir distribution can be established. .	81
5.7	Scanning transmission electron microscope (STEM) images of commercial (a) IrO_x-C , (b) IrCo and (c) IrCo_ae	82
5.8	X-ray photoelectron spectra for O $1s$ in (a) commercial IrO_x-C , (b) IrCo and (c) IrCo_ae deconvoluted into four oxygen chemical states.	82
5.9	Deconvolution of Co $2p$ XPS result for (a) IrCo and (b) IrCo_ae showing the different Co compounds present in each catalyst.	83
5.10	Mass activity (i_{MA}) and Tafel plots in (a,b) 0.5 M H_2SO_4 and (c,d) 1.0 M KOH.	84
5.11	Nitrogen gas adsorption experiments for Brunauer–Emmett–Teller (BET) surface area measurements showing the (a) gas adsorption isotherm and (b) pore diameter distribution calculated from Barrett-Joyner-Halenda (BJH) method for the desorption branch. .	84

5.12	Cyclic voltammetry (CV) curves at different scan rates in (a-c) 0.5 M H ₂ SO ₄ and (d-f) 1.0 M KOH for the double-layer capacitance estimation. The corresponding catalyst are indicated in the plots.	85
5.13	Current density measured at 0.9 V at different scan rates in (a) 0.5 H ₂ SO ₄ and (b) 1.0 M KOH to obtain the double-layer capacitance from the slope of the line.	86
5.14	Cyclic voltammetry (CV) curves for the different catalysts, as indicated in the plots, in (a-c) 0.5 M H ₂ SO ₄ and (d-f) 1.0 M KOH. The upper potential limits are varied to observe different pseudocapacitive redox reactions happening in each catalyst.	87
5.15	Electrochemical impedance spectra obtained in (a-b) 0.5 M H ₂ SO ₄ and (c-d) 1.0 M KOH (a,c,) before and (b,d) after the stability test. Raw data are shown as symbols while the fitted result shown with the solid curves.	87
5.16	Comparison of the ECSA derived from EIS and the measured BET surface area for the different catalysts in both acid and alkaline media.	88
5.17	Rotating ring-disk electrode (RRDE) measurement at 0.4 V ring potential to study oxygen transport efficiency from the catalyst layer in (a,c) 0.5 H ₂ SO ₄ and (b,d) 1.0 M KOH.	89
5.18	Investigation of Ir dissolution in the catalysts using RRDE measurement by setting ring potential at 0.9 V in (a) 0.5 H ₂ SO ₄ and (b) 1.0 M KOH.	89
5.19	Detection of possible peroxide generated from the 2-electron OER pathway using RRDE at 1.4 V ring potential in (a) 0.5 H ₂ SO ₄ and (b) 1.0 M KOH.	90
5.20	Half-cell stability tests by performing 2,000 potential cycles from 0.4 to 1.4 V in (a-c) 0.5 H ₂ SO ₄ and (d-f) 1.0 M KOH.	90
5.21	Linear sweep voltammetry (LSV) curves at the end of the stability tests and the corresponding Tafel plots in (a,b) 0.5 H ₂ SO ₄ and (c,d) 1.0 M KOH.	91

5.22	Full-cell stability tests performed by holding the current density at 50 mA cm ⁻² for (a) IrO _x -C, (b) IrCo, and (c) IrCo _{ae} in both acidic and alkaline media.	91
5.23	X-ray diffractogram of the degraded (a) IrCo and (b) IrCo _{ae} electrodes after the full-cell stability tests in both acid and alkaline media. The full width at half maximum (FWHM) of the IrO ₂ (101) peak in (b) was estimated by fitting the Gaussian distribution for the (c) fresh IrCo _{ae} , (d) acid-degraded IrCo _{ae} and (e) alkaline-degraded IrCo _{ae}	92
5.24	Ir 4f X-ray photoelectron spectra of the degraded electrodes in (a-c) 0.5 H ₂ SO ₄ and (d-f) 1.0 M KOH. The data is deconvoluted for the different Ir chemical states in (a,d) IrO _x -C, (b,e) IrCo and (c,f) IrCo _{ae}	93
6.1	Chemical structure of Pluronic F-127, a surfactant used in the synthesis of the Ir-Co catalysts [192]	95
6.2	(a) X-ray diffractogram data for the Ir-Co samples. (b) Quantification of the Ir/Co molar ratio on the bulk using ICP-MS and on the surface using XPS. (c) Surface area measurement implementing the BET model for N ₂ gas adsorption experiment. . .	96
6.3	Transmission electron micrographs of (a) Ir ₂ Co ₈ , (b) Ir ₆ Co ₄ , (c) Ir ₈ Co ₂ and (d) IrO ₂	98
6.4	Chemical mapping results from STEM-EDS for (a-c) Ir ₂ Co ₈ , (d-f) Ir ₆ Co ₄ , and (g-i) Ir ₈ Co ₂ . Ir signals are shown in purple while Co is in green. Overlap images for the two metals for each sample are shown in a, d and g.	99
6.5	Chemical mapping results obtained from STEM-EELS experiments for (a,d,g) Ir ₂ Co ₈ , (b,e,h) Ir ₆ Co ₄ , and (c,f,i) Ir ₈ Co ₂ . Ir signals are shown in red while Co signals are colored green. The overlap images for the two metals are shown in g,h,and i.	100
6.6	Linear sweep voltammetry (LSV) data collected in (a) 0.5 M H ₂ SO ₄ and (b) 1.0 M KOH at 1 mV/s for samples with different Ir/Co ratios.	101

6.7	(a) Mass activity at 300 mV overpotential normalized to Ir mass estimated using stoichiometry for samples with different Ir/Co ratios. (b) Overpotential at 10 mA/cm ² in both acidic and alkaline media.	102
6.8	(a) Tafel plot derived from LSV in 0.5 M H ₂ SO ₄ as well as in (b) 1.0 M KOH. (c) Summary of the Tafel slopes for all samples with different Ir/Co ratios.	103
6.9	An equivalent circuit model used to fit the EIS data consisting of an inductor, L , solution resistance, R_{Ω} , charge transfer resistance, R_{ct} , double-layer capacitance, Q_1 , and resistance from diffusion/adsorption of intermediates coupled in R_1Q_2	104
6.10	Electrochemical impedance spectra in (a) 0.5 M H ₂ SO ₄ and (b) 1.0 M KOH for samples with different Ir/Co ratios.	104
6.11	Total resistance ($R_{ct} + R_1$) extracted from EIS in 0.5 M H ₂ SO ₄ and 1.0 M KOH for samples with different Ir/Co ratio.	105
6.12	Cyclic voltammetry curves collected at 50 mV/s for samples with different Ir/Co ratios in (a) 0.5 M H ₂ SO ₄ and (b) 1.0 M KOH . . .	106
6.13	Double-layer capacitance (C_{dl}) estimated at 0.9 V using different CV scan rates from 2 mV/s to 150 mV/s.	107
6.14	Comparison of electrochemically active surface areas (ECSA) obtained in acidic and alkaline media using (a) CV method and (b) EIS method.	108
6.15	(a) X-ray diffractogram data for the Ir ₆ Co ₄ samples prepared with and without surfactant and subjected to acid etching. (b) Quantification of the Ir/Co molar ratio on the bulk using ICP-MS and on the surface using XPS. (c) Surface area measurement implementing the BET model for N ₂ gas adsorption experiment. . .	109
6.16	Transmission electron micrographs of (a) Ir ₆ Co ₄ , (b) Ir ₆ Co ₄ -ae, (c) N-Ir ₆ Co ₄ and (d) N-Ir ₆ Co ₄ -ae.	111

6.17	Chemical mapping results from STEM-EDS for (a-c) Ir ₆ Co ₄ , (d-f) Ir ₆ Co ₄ -ae, (g-i) N-Ir ₆ Co ₄ and (j-l) N-Ir ₆ Co ₄ -ae. Ir signals are shown in purple while Co is in green. Overlap images for the two metals for each sample are shown in a, d and g.	112
6.18	Chemical mapping results obtained from STEM-EELS experiments for (a-c) Ir ₆ Co ₄ , (d-f) Ir ₆ Co ₄ -ae, (g-i) N-Ir ₆ Co ₄ , and (j-l) N-Ir ₆ Co ₄ -ae. Ir signals are shown in red while Co signals are colored green. The overlap images for the two metals are shown in g, h, and i.	113
6.19	Linear sweep voltammetry (LSV) data collected at 1 mV/s in (a) 0.5 M H ₂ SO ₄ and (b) 1.0 M KOH for Ir ₆ Co ₄ samples prepared with and without surfactant and subjected to acid etching.	114
6.20	(a) Mass activity at 300 mV overpotential normalized to Ir mass estimated using stoichiometry for Ir ₆ Co ₄ samples prepared with and without surfactant and subjected to acid etching. (b) Overpotential at 10 mA/cm ² in both acidic and alkaline media.	115
6.21	(a) Tafel plot derived from LSV in 0.5 M H ₂ SO ₄ as well as in (b) 1.0 M KOH. (c) Summary of the Tafel slopes for Ir ₆ Co ₄ samples prepared with and without surfactant and subjected to acid etching.	116
6.22	Electrochemical impedance spectra in (a) 0.5 M H ₂ SO ₄ and (b) 1.0 M KOH	117
6.23	Total resistance ($R_{ct} + R_1$) extracted from EIS in 0.5 M H ₂ SO ₄ and 1.0 M KOH for Ir ₆ Co ₄ samples subjected to different conditions.	118
6.24	Cyclic voltammetry curves collected at 50 mV/s in (a) 0.5 M H ₂ SO ₄ and (b) 1.0 M KOH for Ir ₆ Co ₄ samples subjected to different conditions.	119
6.25	Double-layer capacitance (C_{dl}) estimated at 0.9 V using different CV scan rates from 2 mV/s to 150 mV/s for Ir ₆ Co ₄ samples subjected to different conditions.	119
6.26	Comparison of electrochemically active surface areas (ECSA) obtained in acidic and alkaline media using (a) CV method and (B) EIS method for Ir ₆ Co ₄ samples subjected to different conditions.	120

6.27	Stability of the catalyst tracked as the change in the area of the LSV curve after performing 2,000 CV cycles between 0.4 to 1.4 V for (a) samples with different Ir/Co ratios and (b) Ir ₆ Co ₄ samples prepared with different conditions.	121
6.28	Full-cell stability tests in (a,c) 0.5 M H ₂ SO ₄ and (b,d) 1.0 M KOH at a fixed current density of 50 mA/cm ² for synthesized Ir-Co catalysts and acid etched counterparts.	122
6.29	Dissolved metals in the electrolyte after the full cell tests for (a,c) Ir and (b,d) Co in both 0.5 M H ₂ SO ₄ and 1.0 M KOH.	123
6.30	Deconvolution of Ir <i>4f</i> XPS peaks into three Ir chemical states: Ir ⁰ , Ir ³⁺ and Ir ⁴⁺ . The analysis was performed for (a) Ir black, (b) IrO ₂ , (c) Ir ₈₂ , (d) Ir ₆ Co ₄ , (e) Ir ₄ Co ₆ and (f) Ir ₂ Co ₈	124
6.31	Deconvolution of Ir <i>4f</i> XPS peaks into three Ir chemical states: Ir ⁰ , Ir ³⁺ and Ir ⁴⁺ . The analysis was performed for (a) Ir ₆ Co ₄ , (b) Ir ₆ Co ₄ -ae, (c) N-Ir ₆ Co ₄ , and (d) N-Ir ₆ Co ₄ -ae.	125
6.32	Quantification of the different Ir chemical states for samples with (a) different Ir/Co molar ratio and (b) Ir ₆ Co ₄ samples prepared under different conditions.	126
6.33	Second derivative EELS spectra of Ir samples from the Ir O _{2,3} edge. Peak shifts correlate with the oxidation state, as indicated by the reference materials IrCl ₃ for Ir ³⁺ and calcined IrOx_C for Ir ⁴⁺	127
6.34	Quantification of the different Co phases for samples with (a) different Ir/Co molar ratio and (b) Ir ₆ Co ₄ samples prepared under different conditions.	128

LIST OF TABLES

4.1	XPS analysis of C <i>1s</i> peaks for the fresh and degraded Pt/C. . . .	52
4.2	Impedance fitting parameters at 0.85 V obtained in O ₂ -saturated 0.1 M HClO ₄ with 1600 rpm.	57
4.3	Relative amount of different Pt chemical states from Pt <i>4f</i> XPS peak deconvolution on fresh and degraded samples and the average oxidation state calculated as weighted average from each chemical states.	57
5.1	Comparison of the Ir chemical states between the synthesized materials and the commercial catalyst.	71
5.2	Evaluation of iridium and cobalt atomic ratio from X-ray photoelectron spectroscopy (XPS) and inductively coupled plasma mass spectrometry (ICP-MS).	79
5.3	Tabulated results for the relative amounts of oxygen chemical states derived from O <i>1s</i> deconvolution in XPS for IrO _x -C, IrCo and IrCo _{ae}	82
5.4	Distribution of cobalt compounds identified in XPS from Co <i>2p</i> for IrCo and IrCo _{ae}	83
5.5	Surface area and pore size characterization obtained from the gas adsorption measurements for the different catalysts.	85
5.6	Double-layer capacitance obtained from the CV method and the estimated electrochemically active surface area (ECSA) of the different catalysts.	86

5.7	Values of the circuit elements for the fitted electrochemical impedance spectroscopy (EIS) data in 0.5 H ₂ SO ₄ and the calculated ECSA from the EIS-based capacitance.	88
5.8	Values of the circuit elements for the fitted electrochemical impedance spectroscopy (EIS) data in 1.0 M KOH and the calculated ECSA from the EIS-based capacitance.	88
5.9	Relative amounts of the different Ir chemical states estimated from XPS in the degraded electrodes after the full cell stability test. . . .	93
6.1	Porosity and surface area information for the different Ir/Co catalysts obtained from N ₂ gas adsorption experiment.	97
6.2	Values of the circuit elements for the fitted electrochemical impedance spectroscopy (EIS) data in 0.5 H ₂ SO ₄ and the calculated ECSA from the EIS-based capacitance.	105
6.3	Values of the circuit elements for the fitted electrochemical impedance spectroscopy (EIS) data in 1.0 M KOH and the calculated ECSA from the EIS-based capacitance.	106
6.4	Porosity and surface area information for the different Ir/Co catalysts obtained from N ₂ gas adsorption experiment.	110
6.5	Values of the circuit elements for the fitted electrochemical impedance spectroscopy (EIS) data in 0.5 H ₂ SO ₄ and the calculated ECSA from the EIS-based capacitance for Ir ₆ Co ₄ samples subjected to different conditions.	117
6.6	Values of the circuit elements for the fitted electrochemical impedance spectroscopy (EIS) data in 1.0 M KOH and the calculated ECSA from the EIS-based capacitance for Ir ₆ Co ₄ samples subjected to different conditions.	118
6.7	Relative fractions of Co phases determined from XPS as a function or Ir:Co ratios.	128
6.8	Relative fractions of Co phases from XPS as influenced by the presence of surfactant in the synthesis and acid etching process. . .	128

6.9	XPS fitting parameters for the deconvolution of Ir <i>4f</i> spectra. . . .	132
6.10	XPS fitting parameters for the deconvolution of Co <i>2p</i> spectra. . .	133
6.11	Comparison of the Ir fractions obtained for three data sets from Ir ₆ Co ₄	133
6.12	Comparison of the Ir fractions obtained for three data sets from Ir ₆ Co ₄ -ae.	134

LIST OF SYMBOLS

The list describes the mathematical symbols that has been used in this dissertation.

Γ	Standard charge to reduce a monolayer of protons on platinum
δ_O	Thickness of diffusion-convective layer
η	Kinetic overpotential
ν	Kinetic viscosity
v	Scan rate
ω	Frequency
B	Tafel slope
C^0	Reactant concentration
C_O^0	Oxidant concentration in the bulk
C_O^S	Oxidant concentration at the catalyst surface
C_{dl}	Double-layer capacitance
$I_{DC,O}$	Diffusion limited current density
$i_{DC,O}$	Diffusion-convection current density for oxidant species
E^0	Equilibrium potential
E_t	Electrode potential at instantaneous time
E_{RHE}	Potential with reference to reversible hydrogen electrode
E_{WE}	Experimentally obtained working electrode potential against reference electrode
$E_{0,RE}$	Standard potential of reference electrode against standard hydrogen electrode
I	Current
$I_{r,R}$	Ring limiting current
i_k	Kinetic current density
i_0	Exchange current density
i_d	Disk current
i_{dl}	Double-layer capacitive current
i_{lim}	Limiting current density
i_{MA}	Mass activity
L	Inductance
l	Catalyst loading
m_{Ir}	Iridium weight content

N	Collection efficiency
n	Number of electrons transferred
p	Equilibrium pressure
p_0	Saturation pressure
p/p_0	Relative pressure
Q_1	Constant phase element for the electric double layer
q_{Pt}	Hydrogen adsorption charge density
R_{ct}	Charge transfer resistance
R_{Ω}	Ohmic resistance from the bulk solution
R_2Q_2	Resistance and constant phase element from Diffusion/adsorption of reaction intermediate
rf	Roughness factor
t	Time
V	Voltage
v	Applied potential scan rate
y	Distance at vertical direction
Z	Impedance

Chapter 1

INTRODUCTION

1.1 The Climate Crisis and the Role of Hydrogen

1.1.1 Climate Change

The beginning of the industrial revolution in the mid-18th century propelled our society to advance — from steam engines powering trains, ships, and industrial types of machinery. The new source of energy at that time was burning coal, natural gas, and coal. This is followed by the invention of the internal combustion engine which changed the transportation sector and how we move things around the world [1]. Since then, our society has been totally dependent on the fossil fuel supply, which although we know is limited, we keep on exploiting them for our aggressive goal of industrialization. But this comes without a consequence as the uncontrolled burning of these fuels leads to a massive release of harmful gases, which collectively we call greenhouse gases (GHGs).

Carbon dioxide (CO₂) is one of the leading GHGs released into the atmosphere. It has been noted by a lot of research facilities around the world that the concentration of CO₂ in the atmosphere has been constantly increasing in the last few decades. The Keeling Curve, presented in Figure 1.1, monitored by the Scripps Institute of Oceanography at the University of California, San Diego is a great resource to track the CO₂ concentration in the atmosphere. The drastic increase of CO₂ concentration in the atmosphere is echoed in this chart, where recent data shows around 420 ppm of CO₂ in the atmosphere. This is significantly higher than the CO₂ level in 1750 at around 280 ppm.

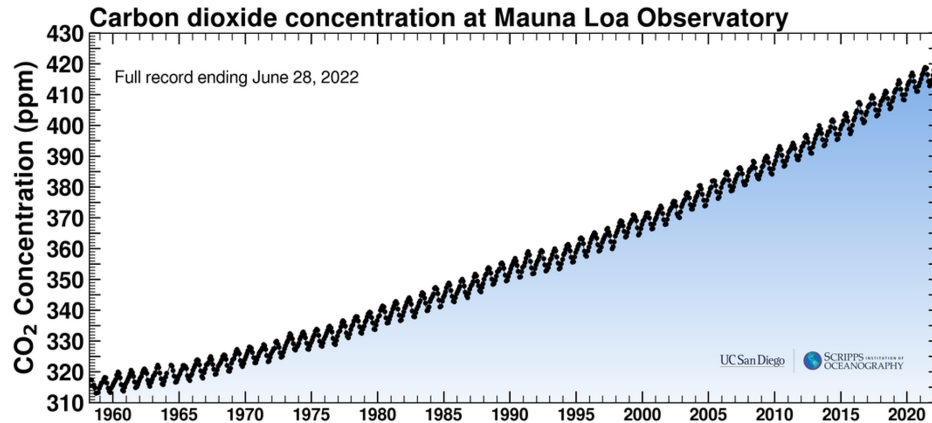


Figure 1.1: The Keeling Curve recording the CO₂ concentration in the atmosphere in the last six decades [2].

The increase in GHGs concentration is driven by the rising global population which in turn demands higher energy usage in recent years compared to previous decades. And the rest is history, where the world we live in right now is suffering from a phenomenon we call global warming. Global warming disrupted the normal daily activities of individuals, especially in developing nations. Climate change is real and is happening right in front of our very own eyes. We experience heatwaves, droughts, extreme flooding, melting ice caps, declining biodiversity, food insecurity, and the list goes on.

There is a consensus in the scientific community that climate warming in the last century is caused by anthropogenic activities [3]. The reports [4] from the Intergovernmental Panel on Climate Change (IPCC) strengthen the correlation between climate change and more frequent severe storms, floods, droughts, and other extreme weather disturbances. GHG emissions from fossil fuel burning endanger the human population but we can still alter the climate story if we collectively put an effort to adapt to the changes that are already happening.

Back in 2015, 196 parties signed the Paris climate agreement during the Conference of the Parties (COP) 21. The goal of this international treaty is to limit global warming to well below 2 °C, and preferably below 1.5 °C compared to the pre-industrial level [5]. This calls for both private and public entities to cooperate and promote a net-zero global economy. One clear path to mitigating global warming is to reduce our carbon emissions by shifting from fossil fuel-based energy to renewable energy systems.

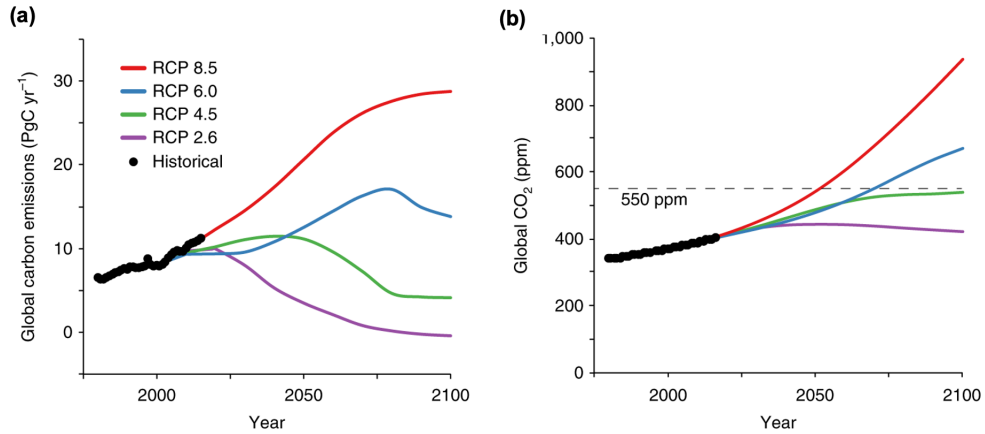


Figure 1.2: (a) Projections of global carbon emissions and (b) CO₂ concentration under different Representative Concentration Pathways (RCP). Image obtained from Smith and Myers [6].

For climate modelers, the concept of Representative Concentration Pathways (RCP) was introduced in 2011 by van Vuren [7] to predict the trajectories of CO₂ emissions and the resulting atmospheric concentration from 2000 to 2100. The four different RCPs, depicted in Figure 1.2, were based on some assumptions for the following parameters: population; economic growth; energy consumption and source; and land use. The scenarios are named from the “radiative forcing” that each of them produces in terms of Watts per square meter (W/m²). It is clear in Figure 1.2b that even after emissions were reduced, the CO₂ concentration continue to rise in RCP 4.5 and RCP 6.0. Thus, it is important that the relationship between emissions and CO₂ concentration in the atmosphere must be understood.

The RCP 8.5 is the worst possibility where the emissions continue to rise until stabilizing by 2100. However, in this case, the CO₂ concentration could reach 950 ppm by 2100 and continue to rise in the next 100 years. Population growth is predicted to be 12 billion by the end of the century, leading to intensive energy demands of about three times of the current levels. On the contrary, RCP 2.6 presents the best alternative where the anthropogenic causes of climate change are limited. In this scenario, the emissions are reduced to zero by the end of the century and the CO₂ concentration can be stabilized at current levels and the global temperature can be controlled at around 1°C compared to 1900’s level [8].

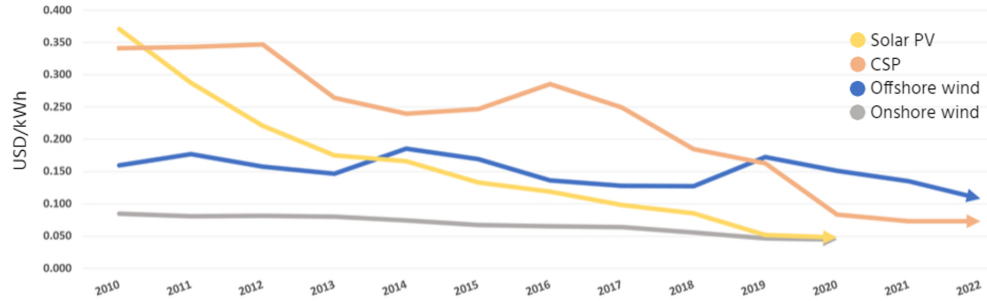


Figure 1.3: Cost projection of renewable energy sources such as solar PV, concentrating solar power (CSP), offshore and onshore wind energy. Figure and data obtained in 2018 by International Renewable Energy Agency (IRENA).

The scenario presented in RCP 2.6 can be a reality considering that recently, the price of renewable power is getting cheaper according to the latest report from the International Renewable Energy Agency (IRENA) in 2019 [9]. The historical and cost projection of the different renewable technologies are shown in Figure 1.3. This strengthens the role of renewable energy as a key to low-cost decarbonization and climate solution, aligning with the Paris agreement.

In the next decades, cost reduction is still expected according to IRENA, where three-quarters of onshore wind and four-fifths of solar PV to be commissioned net year will yield lower prices than the cheapest new coal, oil, or natural gas option. The price of onshore wind and solar PV could now fall in the range of \$ 0.03-0.04 per kilowatt hour (kWh) in areas with good resources and enabling regulatory and institutional frameworks. For instance, in countries such as Chile, Mexico, Peru, Saudi Arabia and United Arab Emirates, the levelized cost of electricity (LCOE) could drop as low as \$ 0.03 per kWh.

1.1.2 Sources of Greenhouse Gas Emissions

The GHG emissions in the US can be broken down according to different economic sectors, presented in Figure 1.4 from the US Environmental Protection Agency (US EPA) database [10]. The major emitters are from electricity at 25% primarily from the burning of coal, natural gas, and oil, and transportation at 29% coming from fossil fuels burned for road, rail, air, and marine transport. Globally, most of the transportation sector is powered by either gasoline or diesel. The transportation sector in California accounts for about 40% of the state’s emissions [11].

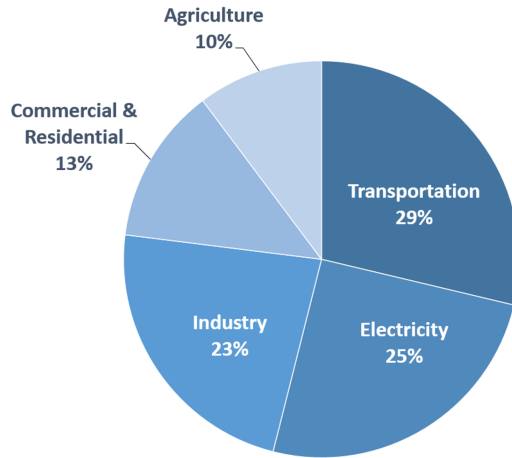


Figure 1.4: Total greenhouse gas emissions from different economic sectors in the US. Data collected from 1990-2019 by US Environmental Protection Agency (2021) [10].

The aviation sector is the leading emitter of GHGs, based on the data presented in Figure 1.5, along with buses besides passenger vehicles. While electric vehicles have been on the rise in recent years, the battery technology is still not mature enough for scaling up to electrify heavy-duty vehicles, aviation, and marine transport. The decarbonization of the transportation sector can significantly reduce our global GHG emissions and limit global warming.

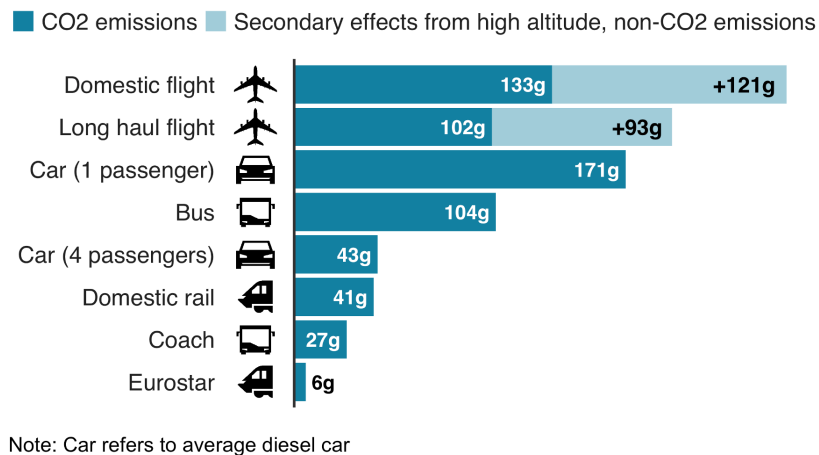


Figure 1.5: CO₂ emissions from different modes of transportation. Data from BEIS/Defra Greenhouse Gas Conversion Factors 2019 [12]

1.1.3 The Hydrogen Economy



Figure 1.6: An infographic of hard-to-decarbonize sectors where direct electrification using battery storage is not feasible with the current state-of-the-art technology. Image obtained from Energy Transitions Commission [13].

The declining cost of renewable energy and the improvement in battery technology have paved the way to decarbonizing electricity and energy storage. Now the challenge remains for the hard-to-decarbonize sectors, some of them shown in Figure 1.6. Altogether, they account for 30% of all emissions [13]. Direct electrification is not feasible for heavy industries and heavy-duty transport. To decarbonize these sectors, we need new technologies or improve the current existing technologies that have not yet reached full commercialization.

An option to decarbonize these heavy sectors is green hydrogen obtained from splitting water and powered by renewable energy like solar and wind. Some advantages of hydrogen include: it can be produced from diverse domestic resources or for export; having the highest energy content by weight among all fuels; it can enable zero or near zero emissions in transportation, stationary or remote power, and portable applications; it can be used as a responsive load on the grid to enable grid stability and energy storage at the same time enhance the utilization of power generators; and it can enable innovations in domestic industries such a transportation. Hydrogen serves as an essential feedstock in the petrochemical sector and as a fuel in the emerging fuel cell technology. There are still areas for hydrogen to expand its value proposition such as steel manufacturing, ammonia production, and others.

The US DOE has launched the H2@Scale initiative [14], illustrated in Figure 1.7, that aims to promote affordable production, storage, transport, and utilization of hydrogen to decarbonize and how it can interact with multiple sectors. Hydrogen

was even further promoted by DOE through the Energy Earthshots Initiative – a series of events to accelerate breakthrough discoveries for abundant, affordable, and reliable clean energy solutions in the decade. This aligns the aggressive goal of the current administration to push net-zero carbon by 2050. The first installment in this initiative is the Hydrogen Shot, which aims to reduce the cost of clean hydrogen to \$1 per 1 kilogram in 1 decade (“1 1 1”) [15].

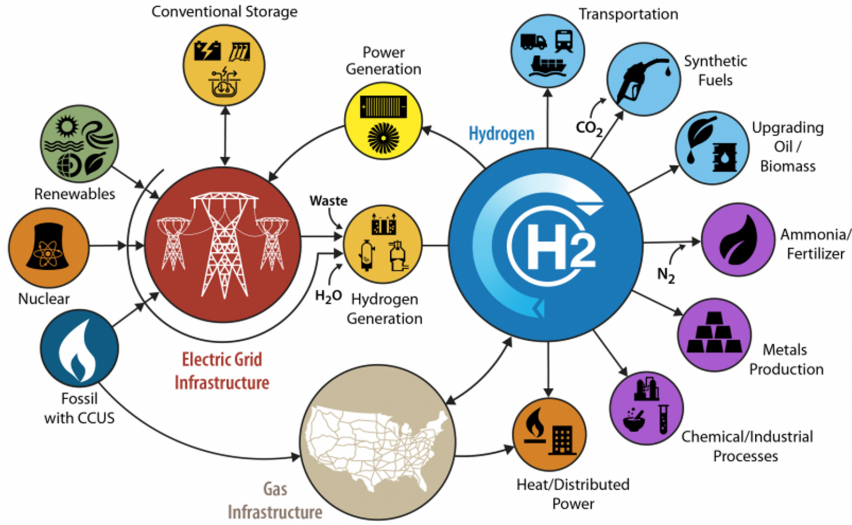
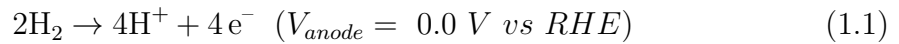


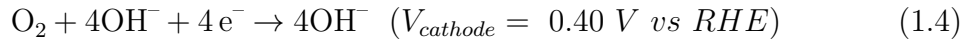
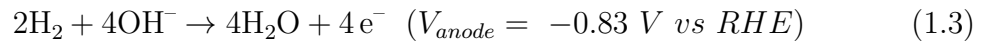
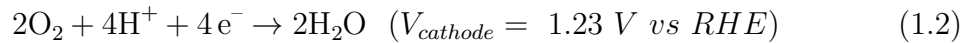
Figure 1.7: Schematics of the H2@Scale initiative of the US Department of Energy (DOE) demonstrating the future of hydrogen economy as a pathway to decarbonization [14]

1.2 Electrochemical Devices for Sustainable Energy

1.2.1 Fuel Cells

A fuel cell is an electrochemical device that converts chemical energy from hydrogen or other fuels directly to electricity. With hydrogen, the only products are electricity, water, and heat. The electrochemical reactions, hydrogen oxidation reaction (HOR) and oxygen reduction reaction (ORR), involved in the fuel cells are expressed in Equation (1.1) and (1.2) for acidic environment and Equations (1.3) and (1.4) for alkaline environments, respectively. The major components and schematics of fuel cell operation is presented in Figure 1.8. A fuel cell is comparable to a battery except that it does not need to be recharged. Rather, a constant supply of fuel is necessary to continue producing electricity and heat.





There are two electrodes in a fuel cell — the negative electrode or the anode and the positive electrode known as the cathode. The fuel is fed to the anode side while air or the oxidant is on the cathode side. On the anode side, there is a catalyst usually made of platinum that separates the hydrogen molecule into protons and electrons, and these two travel in different directions toward the cathode. The electron goes to an external circuit which then generates electricity. The protons, on the other hand, migrate through the electrolyte and combine with oxygen to produce water and heat [16].

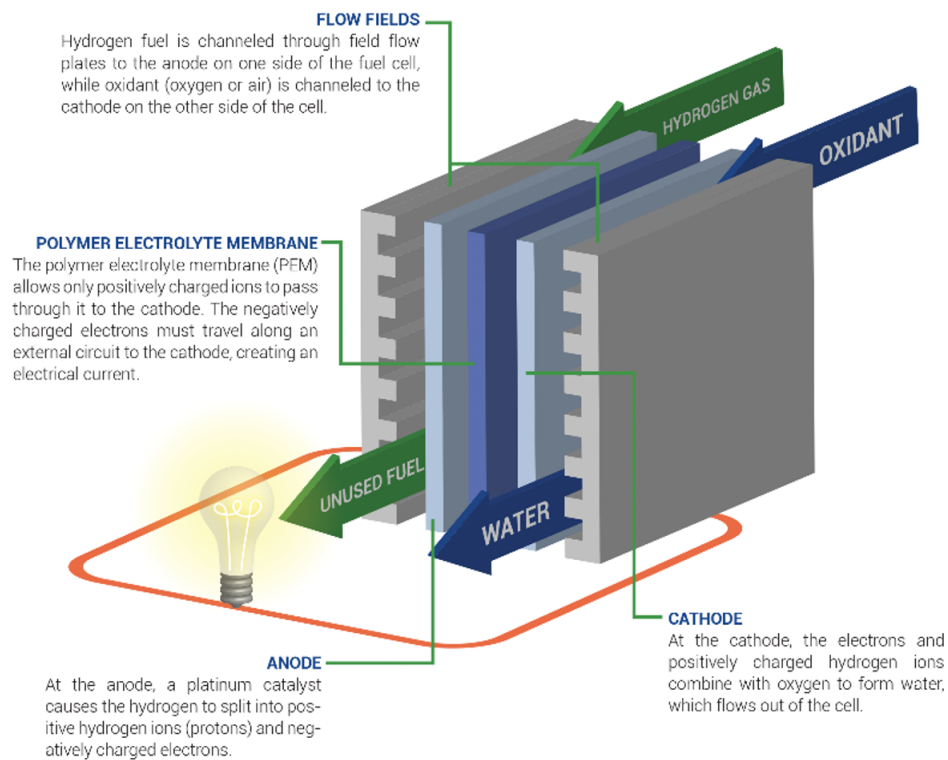


Figure 1.8: A schematic diagram of a hydrogen fuel cell showing the major component of the device. Image provided by Setra Systems, Inc [17]

There are different types of fuel cells depending on the operating conditions

and the type of fuel used. For this dissertation, the focus would be on polymer electrolyte membrane fuel cells (PEMFC), which have been commercialized in fuel cell vehicle applications. The main parts of the PEMFC are shown in Figure 1.9. The membrane electrode assembly (MEA), which consists of membrane, catalyst layer, and gas diffusion layers (GDL), is considered the heart of the PEMFC. The membrane, which is typically Nafion[®] manufactured by DuPont, conducts only protons and blocks electrons. This membrane is usually very thin, under 20 microns, for applications in the automotive industry. On the two sides of the membrane is the catalyst layer made of nanosized platinum dispersed on a high-surface area carbon support. An ion-conducting polymer, known as ionomers, is mixed to act as both binder and ion-conducting pathways. The catalyst layer is sandwiched between the membrane and the GDL. The role of the GDL is to facilitate reactant transport and the removal of water. GDLs are usually made of carbon paper, in which carbon fibers are partially coated with polytetrafluoroethylene (PTFE). There are also hardware components that are incorporated with the MEA such as gaskets that provide a seal around the MEA, preventing leakage of gases, and bipolar plates used to assemble individual PEM fuel cells into a stack that also serve as flow fields or channels for gaseous fuel and air [18].

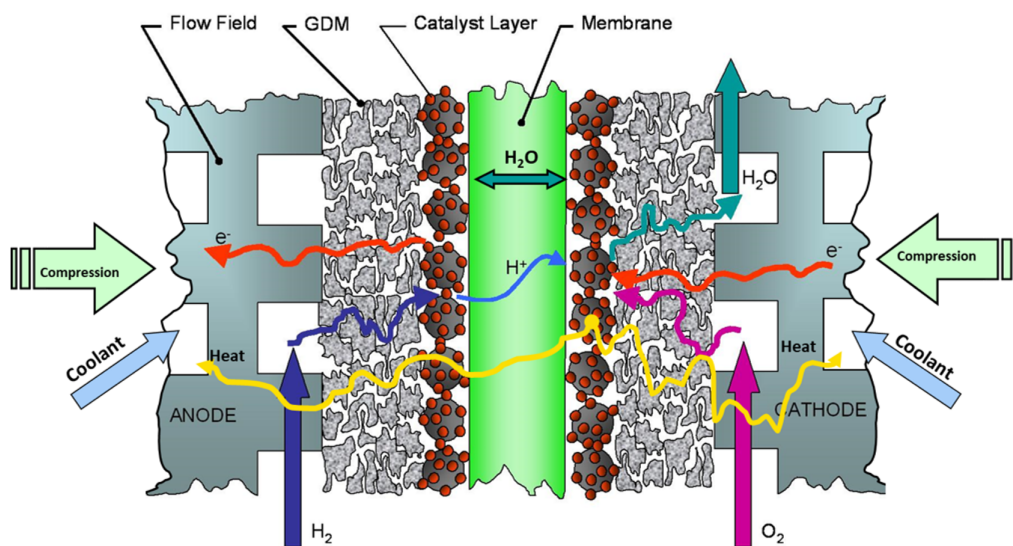


Figure 1.9: A more detailed illustration of the different components of the fuel cell, including the catalyst layer, which is critical to the performance and durability of the device. Image obtained from Prof. Chuang's ME 262 lecture slides at UC Merced.

Fuel cells offer several advantages over conventional combustion-based technologies for power generation and automotive applications. Fuel cells can operate with much higher efficiencies, usually exceeding 60%. With hydrogen as fuel, the only emission from a fuel cell is water, thus presenting a climate solution associated with carbon dioxide emissions. Since there are no moving parts, fuel cells operate quietly.

1.2.2 Electrolyzers

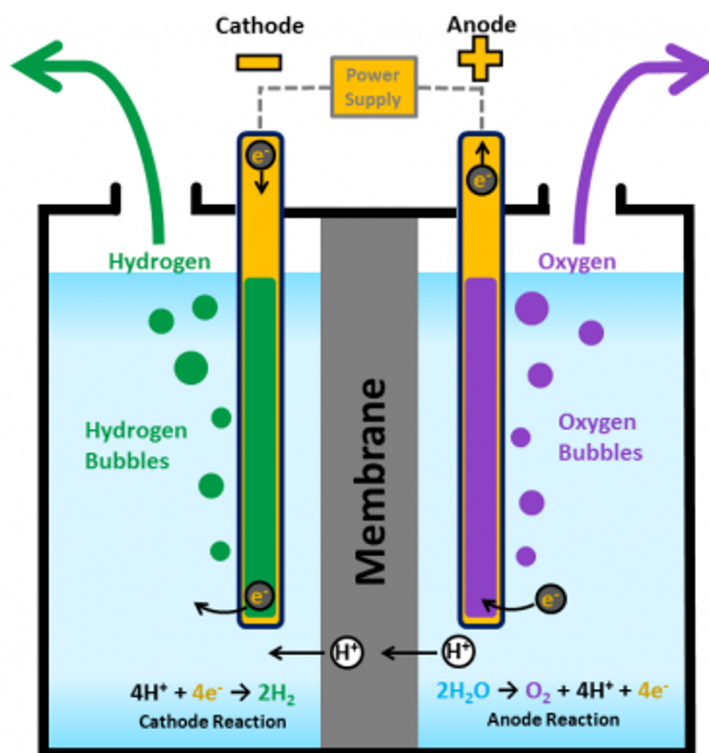
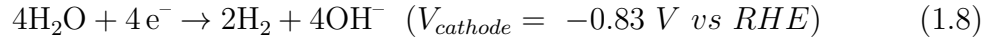
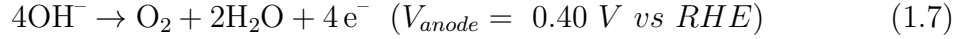
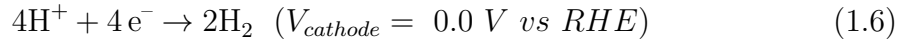


Figure 1.10: Generation of hydrogen from water electrolysis. Image obtained from US Department of Energy (DOE).

An electrolyzer is another electrochemical device that complements a fuel cell for hydrogen production. Hydrogen is generated via water splitting using renewable energy sources in a process known as electrolysis, and Equations (1.5) and (1.7), and Equations (1.6) and (1.8) illustrates the oxygen evolution reaction (OER) and hydrogen evolution reaction (HER) in both acidic and alkaline media, respectively. An electrolyzer unit can vary in size from small, appliance-size to large-scale central production facilities that can be tied to renewable electricity production. Since only

an electrochemical reaction is necessary, water electrolysis does not need any moving parts just like in fuel cell. This process can produce hydrogen at high purity in a non-polluting method unlike in conventional steam methane reforming process. The reaction happening in an electrolyzer is just the opposite of the fuel cell. A typical schematic for the water electrolysis processes shown in 1.10. For fuel cells, the anode is where the hydrogen is consumed but in electrolyzers, hydrogen is produced on the cathode side. Electrolyzers are ideal to be incorporated in stationary, portable, and transportation power systems. Since a significant amount of hydrogen can be produced, it is beneficial to couple it with any system with solar or wind power [19].



There are also different types of fuel cells depending on the condition and the electrolyte used. In this dissertation, it will be focused on the same membrane-based technology like in PEMFC, but for electrolysis application, it is called polymer electrolyte membrane water electrolyzer (PEMWE). Water reacts at the anode to form oxygen and proton. The electron supplied by a power supply travels through an external circuit. The proton would then travel across the membrane until it meets with the electron at the cathode side forming hydrogen [20].

Chapter 2

LITERATURE REVIEW

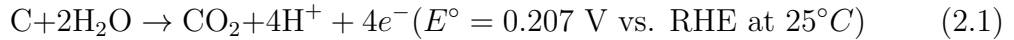
2.1 Catalyst Layer Degradation in Fuel Cells

Clean and efficient energy technologies are currently in demand to address the issues of environmental pollution and the finite fossil fuel supply. Fuel cells are alternative energy conversion devices that offer eco-friendly solutions for both transportation and stationary applications [21]. A polymer electrolyte membrane fuel cell (PEMFC) is one of the most common types of fuel cell that can convert hydrogen and oxygen gases to generate electricity, with water as a by-product [22, 23]. The PEMFC has a niche application in the automobile industry, as demonstrated by the release of commercially available PEMFC vehicles in recent years [24, 25]. However, one of the critical issues of PEMFC is the long-term durability that needs to be met before mass production [26–28].

Ideally, a PEMFC shall meet or exceed the durability requirements of an internal combustion engine to be competitive [29]. For automotive application, the US Department of Energy (DOE) has set an ultimate target of 8,000 hours or equivalent to 150,000 miles of driving with less than 10% loss in performance [30]. These stringent targets shall be met at various operating and ambient conditions, such as dynamic automotive driving load cycles, start-stop operation, road vibrations and shocks and extreme weather from hot and dry to sub-freezing. The highly dynamic operating conditions of PEMFC requires robust and durable materials. Recent findings reveal that the majority of the performance losses are related to the degradation in the catalyst layer (CL) [31], which typically consists of platinum (Pt) nanoparticles dispersed on a carbon support mixed with ionomer electrolytes. Possible degradation modes within the CL can be attributed to Pt loss, ionomer degradation and carbon corrosion [32–35].

During typical operation of a PEMFC, Pt nanoparticles can be agglomerated or detached from the carbon support, reducing the electrochemically active surface area (ECSA) that leads to performance losses [32]. Further, the cycling of the cathode potential could oxidize and reduce Pt surface atoms and result in Pt metal dissolution into ionic species (Pt^{2+}) in the electrolyte. The Pt ions can then be redeposited onto an existing Pt nanoparticle in a process known as Ostwald ripening

[35, 36]. Larger Pt nanoparticles are formed, which also causes a reduction of the Pt surface area, hence losing ECSA [37]. Besides the catalyst, the carbon support can also undergo oxidation reaction causing additional performance loss [38]. The carbon oxidation reaction (COR) and its thermodynamic equilibrium potential under standard conditions can be written as [38]:



Since the reversible potential of COR is less than cathode potential, which is between 0.4 V and 0.9 V under normal fuel cell operating conditions, the carbon support is theoretically unstable. Due to the slow kinetics of the COR, carbon oxidation is mostly negligible at potentials \leq 0.9 V vs. RHE, making it still useful in the cathode CL. However, the potential at open circuit voltage and start-up and shut down (SU/SD) conditions can easily exceed 0.9 V, leading to oxidation of carbon structure or carbon corrosion [39, 40]. Carbon corrosion promotes particle detachment, decreased electrical conductivity, collapse of pore structure and changes in the carbon surface characteristics [41]. It has also been shown that the presence of Pt nanoparticles can catalyze the COR in the presence of water [29, 42, 43]. Hydrogen starvation conditions, where localized regions are temporarily starved of hydrogen, can also cause carbon corrosion at the anode side even under typical fuel cell operating potentials [40, 41]. The combining effects of these conditions make carbon corrosion a major concern in the long-term stability of fuel cells.

Strategies to enhance the lifetime of PEMFCs have been heavily studied, which involves engineering and material solutions [39, 44]. The system level solutions include: (1) limiting cathode voltage to avoid carbon corrosion induced by SU/SD processes and to maintain the carbon support within a safe operating envelope, (2) minimizing local and gross fuel starvation, (3) optimizing cathode outlet opening size, etc. [29]. However, this makes the operation and implementation of PEMFC vehicles more complicated and costly. The other solution to enhance PEMFC durability without complicating the system involves the development of new materials as alternative Pt support. Recently, metal oxides have received strong attention as a possible replacement for carbon [45–47]. Titanium dioxide (TiO_2) is the one of the leading candidates considering its electrochemical stability and resistance to acid dissolution. However, TiO_2 suffers from low electron conductivity that needs to be addressed and has been the focus of many works [48–50]. Researchers also tried graphitic carbon, which has better stability [39], and incorporated it with functional groups and/or other species to have better Pt dispersion [51–55]. However, none of these alternative materials have proven to be successful in commercial scale and there are still technical barriers that needs to be addressed for practical applications [56, 57].

To evaluate the durability of PEMFCs, accelerated durability tests (ADTs) were developed by different groups, such as US DOE, US DRIVE Fuel Cell Tech Team (FCTT), Japan Automobile Research (JARI) and Fuel Cell Commercialization Conference of Japan (FCCJ). These ADTs all involve potential cycling with triangular or square-wave profiles at different potential ranges and ramp rates. The ADTs allow accelerating degradation in a short time to simulate practical conditions for longtime performance. Running the ADTs on a single fuel cell test station can then be used to assess the performance degradation of catalyst, catalyst support and membrane. However, the performance degradation is resulted from different parameters and components, which makes the analysis of various degradation mechanism difficult to deconvolute. Therefore, half-cell tests by means of a rotating disk electrode (RDE) are often used to evaluate catalyst activity and durability [34, 58–63]. Although the RDE test does not reproduce the environment of testing a real PEMFC, the main mechanisms of catalyst degradation can be directly investigated to improve fundamental understanding.

ADT protocols meant to study carbon corrosion are usually performed in the potential range of 1.0 – 1.6 V vs. RHE [34, 59, 64, 65]. Within this range, it is believed that Pt dissolution is minimized due to the formation of passivated layer from Pt-oxide [66] and activity losses can be solely accounted to carbon corrosion. However, Sharma and Anderson [65] reported that the ADT meant for carbon corrosion resulted to about 50% ECSA loss due to Pt particle growth. It was also shown that even with low potential cycling range, i.e. 0.6 – 1.0 V vs. RHE, carbon corrosion would still occur at low rates [29, 59]. Thus, discriminating these two degradation modes is not very direct with potential cycling range.

It has been well established that Pt can catalyze the oxidation of carbon through the formation of carbon surface oxides even at potentials below 1.0 V vs. RHE [29, 42, 43, 67]. But the influence of carbon surface oxides during activity measurement has not been reported in the literature. In alkaline environment, there are limited studies [68–70] discussing carbon corrosion with high potential range cycling ADTs. Early study suggest that the mechanism would be different in acid and alkaline, as demonstrated for glassy carbon electrode [71]. It would be interesting to see how, in the presence of Pt, will carbon corrosion be different in acid and alkaline media and how the formation of carbon surface oxides can alter activity measurements.

To better design catalysts, a detailed investigation of the degradation mechanism of the baseline material is necessary to ascertain the phenomena that are deleterious to the PEMFC performance. In this work, we applied two ADT protocols recommended by US DOE [64] to investigate the corresponding degradation mechanisms. The role of pH on the degradation mechanism of both Pt and the

carbon support was also evaluated. Electrochemical testing and physico-chemical characterizations were performed to analyze the changes in catalyst activity and the structure of the commercial materials after degradation. Particular interest was given to the degradation of carbon support, where multiple steps are involved including the formation of surface oxides.

2.2 Catalyst Development for Water Electrolyzers

Contemporary environmental concerns, such as rapidly accelerating global warming coming from fossil fuel usage, have pushed the transition from non-renewable, carbon-based energy dependence toward clean, low-carbon energy sources. By 2050, it is projected that the contribution of renewable energy in the energy mix will be 3 to 5 times greater than the current amount. Thus, a new energy carrier to store the growing share of decarbonized primary energy [72] is necessary. Hydrogen is one of the options as alternative energy storage over battery, owing to its unique electrochemical properties, high energy density, and covalent and chemical bonds that facilitate its mechanism to store and move energy [73]. Paradoxically, current production methods of hydrogen heavily rely on fossil fuels through steam methane reforming (SMR). In SMR, about 10 tons of carbon dioxide per ton of hydrogen ($t_{\text{CO}_2}/t_{\text{H}_2}$) is generated from natural gas [74]. An eco-friendly alternative for hydrogen generation is water electrolysis [75, 76], if coupled with grid-scale renewable energy technologies, like solar photovoltaics or wind [77].

The actual operating voltage and efficiency of water electrolyzers depend on the kinetics of the reactions and the design of the electrolyzer system [78]. The challenge in water electrolysis technology is the sluggish kinetics of the anode oxygen evolution reaction (OER) that has a large overpotential. Therefore, it requires an operating potential that is much higher than the reversible potential of 1.23 V. The mechanism of OER is not yet fully understood, and an ideal catalyst in terms of activity, stability, and cost is yet to be determined [79]. To improve the efficiency of the electrolyzers, significant efforts have been devoted to the understanding of OER and the development of high-performance and robust OER electrocatalysts [80–83]. Metal oxides are so far the best option for OER, considering their activity and stability [84, 85]. The leading choice and the most commonly used catalyst for OER is iridium oxide (IrO_2) [86]. However, this noble material is scarce and expensive for large-scale applications. In addition, stability issues of Ir-based catalysts also need to be understood at a fundamental level to develop mitigation strategies and increase the lifetime of the catalyst [87, 88].

Iridium oxide (IrO_2) is considered the state-of-the-art catalyst [89, 90] for the oxygen evolution reaction (OER) in water electrolysis to produce green hydrogen. This precious metal oxide can operate at low overpotentials with practical current

density in addition to its stability in corrosive environments typical for electrolysis. However, iridium is one of the least abundant metals, comprising only about 3×10^{-6} parts per million on Earth’s crust [91] and global annual production of only 7.25 tons [92]. The limited availability of iridium makes it expensive, thus hindering the economic viability of water electrolyzers for wide scale decarbonization. In addition, the activity of IrO_2 is still not optimized in the volcano plot, which connects the rate of reaction to a particular descriptor [78]. The binding energetics of iridium oxide with oxygen intermediates is suboptimal, a parameter that is highly correlated with OER activity.

Alloying IrO_2 with other low-cost metals can help reduce the precious metal loading if the performance of such catalyst is similar to that of IrO_2 [93]. Also, alloying has the potential to tune the catalyst intrinsic activity, especially considering Ir oxides have suboptimal oxygen intermediate binding energetics, which is highly correlated with OER activity [94]. Ir-based bimetal alloys in the literature include Ir-Co and Ir-Ni nanowires [95], thin films with Sn, Ti, Ni, and Cr [93], porous microsphere of Ir-Mo mixed oxides [96], and Ir-Y pyrochlores [97]. There are also evidence in the literature that alloying can modulate the electronic structure and improve oxygen binding energetics of IrO_2 [93]. Combining IrO_2 with another metal can also modify the surface chemical properties of the catalyst, creating more active species [82], and improving OER activity. Bimetal Ir-based systems are also described to have improved site-specific activities [95], tunable stoichiometry, and crystallinity [96]. The non-noble metal combined with Ir can undergo dissolution either during the OER process [97] or through acid leaching/etching [95] or dealloying process [98]. The removal of the other metal can create highly active IrO_x layers beneficial for OER. Cobalt is one of the transition metals that could modify the intrinsic activity of Ir aside from its moderate activity for OER as cobalt (II,III) oxide (Co_3O_4) [84, 99–101]

To further improve the activity and stability of the catalysts, researchers perform acid etching on their synthesized materials [95, 102]. Acid etching is performed to preferentially remove Co and the majority of the template material as well as to enhance the porosity of the material to facilitate more active sites for the surface reactions. However, one concern over iridium-cobalt alloys in the literature is that their synthesis procedure has not yet been established well for large-scale production and a detailed analysis on the activity and durability in both acidic and alkaline media is still lacking.

The success of platinum-cobalt (Pt-Co) alloy utilized in the commercial fuel-cell vehicle Toyota Mirai [103] drives the motivation to develop a similar bimetal catalyst system for commercial-scale water electrolyzers. In Pt-Co alloys, it has

been reported that several parameters need to be controlled for heavy-duty applications. These parameters include Pt shell and Pt:Co ratio, crystal structure, carbon structure, as well as Co stabilization, etc. [104]. Similar to Pt, there are also efforts to develop Ir-Co catalysts with different synthesis approach [95, 102, 105–107]. However, unlike in the Pt-Co system which has been used commercially and exhaustively studied, a state-of-the-art commercial Ir-Co catalyst is yet to be developed, and identifying the desired physicochemical properties to balance both activity and stability must be known.

For a pure Ir-based catalyst, it has been shown in recent studies that high OER activity can be ascribed to quasi-amorphous, nanocrystalline Ir(OOH) [108]; high surface concentration of Ir³⁺ and OH [109]; a mixture of tetragonal and orthorhombic phases [110]; and hollandite-like structural domains cross-linked with undercoordinated oxygen/iridium atoms [111]. However, the influence of another metal on these desired Ir properties is still not known. Also, the possible synergistic effects with Co for both activity and stability need to be considered. Thus, the synthesis approach and parameters must be carefully planned to optimize the OER activity and stability. Another consideration for the synthesis method is the scalability of the process, avoiding sophisticated processes and toxic and environmentally harmful chemicals.

Adam’s fusion method is a conventional synthesis route for the production of platinum oxide catalysts at industrial scale [112, 113]. This method has also been adapted for the preparation of IrO₂ nanoparticles, as reported by others [97, 108, 114, 115]. In Adam’s fusion, an Ir metal precursor is combined with a nitrate salt, forming iridium nitrate, and then thermally decomposed through calcination to produce IrO₂ [113]. Bimetal oxide from Adam’s fusion can also be produced, such as iridium-titanium mixed oxide [116].

Different synthesis parameters in Adam’s fusion method can affect the material properties like crystallinity, oxidation state, surface area, etc. For instance, at higher calcination temperatures, IrO₂ becomes more crystalline and the OER stability improves but the surface area and activity are compromised [114, 117]. The OER activity and stability of catalysts are heavily influenced by the structural or morphological properties [118], thus effective control of the shape, size, and atomic arrangements is critical. Surfactants are typically used in the synthesis to aid in the proper control of catalyst morphology [119, 120].

This research examines the use of iridium-cobalt oxide as an electrocatalyst for oxygen evolution reaction to produce hydrogen via water electrolysis. An equimolar IrCo oxide was synthesized through a simple and scalable surfactant-assisted Adam’s fusion method and electrochemically tested both acidic and alkaline media. In this work, it is demonstrated that an IrCo alloy has an improved electrochemical

performance over the commercial $\text{IrO}_x\text{-C}$ and was further enhanced by performing acid etching. However, there is a trade-off in stability as acid-etched Ir-Co suffered a significant activity degradation, especially in the alkaline media. Combining the electrochemical analyses and physicochemical characterization results, the relationship between IrCo oxide catalyst structure and performance is elucidated. Insights regarding the catalyst degradation mechanisms in acidic and alkaline media are also examined. The results from this work would provide some guidelines as to the effective synthesis of catalysts, tailoring the design to enable the balance of both activity and stability with a much cheaper catalyst than the commercially available $\text{IrO}_x\text{-C}$.

In this work, the synthesis parameters in a surfactant-assisted Adam's fusion method to produce iridium-cobalt (IrCo) alloy catalysts, the resulting physicochemical properties, and the proceeding correlation with the OER activity and stability are also systematically studied. Specifically, the effects of (1) iridium and cobalt ratio, (2) the presence of surfactant, (3) acid etching process, (4) and the interaction of these variables on the material properties are investigated. Results from advanced characterization techniques and electrochemical studies are bridged to understand the structure-property relationship.

Chapter 3

EXPERIMENTAL TOOLS

3.1 Electrochemical Methods

3.1.1 Rotating Disk Electrode (RDE) and Rotating-Ring Disk Electrode (RRDE)

An important tool to evaluate electrocatalysts in half-cell environment is rotating disk electrode (RDE). With the RDE apparatus, there is a precise control of electrode rotating rate and control of the diffusion layer thickness. Central to RDE theory is the convection of electrolyte solution [121]. For a rotating ring disk electrode (RRDE), a second working electrode in the form of a ring around the central disk-working electrode is added [122]. This can be useful to study multielectron processes, kinetics of a slow electron transfer, adsorption/desorption steps and electrochemical reaction mechanisms. An illustration of these two apparatus is shown in Figure 3.1b and when they are used as a working electrode shown in Figure 3.1a.

RDE and RRDE techniques are considered hydrodynamic methods that involve convective mass transport of reactants and products. In hydrodynamic methods, a steady state is attained quickly, and high precision measurements can be done. Double-layer charging is also eliminated in the measurement. Since the rate of mass transfer at the electrode surface is much larger than diffusion alone, the contribution of mass transfer to the electron-transfer kinetics is typically reduced [123].

For convective electrode systems, the diffusion-convection current density for an oxidant species ($i_{DC,O}$) can be obtained from the convective-diffusion and hydrodynamic equations, and the final equation is shown in Equation (3.1):

$$i_{DC,O} = nFD_O \frac{C_O^0 - C_O^S}{\delta_O} \quad (3.1)$$

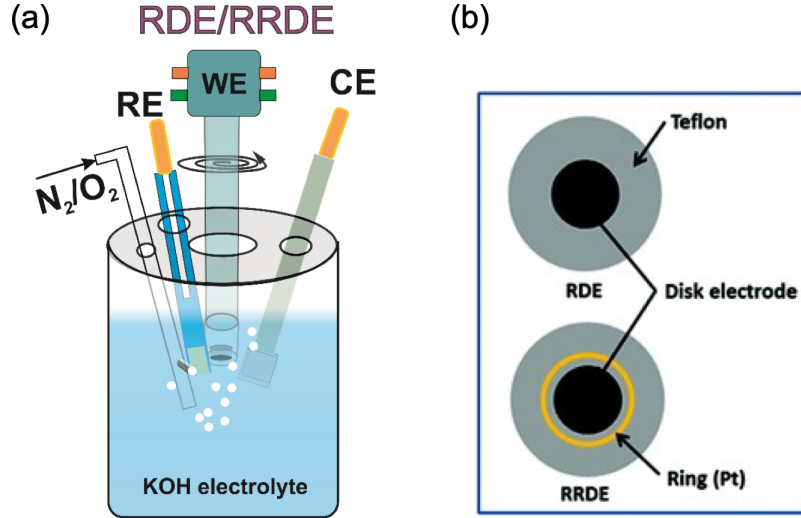


Figure 3.1: (a) An illustration of the half-cell electrochemical set-up with the reference electrode (RE), working electrode (WE), and counter electrode (CE) with gas bubbling condition. (b) Rotating disk electrode (RDE) or rotating ring disk electrode (RRDE) typically used as working electrodes.

Where n is the number of electrons transferred, F is the Faraday's constant (96,485 C/mol), D_O is the diffusion coefficient of the oxidant, δ_O is the thickness of the diffusion-convection layer, and C_O^0 and C_O^S are the oxidant concentration at the bulk and at the electrode surface [121]. When C_O^S approaches zero, $i_{DC,O}$ reaches maximum and is called the diffusion limited current density ($I_{DC,O}$):

$$I_{DC,O} = nFD_O \frac{C_O^0}{\delta_O} \quad (3.2)$$

By approximating δ_O from the convection kinetic theory:

$$I_{DC,O} = nFD_O^{2/3} \nu^{-1/6} y^{-1/2} v_y^{1/2} C_O^0 \quad (3.3)$$

Where ν is the kinetic viscosity, y is the distance at the vertical direction and v_y is the solution flow rate.

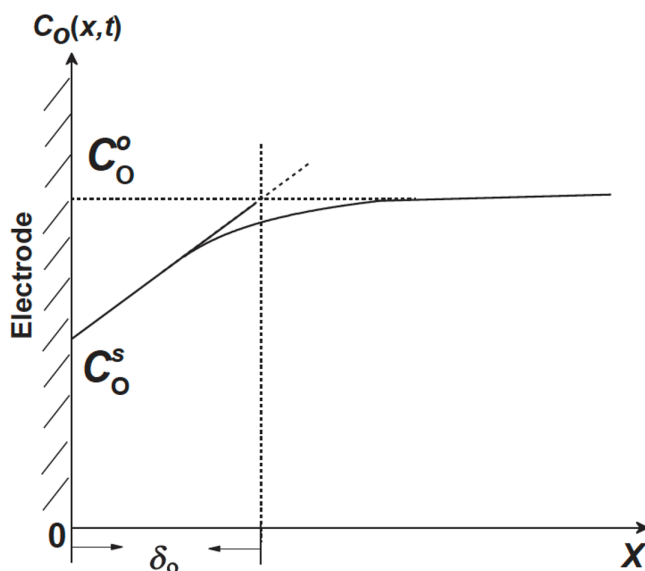


Figure 3.2: Illustration of the concentration profile of the oxidant near the electrode surface [121].

In the RDE, since the products of the electrode reaction is continuously swept away from the disk surface, studying the reverse reaction is not possible. Thus, by adding an additional electrode in the form of ring electrode surrounding the disk makes it possible to study the reverse reaction. From the current measurement at the ring, information regarding the disk reaction can be known. When conducting RRDE, the whole system is rotated and this spinning motion drags the electrolyte solution to the surface due to centrifugal force, The solution is then thrown outwards from the center in the radial direction. The product formed at the disk is then swept to the ring by the radial flow and then oxidized or reduced back to the original reactant. The ring and disk potential can be controlled independently, depending on the targeted reactants.

RRDE experiments are typically conducted with a bipotentiostat since two potentials are being probed, disk and ring potential. Different kinds of experiments can be conducted with RRDE such as collection experiments, where the ring is used to investigate species generated from the disk and shielding experiments, where the disk reaction perturbs the flow of the bulk electroactive species to the ring [123]. In collection studies, the reaction mechanisms can be elucidated from the detection of reaction intermediates or products at the ring. This method has been widely used in ORR studies where the disk can generate either water or peroxide via a four-electron or two-electron process, respectively [122].

An important parameter that needs to be determined in RRDE experiment is the collection efficiency (N), which measures the percentage of the disk product that can be detected on the ring electrode. By determining the disk current (i_d) and ring limiting current, N can be estimated. When the reaction is a steady-state process, and the ring electrode current is at limiting current ($I_{r,R}$) and the disk product does not undergo any chemical decomposition, N can be calculated using Equation (3.4). Since RRDE is a universal tool, the determination of N should be intrinsic and independent on the reaction studied. Only the geometric sizes of the disk and ring determines the N [122].

$$N = \left| \frac{I_{r,R}}{i_d} \right| \quad (3.4)$$

3.1.2 Linear Sweep Voltammetry (LSV)

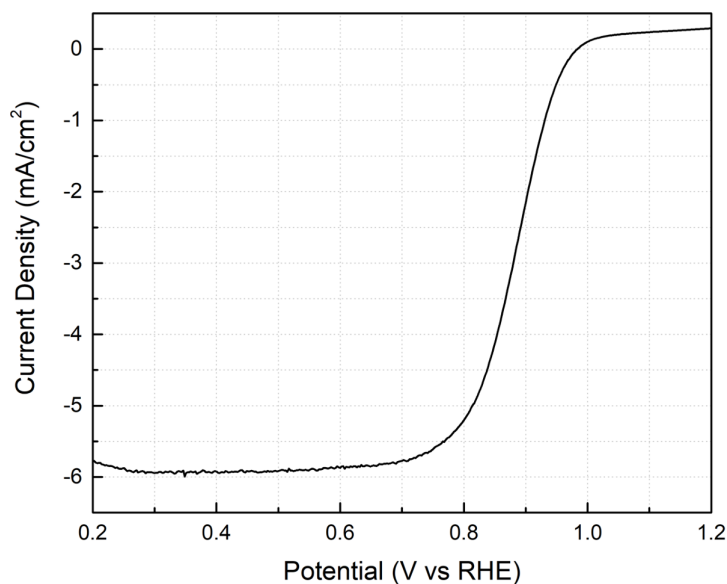


Figure 3.3: Linear sweep voltammetry technique (LSV) used to assess the electrochemical performance of the electrocatalysts.

Linear sweep voltammetry (LSV) is a potential sweep technique where the potential is varied with time within a fixed range at a specified rate, known as the voltage ramp or scan rate (v). Current is then recorded as a function of potential [124]. For electrochemical reactions where mass transfer can be a potential concern such as oxygen reduction evolution reaction, rotation of the working electrode is

typically applied. Factors such as the rate of electron transfer, chemical reactivity of the electroactive species, and voltage scan rate determine the characteristic of the LSV curve. The potential is swept from a point where no electrode reaction occurs then transition to reducing or oxidizing potentials, often through the equilibrium potential, E_0 , of the electroactive species [125]. At any given time, the instantaneous potential can be expressed as:

$$E_t = E_{in} \pm vt \quad (3.5)$$

Where E_t is the electrode potential at instantaneous time t , E_{in} is the starting potential and v is the scan rate.

An example of an LSV curve is shown in Figure 3.3 for an ORR reaction in acidic media (0.1 M HClO₄). In this experiment, electrode rotation was set at 1600 rpm and the electrolyte was saturated with oxygen gas prior to the experiment. The onset potential of the ORR is where the cathodic current starts to rise, in this case around 1.0 V. Further reducing the potential increases the cathodic current, as the potential is more negative than the standard electrode potential. Over time, a limiting current, around 6 mA/cm², has been reached where the rate of electron flow is limited only by the transport of the reactant material to the electrode surface. In comparing catalysts, the kinetic current (i_k) is often the figure of merit used and can be extracted from the Koutecky-Levich equation [123] where a series of LSV curves are generated for different scan rates, as written in equation 3:

$$\frac{1}{i_L} = \frac{1}{i_K} + \left(\frac{1}{0.62nFAD^{2/3}\nu^{-1/6}C_0} \right) \omega^{-1/2} \quad (3.6)$$

Where i_L is the limiting current, i_k is the kinetic current, C_0 is the reactant concentration, A is the electrode area, ν is the kinematic viscosity, D_0 is the diffusion coefficient, and ω is the angular rotation. By plotting the $1/i_L$ and $\omega^{-1/2}$, a straight line will be generated with an intercept that is equal to $1/i_k$. This method provides a quick estimate of the activity of various catalysts by means of LSV.

3.1.3 Cyclic Voltammetry (CV)

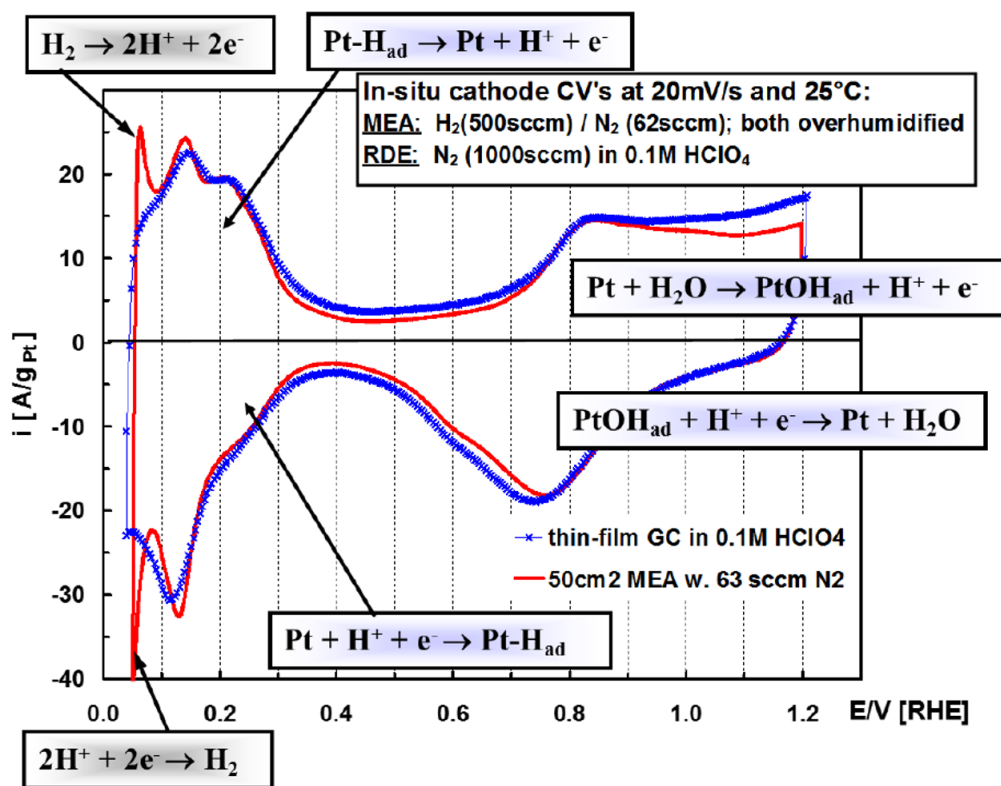


Figure 3.4: A cyclic voltammetry (CV) curve for platinum on carbon support (Pt/C) showing the different redox reactions at varying potentials. Image taken from the lecture slide of Prof. Chuang's ME 262 class at UC Merced.

Cyclic voltammetry (CV) is a tool used to investigate electrode materials and electrochemical reaction, specifically the reduction and oxidation of molecular species. In electrocatalysis, CV can help understand the electron-transfer process. In CV, a voltage is applied to the working electrode and scanned linearly from an initial value, E_1 , to a predetermined limit, E_2 , then scan direction is reversed. The current response is then plotted as a function of the applied potential. Cathodic and anodic peak currents emerge as a result of the change in concentration of the reducing or oxidizing species near the electrode surface and this is in accordance with the Nernst equation. A scan rate (v) is defined in the CV experiment which is the rate of change of the potential, similar to that in LSV. Faster scan rates can reduce the thickness of the diffusion layer, thus generating higher currents. The

Randles-Sevcik equation [126], shown in Equation 3.7, predicts how square root of the scan rate can lead to a linear increase of the peak current, i_p .

$$i_p = 0.446nFAC_0 \left(\frac{nFvD_O}{RT} \right)^{1/2} \quad (3.7)$$

Where n is the number of electrons transferred in the redox process, D_O is the diffusion coefficient of the oxidized analyte, and C_0 is the bulk concentration of the analyte. Deviation from the Randles-Sevcik equation could suggest either electrochemical quasi-reversibility or electron transfer may occur via surface-adsorbed species. When the peak-to-peak separation shifts with scan rate, an electrochemically quasi-reversible process happens but no peak-to-peak separation is observed when a surface-adsorbed species happens [126].

In electrocatalysis, CV can be very useful in determining the types of electrode reactions present as well as in estimating the electrochemically active surface area (ECSA) of the catalysts. For platinum supported on carbon (Pt/C), a typical CV profile in acidic media (perchloric acid, HClO_4) or in a polymer electrolyte membrane fuel cell is shown in Figure 3.4 Different reactions can be observed in the anodic scan, as represented by the peak currents. In the anodic scan, hydrogen oxidation happens at low potential that generates H^+ ions. By increasing the potential, desorption of H^+ ions from the Pt surface occurs and at further oxidizing condition, Pt is oxidized into PtOH_{ad} . On the reverse scan, peak currents are also observed based on the reduction of the same species discussed in the anodic scan. In estimating ECSA, the adsorption of hydrogen on the Pt surface is typically used where the charge generated from the process is normalized to the charge of Pt surface at full coverage, typically reported as $210 \mu\text{C cm}_{\text{Pt}}^{-2}$ [127].

3.1.4 Electrochemical Impedance Spectroscopy (EIS)

Electrochemical impedance spectroscopy (EIS) is an electrochemical technique that can be employed to study different electrochemical phenomena such as electrode kinetics, double-layer structure, corrosion, etc. In this technique, the impedance of the circuit is measured in steady state which can be represented with various equivalent circuits that can be used to explain physical phenomena in the system. EIS is measured by applying an AC potential to an electrochemical cell then measure the current in the cell. A real and imaginary component of the EIS can be collected and is usually plotted in what is known as the Nyquist plot, similar to that in Figure 3.5 [128, 129].

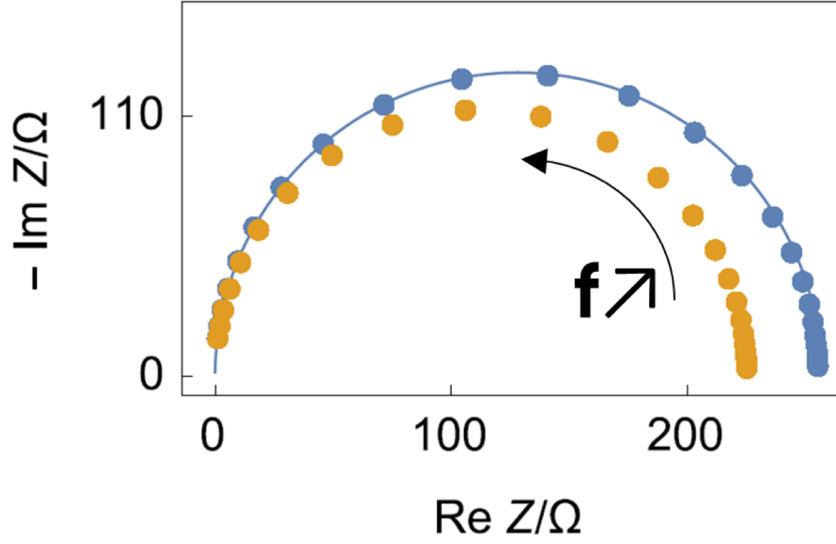


Figure 3.5: A Nyquist plot of an impedance data from an electrochemical system and the imaginary part (I_m) and real part (Re) are indicated as y- and x-axis, respectively. Frequency is labeled as f with the decreasing magnitude from right to left [128]

In an AC system, an analogous equation to that of Ohm’s law for direct current (DC) holds but instead of a static current or voltage, the passing signal oscillates as a sinusoidal wave at a given frequency. Instead of using the resistance, R , impedance is represented by Z and voltage (V) and current (I) are functions of frequency (ω) [129] as shown in Equation 3.8:

$$Z = \frac{V(\omega)}{I(\omega)} \tag{3.8}$$

In EIS, the amplitude and frequency of the input signal can be defined by the user and the measured output signal can have the same frequency as the input signal but could be the phase can be shifted by a finite amount, known as the phase shift or phase angle. Figure 3.6 summarizes the relationship between input and output signals in an EIS measurement with a given the phase angle, ϕ .

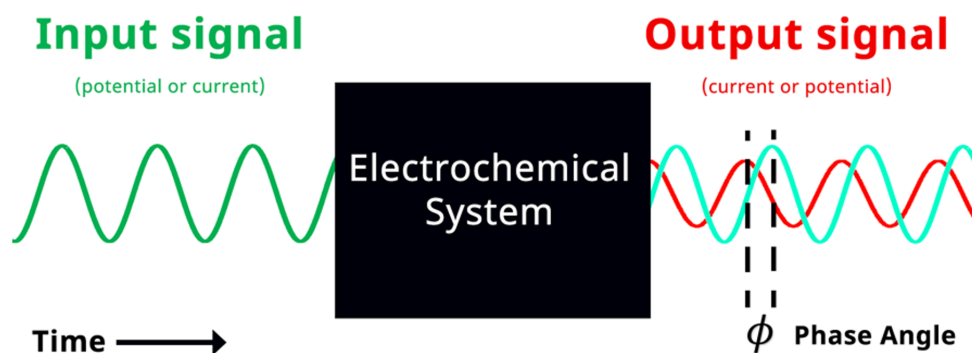


Figure 3.6: Schematics of an EIS measurement where the input and output signal have the same frequency, but a phase angle exists when both signals are overlapped [130]

By using polar coordinates, impedance can be expressed as a sum of both x- and y-components:

$$Z_x = |Z|\cos(\phi) \quad (3.9)$$

$$Z_y = |Z|\sin(\phi) \quad (3.10)$$

The x-component of the impedance is considered as the real impedance and the y-component is the imaginary impedance and plotting these two gives the Nyquist plot shown in Figure 3.5. The total impedance of the electrochemical system can then be modeled with known circuit elements that are well-characterized such as resistor for electron transfer across an interface; capacitor, usually for non-Faradaic charging at an interface; inductor, for magnetic inductance; constant phase element, to account non-ideality in capacitors; and a Warburg element, for diffusion or movement of electrons or ions in solid or liquid phases [130].

For electrochemical systems like fuel cells and electrolyzers, EIS can offer some advantages as a diagnostic tool that the entire frequency response can be correlated to non-Faradaic reaction mechanisms, water management, ohmic losses and ionic conductivity. EIS can probe electrochemical processes that are happening at the same time but on different time scales. For instance, the electrochemical double-layer charging can happen in microseconds while diffusion typically occurs on hundreds of milliseconds time scale [130].

EIS can also pinpoint possible failure modes within the fuel cell components. As a diagnostic tool, EIS can identify individual contributor to impedance such

as ohmic resistance, interfacial charge-transfer resistance, and mass transport resistance in a short amount of time. After identifying the individual contributors to impedance, the performance of the electrochemical device can be optimized including humidification, temperature, back-pressure, and reactant flow rates. Some problems that can be identified by EIS to prevent performance failure and collapse are catalyst coarsening, membrane degradation, bipolar plate corrosion, etc. [131].

However, EIS also has some drawbacks as there are difficulties in implementing impedance methods and fitting the data to the model to obtain the relevant electrochemical parameters. These limitations come from the conditions necessary for an EIS measurement to be valid –linearity, stability, and causality. In linearity, the amplitude of the AC signal must be low enough to make sure that the response of the electrochemical system behaves linearly. However, it also needs to be large so the signal can be recognized otherwise, the signal might be buried in the noise leading to poor accuracy. Drift in the system should also be avoided to minimize problems in EIS measurement, thus the system needs to be stable while the experiment is ongoing. A steady-state environment must be attained first before collecting any impedance measurement. Lastly, causality must be established that the output of the system should be from the perturbing input. The phase and amplitude of the impedance must be related to each other in a linear system, and if the frequency dependence of the phase, the amplitude of the impedance can also be calculated. A useful check on the validity of the measured impedance is typically achieved using the Kramers-Kronig (K-K) transforms [131]. If all those three requirements are met, a reliable EIS spectrum can be a powerful tool to improve the current status of electrochemical energy devices.

3.2 Material Characterization Techniques

3.2.1 Gas Adsorption Porosimetry

The porosity and surface area of the catalysts are essential to their electrochemical performance and as it provides an idea of the density of the active sites necessary for the reactions to happen. Gas adsorption technique was implemented in this work which is based on capillary condensation of a condensable gas, such as nitrogen (N_2) at used in this work. The modelling approaches for the gas adsorption isotherm used here are Brunauer-Emmett-Teller (BET) for surface area and Barrett-Joyner-Halenda for pore size distribution. In these capillary models, different pores are treated as capillaries with various sizes and are interconnected to form the porous body. The porosity information can be calculated from the amount of gas adsorbed at a specified temperature and pressure. If the equilibrium pressure (p) is much lower than the saturation pressure (p_0), the adsorbed gas will condense at the meniscus of liquid in the capillary. The diameter of the pore can then be estimated

using the relative pressure (p/p_0). As the gas pressure is reduced, evaporation of condensed gases begins from large to small pores and the pore wall will be left with an adsorbed layer [132].

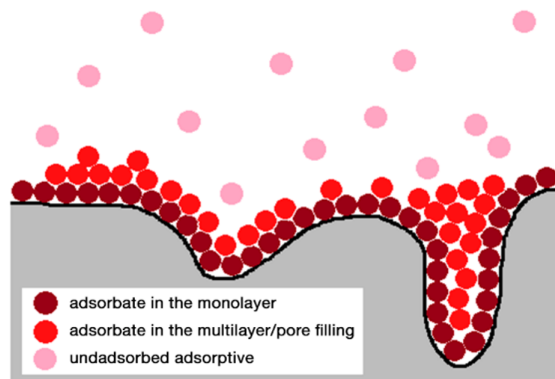


Figure 3.7: An illustration of the gas adsorption process for the surface area and porosity measurement [133]

3.2.2 Inductively Coupled Plasma Mass Spectrometry (ICP-MS)

The identification of exact metallic composition of the catalysts as well as the dissolved metals in the electrolyte after the stability test was achieved using ICP-MS, an analytical technique based on the ionization of the elements. The instrument consists of an ion source (ICP), a mass spectrometer (MS) typically a scanning quadrupole mass filter, and a detector. In terms of operating pressure, the ICP is at ambient pressure while the MS and detector are under vacuum chamber, which requires a vacuum pump, vacuum interface and some electrostatic ion lenses for focusing the ions through the system [134]. The MS separates the ions in the sample matrix by discriminating them based on mass-to-charge ratio and the concentration of each element are determined by the detector that counts the number of selected ions per second. The solid catalysts in this study needed to be digested first prior to analysis as ICP requires liquefied samples. An argon (Ar) carrier gas then aerosolizes the sample and sends only the smallest droplets through the chamber and into the Ar plasma torch to desolvate and ionize the samples [135].

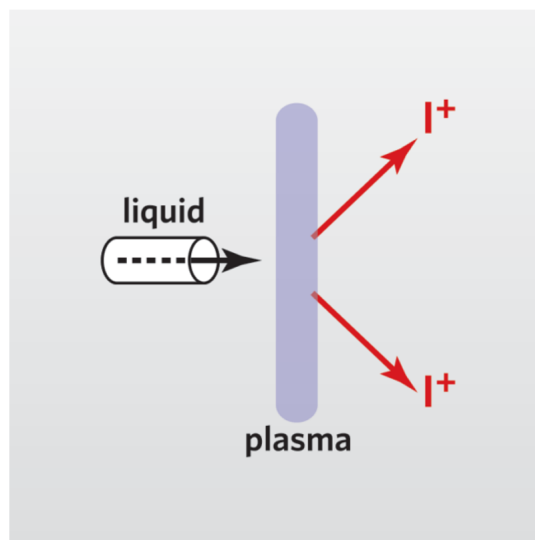


Figure 3.8: A schematic of the ICP-MS process where a sample is being ionized using a plasma source [136].

3.2.3 X-ray diffraction (XRD)

XRD can be used to analyze the crystalline properties of the catalysts used in this work as well as the changes that happened after subjecting them to degradation tests. The materials are analyzed based on their diffraction patterns formed by the reflection of the X-rays from the source that are scattered by the sample and to the detector. By applying Bragg's Law, various characteristics of the materials can be determined. The pattern collected after performing XRD is known as a diffractogram with y-axis as the intensity and x-axis is a function of the scanning angle. The peak positions in the diffractogram give information such as crystalline structure, qualitative phase information, and space group symmetry. The intensity can also provide point symmetry and quantitative phase fractions. The crystallite size and stacking faults, and antiphase boundaries can be extracted from the peak shapes and peak width. XRD can be applied in many different applications such as thin film analysis, sample texture evaluation, monitoring of crystalline phase and structure, and investigation of sample stress and strain [137].

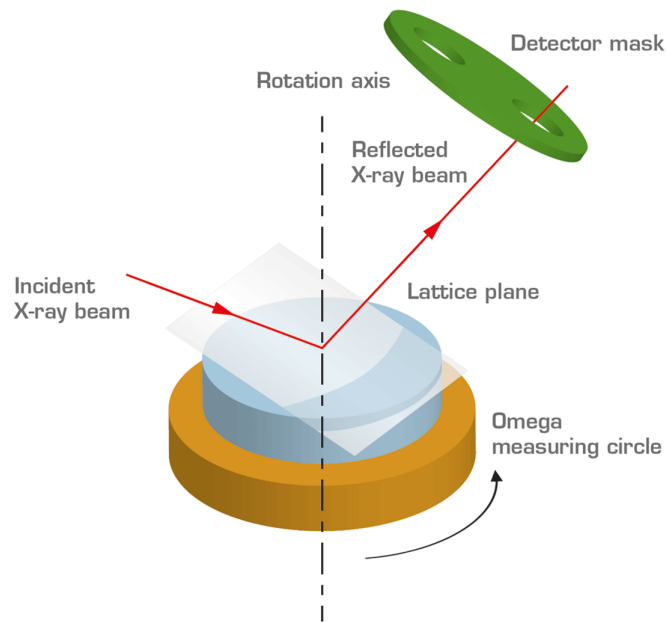


Figure 3.9: A depiction of the X-ray diffraction process to study crystallographic information of materials [138]

3.2.4 Electron Microscopy

Electron microscopy (EM) is an imaging technique that can obtain high resolution images of different types of materials using high beam of highly energetic electrons. Different information can be obtained using EM such as topography, morphology, composition, and crystallography. EMs were developed to address the limitations of light microscopes that can only work up to 500 to 1000 times magnification and a resolution of 0.2 micrometers. The basic operating principles in any kind of EM involve: 1.) formation of stream of electrons from the electron source and acceleration towards the sample by means of a positive electrical potential; 2.) confinement and focusing of the stream of electrons using metal apertures and magnetic lenses into a thin, focused, monochromatic beam; 3.) focusing of the sample onto the sample using a magnetic lens; and 4.) electron-beam sample interaction upon irradiation. The interaction with the electron beam and the sample then yields signals that can now be transformed into an image [139].

The sample-electron beam can interact in different ways, as summarized in Figure 3.10. A volume of primary excitation is generated when an electron beam impinges a sample, which leads to electron scattering and photon and X-ray production. The interaction volume depends on several factors such as accelerating potential, mean atomic weight, sample tilt relative to impinging electron beam.

The interaction can lead into elastic scattering, inelastic scattering, or no interaction at all. The scattering effect can produce signals that can be used for imaging, quantitative and semi-quantitative information, and generation of an X-ray source. For imaging, secondary electrons (SE), backscattered electrons (BSE), cathodoluminescence (CL), auger electrons (AE) and characteristic X-rays are often used for imaging. The characteristic X-ray can be used to obtain quantitative and semi-quantitative elemental mapping. The two basic types of electron microscopes are the scanning electron microscope (SEM) and transmission electron microscope (TEM), which are discussed more in the next sections [140].

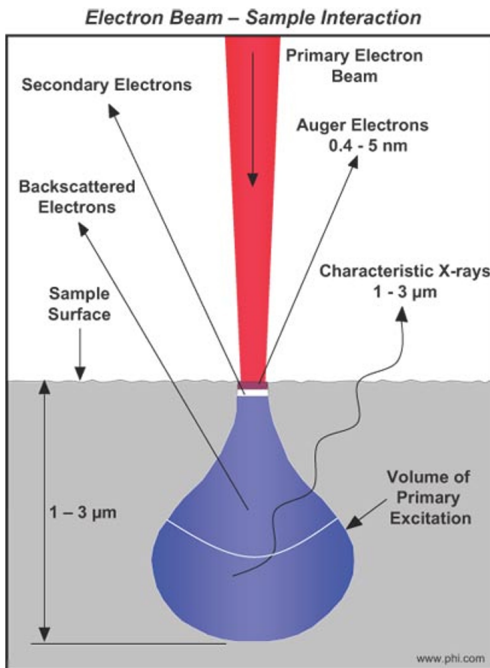


Figure 3.10: Electron beam-sample interaction with at different depths and different signals for analyzing surface properties of materials [141]

3.2.4.1 Scanning Electron Microscopy (SEM)

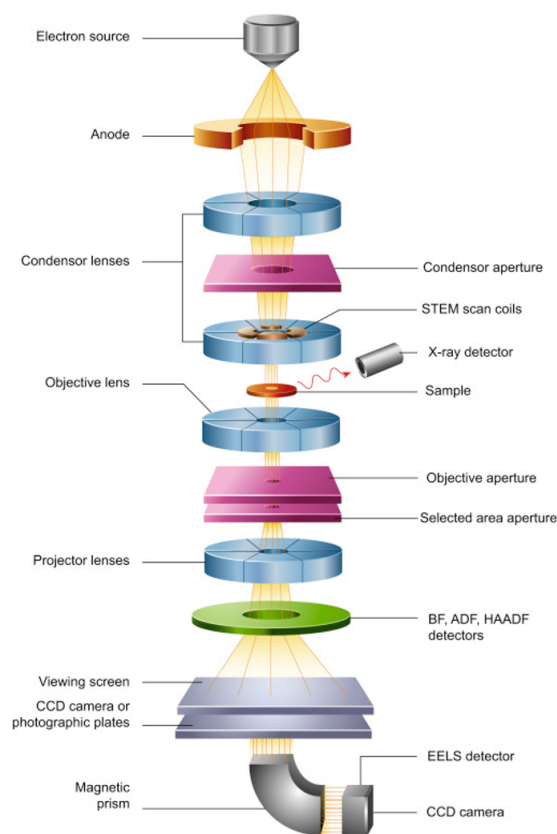


Figure 3.11: Different parts of a scanning electron microscopy (SEM) to study the morphology of materials [142]

A scanning electron microscope (SEM) is a technique often used to analyze surfaces and the typical layout of its parts are shown Figure 3.11, which consist of the electron gun (electron source and accelerating anode), electromagnetic lenses, vacuum chamber containing the specimen stage, and detectors that collect signals emitted by the sample [142]. Compared to a transmission electron microscope (TEM), the column is shorter since the only lenses needed are those above the specimen to focus the electrons into fine spot on the sample surface. The sample chamber, on the other hand, can be larger since there are no restriction on sample size other than the chamber itself. The sample does not need to be thin, thus simplifying sample preparation. The electron gun at the top of the column emits electron beam that is focused into a small 1 nm spot on the specimen surface unlike the broad static beam used in TEM. The specimen is then scanned by the focused electron beam in

a rectangular raster fashion, generating signals from the interaction and the intensities of different signals are stored on a computer memory. The secondary electron is the most typically used for image processing which varies with the topography of the sample. Compared to TEM, the accelerating voltage is much lower ranging from 50 V to 30 kV [143].

3.2.4.2 Transmission Electron Microscopy (TEM) and Scanning Transmission Electron Microscopy (STEM)

When looking at the internal microstructures, evaluate nanostructures like particles, fibers and thin films, and atomic resolution imaging, transmission electron microscope (TEM) is the appropriate imaging technique [142]. The basic components of a TEM include electron gun, electrostatic lenses for focusing the electrons before and after specimen, and a transmitted electron detection system, all shown in Figure 3.12. The microscope can be fully enclosed to avoid interference from the environment and operated remotely using control panels.

For modern TEM, a major advancement is the aberration-corrected capability. Without correction, the image quality is often hindered by spherical aberration that leads to blurred image and also the appearance of periodic structures that appear to extend beyond the actual physical boundaries, known as delocalization [144]. A parallel beam of electrons is required to illuminate the specimen observed in TEM. While travelling down the column, the condenser system made of different magnetic lenses and apertures focus the electrons into a particular beam suitable for imaging. TEM instruments also have the option to operate in scanning transmission electron microscope (STEM) mode, which requires flexibility in the illumination conditions [145]. The ray path differentiating TEM and STEM is illustrated in Figure 3.13.

STEM combines the principles in TEM and SEM and unlike in TEM where a parallel illumination is needed, a tiny convergent electron beam with selected convergent angles is necessary for STEM to form the image. The convergent beam scans a defined specimen area and the signals produced are recorded spot-by-spot to form the image on a screen. A thin sample is also required to analyze with STEM. An advantage of STEM over TEM is the ability to collect signals that cannot be spatially correlated in TEM such as secondary electrons, scattered beam electrons, characteristic X-rays, and electron energy loss. Compared to conventional SEM, STEM has an improved spatial resolution [142, 146].

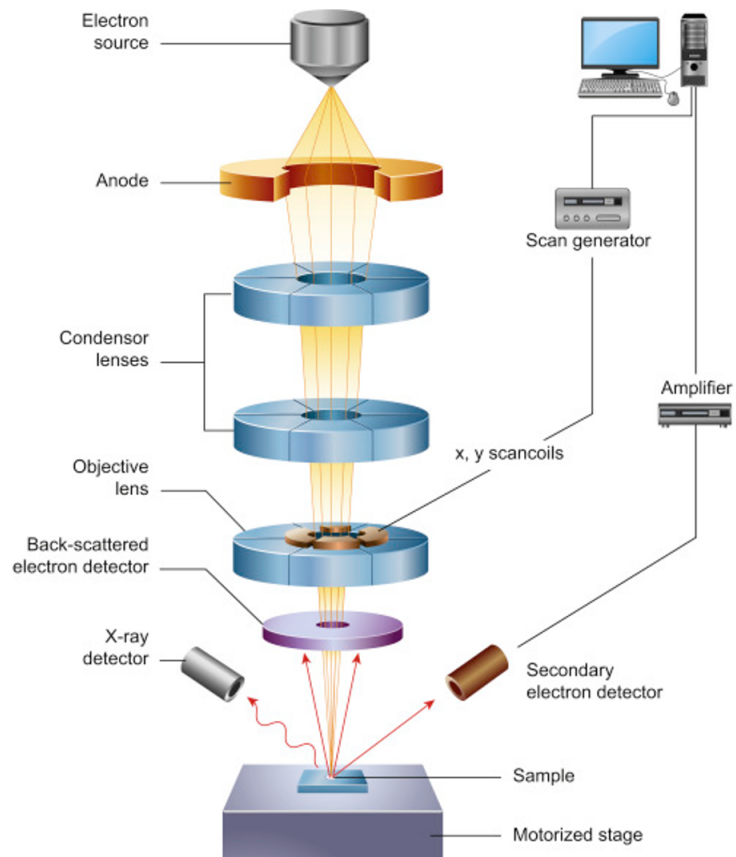


Figure 3.12: A breakdown of the components inside a transmission electron microscope (TEM) [142]

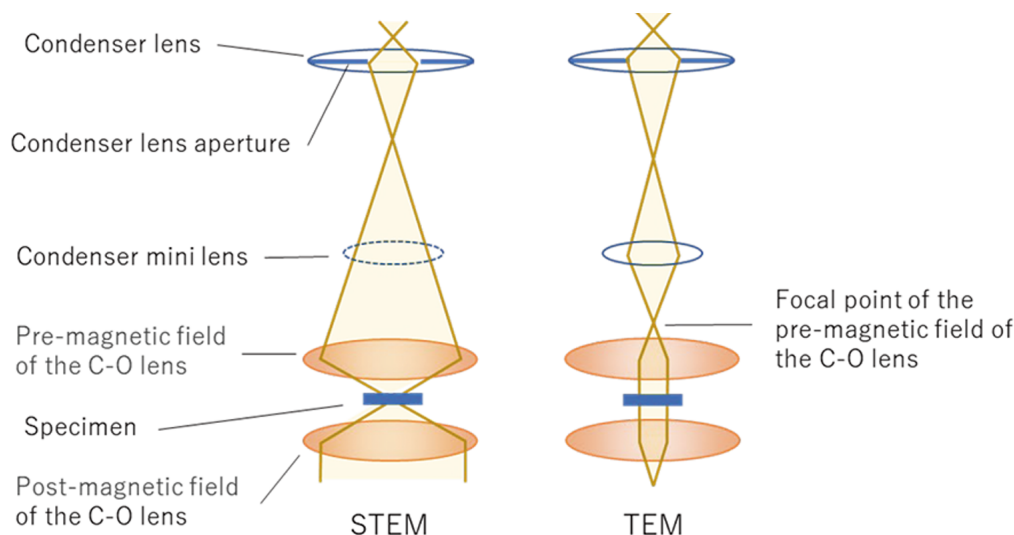


Figure 3.13: Ray path for the STEM and TEM mode [147]

3.2.5 Spectroscopy

Spectroscopy is the science of investigating and measuring spectra generated by the interaction between a matter and an electromagnetic radiation. Spectroscopy broadly covers any measurement of a quantity as a function of wavelength or frequency, resulting from the interaction between particles and electrons, photons, ions as well as their interaction with other particles as a function of collision energy. These interaction may lead into either absorption, where a sample absorbs the energy from the radiation source, or emission, when the sample emits radiation of a different wavelength other than the source. Spectroscopy has been crucial in many different fields and can also be applied to advance the understanding of material development [148, 149]. In this work, three major spectroscopic techniques were employed to study the catalysts: energy-dispersive X-ray spectroscopy (EDS), energy electron loss spectroscopy (EELS), and X-ray photoelectron spectroscopy (XPS).

3.2.6 Energy-dispersive X-ray spectroscopy (EDS)

Energy-dispersive X-ray spectroscopy (EDS) is an analytical technique that allows elemental and compositional analysis of different materials, and in this case was applied to understand the catalysts. With the addition of an EDS detector to an electron microscope, chemical composition down to atomic level resolution can be possible. Elemental composition maps over a broader raster area can be constructed with EDS by combining chemical information from a spot size of a few microns. These capabilities advance the fundamental compositional knowledge in wide range of materials. For STEM-EDS, a sample is excited by the electron beam

which then dissipates some of the absorbed energy by ejecting a core-shell electron. This empty place in the core level is then filled by a higher energy outer shell electron, thus releasing an X-ray with a characteristic spectrum based on its origin. As the electron probe is scanned across the sample, characteristic X-rays are emitted, and the spectrum is mapped to specific locations on the sample. The EDS detector separates the characteristic X-rays of different elements into an energy spectrum and a software usually aids the analysis of this spectrum to identify the abundance of specific elements. Peak positions in the spectrum are used to discriminate the elements while signal intensity represents the concentration of the elements. EDS can be applied semi-quantitatively to determine chemical composition by using the peak-height ratio relative to a standard. The data quality depends on the signal strength and cleanliness of the spectrum, which relies on a good signal-to-noise ratio especially for trace elements [142, 150, 151].

3.2.6.1 Energy electron loss spectroscopy (EELS)

Energy electron loss spectroscopy (EELS) are typically installed with TEM instrument with an acceleration that could range between 60-300 kV to analyze the samples. Since this technique is TEM-based, thin samples are still needed so electrons can transmit through the sample. EELS exploits the inelastic scattering between the sample and the electron beam to extract information about the sample. These inelastic scattering causes the primary electrons to lose energy, and this can be quantified and detected by passing the transmitted electrons through energy filters that separate the electrons by their energy loss. The electron energy loss values can also be linked to different scattering mechanisms such as plasmon scattering, phonon scattering, secondary electron emission, and fine detail of atomic bonding in different crystal structures. Based on this electron loss, an EELS spectrum can be constructed with typical resolution of 0.5 to 1 eV. By taking multiple sequential EELS spectra, a spectrum image can be obtained, and different types of information can be extracted from the material such as specimen thickness, valency, optical response, band structure, elemental composition, etc.[152].

For this work, EELS was mostly used to study the valency of iridium (Ir) and cobalt (Co). Combined with an imaging optics, chemical mapping can also be performed by using the contrast created by the energy loss properties of different elements and this is referred to as an energy filtered TEM (EFTEM) image. In the second project of this work, EFTEM images were also constructed to map out the distribution of Ir and Co in the samples. The major drawback in the EELS technique is sample thickness where the thicker the sample, the stronger the interaction of the primary electron resulting into multiple energy loss events. This scenario would reduce the signal-to-background ratio of the EELS edges and the visibility of the edges becomes less. Nevertheless, EELS is still valuable especially

in determining the distribution of lighter elements such as boron (B), carbon (C), nitrogen (N) and oxygen (O), whose X-rays are low enough to be absorbed by the specimens and detectors, making them hard to analyze [142]. Thus, EELS and EDS are complementary techniques that can be used to analyze any type of sample and a typical layout for a TEM instrumentation with both EELS and EDS capabilities is illustrated in Figure 3.14.

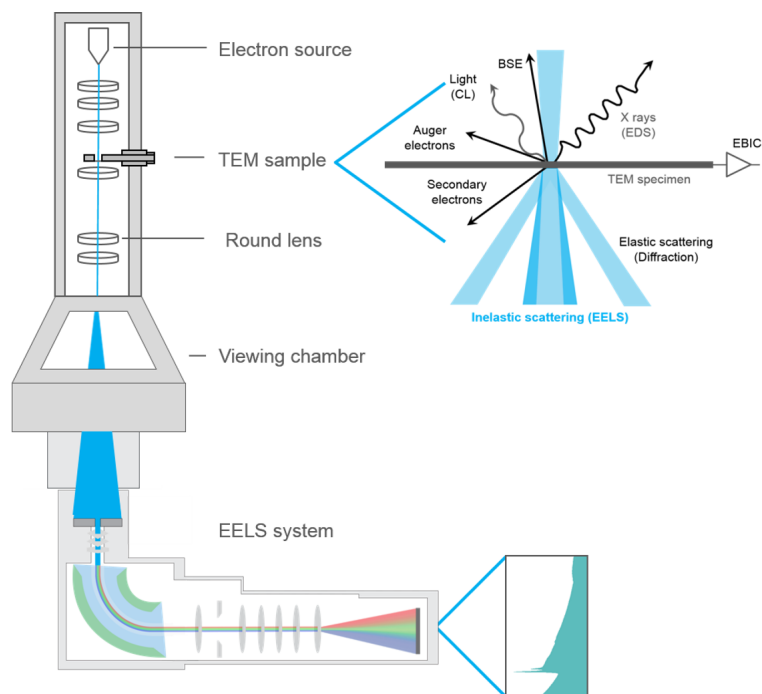


Figure 3.14: An illustration of EDS and EELS signals obtained from TEM [152]

3.2.6.2 X-ray photoelectron spectroscopy (XPS)

The chemical nature of the catalysts in this work was investigated using X-ray photoelectron spectroscopy (XPS) shown in Figure 3.15, a surface sensitive and non-destructive technique that probes the outermost layer, about 5-10 nm from the surface. The photoelectric effect is the fundamental principle that makes XPS possible, in which electrons are emitted from atoms after being exposed to an electromagnetic radiation. Photoelectrons are emitted from the material when the energy of the impinging photon is higher than the binding energy of the material. Typical X-ray source for XPS is a mono-energetic aluminum (Al) $K\alpha$. The kinetic energy of the emitted electrons is then measured by an electron energy analyzer. XPS is also known as electron spectroscopy for chemical analysis (ESCA) and can provide

chemical quantification and chemical state information from the surface of the material being studied based on the binding energy and photoelectron peak intensity. The subsurface chemical information or depth distribution can also be probed by combining XPS with ion sputtering to analyze thin film structures [153, 154].

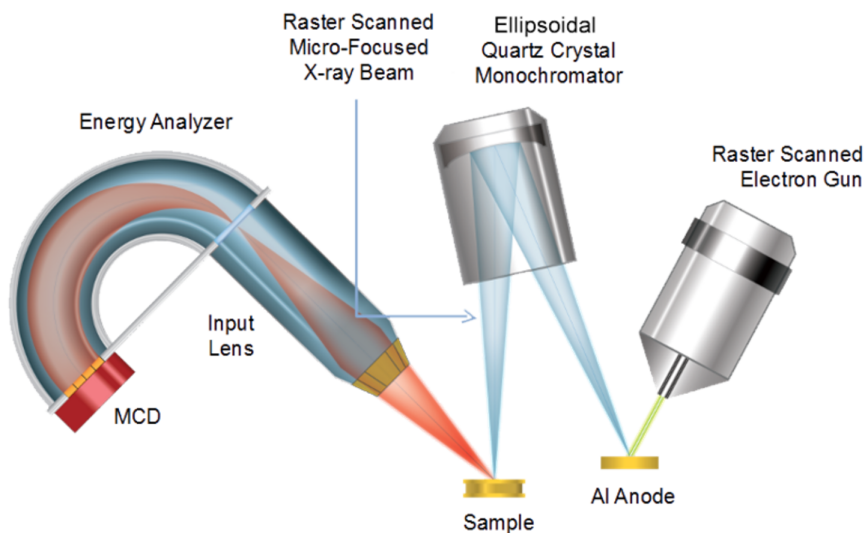


Figure 3.15: X-ray photoelectron spectroscopy (XPS) for quantification of surface composition and chemical states [154]

Chapter 4

DEGRADATION BEHAVIOR OF PLATINUM-CARBON CATALYST FOR OXYGEN REDUCTION REACTION (ORR) IN ACIDIC AND ALKALINE MEDIA

This chapter is taken from the published article “*Insights on platinum-carbon catalyst degradation mechanism for oxygen reduction reaction in acidic and alkaline media*” in the Journal of Power Sources [155].

4.1 Abstract

Developing durable electrocatalyst for oxygen reduction reaction (ORR) is essential for fuel cell commercialization. Herein, we perform a study of platinum-carbon (Pt/C) degradation mechanisms using potential cycling of accelerated durability testing protocols in alkaline and acidic media. Physicochemical results indicate that carbon surface oxides are formed after high-potential cycling in acid causing an increase in the double-layer capacitance and severe ORR activity loss due to Pt poisoning. Whereas, low-potential cycling in acid shows less ORR activity loss, mainly caused by Pt Ostwald ripening, and does not lead to a significant change in double-layer capacitance. In alkaline, the Pt/C catalyst after high-potential cycling shows a decrease of double-layer capacitance over time because of carbon layer dissolution. TEM images reveal larger Pt agglomerates in alkaline, due to high Pt mobility. These findings provide new insights into the role of catalyst and carbon support interface in developing mitigation strategies for stable fuel cell operation.

4.2 Physicochemical, Performance and Durability Assessment Tools

4.2.1 Chemicals

The chemicals and their suppliers used in this work include perchloric acid (HClO_4 , 69-72% Certified ACS), ethanol ($\geq 95\%$) and potassium hydroxide (KOH, $\geq 90\%$) from Sigma-Aldrich, isopropanol (IPA, 99.5 %, ACS), and 20% platinum on carbon black (Pt/C, HiSPEC-3000) from Alfa Aesar, and 5% D2020 Nafion[®] solution from Ion Power. All solutions were prepared with ultrapure deionized water

(> 18 M Ω ·cm resistivity) supplied by a water purification system from Thermo Scientific Barnstead Nanopure.

4.2.2 Electrode Preparation and Electrochemical Tests

Half-cell electrochemical tests were conducted with Autolab Metrohm PG-STAT128N potentiostat/galvanostat at room temperature and ambient pressure. Thin-film rotating disk electrode (TF-RDE) measurements were performed with a three-electrode electrochemical set-up in a modulated speed rotator from Pine Research Instrumentation, Inc. A saturated calomel electrode (SCE) and a Hg/HgO electrode (filled with 1 M KOH) were used as the reference electrode in acid and alkaline electrolyte, respectively. A 1.5 cm² Pt mesh was used as the counter electrode and E3 series RDE (OD = 5 mm) with glassy carbon (GC) disk as the working electrode. All potentials shown in this work were converted to a reversible hydrogen electrode (RHE) using:

$$E_{RHE} = E_{WE} + E_{0,RE} \quad (4.1)$$

where E_{WE} is the experimentally obtained working electrode potential against the reference electrode, and $E_{0,RE}$ is the standard potential of the reference electrode vs. RHE. The pH of applied electrolytes was measured using the Mettler ToledoTM S220, which was calibrated by a standard buffer solution (pH = 4.01, 7.0, and 10.0) before use. Based on the measured PH, the SCE potential was adjusted to be 0.312 V at 0.1 M HClO₄ [123] and the Hg/HgO potential was 0.839 V at 0.1 M KOH according to our previous work [156].

The catalyst ink was prepared by mixing commercial 20 wt.% Pt/C in 24 vol.% IPA-water solution with a Nafion ionomer/carbon weight ratio (I/C) of 0.125. To obtain uniform dispersion, the catalyst ink was sonicated for 30 minutes at < 35 °C temperature. Before ink deposition, the GC disk of RDE was polished for 2–3 minutes with a rayon micro-cloth wetted with the 50 nm aluminum oxide (Al₂O₃) suspension. A controlled volume of catalyst ink was then deposited on the clean disk and dried with a 250 W infrared lamp. For each studied sample, the target catalyst loading is 0.1 mg/cm².

Cyclic voltammetry (CV), linear sweep voltammetry (LSV), and electrochemical impedance spectroscopy (EIS) were first measured in N₂-saturated 0.1 M HClO₄ or 0.1 M KOH. The sequence of electrochemical tests is: 1) surface activation through CV from 0.0125 to 1.2 V for 50 cycles at 500 mV/s, 2) another CV in the same potential range for 3 cycles at 20 mV/s, 3) a background current obtained with LSV from -0.01 to 1.2 V at 20 mV/s with 1600 rpm rotating speed, and 4) EIS at a DC potential of 0.4 V with a frequency range from 100 kHz to

0.1 Hz and 10 mV AC amplitude. Then, measurements were performed in 0.1 M O₂-saturated electrolyte solution with 1600 rpm rotating speed: 1) LSV at 20 mV/s to obtain ORR activity and 2) EIS at 0.85 V DC potential with 10 mV AC amplitude from 100 kHz to 0.1 Hz. For the degradation protocols, 5, 000 potential cycles were conducted in N₂-saturated electrolyte. Two ADT protocols were performed including the potential cycling of 0.6–1.0 V at 50 mV s⁻¹ and 1.0–1.6 V at 100 mV s⁻¹, which are referred to as low-potential cycling (LPC) and high-potential cycling (HPC) tests, respectively. Accordingly, the measurements taken before and after the 5,000 durability cycles are referred to as beginning-of-life (BOL) and end-of-life (EOL), respectively. All measurements were performed more than three times to ensure data reproducibility.

4.2.3 Physicochemical characterization

The RDE, after degradation test, was gently sonicated in ethanol to detach the catalyst layer from the disk substrate. After being loaded on a 300 mesh Lacey Carbon Type A copper grid supplied by Ted Pella, Inc., fresh and degraded samples were analyzed using a transmission electron microscope (TEM, JEOL 2100) operated at 200 kV. Scanning electron microscopy (SEM, Field Emission Gemini 500) at 3 kV was done on catalyst layers deposited on a removable RDE disk to capture the actual physical degradation on the thin film.

X-ray photoelectron spectroscopy (XPS) was performed with Thermo Scientific K-Alpha Plus using a monochromatic aluminum X-ray source. Each sample was repeated for three different locations with an X-ray spot of 400 μm. For the degraded samples, XPS measurements were conducted directly on the catalyst layer of a removable RDE disk, similar to SEM, to ensure data quality. Avantage software was used to post-process the XPS data of C *1s* and Pt *4f* spectra.

4.3 ORR Performance Loss

Figure 4.1a displays the CV curves obtained every 1,000 ADT cycles of LPC_Acid and the four reaction regions. The current densities in regions I, II, and IV reduce with increasing durability cycles, highlighting the loss of ECSA. Further, the Pt reduction peak potential in region IV becomes more positive with cycling time resulting from the increase of Pt particle size [157], most likely due to Ostwald ripening [36].

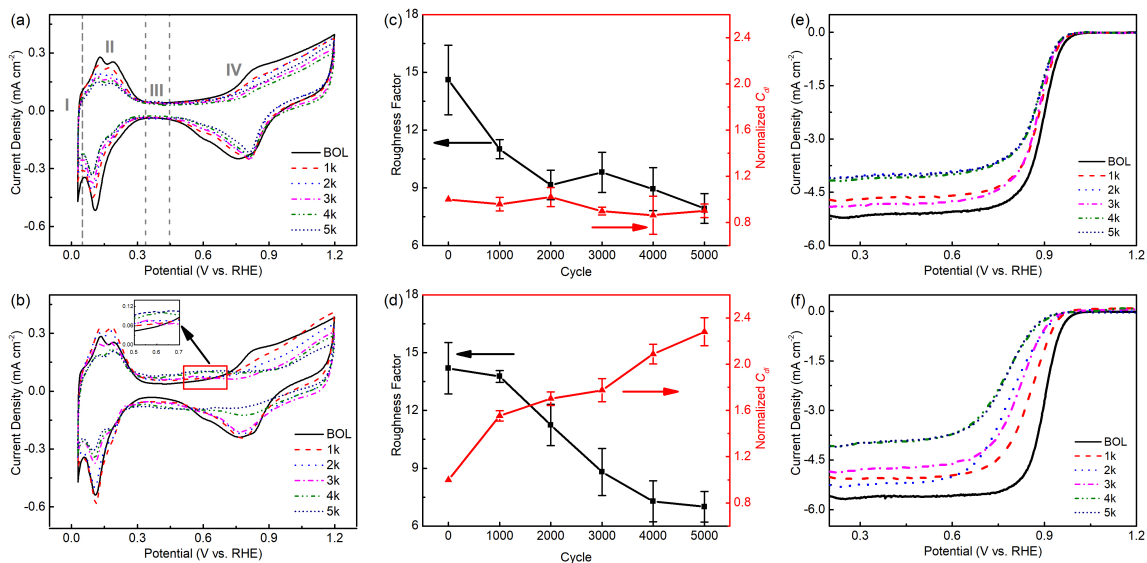


Figure 4.1: Electrochemical acid degradation data (0.1 M HClO₄) for LPC_Acid (a,c,e) and HPC_Acid (b,d,f) recorded every 1,000 cycles: (a,b) CV recorded in N₂-purged electrolyte, (c,d) changes in roughness factor and normalized C_{dl} and (e,f) LSV results in O₂-saturated electrolyte at 1600 rpm.

4.4 Catalyst utilization via Tafel analysis

The ECSA, estimated by HAD, is widely considered as an indicator of catalyst activity and can be monitored for degradation studies [58, 61, 65, 158]. During the long-term potential cycling, identifying the ECSA loss would have an underlying assumption that the mass loading of Pt catalyst remains unchanged. To avoid the effect of Pt mass loss, roughness factor (rf) is used instead, which represents a ratio between the electrochemically active Pt area and the geometric area of the working electrode:

$$rf = \frac{q_{Pt}}{\Gamma} \quad (4.2)$$

where q_{Pt} is the hydrogen adsorption charge density (in C cm⁻²_{geo}) and Γ is the standard charge to reduce a monolayer of protons on Pt (210 μ C cm⁻²_{Pt}) [159]. From Figure 4.1c and d, LPC_Acid and HPC_Acid are found to have similar rf losses of around 50% after 5,000 cycles. This agrees well with the results reported by Pizzutilo et al. [59] and Weber et al. [58]. For LPC_Acid, the majority of the rf losses are in the first 2,000 cycles, then the rf reaches a plateau, owing to the formation of a steady-state electrode/electrolyte interface and possibly a stable Pt size. In the case of HPC_Acid, the initial rf degradation appears to be linear from

1,000 to 4,000 cycles, most likely coming from Pt dissolution and detachment from the carbon support, then begin to plateau in the last 1,000 cycles.

The ORR activity, which typically correlates well with the rf , was evaluated using linear sweep voltammetry (LSV) performed in O₂-saturated 0.1 M HClO₄ after every 1,000 ADT cycles. The results for LPC_Acid and HPC_Acid are shown in Figure 4.1e and f, respectively. Compared with LPC_Acid, the HPC_Acid sample suffered from severe kinetic losses, as observed from the ORR onset potential, despite having the same rf loss. Meanwhile, the limiting current density on these two samples is very similar after 5,000 ADT cycles. This observation can be explained by the similar rf losses since the diffusion layer thickness and the catalyst layer structure determine the limiting current according to the Koutecky-Levich equation [123].

To study the ORR electrocatalytic resistance, EIS was also conducted in an O₂-saturated 0.1 M HClO₄ electrolyte at 0.85 V. The EIS spectra of LPC and HPC samples are shown in Figure 4.2a and b, respectively. EIS also allows the differentiation of catalyst and carbon support degradation [160]. The experimental results are simulated by an equivalent circuit (inset of Figure 4.2c), consisting of a charge transfer resistance (R_1), a constant phase element (CPE) corresponding to a double-layer capacitance (Q_1), a mass transfer resistance (R_2), another CPE simulating the diffusion process (Q_2) and an ohmic resistance (R_o) [161]. All fitted results are summarized in Table 4.2 (refer to Appendix). Throughout 5,000 ADT cycles, the total polarization resistance, $R_1 + R_2$, increased drastically for HPC_Acid in contrast to the slight change for the LPC sample, as shown in Figure 4.2c. Such observation also agrees well with the change of ORR activity shown in Figure 4.1e and f.

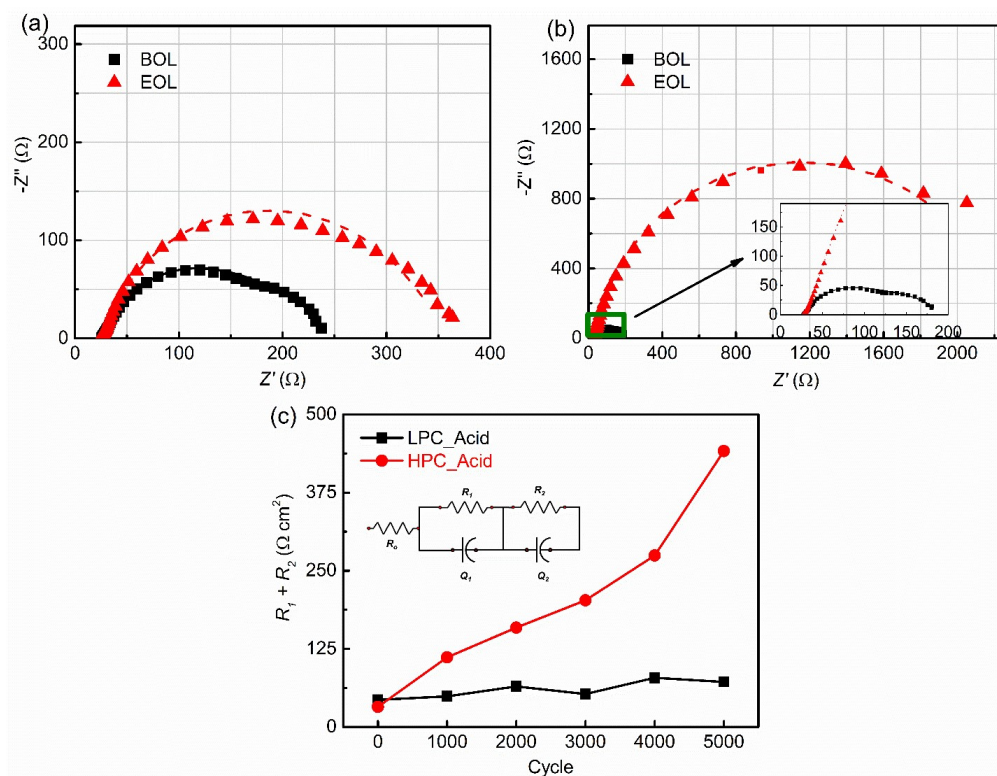


Figure 4.2: Electrochemical impedance spectroscopy (EIS) data in O_2 -saturated 0.1 M $HClO_4$ at 0.85 V with 1600 rpm recorded at beginning-of-life (BOL) and end-of-life (EOL) for (a) LPC_Acid and (b) HPC_Acid. Symbols represent raw data and dashed lines are the fitting results. (c) Total resistance ($R_1 + R_2$) as a function of cycle number along with the equivalent circuit used in the simulation.

High-potential cycling was also performed in alkaline media (HPC_Alkaline) consisting of N_2 -saturated 0.1 M potassium hydroxide (KOH) to compare the degradation mechanism of HPC in acidic media. Similar to that in the acidic media (Figure 4.1a), the measured CV curves of Pt/C catalyst in alkaline media have the characteristic pseudocapacitive features, including HAD below 0.3 V and Pt oxide formation at over 0.7 V as shown in Figure 4.3a. Note that the oxide formation on Pt surface in alkaline media originates from the specific OH^- adsorption, whereas in acidic media, it is due to the activation of solvent water molecules [159]. At any given potential, the CV current density decreases drastically during the first 1,000 cycles, revealing that HPC_Alkaline sample suffers from significant catalyst loss and/or irreversible chemical and structural reconstruction. After the first 1,000 cycles, the alkaline CV results indicate that a stable reaction interface has formed gradually throughout the next 4,000 cycles.

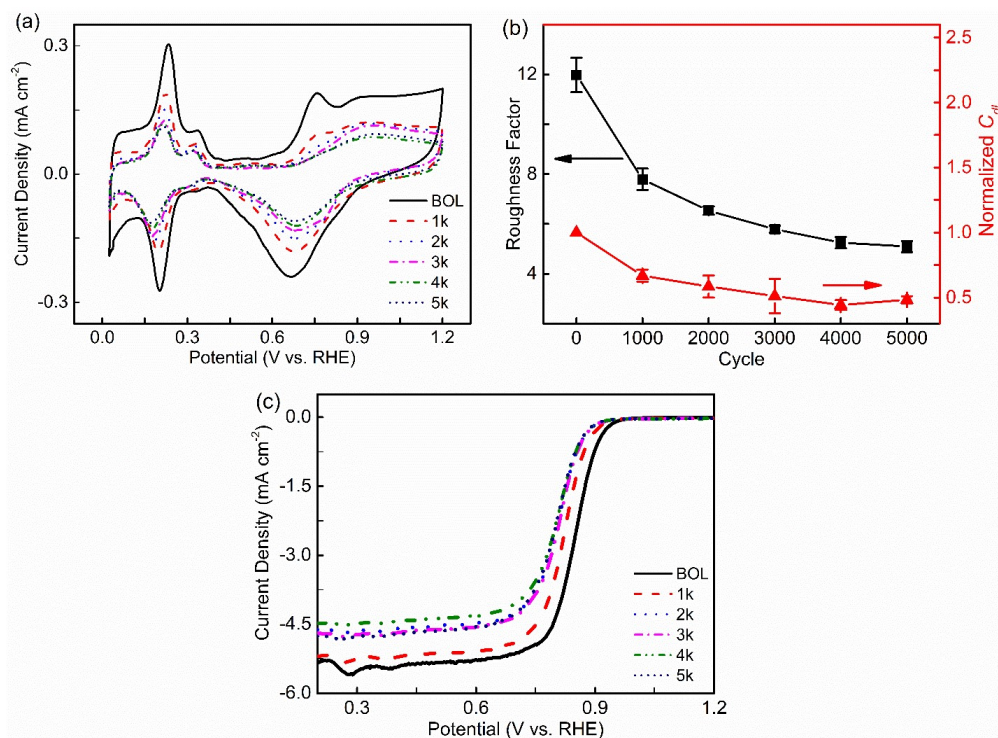


Figure 4.3: Electrochemical data for alkaline degradation (0.1 M KOH) collected every 1,000 cycles: (a) CV results in N₂-saturated electrolyte, (b) roughness factor and normalized C_{dl} change, and (c) LSV curve in O₂-saturated electrolyte at 1600 rpm.

For rf estimation in alkaline media, a method developed by Vidal-Iglesias et al. [162] uses a reference total charge of $390 \mu\text{C cm}_{\text{Pt}}^{-2}$ taken between 0.06–0.9 V considering both H⁺ and OH⁻ adsorption. In Figure 4.3b, the rf decreases 57% after 5,000 cycles of HPC compared to a 50% loss in HPC_Acid. Alkaline electrolytes typically show more severe ECSA degradation of Pt/C than acidic media. In alkaline media, particle detachment is related to both the change in carbon support chemistry, which alters the anchoring sites between the Pt NPs and the carbon support and the associated carbon corrosion in the vicinity of the Pt NPs. [69, 70]. In O₂-saturated 0.1 M KOH, the ORR activity in HPC_Alkaline was assessed as shown in Figure 4.3c. At BOL, HPC_Alkaline demonstrates higher kinetic overpotential as compared to that in acidic media (Figure 4.1f) due to increased Pt-OH coverage [163]. However, based on the Tafel plots of Figure 4.9b and c (see Appendix), the ORR activity degradation of HPC_Alkaline is not as severe compared to HPC_Acid. These combined results further suggested that the inconsistent trend between the measured rf and ORR activity in HPC_Acid is likely related to the Pt and carbon support interaction, to be discussed in the succeeding sections.

To analyze ORR kinetics, Tafel model approximation of the classic Butler-Volmer equation can be represented in the following form:

$$i_k = 10^{(\eta/B)} \times i_0 \times rf \quad (4.3)$$

where i_k and i_0 are the kinetic and exchange current densities (mA cm_{geo}^{-2}), respectively, η is overpotential (V), and B denotes the Tafel slope. When describing the real reaction rate, kinetic current density (i_k) was employed instead of mass activity to minimize the influence of Pt mass loss throughout the degradation cycles. The Tafel slope and exchange current density can be obtained experimentally from the kinetic dominant region of the LSV data using Tafel plots (i.e. $\log(i)$ vs η) as shown in Figure 4.9 (see Appendix). For LPC_Acid, the fitted values of B and i_0 are 56 mV dec^{-1} and $3.35 \times 10^{-7} \text{ mA cm}_{Pt}^{-2}$, respectively, presented in 4.10a. Furthermore, these two parameters are roughly constant during 5,000 potential cycles, implying no significant changes in terms of the reaction rate-determining step and intrinsic kinetic rate in the whole measurement period. The i_k at $\eta = 0.33 \text{ V}$ for the LPC_Acid per 1,000 cycles was estimated according to Equation (4.3) and was compared to the experimental results derived by:

$$i_k = \frac{i_{lim} \times i_{0.9}}{i_{lim} - i_{0.9}} \quad (4.4)$$

where $i_{0.9}$ is the current density from LSV obtained at 0.9 V (corresponding to $\eta = 0.33$). The reasons for the choice of 0.9 V to represent the catalyst activity are discussed in the literature [164]. The estimated i_k values for LPC_Acid correspond well with the experimental results as shown in Figure 4.4a, demonstrating the reliability of the Tafel approximation method. After 5,000 cycles, the loss ($\sim 55\%$) is consistent with the decrease of rf ($\sim 46\%$), with B and i_0 remain unchanged during the low-potential cycling. Similarly, the fitted value of B and i_0 for HPC_Alkaline remains almost constant throughout the 5,000 ADT cycles as shown in Figure 4.10c. The average values in HPC_Alkaline for Tafel slope and exchange current density are $B = 68.0 \text{ mV dec}^{-1}$ and $i_0 = 4.81 \times 10^{-7} \text{ mA cm}_{Pt}^{-2}$, respectively. El-Sayed et al. [165] used similar Tafel analysis to investigate catalyst degradation for oxygen evolution reaction by assuming constant B and i_0 .

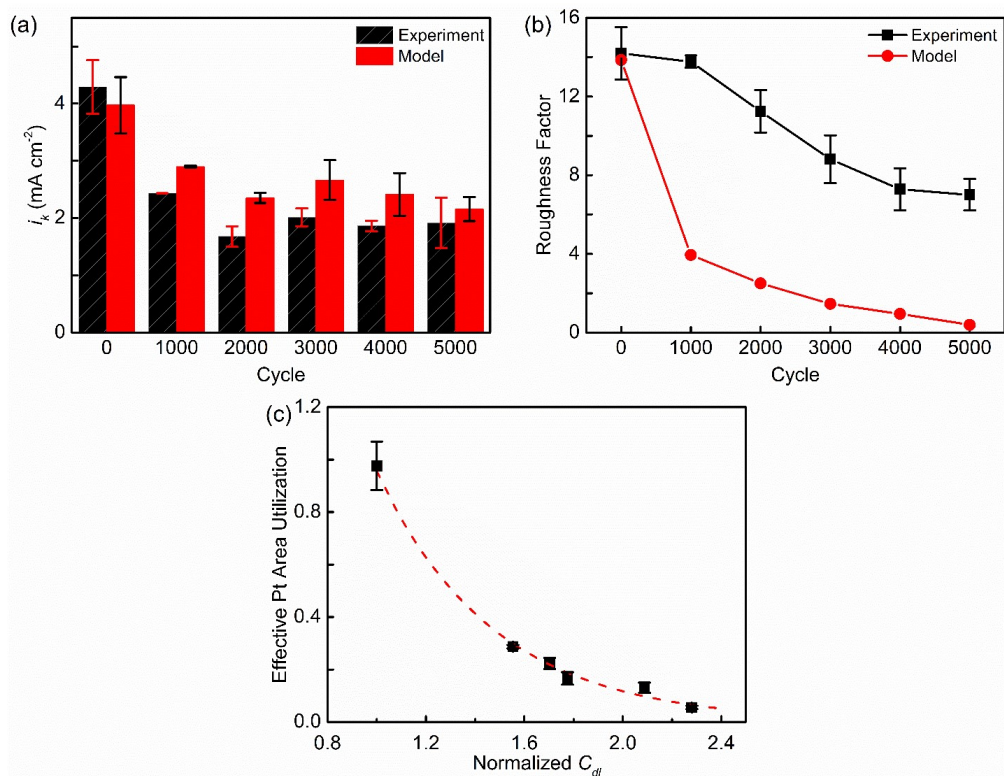


Figure 4.4: (a) Analysis with the Tafel approximation showing the model predicted and experimental values for kinetic current (i_k) in LPC_Acid. (b) Comparison of the model and experimental values of rf in HPC_Acid. (c) Correlation of the effective Pt area utilization (model predicted rf divided by experimentally measured rf) with the normalized C_{dl} for HPC_Acid.

On the other hand, the experimentally measured loss ($\sim 97\%$) is much greater than the rf degradation ($\sim 50\%$) measured by CV for HPC_Acid after 5,000 cycles, as illustrated in Figure 4.11 (see Appendix). To further investigate this discrepancy, the Tafel model in Equation (4.3) was also employed for HPC_Acid. The fitted values of i_0 and B for HPC_Acid are plotted in Figure 4.10b (see Appendix), which significantly shows variation throughout the ADT process, indicating a change of reaction kinetics. Using the i_0 and B obtained at BOL, the theoretical rf can be calculated by the Tafel approximation based on the i_k measured experimentally for HPC_Acid. Figure 4.4b shows a significant discrepancy of the rf between the Tafel model and the CV measurement, which can be ascribed to the growing number of inaccessible active sites for ORR during the high-potential cycling. For further analysis, the effective Pt area utilization, calculated from model predicted rf divided by the measured rf , is plotted as a function of the normalized C_{dl} in Figure 4.4c.

The results show that effective Pt utilization reduces exponentially with increasing double-layer capacitance, confirming that the majority of the catalyst surface sites are not catalytically active towards ORR after 5,000 cycles. Moreover, the resulting trend in Figure 4.4c resembles that in Figure 4.12, which is comparable to Langmuir-like adsorption of carbon surface oxides on Pt surface, as elucidated in the Appendix. Thus, for HPC_Acid, the carbon surface oxides improve the electric double-layer (EDL) charging capacitive behaviors but disrupt the accessible active sites or the Faradaic electron transfer for ORR. In contrast to HPC_Acid, HPC_Alkaline yield a high effective Pt surface area utilization by applying the same Tafel analysis in Equation (4.3) over the entire HPC process, as shown in Figure 4.13 (see Appendix). The high Pt utilization of HPC_Alkaline agrees with the less severe ORR activity loss measured in LSV (Figure 4.3c).

4.5 Degradation of carbon support

The condition of the carbon support can be deduced from the region III in the CV (Figure 4.1a and b), where the DL charging capacitive current remains almost constant throughout the ADT for LPC_Acid. It can be concluded that the surface of the carbon support is not modified significantly. In contrast, Figure 4.1b for HPC_Acid demonstrates increasing DL capacitive current, suggesting oxidation of the carbon support. In region IV, the Pt reduction peak current decreases with potential cycling, which could be interpreted as alternations of adsorbed species generated by carbon corrosion [65]. Besides, as illustrated in Figure 4.1b, a small oxidation peak at around 0.6 V is slowly forming over time, which can be assigned to the formation of electro-active carbon species, such as quinone/hydroquinone [67, 166]. To further investigate the degradation of the carbon support, double-layer capacitance, C_{dl} (mF cm_{geo}^{-2}) is calculated as:

$$C_{dl} = \frac{i_{dl}}{v} \quad (4.5)$$

where i_{dl} is the DL charging capacitive current density ($\text{mA cm}_g^{-2}eo$) and v is the applied potential scan rate (mV s^{-1}). The calculated C_{dl} is then normalized to that of the BOL condition. As shown in 4.1c and d, the C_{dl} remains almost unchanged for LPC_Acid, but is more than doubled for HPC_Acid, indicating only the latter underwent considerable oxidation of carbon support surface. The increase in for HPC_Acid could be ascribed to the formation of carbon surface oxides, which increases the interfacial wettability of the carbon surface and attracts more electrolyte [167], thus facilitating the ion transport and adsorption for DL capacitive behaviors.

Another tool to study EDL is through electrochemical impedance spectroscopy (EIS). The EIS results of the samples in the N_2 -saturated acid electrolyte at 0.4 V from the LPC and HPC ADTs are shown in Figure 4.5a and b, with the expanded view of the high-frequency region in the inset. Without the Faradaic electron transfer reaction, the impedance at the high-frequency region is dominated by the proton transport in acid [31]. Compared with LPC_Acid, HPC_Acid experiences a prominent increase in proton transport resistance with cycling time, possibly due to increasing non-covalent interaction between the adsorbed proton and the oxide species on the carbon surface.

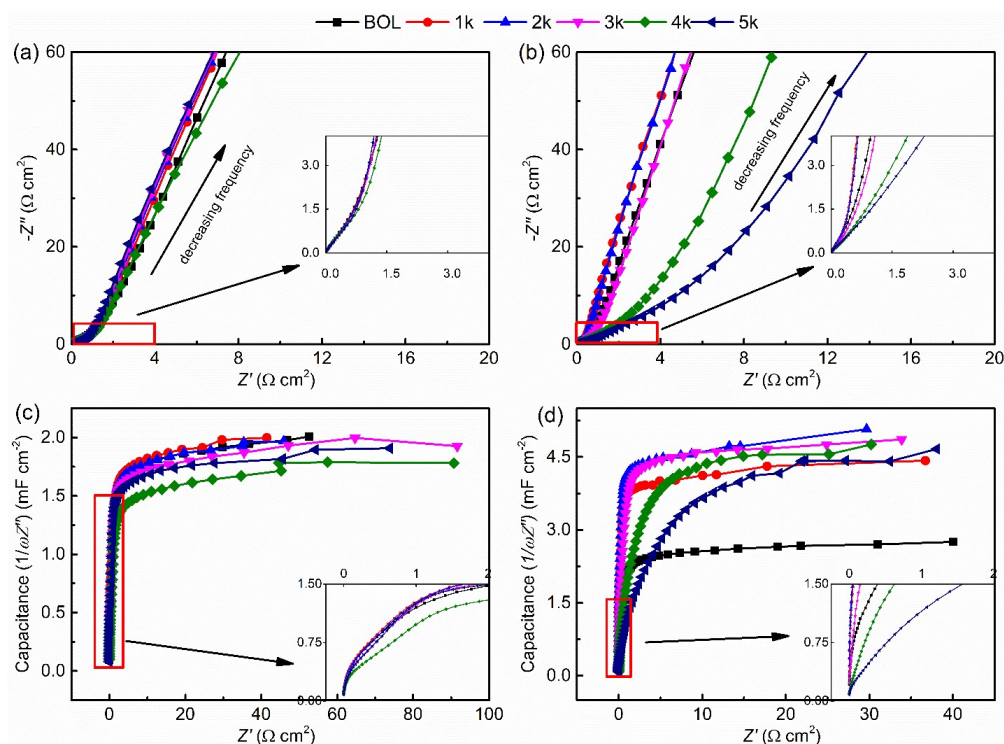


Figure 4.5: Electrochemical impedance spectroscopy (EIS) response and the corresponding capacitance plots in N_2 -saturated 0.1 M $HClO_4$ at 0.4 V for (a,c) LPC_Acid and (b,d) HPC_Acid.

Capacitance plots processed from the EIS data (Figure 4.5c and d) provide valuable information on the charge conductivity within the catalyst layer and the available surface area simultaneously [31]. Also, the maximum capacitance is proportional to the utilization of the available surface area of both Pt and the carbon support [31]. The maximum capacitances throughout 5,000 durability cycles for LPC_Acid remain almost constant in the range of 1.5–2.0 $mF\ cm^{-2}$, but more than

doubled for HPC_Acid, correlating with the C_{dl} measured from CV (Figure 4.1c and d).

For HPC_Alkaline, the apparent C_{dl} was estimated at 0.4 V, where the detected current is purely attributed to the DL charging and discharging capacitive behaviors. Contrary to HPC_Acid, the measured C_{dl} , shown in Figure 4.3b and Figure 4.14b from EIS (see Appendix), decreases throughout the HPC process, suggesting the prominent carbon surface area loss. In summary, the observations from C_{dl} demonstrate the electrolyte-dependent degradation mechanism of carbon corrosion, which will be further discussed.

To track the chemical changes in the carbon support and to explain the electrochemical behaviors observed, XPS was performed on fresh and degraded Pt/C samples in both acidic and alkaline media, in Figure 4.15 (See Appendix). The collected C 1s spectrum is analyzed by six different carbon chemical states, including C–C at 284.3 eV, three C oxidized species, and two C–F bonds from Nafion ionomer, as shown in Figure 4.6. The fitted results are summarized in Table 4.1. Compared with the fresh Pt/C, only slight oxidation of carbon surface is observed in LPC_Acid, consistent with the C_{dl} observation in Figure 4.1c. In contrast, high-potential cycling exhibits significant carbon oxidation and forms the carboxyl (O–C=O) and carbonyl (C=O) groups in acidic and alkaline media, respectively. In addition, the C–C bonding in HPC_Acid decreased significantly compared to other samples, implying the severe carbon surface oxide formation on the sample.

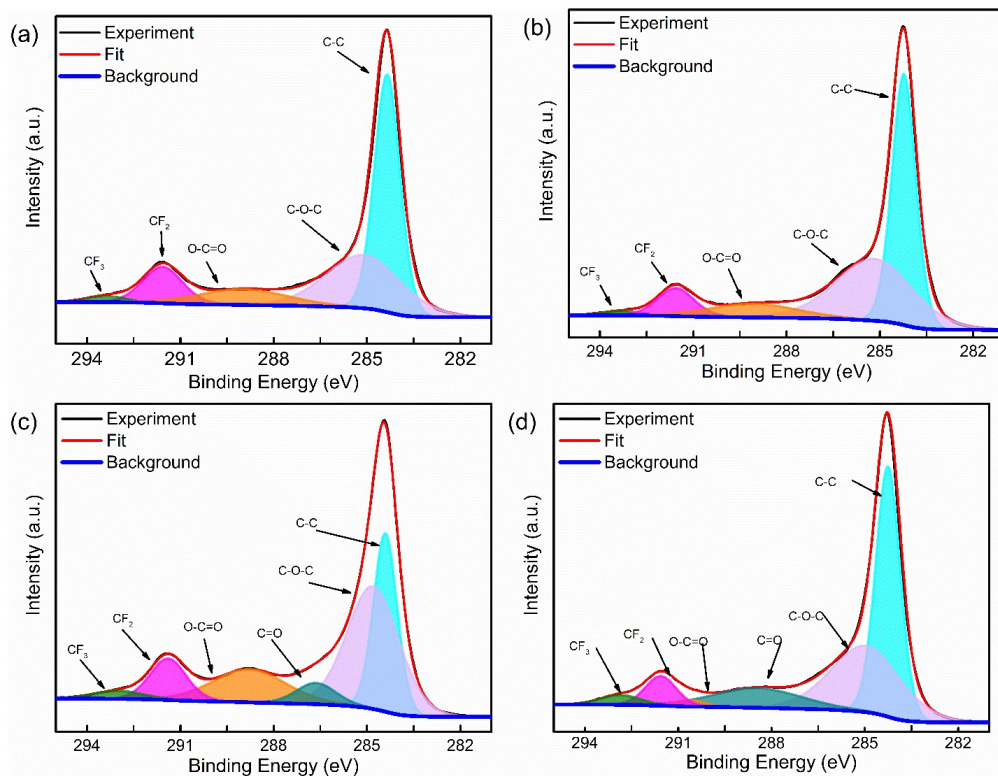


Figure 4.6: XPS peak deconvolution of C $1s$ spectrum collected from glassy carbon electrode coated with catalyst layers for (a) fresh, (b) LPC_Acid, (c), HPC_Acid, and (d) HPC_Alkaline samples.

Table 4.1: XPS analysis of C $1s$ peaks for the fresh and degraded Pt/C.

Chemical State	Peak Relative Distribution (%)				Binding Energy (eV)	Reference
	Fresh	LPC_Acid	HPC_Acid	HPC_Alkaline		
C-C	45.42	45.55	26.73	43.8	284.3	[166]
C-O-C	30.67	36.1	40.41	32.92	285.7	[166]
C=O	-	-	5.33	12.44	287.0	[166, 168]
O-C=O	10.73	9.22	15.34	1.4	289.2	[169, 170]
CF ₂	11.23	7.84	9.59	6.6	~292.0	[169]
CF ₃	1.95	1.29	2.61	2.84	~294.0	[169]

The XPS results provide direct evidence that the carbon corrosion mechanism strongly depends on the electrolyte environment despite having similar ADT conditions. In an earlier investigation [71], carbon surface oxides were observed to form in an acidic environment through acid-catalyzed ring-opening in the graphitic structure. The formed carbon surface oxides may include phenols, ethers, ketones,

and carboxylic acids among others [29]. The carbon surface oxides in the acidic environment, mostly O–C=O, increases the wettability of the carbon support and improves the ion migration, making it easier to form a double-layer [167]. This phenomenon then leads to a considerable increase in the measured C_{dl} . For the alkaline condition in the same study [71], hydroxyl radical (OH·) preferentially reacts with the alkyl side chains, causing oxidation of the carbon layers. The oxidation process in alkaline media weakens the $\pi-\pi$ interactions between the graphitic layers, turning the carbon surface to be more hydrophilic and eventually dissolve in the electrolyte. This mechanism is consistent with the observed decrease in HPC_Alkaline. The detachment of carbon layers in alkaline media also exposes more C=O functional groups [71].

At potentials between 0.6–0.8 V, Pt is known to be an active catalyst for COR upon interaction with the carbon surface oxide generated in the degradation process [61]. However, during ORR activity measurement, the carbon surface oxides could be adsorbed onto the Pt surface, which blocks the active sites for ORR. This strengthens the idea that the ORR activity decline in HPC_Acid is mostly due to the poisoning of Pt active sites. The poisoning effect of carbon surface oxides on Pt for ORR is also observed by another work [171] using scanning electrochemical cell microscopy. Furthermore, the discrepancy between the measured and model calculated rf (Figure 4.2b) in HPC_Acid affirms Pt poisoning from the carbon surface oxide, predominantly due to O–C=O. The estimation of the active Pt surface area from a CV in the potential range 0.05–0.4 V has been established to have less influence from the carbon support and Pt oxide reaction compared to other regions [43]. Thus, the measured rf is not affected by possible carbon surface oxide, while the actual Pt surface available for ORR is much lower. Moreover, the peak current of Pt-oxide reduction in Figure 4.1b diminishes gradually throughout high-potential cycling, which also indicates a strong interaction between the Pt surface and the adsorbed carbon surface oxides [65].

The mechanisms for the Pt and carbon degradation in different ADT conditions can be deduced from a study by Pandey et al. [42]. During LPC_Acid, unstable carbon surface oxides can be formed even at low potentials. Amorphous carbon domains can be corroded in the potential range of 0.40–1.00 V. The unstable carbon oxides can be further oxidized by water activation at 0.95 V or upon reaction with Pt-OH_{ads} at 0.65 V. After the oxidation process, CO₂ and carbon defect sites are formed. Since the majority of the generated carbon surface oxides in LPC_Acid are converted to CO₂, this explains why carbon surface oxide poisoning is not primarily observed in the sample. At potentials higher than 1.0 V, the ordered graphitic domain starts to corrode [67]. This could be happening in HPC_Acid, where unstable carbon surface oxides are generated from the ordered domains of the carbon support and are not fully converted to CO₂. These species then heavily affect the

Pt ORR performance, with O=C=O groups mainly poisoning the Pt surface sites in HPC_Acid. In general, CO and CO₂ are known contaminants that poison the Pt and Pt-alloy catalysts in PEMFC even at high temperatures [172].

In alkaline media, the carbon surface oxides are also generated and can be converted to CO₂ either by directly reacting with Pt-OH_{ads} through the spillover mechanism or by adsorbing onto Pt first to form Pt-CO_{ads} followed by the reaction with Pt-OH_{ads} [69]. Pt also acts as a catalyst for CO₂ evolution in alkaline media, however, carbon layers dissolve in the alkaline electrolyte, thus severe Pt poisoning effect could have been avoided. The generated CO₂ can also interact with K⁺ to form solid potassium carbonate (K₂CO₃) in the KOH solution. The solid carbonates near the Pt NPs are believed to facilitate the detachment of Pt on the carbon support [69].

4.6 Pt degradation and interfacial interactions with carbon support

To investigate the chemical change of the Pt catalyst, the Pt *4f* XPS spectrum shown in Figure 4.16 (see Appendix) and Table 4.3 (see Appendix) reveal the oxide species (i.e. PtO and PtO₂) on the Pt surface. Overall, similar Pt oxidation states can be observed between the fresh and the degraded samples. This can be explained by the instability of the generated Pt oxides in the hydrated form which could be dissolved in the electrolyte solution.

The morphological changes on the Pt NPs were investigated using TEM (Figure 4.7a-d). These images were analyzed using ImageJ software to estimate the size and number of Pt NPs of all studied samples, and the results are summarized in Figure 4.7h. To ensure data quality, the entire area of the TEM image was processed to capture the maximum sample size. As a result, the number of Pt particles analyzed from the fresh, LPC_Acid and HPC_Acid samples were 488, 288, and 105, respectively. Figure 4.7e-g illustrate the observed size and distribution of Pt NPs for fresh, LPC_Acid and HPC_Acid samples, respectively. The fresh Pt NPs have an average diameter of 2.6 nm with uniform dispersion on the carbon support. In LPC_Acid, significant Pt particle growth can be observed due to agglomeration and Ostwald ripening. The larger particles formed in LPC_Acid (> 8 nm) can be due to Pt redeposition, happening at potentials less than 1.0 V [173]. For HPC_Acid, the Pt size increases slightly to an average of 3.2 nm, with Pt agglomeration and particle detachment being the primary mechanisms, as observed from Figure 4.7c. Due to Ostwald ripening and Pt detachment occurring in LPC_Acid and HPC_Acid, respectively, the final Pt surface area (or *rf*) after ADT can be similar as measured from CV shown in Figure 4.1c and d. This behavior for the two ADT conditions is further explained in the Appendix.

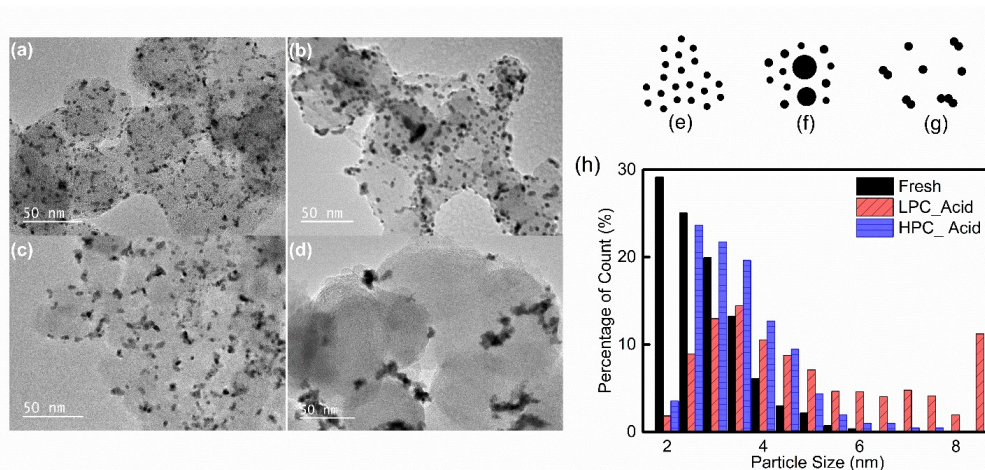


Figure 4.7: TEM images for (a) fresh samples, (b) LPC_Acid, (c) HPC_Acid, and (d) HPC_Alkaline showing the different Pt particle distribution and physical degradation. Illustration of Pt particle evolution from (e) well-dispersed fresh sample to (f) LPC_Acid demonstrating severe Ostwald ripening and (g) agglomerated Pt particles in HPC_Acid with significant Pt detachment due to carbon corrosion. (h) Particle size distribution based on (a-c) comparing fresh and acid degraded samples.

Interestingly, the Pt agglomeration after degradation in alkaline media is significantly different from that in acid; much larger chain-like Pt agglomerations are observed in HPC_Alkaline. Due to the difficulty in identifying individual Pt NPs in HPC_Alkaline, quantification of the size distribution with TEM images was not performed. Nevertheless, prominent surface mobility and detachment of Pt in the HPC_Alkaline sample can be noted, which is not observed in HPC_Acid. Similar observations are supported by the SEM images in Figure 4.17. Since the XPS results of Pt do not show any significant difference, the Pt mobility should be mainly influenced by the carbon support chemistry. Kim et al. [174] showed that there is a higher adhesion force between the Pt-probe and an acid-treated carbon with C/O functional groups using atomic force microscopy techniques. Another study [175] reported that the modification of the carbon surface with O–C=O improved Pt dispersion and strengthened the interaction between the carbon support and the Pt NPs through coordination or electrostatic interaction. Therefore, the presence of O–C=O, groups, which is abundant in HPC_Acid but scarce in HPC_Alkaline, could play an important role in stabilizing the Pt NPs on the carbon surface, keeping them from being mobile.

Schematic illustrations summarizing the various degradation mechanisms in

all studied samples are depicted in Figure 4.8. The Pt/C degradation mechanisms are elucidated to be dependent on the ADT operating conditions and the applied electrolyte environment. The ORR activity loss can be attributed to the combination of carbon corrosion, Pt degradation, and the interfacial interaction between carbon and Pt.

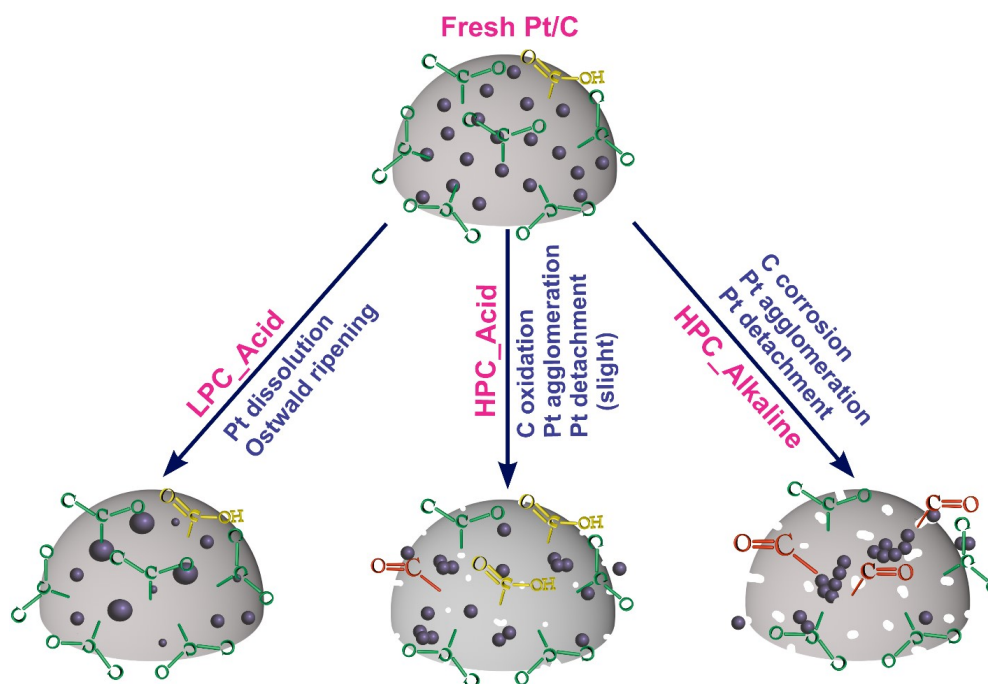


Figure 4.8: Schematic illustration of the degradation of both Pt and carbon support after being subjected to different potential cycling condition in acid and alkaline electrolyte. Major degradation mechanisms are also listed for each accelerated durability test (ADT) conditions.

4.7 Conclusion

The degradation mechanisms of Pt/C catalyst for ORR in acidic and alkaline media were investigated. Low-potential and high-potential cycling in acid yield comparable electrochemical active surface area at the end of their respective accelerated durability tests. However, their primary degradation mechanisms are different, where Oswald ripening is dominant in low-potential cycling and Pt detachment and agglomeration for high-potential cycling. Carbon surface oxides, predominantly O–C=O functional groups, are generated after high-potential cycling in acid. These species enhance the wettability of the carbon support, leading to the increase of double-layer capacitance, but also impede the ORR activity by adsorbing unto the Pt active sites and cause poisoning. After high-potential cycling in alkaline media,

the presence of O–C=O groups was scarce, and the ORR activity degradation is not as severe as in acid, thus supporting the poisoning effect of O–C=O groups to cause ORR activity degradation in acid. These results demonstrate the effects of different carbon corrosion mechanisms in acidic and alkaline media and its impacts on the measured ORR activity. The carbon corrosion mechanism also affects the mobility of Pt on the carbon support, as exemplified from high-potential cycling samples in alkaline, where larger chain-like Pt agglomerations are formed. The presence of O–C=O in high-potential cycling samples in acid strengthened the interaction and bonding between the Pt nanoparticles and the carbon support. It is emphasized in this work that the measured electrochemically active Pt area from the HAD method might not be fully utilized for ORR, as there could be poisoning effect. The results from this work contribute to the fundamental understanding of the degradation mechanisms of the commercial catalysts for developing more durable ORR catalysts. Implementing the optimized operating strategy and corrosion-resistant supports are the key to enable long-term fuel cell operation.

4.8 Appendix

Table 4.2: Impedance fitting parameters at 0.85 V obtained in O₂-saturated 0.1 M HClO₄ with 1600 rpm.

Cycle No.	LPC_Acid		HPC_Acid	
	R_o (Ω)	$R_1 + R_2$ ($\Omega \cdot \text{cm}^2$)	R_o (Ω)	$R_1 + R_2$ ($\Omega \cdot \text{cm}^2$)
0	26.0	43.9	28.4	32.4
1,000	25.1	49.1	27.7	115.6
2,000	23.6	59.3	28	159.0
3,000	24.1	53.3	26.7	202.7
4,000	23.6	80.9	27.8	280.9
5,000	24.3	72.1	27.2	441.4

Table 4.3: Relative amount of different Pt chemical states from Pt *4f* XPS peak deconvolution on fresh and degraded samples and the average oxidation state calculated as weighted average from each chemical states.

Chemical State	Fresh	HPC_Acid	HPC_Alkaline
Pt ⁰	43%	45%	41%
PtO (Pt ²⁺)	34%	34%	32%
PtO ₂ (Pt ⁴⁺)	23%	21%	27%
Average Oxidation State	1.61	1.51	1.70

4.8.1 Particle Size and roughness factor (rf) in acid

To justify the similarities in rf for LPC and HPC in acid, consider two samples with similar total Pt masses but with different Pt nanoparticle (NP) diameters. Assuming the density (ρ) of Pt NPs is constant, the total Pt mass (m) can be expressed as:

$$m = \rho n_1 V_1 = \rho n_2 V_2 \quad (4.6)$$

where the subscripts 1 and 2 denote LPC_Acid and HPC_Acid, respectively and n and V are the number and volume of Pt NPs. Consider a scenario where Ostwald ripening is more severe in LPC_Acid, thus having larger Pt NPs than HPC_Acid, i.e. $r_1 \gg r_2$. The number of Pt NPs (n_2) in HPC_Acid, with smaller radius r_2 , can be calculated:

$$n_2 = \frac{n_1 V_1}{V_2} \quad (4.7)$$

The total surface area for LPC_Acid and HPC_Acid are:

$$A_1 = 4\pi r_1^2 n_1 \times (1 - OR_1) \quad (4.8)$$

$$A_2 = 4\pi r_2^2 n_2 \times (1 - OR_2) \quad (4.9)$$

where OR is the overlap ratio between Pt NPs, accounting for agglomeration, and assumed to be zero for LPC_Acid ($OR_1 = 0$). Getting the ratio for A_2/A_1 and expressing n_2 using Equation 4.7:

$$\frac{A_2}{A_1} = \frac{r_2^2}{r_1^2} \times \frac{V_1}{V_2} \times (1 - OR_2) \quad (4.10)$$

The volume ratio can be expressed as:

$$\frac{V_1}{V_2} = \frac{r_1^3}{r_2^3} \quad (4.11)$$

Then, the area ratio can be simplified as:

$$\frac{A_2}{A_1} = \frac{r_1}{r_2} \times (1 - OR_2) \quad (4.12)$$

Since $r_1 \gg r_2$, then A_2 for HPC_Acid is greater than A_1 of LPC_Acid. Therefore, to match the rf of HPC_Acid, i.e. $A_1 \approx A_2$, additional smaller-sized Pt NPs are necessary for LPC_Acid. The total Pt masses in LPC_Acid and HPC_Acid do not necessarily have to be the same. This justifies that even with Pt detachment in HPC_Acid that results in reduced Pt mass loading, a similar rf with LPC_Acid would still be obtained.

4.8.2 Langmuir adsorption isotherm and the available Pt sites for HPC_Acid

The characteristic profile illustrated in Figure 4.4c for HPC_Acid can be explained by approximating the adsorption of the carbon surface oxides (CO_x) on the Pt surface sites (*) with the Langmuir adsorption isotherm [176], described as:



where CO_x* is the chemisorbed state of CO_x and k_{ads} and k_{des} are the rate constants for adsorption and desorption, respectively. The net rate of adsorption can be written as:

$$r = k_{ads}[CO_x][*] - k_{des}[CO_x*] \quad (4.14)$$

At equilibrium, the net rate of adsorption is zero and the relationship can be expressed as:

$$r = k_{ads}[CO_x][*] - k_{des}[CO_x*] \quad (4.15)$$

Performing a site balance with $[*]_0$ as the total adsorption sites, the fractional coverage of CO_x (θ_{CO_x}) on the Pt surface can be derived:

$$[*]_0 = [*] + [CO_x*] \quad (4.16)$$

$$\theta_{CO_x} = \frac{[CO_x*]}{[*]_0} \quad (4.17)$$

Expressing (θ_{CO_x}) in terms of measurable quantities, $[CO_x]$ and K_{ads} , then combining the above equations:

$$\theta_{CO_x} = \frac{K_{ads}[CO_x]}{1 + K_{ads}[CO_x]} \quad (4.18)$$

Consider the case for $K_{ads}=10$, can be estimated with Equation (4.18) along with the Pt vacant sites, expressed as $(1 - \theta_{CO_x})$, as shown in Figure 4.12. For HPC_Acid, the concentration of CO_x is proportional to the C_{dl} , thus justifying the relationship in Figure 4.4c for C_{dl} and the effective Pt area utilization, which represents the vacant sites available for ORR.

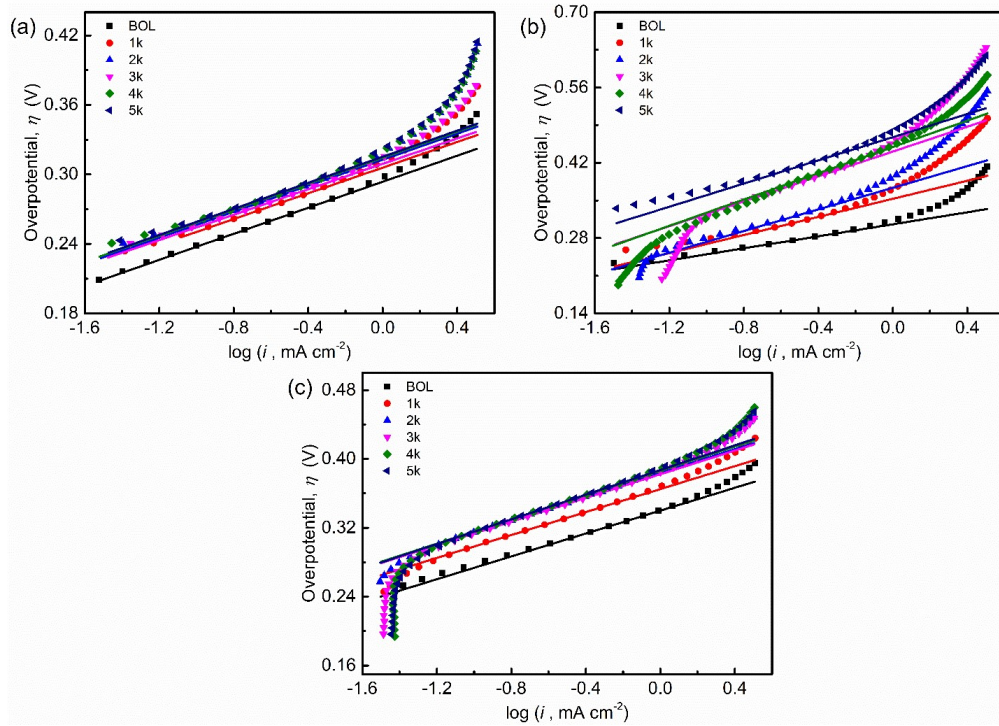


Figure 4.9: Tafel plots for (a) LPC_Acid, (b) HPC_Acid, (c) and HPC_Alkaline every 1,000 cycles. Symbols represent raw data and solid lines are simulation results.

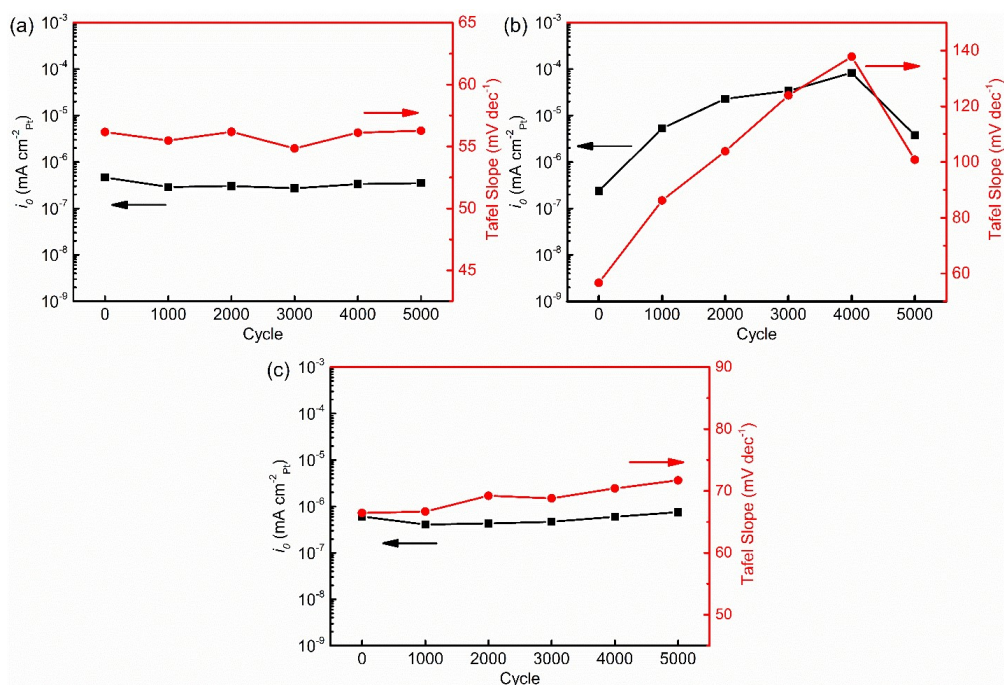


Figure 4.10: Tafel slopes and exchange current density, i_0 , for (a) LPC_Acid, (b) HPC_Acid and (c) HPC_Alkaline every 1,000 cycles.

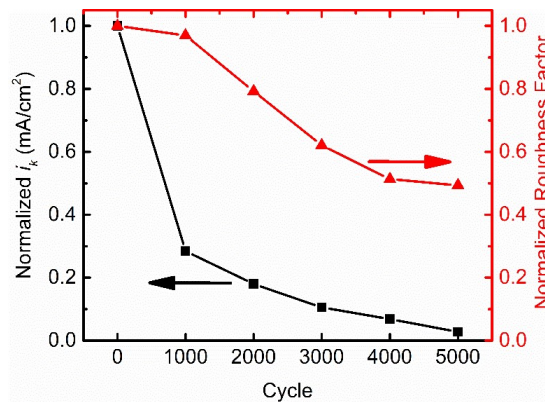


Figure 4.11: HPC_Acid normalized kinetic current (i_k) and roughness factor obtained from the experiment.

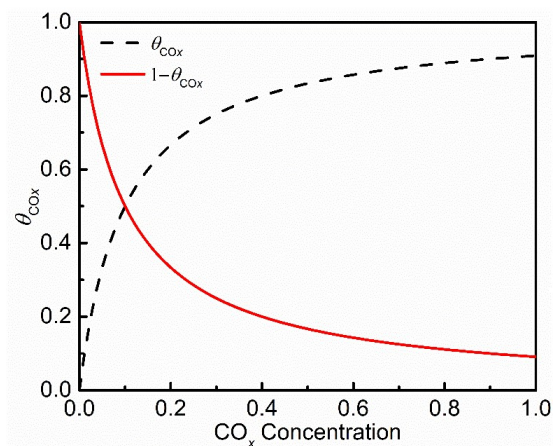


Figure 4.12: Fractional coverage of CO_x (θ_{CO_x}) as a function of concentration approximated using Langmuir adsorption model.

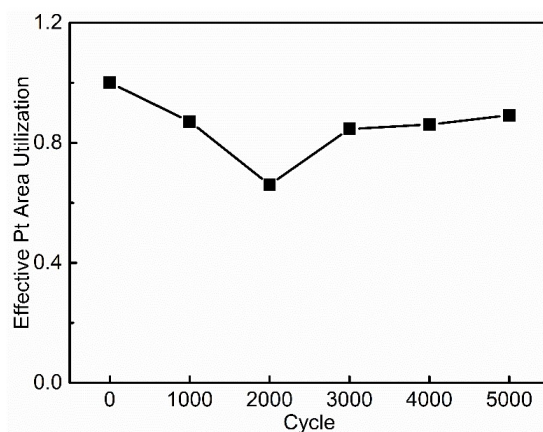


Figure 4.13: Effective Pt area utilization in HPC_Alkaline estimated by dividing the model predicted rf obtained from Tafel equation model with the experimentally measured rf .

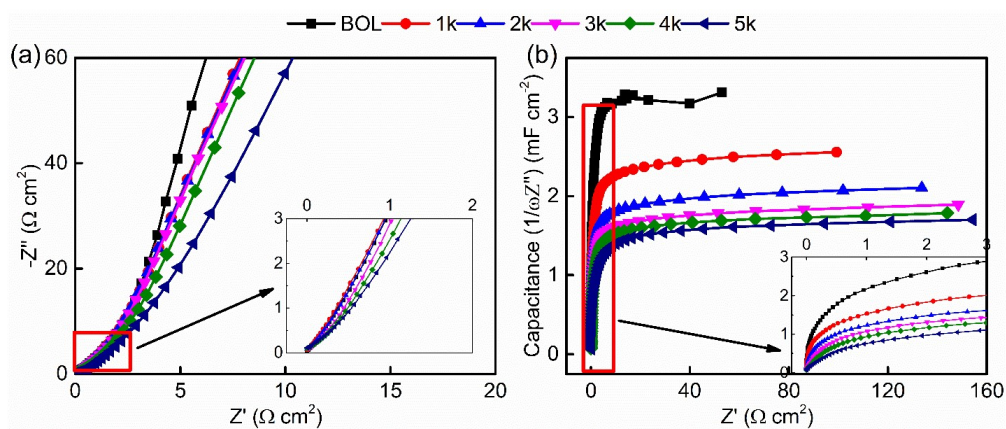


Figure 4.14: (a) Electrochemical impedance spectra and (b) capacitance plot for HPC_Alkaline in N_2 -saturated 0.1 M KOH recorded at 0.4 V.

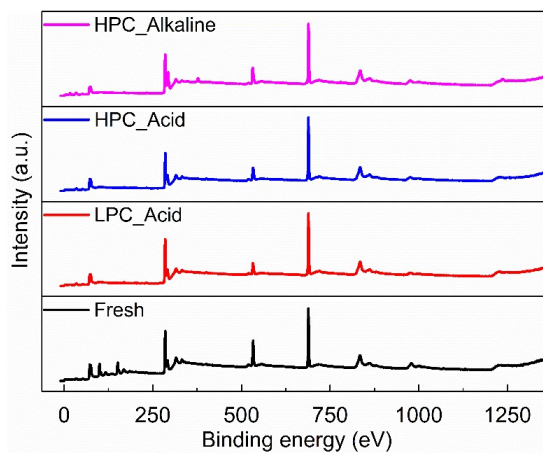


Figure 4.15: XPS survey spectra for fresh and degraded Pt/C samples.

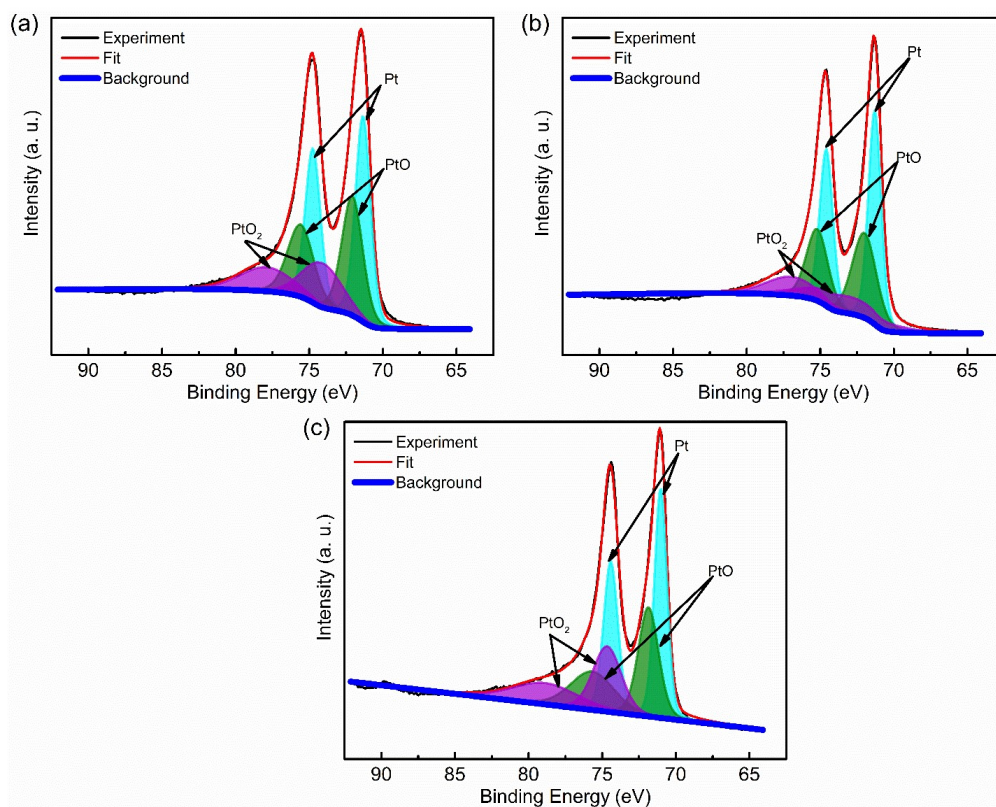


Figure 4.16: XPS peak deconvolution of Pt $4f$ spectrum, showing the different Pt chemical states present in (a) fresh sample, (b) HPC_Acid, and (c) HPC_Alkaline.

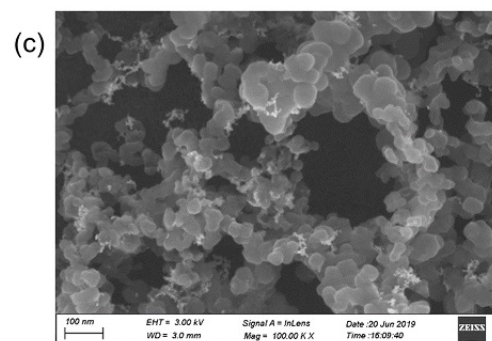
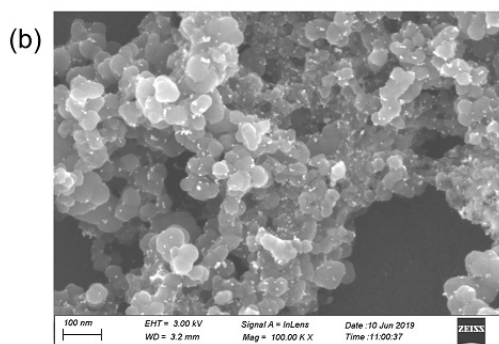
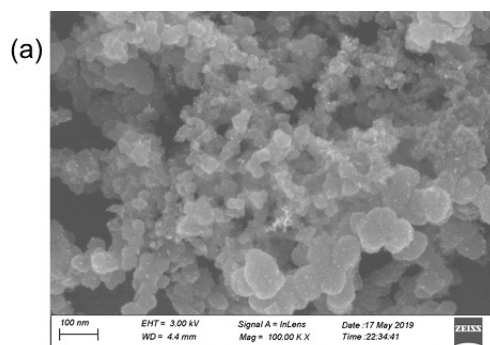


Figure 4.17: SEM images for (a) fresh sample, (b), HPC_Acid, and (c) HPC_Alkaline.

Chapter 5

DEVELOPMENT OF IRIIDIUM-COBALT OXIDE AS AN ALTERNATIVE CATALYST FOR OXYGEN EVOLUTION REACTION (OER)

5.1 Abstract

Green hydrogen from water electrolysis can be a commercially viable path towards decarbonization if cost reduction can be achieved. The iridium-based anode catalyst is one of the most expensive components in electrolyzers. We propose to reduce iridium usage by alloying with cobalt (IrCo), being a less expensive metal. Surfactant-assisted Adam's fusion synthesis technique was developed here as a scalable method to produce IrCo alloy. The synthesized material outperforms a commercial baseline, iridium oxide (IrO_x-C), in both acidic and alkaline media. Further activity enhancement was achieved through acid etching (IrCo_{ae}), preferentially removing Co to generate more active sites. IrCo_{ae} obtained a much lower overpotential at 10 mA cm⁻² compared to IrO_x-C by ~18% and ~14% in acid and alkaline, respectively. This work shows that effective Ir utilization is possible with the proposed synthesis method and can be tailored to improve the catalyst stability for green hydrogen production.

5.2 Catalyst Synthesis and Testing Protocols

5.2.1 Catalyst Synthesis

IrCo oxide was synthesized using a surfactant-assisted Adam's fusion method. Pluronic F-127, a triblock copolymer, was used as a surfactant to control the morphology and stirred for 4 hours. H₂IrCl₆ and Co(NO₃)₂, as Ir and Co precursors, were mixed in a KNO₃ solution with a total metal content of 1 mM and added to the surfactant in a dropwise fashion. The solution is then stirred for 12 hours at 80 °C and evaporated at 98.5 °C to obtain a polymerized particle. Calcination was then performed in the air for 2 hours at 400 °C and the particle was washed with ethanol and water to remove excess reactants and surfactants. The samples are then air-dried. Acid etching was employed by soaking the catalyst powders in HNO₃ solution (0.5 M) for 48 hours and recovered through centrifugation.

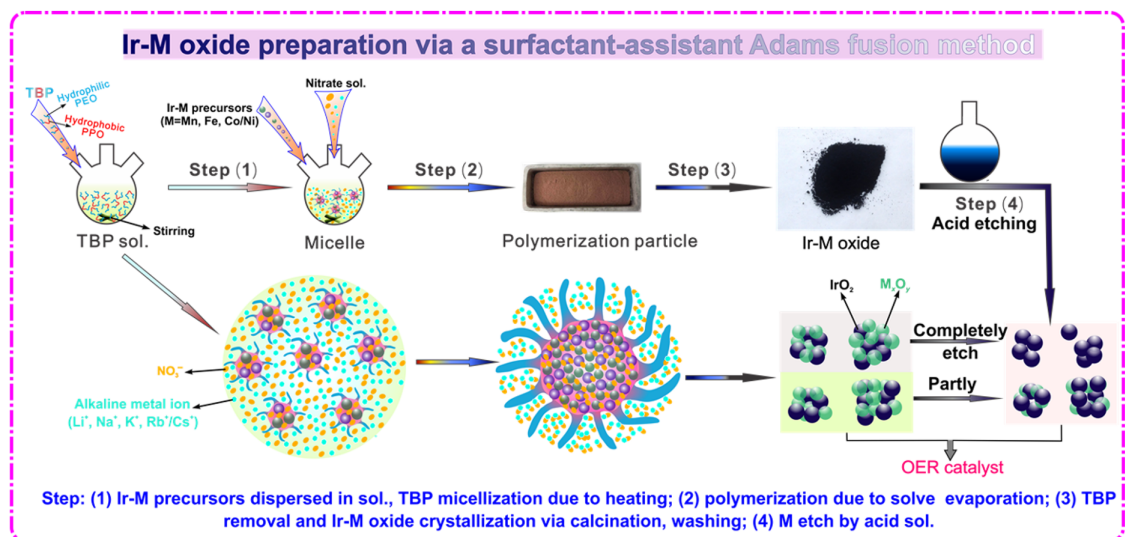


Figure 5.1: A general schematic for the surfactant-assisted Adam’s fusion method developed in this study as illustrated by Dr. Guangfu Li of Thermal and Electrochemical Energy Laboratory (TEEL).

5.2.2 Physicochemical Characterization

X-ray diffraction results are obtained using PANalytical X’Pert PRO with a Co radiation ($\lambda= 1.7902 \text{ \AA}$) at 40 kV and 45 mA. Chemical oxidation states of Ir and Co were analyzed using X-ray photoelectron spectroscopy (XPS, Thermo Fisher Nexsa) with a monochromated Al $K\alpha$ X-ray source (400 μm spot size). Structural analysis and chemical composition of the particles was also performed using transmission electron microscopy and energy-dispersive X-ray spectroscopy (EDS) taken with JEOL 2100-F with an accelerating voltage of 200 kV. Scanning transmission electron microscope (STEM) images are also obtained using TitanX at 300 kV including additional EDS chemical maps at higher resolution. Surface area and porosity estimation were done with N_2 physisorption (TriStar II Plus Micromiretics) using Brunauer-Emmet-Teller (BET) and Barrett-Joyner-Halenda (BJH), respectively. Ir and Co content in the bulk material, as well as the metal dissolution in the electrolyte from full cell stability tests, were measured from inductively coupled plasma-mass spectrometry (ICP-MS) using Agilent 7500ce.

5.2.3 Electrochemical Tests

Electrochemical performance of the catalysts was assessed in half-cell technique, both in HClO_4 (0.5 M) and KOH (1 M) as acidic and alkaline media, respectively, were measured using a CHI 750 E bipotentiostat at room temperature and pressure. Reference electrodes used were Hg/HgO (filled with 1 M KOH) for alkaline and saturated calomel electrode (SCE) for acidic. Pt mesh (1.5 cm^2) serves as the counter electrode. All potentials are converted to a reversible hydrogen electrode (RHE) in this study using:

$$E_{RHE} = E_{WE} + E_{0,RE} \quad (5.1)$$

where E_{WE} is obtained from the working electrode with respect to the reference electrode, E_0 , RE is the standard potential of the reference electrode vs. RHE. The reference electrode potential for SCE from the literature is 0.241 V¹²⁵ while the Hg/HgO potential was adjusted to be 0.9 V at 1.0 M KOH from our previous study¹⁵⁸. Mettler ToledoTM S220 was used to measure the pH of the electrolytes and calibrated by standard buffer solutions (pH = 4.01, 7.0, and 10.0) prior to its use.

A thin-film (TF) catalyst layer was coated on a glassy carbon disk of a TF-RDE (E3 series, OD = 5 mm) and TF-RRDE (E7R9 series, GC disk OD = 5.61 mm, Pt ring OD = 7.92 mm, ID = 6.25 mm) and served as the working electrode. For the catalyst layer preparation, 5 mg of catalyst powder was sonicated with 4 mL of ethanol-water solution (1:3 weight ratio) and 5 wt% Nafion ionomer (I/C = 0.5). The desired amount of catalyst ink was drop cast on a cleaned GC disk to form a uniform thin film and achieve a loading of 0.1 mg/cm^2 .

Before the electrochemical measurement, the electrolyte was purged with N_2 for at least 30 minutes. For TF-RDE, classical voltammetry techniques (cyclic voltammetry, linear sweep voltammetry, and electrochemical impedance spectroscopy) were employed to assess the materials. The CV curves were obtained at static conditions while LSV and EIS results were generated with electrode rotation at 1600 rpm using a modulated speed rotator (MSR) to enhance mass transport and O_2 removal. Nyquist plots from EIS within the range of 100 kHz to 0.1 Hz and collected at 1.55 V were simulated using a built-in CHI program. Electrode rotation was also employed with TF-RRDE and the Pt ring potential was set at 0.4 V to study oxygen transport, 0.9 V metal dissolution study, and 1.4 V to detect hydrogen peroxide (H_2O_2) generation.

Stability evaluation was performed in half-cell by applying 2,000 potential cycles between 0.4-1.4 V at 100 mV/s and the electrochemical performance of the

catalyst are evaluated at end-of-life (EOL). An extended stability test was also performed in full-cell configuration using a working electrode prepared by coating the catalyst ink (loading = 3 mg/cm²) on a carbon paper with a microporous layer (1 cm²) and a Pt plate counter electrode. Current control (50 mA/cm²) using a power source (BK Precision 9120A) was used for stability evaluation at 100 hours and the electrode was collected for post-mortem characterization as well as the electrolyte to detect any metal dissolution using ICP.

5.2.4 Turnover Frequency

Turnover frequency is estimated at 250 mV overpotential where the kinetic region is dominant. Using Equation (5.2) below, TOF is calculated:

$$TOF = \frac{j \times A}{4 \times n \times F} \quad (5.2)$$

Where j is the current density (mA cm⁻²) at 250 mV overpotential, A is the geometric area of the rotating disk electrode (0.196 cm²), n is the number of moles of Ir atoms assuming it is the dominant active site.

5.2.5 Mass Activity Conversion

To convert the geometric current density (mA cm⁻²) to mass activity and assess the Ir utilization, Equation (5.3) below was used:

$$i_{MA} = \frac{j}{l \times m_{Ir} \times 1000} \quad (5.3)$$

Where i_{MA} is the mass activity (A g_{Ir}⁻¹), j is the current density (mA cm⁻²), l is the catalyst loading (0.1 mg cm⁻²) and m_{Ir} is the Ir weight content of the catalysts estimated from XPS coupled with ion etching.

5.3 Material Characterization

Iridium-cobalt oxide (IrCo) was prepared using a surfactant-assisted Adam's fusion method as a catalyst for OER. To enhance the surface area and porosity of the synthesized catalyst, the prepared IrCo material was subjected to an acid etching process with nitric acid (HNO₃), thus partially removing Co (IrCo_{ae}). Both catalysts were compared to a commercial iridium oxide (IrO_x-C) typically used in electrolyzers. The crystalline structure of the materials was investigated using X-ray diffraction (XRD). In Figure 1a, two major peaks appear in IrCo at around 34.7° and 36.8°, with respect to copper K α , that matches the pattern for rutile IrO₂ (101) (IrO₂ rutile, JCPDS 88-0288) and Co₃O₄ (311) (Co₃O₄, JCPDS 74-2120),

respectively. However, after acid etching, the Co_3O_4 (311) pattern disappeared while the IrO_2 (101) was retained in IrCo_ae. Similar observations were obtained from electron diffraction (see Figure 5.5) where most of the d-spacings that correspond to Co_3O_4 patterns in IrCo cannot be found in IrCo_ae and only d-spacings related to IrO_2 (101) was present. Reduced d-spacings in IrCo_ae at around 0.245–0.249 nm (see Figure 5.5f) suggest that lattice contraction is possible, where Co atoms could substitute Ir atoms in the Ir oxide matrix. Compared to the synthesized materials, the commercial $\text{IrO}_x\text{-C}$ shows mostly amorphous, although some reflections coming from the Ir metal are also present.

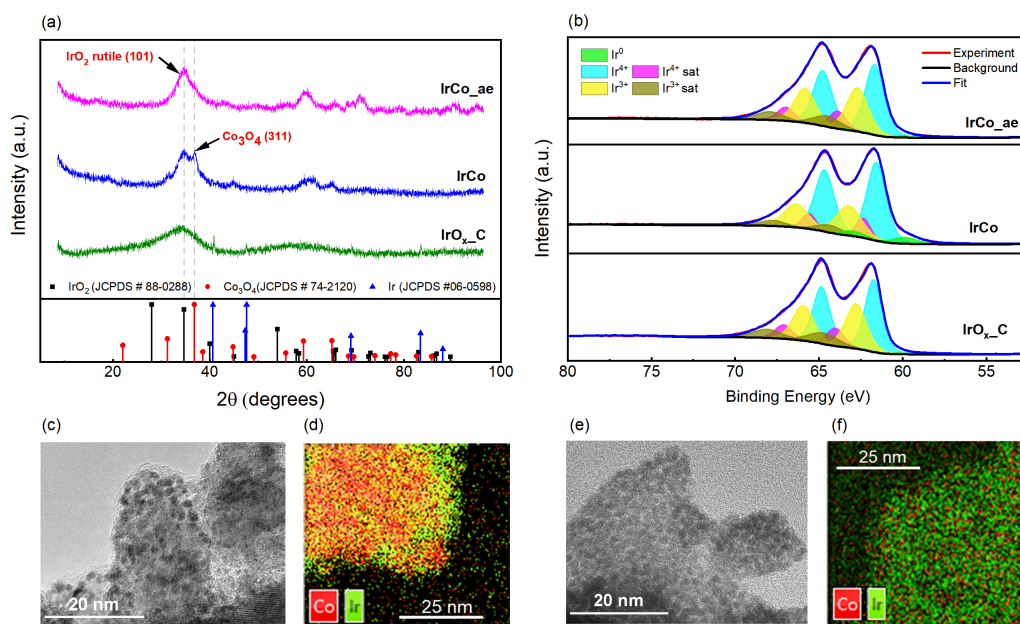


Figure 5.2: (a) X-ray diffractogram of the three catalysts being compared as well as reference patterns for standard materials, (b) X-ray photoelectron spectra for Ir 4f and the deconvoluted peaks of the Ir chemical states among the samples. Electron micrographs and Ir and Co chemical mapping from EDS for (c,d,) IrCo and (e,f) IrCo_ae.

The electronic structure of the catalysts was also investigated using X-ray photoelectron spectroscopy (XPS), shown in Figure 5.2b, and the distribution of three Ir chemical states by deconvoluting the Ir $4f$ spectra, are presented in Table 5.1. For $\text{IrO}_x\text{-C}$, although Ir metallic peaks are obtained in XRD, the presence of Ir^0 on the surface is limited. This can be due to a thick oxide shell or a low dispersion of the metallic state [177, 178]. A mixed valency of $\text{Ir}^{3+}/\text{Ir}^{4+}$, as summarized in Table 5.1, exists for $\text{IrO}_x\text{-C}$. A mix of $\text{Ir}^{3+}/\text{Ir}^{4+}$ is also obtained for IrCo but a higher Ir^0

fraction at 6.67%. After the acid etching process, the relative amount of Ir³⁺ state increased by around 10% while Ir⁰ dropped to 1.43%. The Co *2p* fitting results in Figure 5.9 and Table 5.4 reveal a transformation of a Co₃O₄ dominant phase in the IrCo to a CoO-dominated surface in IrCo_ae. The metallic Co⁰ composition increased from 2.70% to 15.85% after acid etching. It is possible that the acid etching removed most of the Co₃O₄ phase, consistent with what is also observed in the XRD results in Figure 1a and exposing more metallic Co on the surface that are more resistant to acid etching. Acid etching could have also promoted the oxidation of the Ir metals leading to an increase in the metal-oxide concentration in O *1s*. For the O *1s* spectra, four different chemical states were fitted, as tabulated in Table 5.3. A higher defect site for low oxygen coordination was observed for IrCo and IrCo_ae at 42.38% and 31.15%, respectively compared to IrO_x-C at 23.75%.

Table 5.1: Comparison of the Ir chemical states between the synthesized materials and the commercial catalyst.

Ir Oxidation State	Peak Relative Distribution (%)			Ir <i>4f</i> 7/2 Binding Energy (eV)
	IrO _x -C	IrCo	IrCo_ae	
Ir ⁰	0.72	6.67	1.43	60.8
Ir ³⁺	42.68	30.66	40.12	62.2
Ir ⁴⁺	56.6	62.67	58.45	61.9

The morphology of the synthesized materials was examined using transmission electron microscope (TEM). From Figure 5.2c and e, particles of about 2 nm are highly agglomerated on a nanosheet. Additional images using scanning transmission electron microscopy (STEM) are also presented in Figure 5.7. Before acid etching, fringes with large spacings are observed in IrCo which could be from the salts used in the synthesis. After acid etching, the wide fringes are removed and the finer lattice fringes on each particle are more visible.

Using elemental mapping through energy-dispersive X-ray spectroscopy (EDS) at high resolution (see Figure 5.6), the nanoparticles are confirmed to be made of pure iridium atoms; however, the matrix where these nanoparticles are embedded can either be a pure cobalt oxide matrix or in combination with iridium oxide. The EDS chemical mapping in Figure 5.2d and f also agrees with XPS quantification data (Table 5.2), where initially an Ir:Co atomic ratio of 1.59 was obtained for IrCo then increased to 5.62 after acid etching, proving the preferential removal of Co. Powder samples were also digested and analyzed using ICP-MS and bulk metal atomic ratios agree well with the XPS data.

5.4 Electrochemical Performance

The cyclic voltammetry curves in Figure 5.3a demonstrate the sharp redox peak at ~ 0.73 V for the $\text{Ir}^{3+}/\text{Ir}^{4+}$ pair transition in acid while Figure 5.3b shows the same redox pair in alkaline at ~ 0.55 V, although not as distinct as that in acid. The shift in redox peak with respect to pH has been referred to as the “super-Nernstian” behavior of the $\text{Ir}^{3+}/\text{Ir}^{4+}$ redox transition [179]. Additionally, the redox peak in Figure 5.3a for the synthesized oxides (IrCo and IrCo_ae) is much higher in current density compared to the commercial $\text{IrO}_x\text{-C}$. It could be related to the generation of more Ir^{3+} oxides from the exposed Ir^0 in the synthesized material, compared to a negligible Ir^0 peak from the commercial $\text{IrO}_x\text{-C}$. According to Steegstra et al. [179], there is an increased oxide formation in acidic pH, thus might explain why the enhanced $\text{Ir}^{3+}/\text{Ir}^{4+}$ peak was not observed in the alkaline conditions.

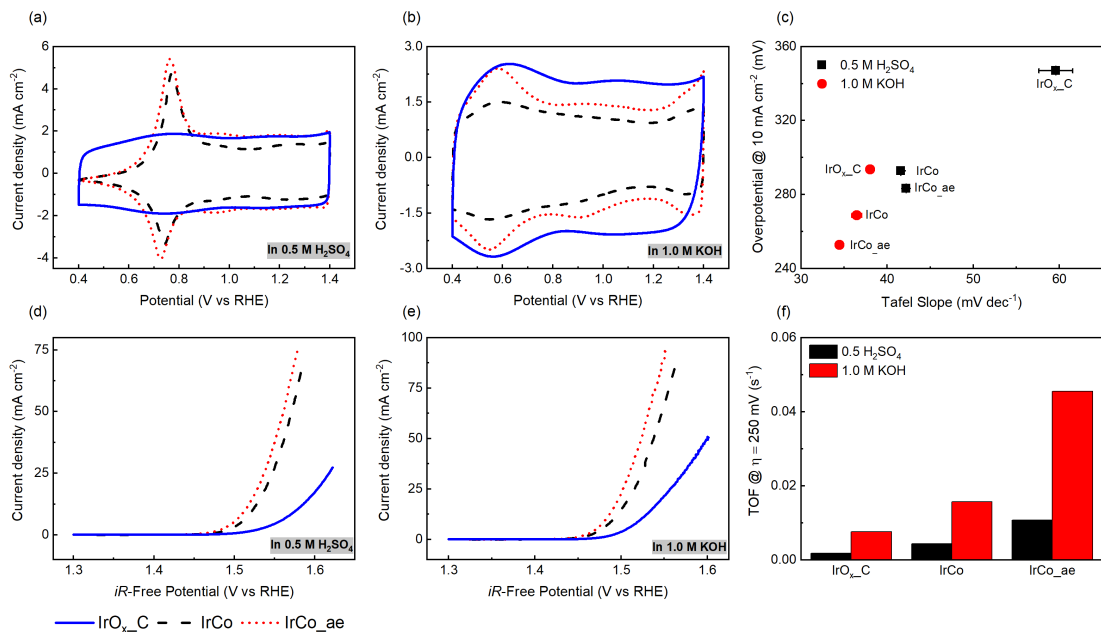


Figure 5.3: Cyclic voltammety curves of $\text{IrO}_x\text{-C}$, IrCo and IrCo_ae in (a) acid and (b) alkaline media collected at 50 mV/s . (c) Compiled overpotential at 10 mA/cm^2 and Tafel slopes of the three different catalysts. Linear sweep voltammety at 20 mV/s in (d) acid and (e) alkaline media. (f). Turnover frequency (TOF) was estimated from the LSV curves at an overpotential of 250 mV in acidic and alkaline media.

The electrochemical performance of the catalysts was assessed by linear sweep voltammety, presented in Figure 5.3d and e for acidic media and alkaline media,

respectively. To compare the catalytic performance, OER kinetic parameters were extracted from the LSV curves and are summarized in Figures 5.3c and f. The most active catalyst in both acidic and alkaline media is IrCo_ae, where the Tafel slopes are 42.2 mV/dec and 34.5 mV/dec, respectively. These slopes are preferred compared to a relatively higher Tafel slope from IrO_x-C at 59.6 mV/dec in acid and 38.0 mV/dec in alkaline media. The large difference in the Tafel slope between IrCo_ae and IrO_x-C in the acidic media can indicate their different rate determining steps [180]. Interestingly, this also coincides with the observed CV peak difference in acidic media between the synthesized oxides and the commercial catalyst and that the Ir³⁺/Ir⁴⁺ redox peak might influence the rate determining steps. IrCo_ae also has the lowest overpotentials at 10 mA/cm², yielding 283.3 mV and 252.7 mV in acidic and alkaline media, respectively.

As to the effect of acid etching, the Tafel slopes were not changed significantly from IrCo to IrCo_ae, both in acidic and alkaline media, but the improvement in the catalytic activity is magnified in the turnover frequency (TOF), representing the amount of product formed per unit time per amount of catalyst [181]. The TOF after acid etching increased from 0.0044 s⁻¹ to 0.011s⁻¹ in acid and 0.016 s⁻¹ to 0.045 s⁻¹ in alkaline after the acid etching process. Mass activities (see Figure 5.10) were also obtained with respect to the amount of Ir in the catalyst, and it becomes clearer that both IrCo and IrCo_ae have more effective Ir utilization than the IrO_x-C.

A rotating ring-disk electrode study was also performed to evaluate the oxygen transport efficiency (see Figure 5.17) of the catalysts, where IrCo_ae demonstrates the most efficient O₂ transport in both electrolytes. This can be attributed to an optimized pore size and surface that allows the efficient removal of O₂ bubbles [156]. In addition, the OER pathway was also assessed with the ring potential set at 1.4 V to detect peroxide formation (see Figure 5.19). The anodic current detected on the ring is negligible, suggesting that a 4-electron path is preferred for all catalysts.

The OER performance is dictated by the availability of the active sites. The BET surface areas obtained from N₂ adsorption experiment are as follows: 44.97 cm² g⁻¹ for IrO_x-C, 135.57 cm² g⁻¹ for IrCo and 273.17 cm² g⁻¹ for IrCo_ae. All other information related to pore size is summarized in Table 5.5. IrCo shows a much higher BET surface area than IrO_x-C which could indicate more reaction sites for OER. However, BET surface area does not directly translate to the electrochemically active surface area (ECSA). In the literature [182], the double-layer capacitance of Ir-catalysts has been associated with the ECSA unlike in Pt-based systems where hydrogen adsorption and desorption can be utilized for ECSA measurement [155]. The measured electrode double-layer capacitance (C_{dl}) is more commonly used and can be converted into ECSA by assuming a specific areal capacitance. Single-point

C_{dl} measurement at 0.9 V (Figure 5.12 and Figure 5.13) with scan rates ranging from 2 to 150 mV/s was performed to estimate the ECSA using an areal specific capacitance from the literature [183] of 1.3 F m⁻². However, the obtained double-layer capacitance (C_{dl}) for IrO_x-C is much larger, resulting in an order of magnitude difference in the calculated ECSA compared to its BET surface area. In alkaline media, IrO_x-C yields the highest ECSA (see Table 5.6) from the single-point C_{dl} measurement. This might be due to the pore size of IrO_x-C being much larger than those of IrCo and IrCo_{ae}, hence making it more accessible for ions to get transported and collect on its surface especially at higher current density. Also, the hydrophilicity of IrO_x, considering its higher metal-oxide concentration from XPS, could improve the wettability and transport of ions on its surface and lead to a higher capacitive current [182].

Another technique that can be used to estimate ECSA is by using electrochemical impedance spectroscopy (EIS). Here, an AC perturbation was applied at 10 mA and the corresponding Nyquist plot is presented in Figure 5.15. Also, in EIS the voltage was set at 1.5 V which is in the OER region and can probe the actual interface participating in the reaction. The chemical interface is influenced by the applied potential, as illustrated in Figure 5.14, where the CV curves evolve with the upper potential limit. An equivalent circuit model was used to fit the data, as discussed in detail in a previous work [182] and the effective capacitance was used to estimate ECSA. Compared to the single-point C_{dl} method, the ECSA obtained from the EIS method now scales better with the BET surface area, as shown in Figure 5.16.

The enhanced OER activity of the synthesized catalysts, IrCo and IrCo_{ae}, compared to the commercial catalysts is not only influenced by its physical extensive property, such as ECSA which can be interpreted as the abundance of the active sites but also in the intrinsic nature of the material that drives the OER reaction faster. This intrinsic property of the catalyst is often assessed in terms of the exchange current density (i_0) and Tafel slope. However, obtaining a reliable i_0 is inherently difficult and has been subject to a lot of criticisms in the literature [85]. Nevertheless, with the lower overpotential for OER and the Tafel slopes in the synthesized catalysts compared to IrO_x-C, it can be surmised that the intrinsic activities of the IrCo and IrCo_{ae} catalysts are much higher than IrO_x-C.

The conductivity of the catalysts can potentially enhance their activity by reducing the charge transfer resistance (R_{ct}) [78]. It has also been shown in the literature that Ir metal has much better OER performance than its oxide counterpart [180] and that an Ir metallic core can provide a better electronic pathway than that of a pure oxide catalyst 100. The presence of metallic states in IrCo and IrCo_{ae}, as revealed by the XPS data, shows that it could have resulted in improved

conductivity, thus lowering the R_{ct} . Interestingly, the EIS data also agree that the R_{ct} of IrCo and IrCo_ae are much lower compared to IrO_x-C (Table 5.7 and 5.8).

The presence of higher defect sites in the IrCo-based catalysts from the O 1s XPS data could also play a role in OER activity enhancement. Defect sites are often regarded as essential for the electrochemical reaction that present unique electrochemical properties and bind reaction intermediates to optimize activity and selectivity [189]. With regards to which valence state of Ir can be a key indicator of its high activity, some literature [184] suggest Ir⁴⁺, considering it is a precursor to the OER binuclear mechanism while others [108, 109, 185] report the high presence of Ir³⁺. In this case, the IrCo and IrCo_ae catalyst have higher Ir⁴⁺/ Ir³⁺ obtained from the XPS data compared to the IrO_x-C, which seems to agree with one study [184]. On the other hand, after performing acid etching and comparing analogous catalysts, IrCo and IrCo_ae, the increase in the surface area is accompanied by an enrichment of Ir³⁺ species, which is considered a more active species by other studies [108, 109, 185]. The presence of cobalt in the alloy might also have some benefits. A substitution of Co in the Ir oxide, suggested by the slightly smaller d-spacings from TEM for IrCo_ae, would cause a lattice strain. These lattice strains can lower the Ir-Ir distance, and in effect, the distance between the nearest neighboring OH-adsorbates, thus improving the OER activity [186].

Overall, the enhanced OER activity of the catalyst cannot be solely attributed to a single physicochemical property, especially for very different materials, but rather a combination or interactions of those properties. Decoupling the contributions of each parameter would seem very complex, if not impossible.

5.5 Stability Insights

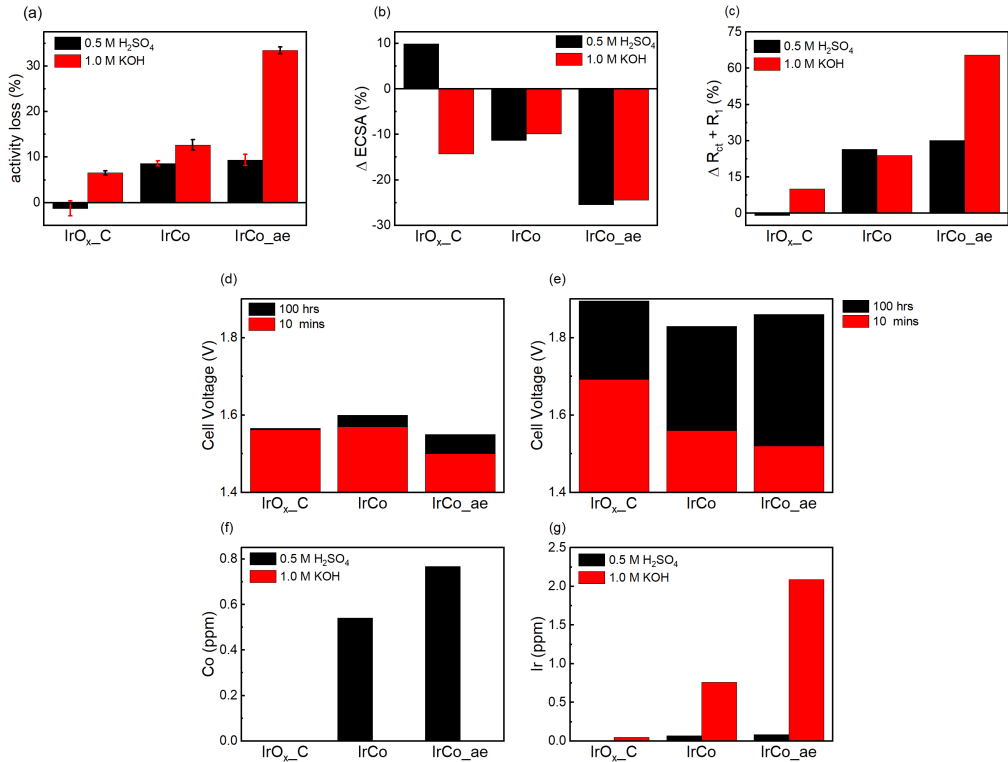


Figure 5.4: (a) Activity loss after degradation in half-cell for acidic and alkaline media determined from the area under the LSV curves before and after the stability tests. The change in (b) electrochemically active surface area (ECSA) and (c) total resistance, $R_{ct} + R_1$, both obtained from electrochemical impedance spectroscopy (EIS) before and after the stability tests. Full-cell stability tests in (d) 0.5 M H₂SO₄ and (e) 1.0 M KOH at a fixed current density of 50 mA/cm² and the corresponding metal concentration in the electrolytes after the test detected using inductively coupled plasma mass spectrometry (ICP-MS).

To evaluate the stability of the catalysts, both half-cell and full cell testing were performed in acidic and alkaline media. The half-cell test was conducted by subjecting the catalysts to 2,000 potential cycles from 0.4 to 1.4 V. Comparing the activity before and after the stability test, the loss in activity was measured by the area under the LSV curve, as shown in Fig. 3a. The activity loss is more severe in alkaline media than in acidic media for all catalysts. This can be attributed to the dissolution behavior of Ir in the alkaline media from the Pourbaix diagram [187].

IrCo_{ae}, which shows the best OER performance in the alkaline media, happens to have the worst stability in the same condition agreeing with previous literature 119 on the inverse correlation between activity and stability. IrCo_{ae} also happens to have the highest loss in ECSA, estimated using the EIS method, at 25.46% and 24.41% in acidic and alkaline media, respectively. Although Ir dissolution is presumed to be dominant in the alkaline media, the ECSA loss in acidic media might be driven by other mechanisms, such as particle growth, which is not probed in this work.

The EIS data at the end of the durability test can also provide information regarding the resistances. Still, IrCo_{ae} had the largest increase in the combined resistance consisting of charge transfer resistance (R_{ct}) and due to diffusion/ad-sorption of reaction intermediates (R_1) [182]. The increase in total resistance can potentially explain why the activity loss in alkaline is much higher than in acid despite having comparable ECSA losses. Nevertheless, the OER activity of the synthesized catalysts, IrCo and IrCo_{ae}, still perform much better than the commercial IrO_x-C in Figure 5.21. No significant change in Tafel slopes (see Figure 5.21b,d) after degradation for all catalysts, suggesting the rate determining step for OER reaction mechanism remains the same.

A full-cell liquid electrolyzer was also constructed to study degradation at a longer duration. The catalyst ink was coated on a carbon paper (SGL 10 BC) with a targeted loading of 3 mg/cm² on the anode side while a Pt plate (4 cm²) was used as cathode. The durability test was performed by fixing the current density at 50 mA/cm² for 100 hours and the change in potential was tracked. The performance of IrCo_{ae} is still much better compared to other samples in both media, with initial cell potential of 1.50 V and 1.52 V in acidic and alkaline media, respectively. Interestingly, although different degradation protocol was performed in half-cell and full-cell test, the same trend was obtained where alkaline media yields the highest increase in overpotential for all samples, comparing Figure 5.4d and e.

Metal dissolution was investigated using ICP-MS by collecting the electrolytes on the anode side as well as post-mortem characterization of the anodes using XRD and XPS. The detected metal contents in acidic electrolytes show a much higher Co content than Ir, with IrCo_{ae} showing 0.767 ppm and 0.541 ppm for IrCo. On the other hand, in alkaline electrolytes, the situation is reversed where the majority of metals detected is coming from Ir, with IrCo_{ae} giving the highest dissolved Ir at 2.09 ppm while Co is below the detection limit for both IrCo_{ae} and IrCo. The higher Ir dissolution in IrCo_{ae} compared to IrO_x-C might be due to the participation of the lattice oxygen in the OER, which has been recently discussed in the literature to trigger Ir dissolution [185]. Metal dissolution was also studied in the rotating-ring disk electrode by setting the ring potential at 0.9 V (Figure 5.18). It

can be noted that the ring current starts to increase in the alkaline media even before the OER onset. This is possible, suggesting that Ir dissolution can proceed before OER [180].

Evaluating the evolution of the electrodes after the durability test from XRD reveals that in alkaline media, the IrO₂ (101) peak in IrCo is reduced compared to the data from the powder catalysts but is not observed in acidic media (see Figure 5.23a). This agrees with the ICP-MS data that the IrO₂ component is highly unstable in alkaline as compared to acidic media. On the other hand, Co₃O₄ (311) peak is reduced and less sharp in acid compared to the alkaline media. For IrCo_{ae}, since there is only one recognizable peak from IrO₂ (101), analysis of the full-width half maximum (FWHM) was done to compare the degradation of the catalyst in both media (see Figure 5.23c-e). An increasing trend was observed from the fresh sample at 0.0778 rad to the acid degraded at 0.0836 rad and 0.0887 rad in the alkaline degraded anode. It proves that the structure of the catalysts becomes less crystalline or the particle size increases due to agglomeration or coarsening [188].

The change in the valance state of Ir was also investigated using XPS, presented in Figure 5.24 and the quantification is listed on Table 5.9. For the commercial IrO_x-C, there is no significant difference in the acidic and alkaline media where a comparable mix between Ir³⁺ and Ir⁴⁺ states can still be observed. However, for the synthesized catalysts, degradation in the acid lead to an increase in Ir³⁺ oxidation state and a reduced Ir⁴⁺ state compared to the original powder catalysts for both IrCo and IrCo_{ae}. In alkaline media, an even lower Ir⁴⁺ distribution is observed with an increase in metallic Ir⁰. This can be caused by the exposure of metallic surface once the oxide layer, predominantly from Ir⁴⁺ state, has been dissolved in the electrolyte or resulting from redeposition of dissolved Ir ions. The increase in Ir³⁺ state was also observed in other works [117, 185], which can possibly be formed from the cyclic transition between Ir⁵⁺/Ir³⁺ [156]. However, there is still no clear understanding of the underlying degradation mechanism. As to how the catalyst morphology and electronic structure can induce a different degradation path, and would need further study to validate the results from this work.

5.6 Conclusions

The ambitious goal of US DOE to make green hydrogen more affordable at \$1 per kg in one decade would necessitate a cheaper process from water electrolyzers. There is a cost-saving benefit from catalysts with a much lower Ir content but better OER performance. That catalyst could promote both the efficient use of the scarce Ir resource and a sustainable and affordable energy system to meet the net-zero carbon emission goal by 2050. Here, a synthesized IrCo alloy was able to achieve a more enhanced OER catalytic activity over the commercially available

IrO_x-C and at a reduced Ir content. The overpotential at 10 mA/cm² for IrCo_{ae} are 283.3 mV and 252.7 mV in acid and alkaline media, respectively. These are much lower compared to IrO_x-C which are at 347.0 mV and 293.5 mV in acid and alkaline media, respectively. Implementing the surfactant-assisted Adam’s fusion method can produce catalysts with a higher BET surface area, which translates to more available active sites for OER, and a higher Ir metallic content that can improve the conductivity of the material. However, the role of cobalt is still not clearly understood as that would entail further experiments and computational work outside the scope of this study.

A more pressing concern is the stability of the catalyst for long-term operation. The degradation study of IrCo_{ae} in half cell condition reveals higher activity loss compared to IrO_x-C, relative to their initial OER activities. Nevertheless, the OER activity at the end of the stability test of IrCo_{ae} is still superior to IrO_x-C, making it a good candidate for OER catalyst development. Further understanding of the catalyst degradation mechanism can provide knowledge on how to mitigate performance losses. A better understanding of the structure-function of the catalyst can provide insights on tailoring the design of the materials to balance both activity and stability. With the promising results from this work, a follow-up study on the effects of other synthesis parameters such as Ir and Co content, surfactant effect, an acid etching process, and the interaction of these variables is being planned. This will facilitate the development of a cheaper catalyst for water electrolyzers with a readily scalable synthesis method.

5.7 Appendix

Table 5.2: Evaluation of iridium and cobalt atomic ratio from X-ray photoelectron spectroscopy (XPS) and inductively coupled plasma mass spectrometry (ICP-MS).

Catalyst	XPS			ICP-MS	
	Ir (at%)	Co (at%)	O (at%)	Ir:Co atomic ratio	Ir:Co atomic ratio
IrO _x -C	24.97	-	75.03	-	-
IrCo	18.26	11.46	70.29	1.59	1.06
IrCo _{ae}	23.61	4.2	72.19	5.62	5.94

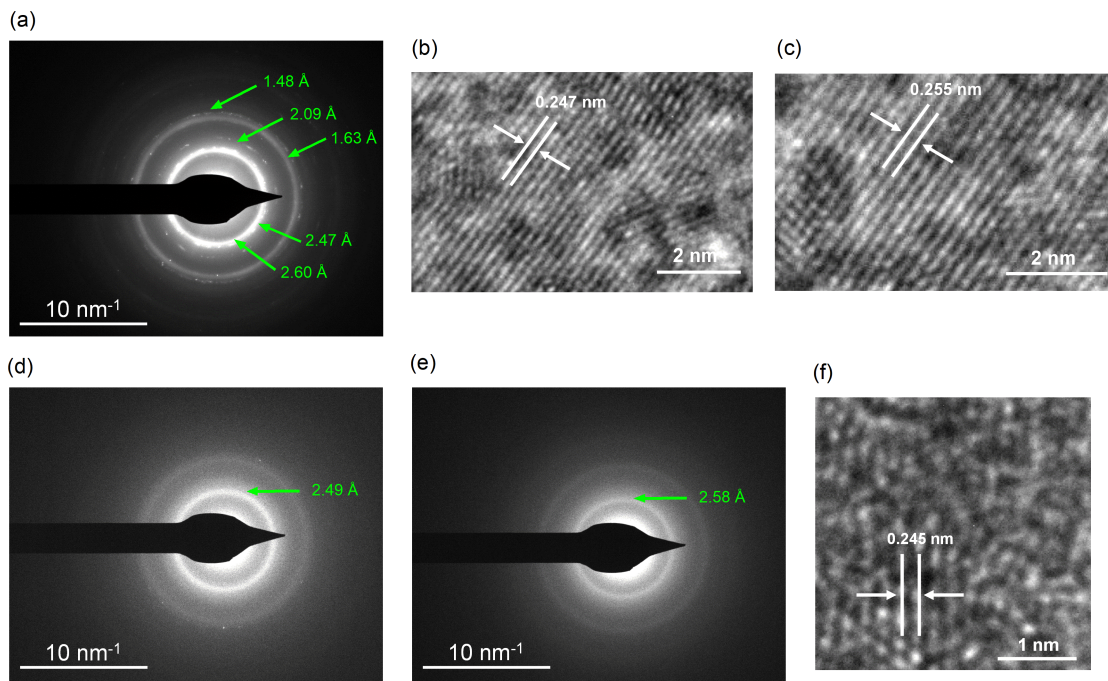


Figure 5.5: Electron diffraction for (a) IrCo showing the patterns for Co_3O_4 and IrO_2 rutile (101) and (d) possibly a Co-substituted IrO_2 matrix and (e) IrO_2 (101) in IrCo_ae. Lattice fringes for (b,c) IrCo showing Co_3O_4 (311) and IrO_2 (10) rutile while a reduced d-spacing for (f) IrCo_ae also supports Co-substituted IrO_2 matrix.

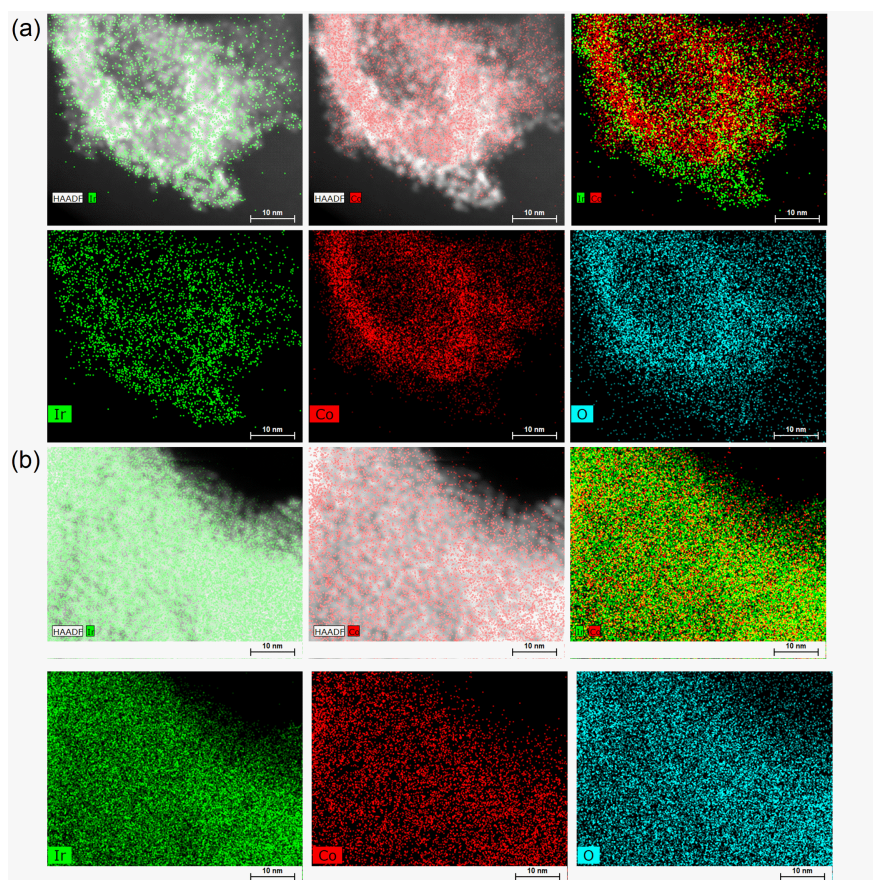


Figure 5.6: Chemical mapping of iridium and cobalt using energy-dispersive X-ray spectroscopy (EDS) for (a) IrCo and (b) IrCo_{ae}. Overlap images for Ir (green) and Co (red) are shown for both catalysts where a strong spatial correlation between the nanoparticles, represented as bright spots, and Ir distribution can be established.

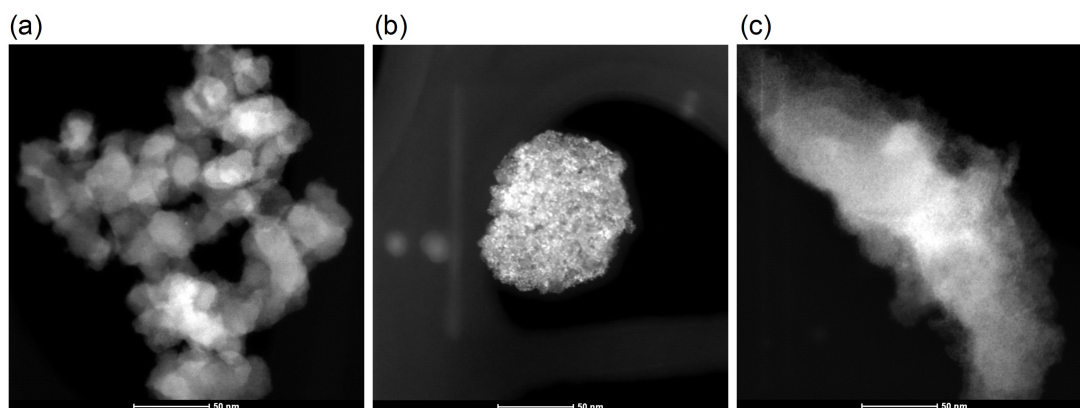


Figure 5.7: Scanning transmission electron microscope (STEM) images of commercial (a) IrO_x-C, (b) IrCo and (c) IrCo_{ae}

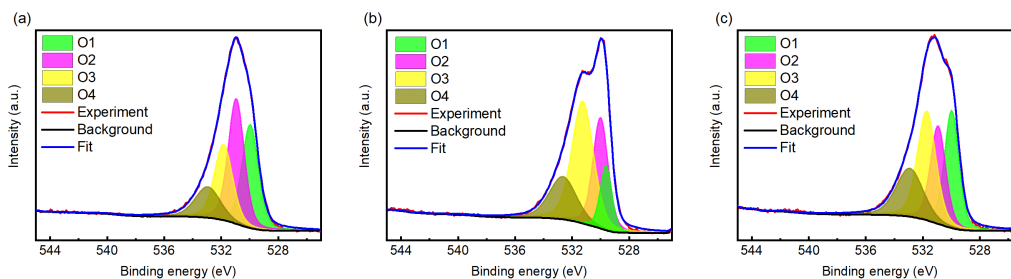


Figure 5.8: X-ray photoelectron spectra for O *1s* in (a) commercial IrO_x-C, (b) IrCo and (c) IrCo_{ae} deconvoluted into four oxygen chemical states.

Table 5.3: Tabulated results for the relative amounts of oxygen chemical states derived from O *1s* deconvolution in XPS for IrO_x-C, IrCo and IrCo_{ae}.

O <i>1s</i> peak	Chemical State	Binding Energy (eV)	Peak Relative Distribution (%)		
			IrO _x -C	IrCo	IrCo _{ae}
O _I	Metal-oxygen bonds (oxide)	529.4	28.88	12.12	25.93
O _{II}	Hydroxylated metals (M-OH ₂ or M-OH)	530	34.11	27.03	23.06
O _{III}	Defect sites with low oxygen coordination	531	23.75	42.28	31.15
O _{IV}	Physisorbed and/or chemisorbed water at or near the surface	533	13.27	18.57	19.87

Table 5.4: Distribution of cobalt compounds identified in XPS from Co $2p$ for IrCo and IrCo_{ae}.

Compound	IrCo		IrCo _{ae}	
	Associated Peaks (eV)	Peak Distribution (%)	Associated Peaks (eV)	Peak Distribution (%)
Co ⁰	778.4, 780.8, 783.38	21.59	778.1, 781.1, 783.1	15.85
Co(OH) ₂	780.19, 781.9, 786.03, 790.17	11.21	-	-
CoO	-	-	780.0, 782.1, 785.5, 786.5	70.12
Co ₃ O ₄	779.3, 780.7, 781.9, 785, 789.2	67.2	779.6, 780.9, 782.2, 785.2, 789.5	14.03

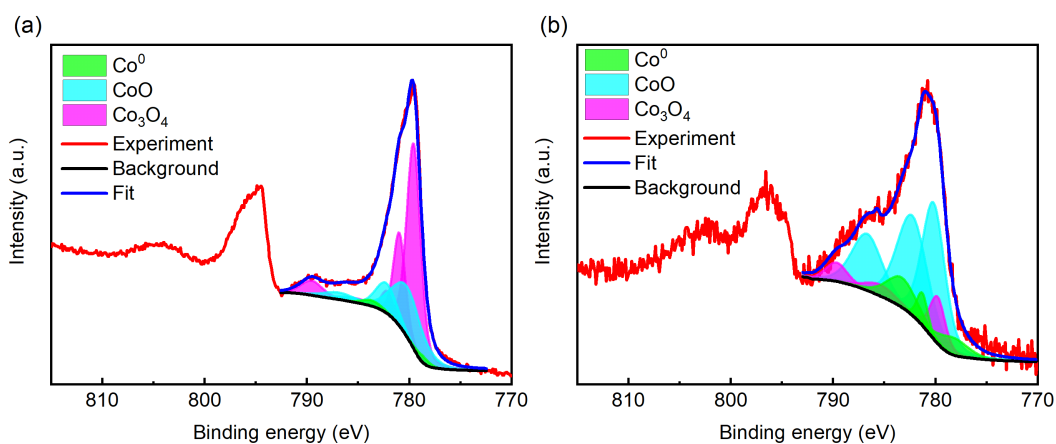


Figure 5.9: Deconvolution of Co $2p$ XPS result for (a) IrCo and (b) IrCo_{ae} showing the different Co compounds present in each catalyst.

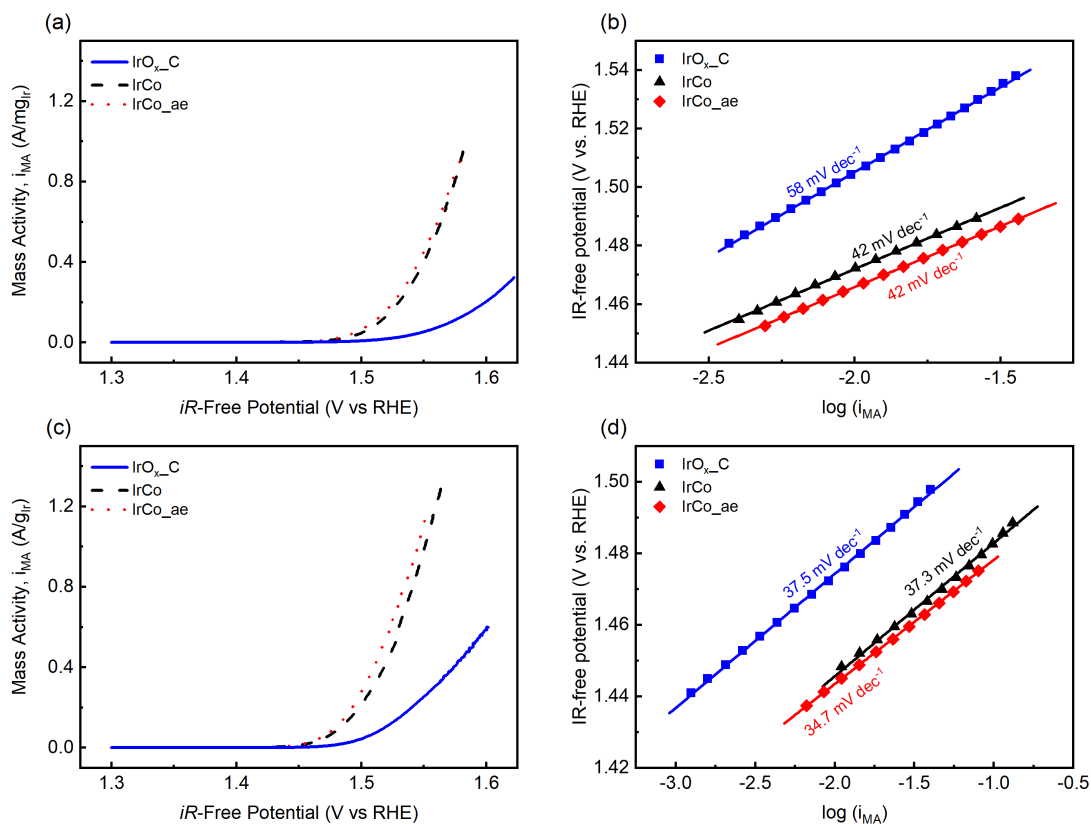


Figure 5.10: Mass activity (i_{MA}) and Tafel plots in (a,b) 0.5 M H₂SO₄ and (c,d) 1.0 M KOH.

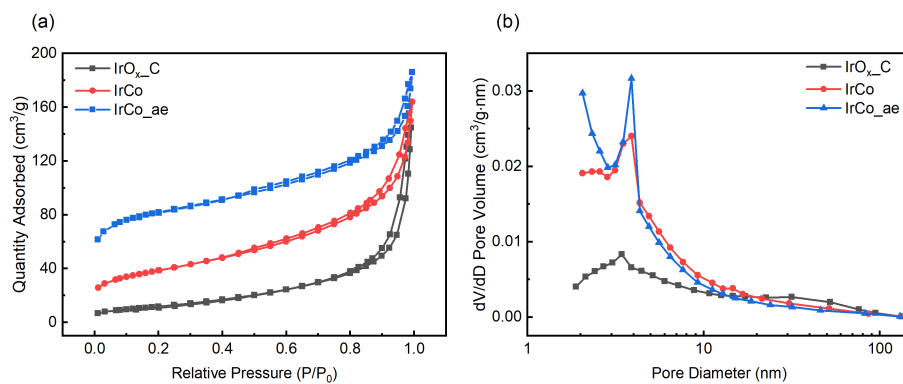


Figure 5.11: Nitrogen gas adsorption experiments for Brunauer–Emmett–Teller (BET) surface area measurements showing the (a) gas adsorption isotherm and (b) pore diameter distribution calculated from Barrett–Joyner–Halenda (BJH) method for the desorption branch.

Table 5.5: Surface area and pore size characterization obtained from the gas adsorption measurements for the different catalysts.

Catalyst	BET surface area	BET desorption	Single point	BJH desorption
	($\text{cm}^2 \text{g}^{-1}$)	total pore size diameter (nm)	total pore volume ($\text{cm}^3 \text{g}^{-1}$)	pore volume ($\text{cm}^3 \text{g}^{-1}$)
$\text{IrO}_x\text{-C}$	44.97	19.96	0.2244	0.2246
IrCo	135.57	7.50	0.2541	0.2491
IrCo_{ae}	273.17	4.20	0.2884	0.2187

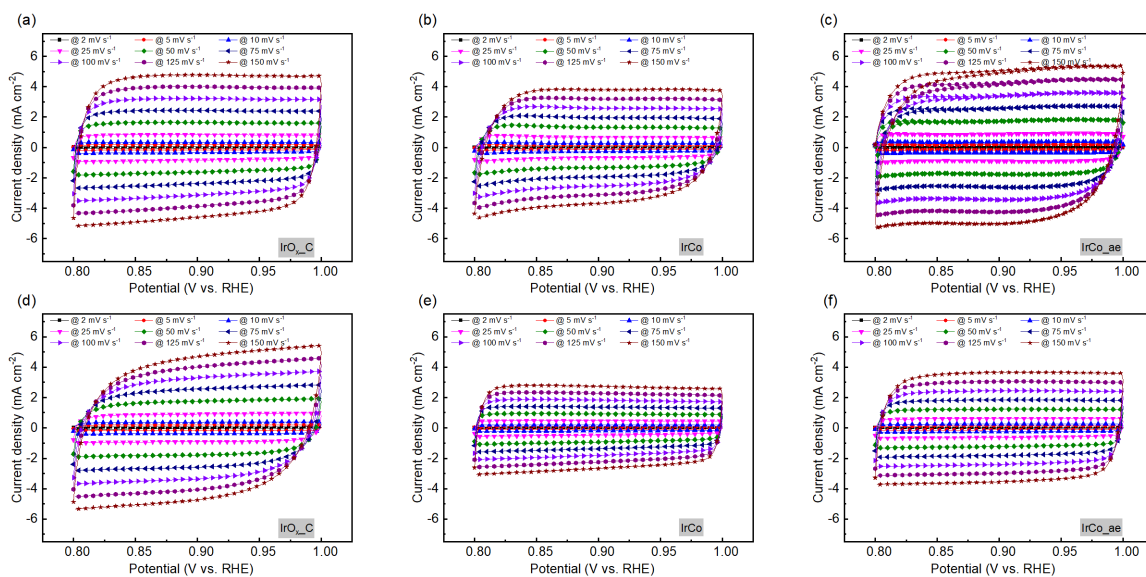


Figure 5.12: Cyclic voltammetry (CV) curves at different scan rates in (a-c) 0.5 M H_2SO_4 and (d-f) 1.0 M KOH for the double-layer capacitance estimation. The corresponding catalyst are indicated in the plots.

Table 5.6: Double-layer capacitance obtained from the CV method and the estimated electrochemically active surface area (ECSA) of the different catalysts.

Catalyst	0.5 M H ₂ SO ₄		1.0 M KOH	
	C _{dl} (mF cm ⁻²)	ECSA (m ² g ⁻¹)	C _{dl} (mF cm ⁻²)	ECSA (m ² g ⁻¹)
IrO _x -C	31.07 ± 0.17	238.98 ± 1.32	31.99 ± 0.28	246.10 ± 2.10
IrCo	24.66 ± 0.38	189.69 ± 2.92	18.14 ± 0.04	139.5 ± 0.31
IrCo_ae	33.23 ± 0.49	255.62 ± 3.77	24.4 ± 0.30	187.69 ± 2.27

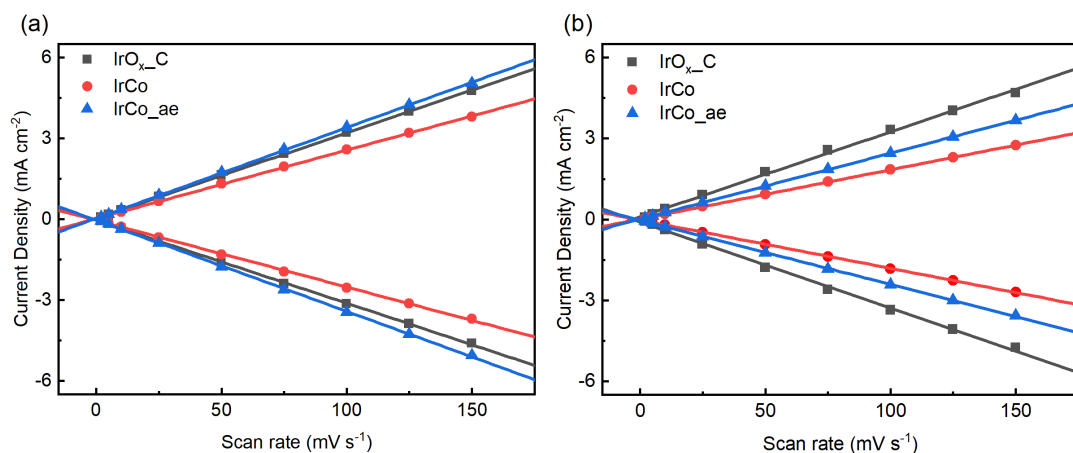


Figure 5.13: Current density measured at 0.9 V at different scan rates in (a) 0.5 H₂SO₄ and (b) 1.0 M KOH to obtain the double-layer capacitance from the slope of the line.

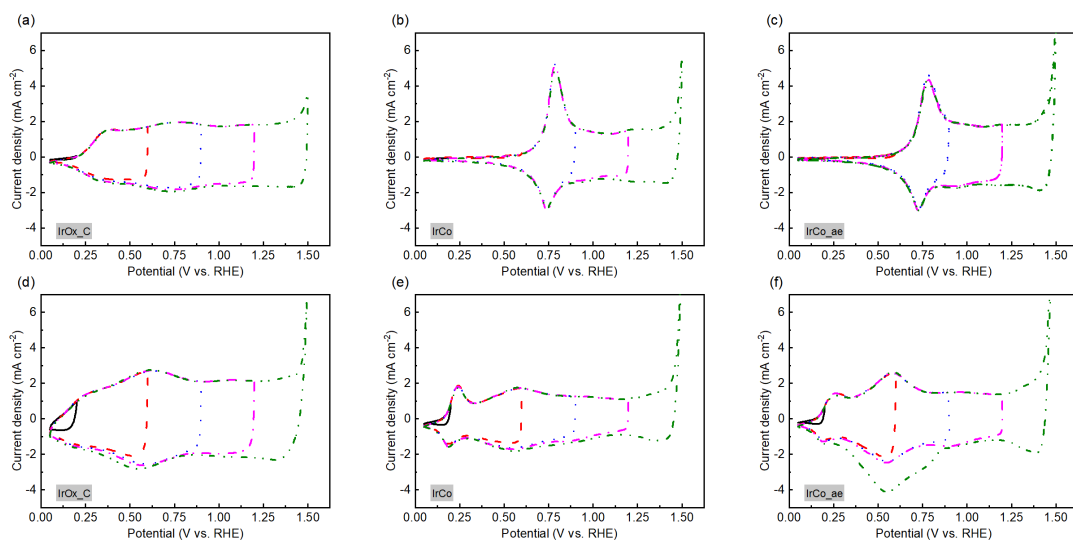


Figure 5.14: Cyclic voltammetry (CV) curves for the different catalysts, as indicated in the plots, in (a-c) 0.5 M H_2SO_4 and (d-f) 1.0 M KOH . The upper potential limits are varied to observe different pseudocapacitive redox reactions happening in each catalyst.

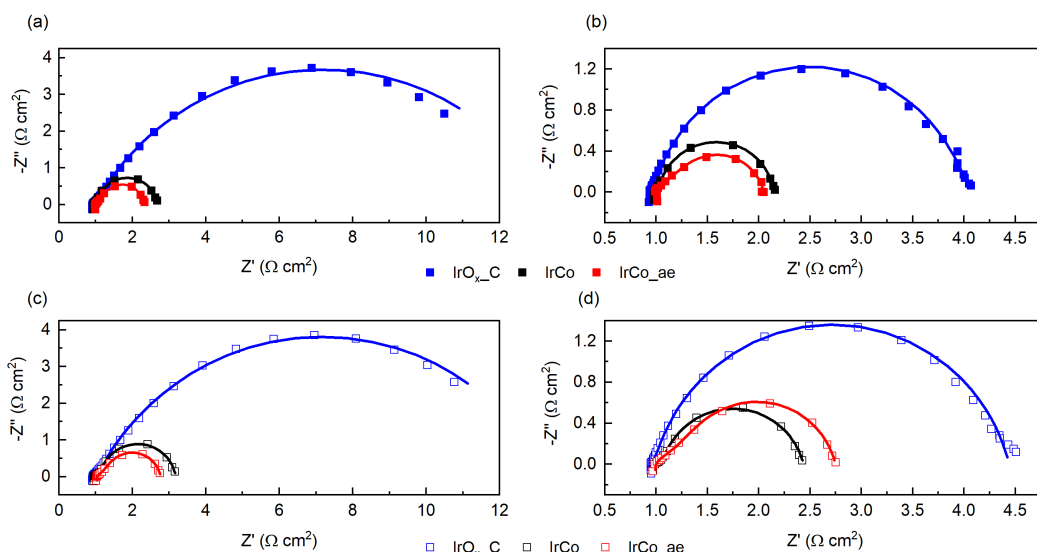


Figure 5.15: Electrochemical impedance spectra obtained in (a-b) 0.5 M H_2SO_4 and (c-d) 1.0 M KOH (a,c) before and (b,d) after the stability test. Raw data are shown as symbols while the fitted result shown with the solid curves.

Table 5.7: Values of the circuit elements for the fitted electrochemical impedance spectroscopy (EIS) data in 0.5 H₂SO₄ and the calculated ECSA from the EIS-based capacitance.

Catalyst		L	R_{Ω}	$R_{ct} + R_1$	C_1	n_1	C_2	n_2	C	ECSA @
		E ⁻⁷ H cm ²	Ω cm ²	Ω cm ²	E ⁻³ F s ⁿ⁻¹ cm ²		E ⁻³ F s ⁿ⁻¹ cm ²		mF	$C_s = 1.3$ F m ⁻² m ² /g
IrO _x -C	BOL	2.50	0.91	12.50	1.54	0.68	1.61	0.73	1.54	60.42
	EOL	2.34	0.93	12.38	1.69	0.71	4.99	0.68	1.69	66.40
IrCo	BOL	2.63	0.94	1.74	5.34	0.92	10.01	0.65	5.34	209.49
	EOL	2.36	0.97	2.20	4.73	0.91	5.96	0.65	4.73	185.68
IrCo _{ae}	BOL	2.73	1.00	1.33	7.98	0.95	42.06	0.56	7.98	313.12
	EOL	2.15	1.03	1.73	5.95	0.91	19.40	0.57	5.95	233.39

Table 5.8: Values of the circuit elements for the fitted electrochemical impedance spectroscopy (EIS) data in 1.0 M KOH and the calculated ECSA from the EIS-based capacitance.

Catalyst		L	R_{Ω}	$R_{ct} + R_1$	C_1	n_1	C_2	n_2	C	ECSA @
		E ⁻⁷ H cm ²	Ω cm ²	Ω cm ²	E ⁻³ F s ⁿ⁻¹ cm ²		E ⁻³ F s ⁿ⁻¹ cm ²		mF	$C_s = 1.3$ F m ⁻² m ² /g
IrO _x -C	BOL	1.95	0.93	3.16	0.32	0.88	22.52	0.43	0.81	31.76
	EOL	1.65	0.95	3.48	0.33	0.85	0.99	0.74	0.69	27.22
IrCo	BOL	1.61	0.98	1.17	0.97	0.91	8.20	0.56	3.26	127.77
	EOL	1.17	0.98	1.45	1.17	0.85	0.65	0.66	2.93	115.14
IrCo _{ae}	BOL	1.87	0.98	1.07	1.32	0.88	3.06	0.58	3.96	155.37
	EOL	1.34	0.98	1.77	1.04	0.88	3.28	0.51	2.99	117.44

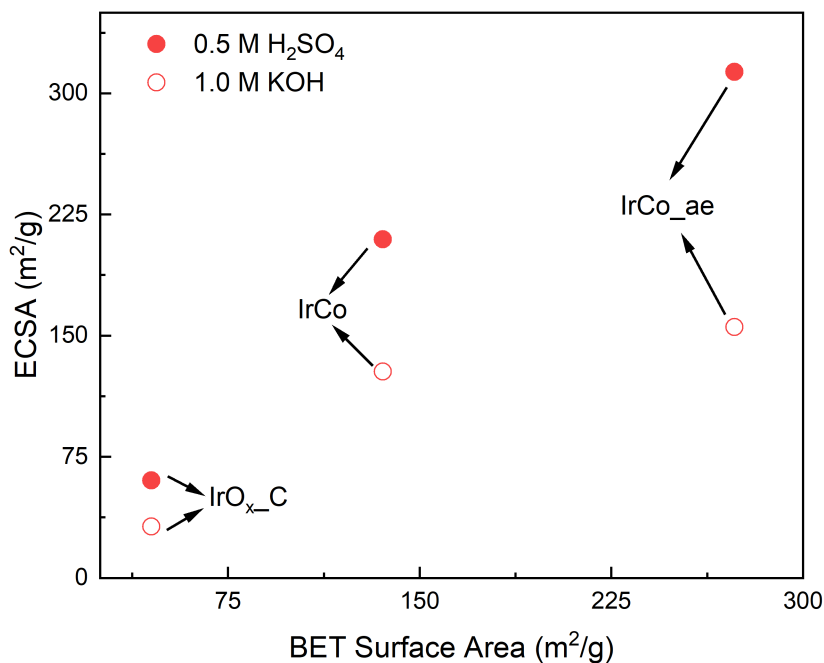


Figure 5.16: Comparison of the ECSA derived from EIS and the measured BET surface area for the different catalysts in both acid and alkaline media.

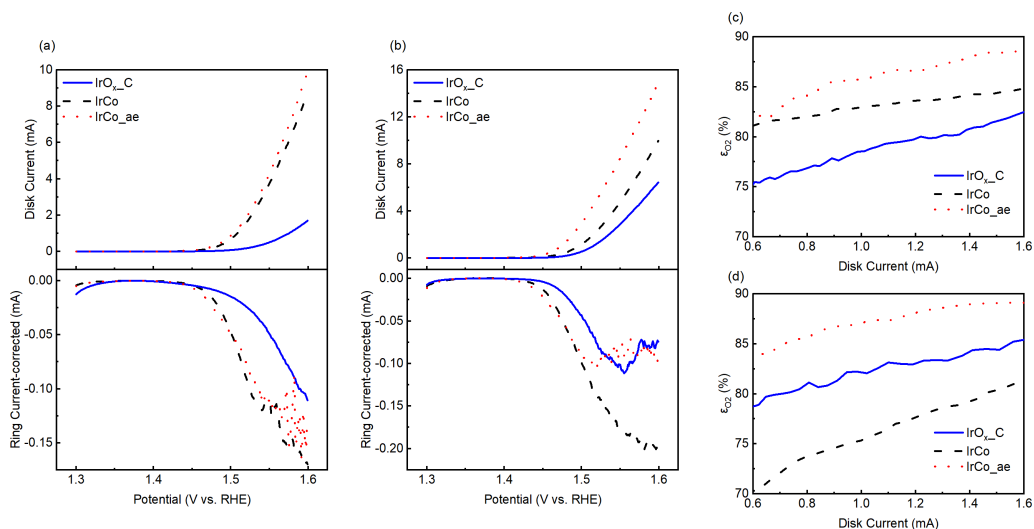


Figure 5.17: Rotating ring-disk electrode (RRDE) measurement at 0.4 V ring potential to study oxygen transport efficiency from the catalyst layer in (a,c) 0.5 H₂SO₄ and (b,d) 1.0 M KOH.

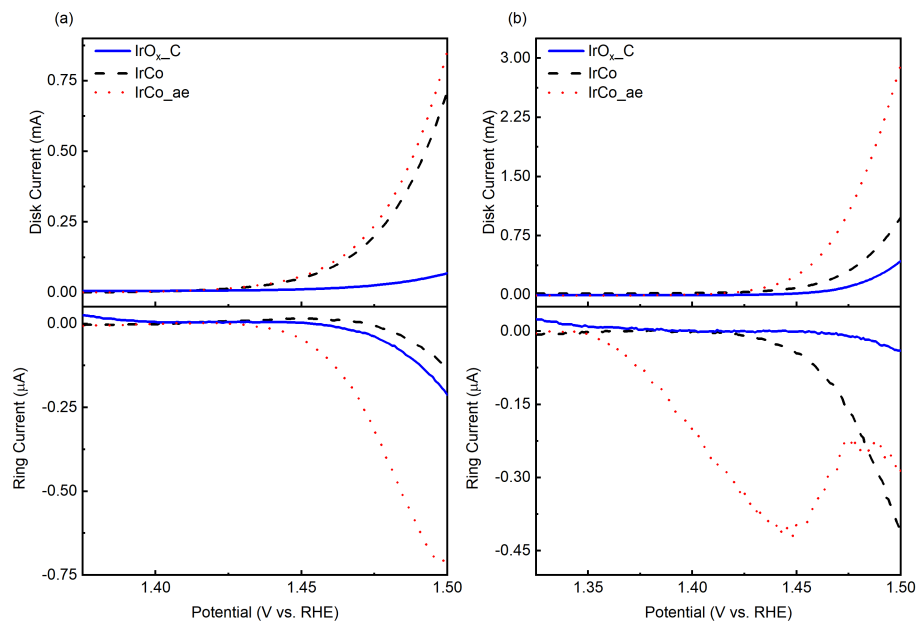


Figure 5.18: Investigation of Ir dissolution in the catalysts using RRDE measurement by setting ring potential at 0.9 V in (a) 0.5 H₂SO₄ and (b) 1.0 M KOH.

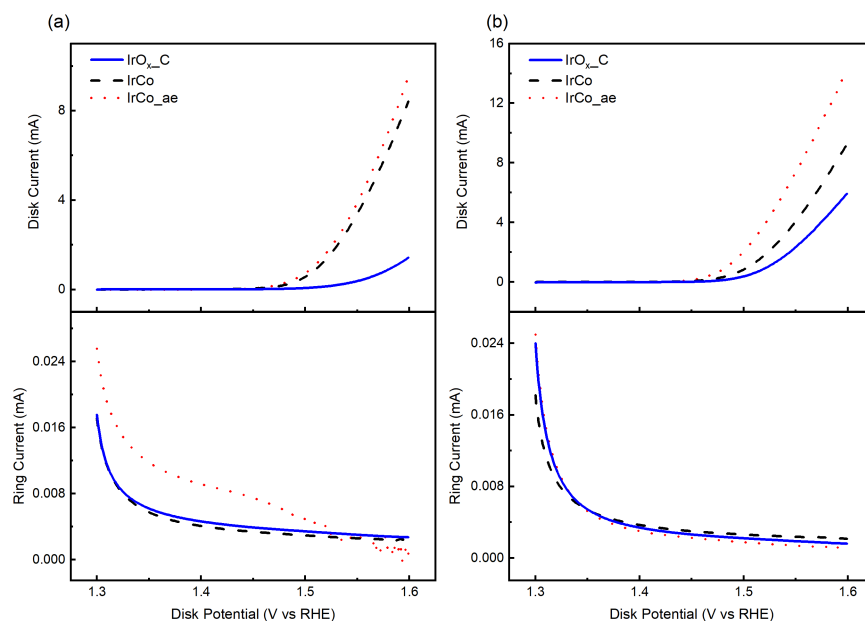


Figure 5.19: Detection of possible peroxide generated from the 2-electron OER pathway using RRDE at 1.4 V ring potential in (a) 0.5 H₂SO₄ and (b) 1.0 M KOH.

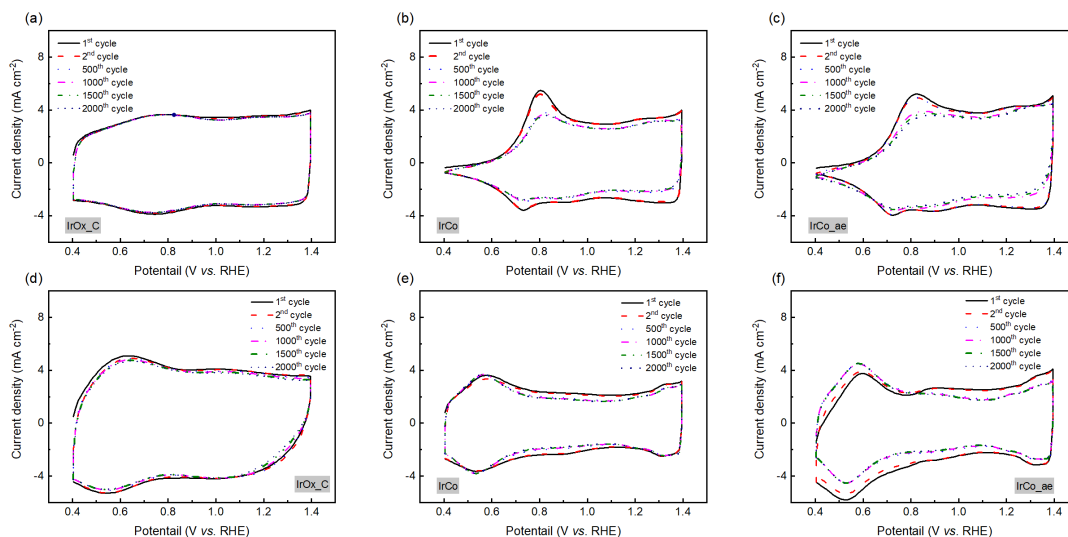


Figure 5.20: Half-cell stability tests by performing 2,000 potential cycles from 0.4 to 1.4 V in (a-c) 0.5 H₂SO₄ and (d-f) 1.0 M KOH.

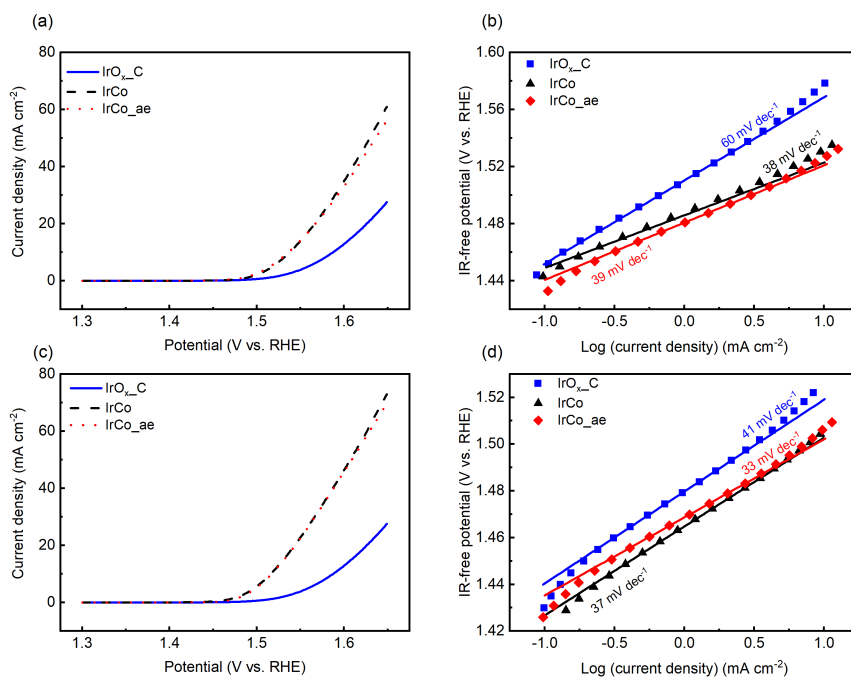


Figure 5.21: Linear sweep voltammetry (LSV) curves at the end of the stability tests and the corresponding Tafel plots in (a,b) 0.5 H₂SO₄ and (c,d) 1.0 M KOH.

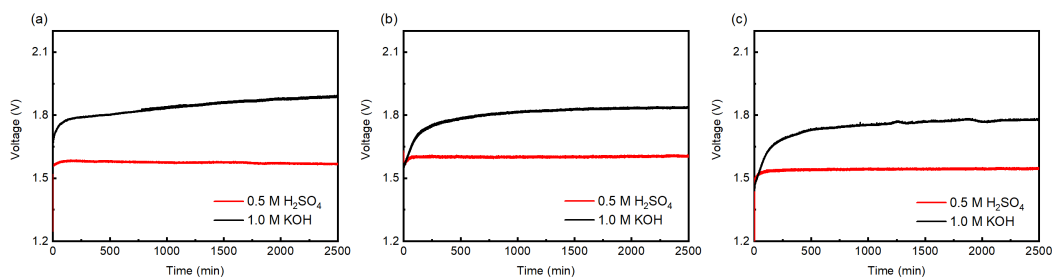


Figure 5.22: Full-cell stability tests performed by holding the current density at 50 mA cm⁻² for (a) IrO_x-C, (b) IrCo, and (c) IrCo_{ae} in both acidic and alkaline media.

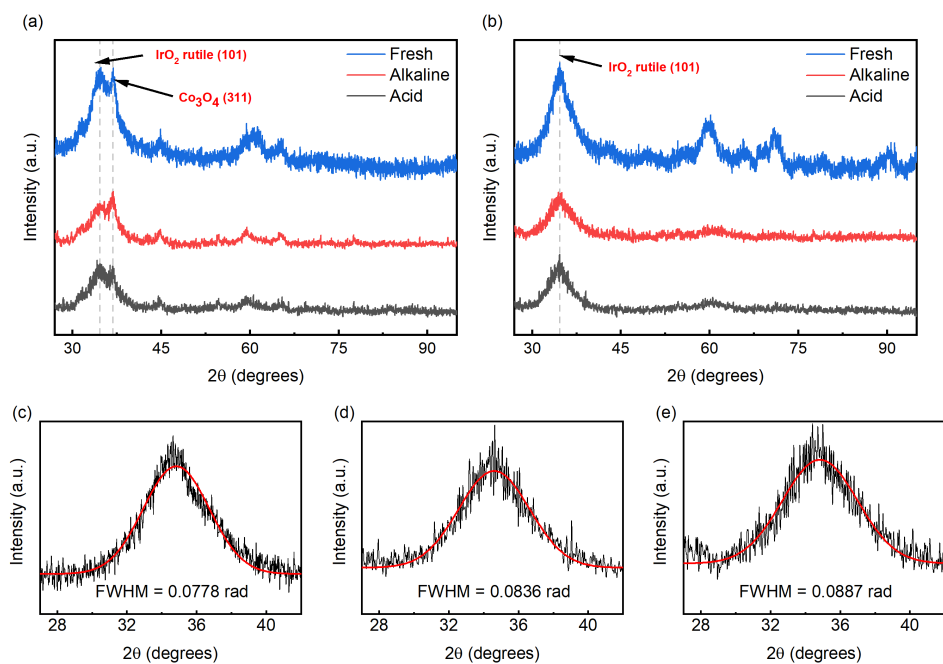


Figure 5.23: X-ray diffractogram of the degraded (a) IrCo and (b) IrCo_ae electrodes after the full-cell stability tests in both acid and alkaline media. The full width at half maximum (FWHM) of the IrO₂ (101) peak in (b) was estimated by fitting the Gaussian distribution for the (c) fresh IrCo_ae, (d) acid-degraded IrCo_ae and (e) alkaline-degraded IrCo_ae.

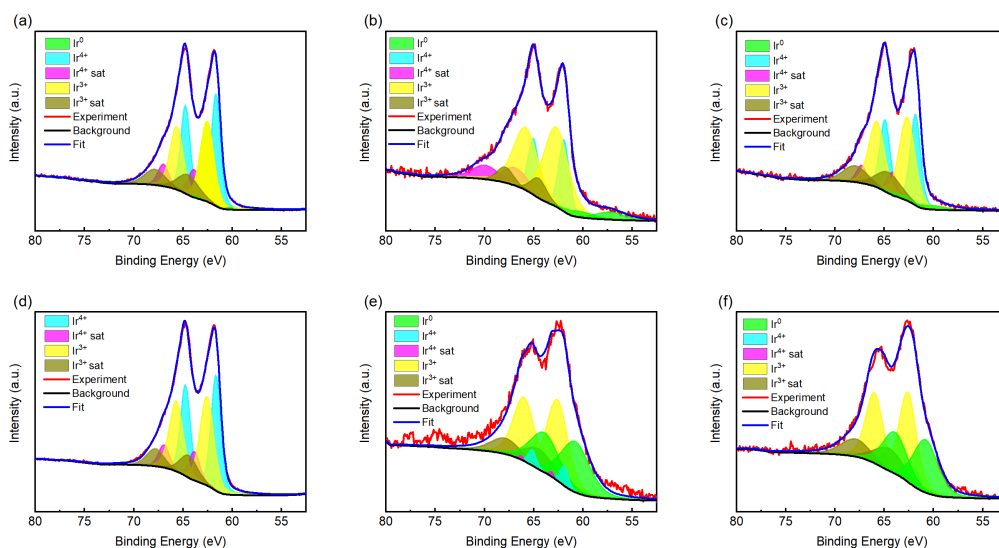


Figure 5.24: Ir $4f$ X-ray photoelectron spectra of the degraded electrodes in (a-c) $0.5 \text{ H}_2\text{SO}_4$ and (d-f) 1.0 M KOH . The data is deconvoluted for the different Ir chemical states in (a,d) $\text{IrO}_x\text{-C}$, (b,e) IrCo and (c,f) IrCo_{ae} .

Table 5.9: Relative amounts of the different Ir chemical states estimated from XPS in the degraded electrodes after the full cell stability test.

Ir Oxidation State	Ir $4f_{7/2}$ Binding Energy (eV)	Peak Relative Distribution (%)					
		0.5 M H_2SO_4			1.0 M KOH		
		$\text{IrO}_x\text{-C}$	IrCo	IrCo_{ae}	$\text{IrO}_x\text{-C}$	IrCo	IrCo_{ae}
Ir^0	60.8	0.91	7.40	5.08	-	43.35	42.43
Ir^{3+}	62.2	49.63	66.36	55.37	51.53	51.75	51.65
Ir^{4+}	61.9	49.45	26.24	39.55	48.47	4.90	5.92

Chapter 6

INVESTIGATING MATERIAL SYNTHESIS CONDITIONS OF IRIDIUM-COBALT ALLOY

6.1 Abstract

The synthesis conditions for the modified Adam's fusion method were investigated here to understand the effects of iridium and cobalt (Ir/Co) molar ratio, the use of surfactant and its interaction with the acid etching process. The dominant crystal plane in the material changes from IrO₂ (101) for Ir-rich samples to Co₃O₄ (311) with Co-rich samples. Surface segregation exists for all samples where Ir surface enrichment occurs. Without the surfactant (N-Ir₆Co₄), the segregation of Ir and Co is much stronger forming a Co core and an Ir shell. After acid etching, Co was almost leached out completely with the surfactant-assisted synthesis (Ir₆Co₄). In N-Ir₆Co₄, the thick Ir on the surface forms a protective layer, preserving the Co core. In any case, the acid etching process leads to enhanced surface area but is more pronounced in the Ir₆Co₄. An optimized mass activity based on Ir content and overpotential at 10 mA/cm² was attained with Ir₆Co₄ in both acidic and alkaline media. The results also show that surfactant improves the interaction of Ir and Co, leading to a much better OER performance. In terms of stability, the dissolution of Ir in the alkaline media is a critical concern for the catalysts developed here. The possible role of Ir³⁺ surface concentration to achieve high OER activity, especially in the acidic media, is highlighted in the study. The dependence of Ir and Co valency as a function of Ir/Co ratio is also probed.

6.2 Modification of the Adam's Fusion Method

The same surfactant-assisted Adam's fusion method technique implemented in the previous chapter (Chapter 5) was used here but was expanded to alter different synthesis parameters. A surfactant Pluronic F-127, a triblock copolymer of poly(ethylene oxide)(PEO)-poly(propylene oxide)(PPO)-poly(ethylene oxide) (PEO) with the chemical formula shown in Figure 6.1, was used to synthesize the Ir-Co alloys. This particular surfactant was added based on previous works showing how Pluronic F-127 can enhance the synthesis of gold nanoparticles [189], mesoporous silica material [190], and silver metal nanoparticles [191]. It is hypothesized that by adding a surfactant in the Adam's fusion method, these surfactant

molecules can self-organize into aggregated micelles after its microphase separation in the precursor solution. The self-organized micelles can then help control the formation of the Ir nitrate intermediate by acting as a soft template. This templating method then translates into a better formation of oxide particles during calcination, minimizing the possibility of sintering.

Different Ir:Co ratios were designed as follows: 8:2, 6:4, 4:6 and 2:8. These samples are nominally labeled as Ir_8Co_2 , Ir_6Co_4 , Ir_4Co_6 and Ir_2Co_8 . At the same time, a pure IrO_2 catalyst was also prepared to see the benefit of adding Co in the material. Another set of catalyst without the surfactant, N- Ir_6Co_4 , was prepared to see how the surfactant can affect the physicochemical property of the catalyst and its activity and stability towards OER. Comparing both Ir_6Co_4 (with surfactant) and N- Ir_6Co_4 , both were subjected to 0.5 M nitric acid (HNO_3) solution etching process, creating $\text{Ir}_6\text{Co}_4\text{-ae}$ and N- $\text{Ir}_6\text{Co}_4\text{-ae}$. The change in both physicochemical and electrochemical properties were assessed and correlated.

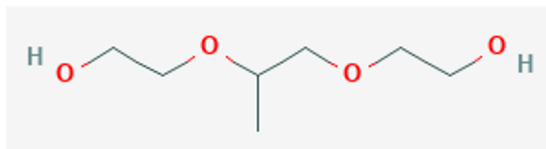


Figure 6.1: Chemical structure of Pluronic F-127, a surfactant used in the synthesis of the Ir-Co catalysts [192]

6.3 Characterization with Energy Electron Loss Spectroscopy (EELS)

In the work presented here, EELS spectra were collected in dual EELS mode using TEAM 1.0 microscope at the National Center for Electron Microscopy (NCEM) in Lawrence Berkeley National Laboratory equipped with Gatan Imaging Filter (GIF).

Three scans were performed to: 1.) collect Ir and Co chemical maps (500 eV low loss, 2,000 eV high loss); 2.) evaluate Ir valency (0 eV low loss, 30 eV high loss); and 3. evaluate Co and O valency (0 eV low loss, 530 eV high loss). To avoid sample damage, 80 kV primary energy was set. All measurements were collected with a 5 mm spectrometer aperture. The channel dispersions and screen currents were set at 90 meV/Ch and ~ 0.70 nA for Ir, Co and O valence evaluation while 0.25 eV/Ch and ~ 0.150 nA was set for Ir and Co chemical mapping.

For all other characterization techniques used, similar operating conditions were applied from Chapter 5.

6.4 Effect of Iridium-Cobalt (Ir-Co) Ratio

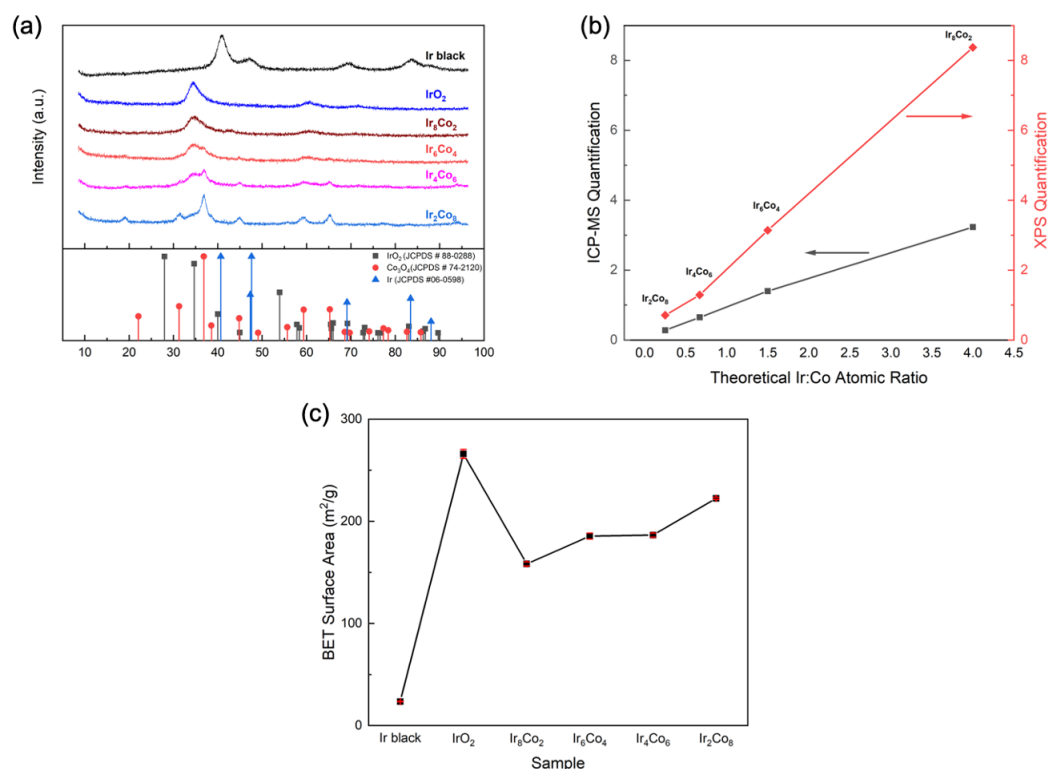


Figure 6.2: (a) X-ray diffractogram data for the Ir-Co samples. (b) Quantification of the Ir/Co molar ratio on the bulk using ICP-MS and on the surface using XPS. (c) Surface area measurement implementing the BET model for N₂ gas adsorption experiment.

For the investigation of the effect of iridium-cobalt atomic ratio in the catalyst, the nominal values from the synthesis design were first validated using material characterization techniques such as: 1.) X-ray diffraction for the crystallographic information; 2.) ICP-MS and XPS for bulk and surface composition quantification, respectively; and 3.) surface area using nitrogen gas adsorption experiment and applying the Brunauer-Emmet-Teller (BET) model.

The XRD patterns in Figure 6.2a shows that IrO₂ exhibits IrO₂ rutile (101) plane at $\sim 35^\circ$ and these peak decreases as cobalt content increases, accompanied with an increase of Co₃O₄ (311) peak at $\sim 37^\circ$. With Ir₄Co₆, weaker peaks of Co₃O₄ (400) at $\sim 45^\circ$ and (511) at $\sim 59^\circ$ and (440) at $\sim 65^\circ$ also emerge. Ultimately, with Ir₂Co₈, the crystal structure matches that of Co₃O₄ with none of the iridium peaks detected.

For the bulk composition in in Figure 6.2b, ICP-MS indicates that the atomic ratio of Ir and Co closely matches that of the theoretical atomic ratio based on the synthesis design. However, from XPS analysis, there seems to be a discrepancy between bulk and surface amount of Ir, suggesting Ir surface enrichment. This agrees with the literature [113] that Ir prefers to be on the surface of the alloy based on the surface energies of the metals. The Ir enrichment becomes more pronounced as Ir content increases in the material.

Surface area is one critical property for catalysis as this indicates the availability of active sites for the reaction. In the BET quantification shown in in Figure 6.2c, Ir black has the lowest surface area at $23.53 \pm 0.27 \text{ m}^2/\text{g}$, which agrees with some literature values [193]. Surprisingly, with pure IrO_2 in the synthesis, it yielded the highest BET surface area of $222.53 \pm 1.02 \text{ m}^2/\text{g}$, comparable to those in the literature [108] reported for Ir oxide catalysts synthesized from Adam’s fusion method. Then a sudden decrease in BET surface area happens upon the slight addition of cobalt in Ir_8Co_2 . However, the surface area tends to increase as more cobalt is added, where Ir_2Co_8 had the highest value among the Ir-Co alloys. Nevertheless, the range of surface area seems to fall within the range of 158-267 m^2/g . More information on the porosity of the materials is provided in Table 6.1

Table 6.1: Porosity and surface area information for the different Ir/Co catalysts obtained from N_2 gas adsorption experiment.

Catalyst	BET surface area ($\text{m}^2 \text{ g}^{-1}$)	BET desorption pore size diameter (nm)	Single point total pore volume ($\text{cm}^3 \text{ g}^{-1}$)	BJH desorption pore volume ($\text{cm}^3 \text{ g}^{-1}$)
Ir_2Co_8	222.53 ± 1.02	0.2896	5.21	5.56
Ir_4Co_6	186.52 ± 2.05	0.2633	5.65	7.11
Ir_6Co_4	185.51 ± 2.92	0.2464	5.31	7.20
Ir_8Co_2	158.30 ± 2.00	0.2481	6.27	8.70
IrO_2	265.99 ± 4.40	0.2808	4.22	6.66
Ir black	23.53 ± 0.27	0.0591	10.04	7.83

The structure and morphology of the electrocatalysts were also probed using transmission electron microscopy (TEM), shown in Figure 6.3. The trend that can be observed in the structure is that as more Ir is added to the material, the density of the nanoparticles suspended on the matrix also increases, comparing Ir_2Co_8 and Ir_8Co_2 in Figure 6.3a and Figure 6.3c, respectively. It has been proven in Chapter 5 that these nanoparticles are solely made of Ir and the matrix could potentially be a Co oxide or a mix of both Ir and Co oxides. This is even more evident in the case of pure IrO_2 in Figure 6.3d where the Ir nanoparticles are more closely packed. This close packing in IrO_2 might have given rise to its high surface area, as measured in nitrogen gas adsorption in Figure 6.2c. The host matrix seen in the Ir-Co alloys is

not observed for IrO_2 , suggesting that this only forms upon the introduction of Co in the material and forming a separate phase with Ir.

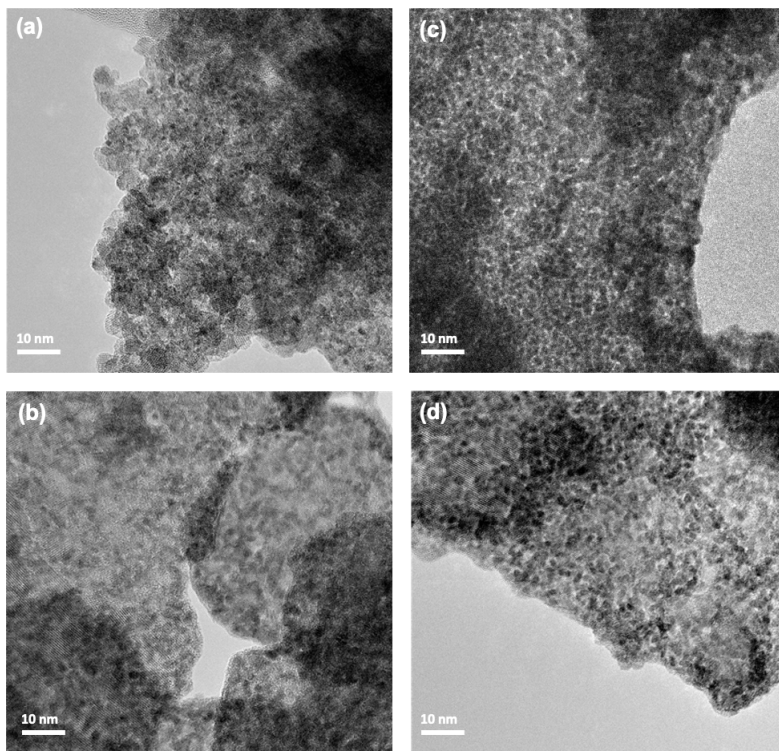


Figure 6.3: Transmission electron micrographs of (a) Ir_2Co_8 , (b) Ir_6Co_4 , (c) Ir_8Co_2 and (d) IrO_2 .

To validate the distribution of Ir and Co, chemical mapping tools such as energy-dispersive X-ray spectroscopy (EDS) and energy-electron loss spectroscopy (EELS) both from scanning transmission electron microscopy (STEM) were performed. In the EDS overlap images in Figure 6.4, it can be observed that the Ir signal, symbolized by the purple, increases as more Ir is added to the material. There is some degree of separation between Ir and Co phases but there are also regions where these two metals overlap and interact. In the Ir_2Co_8 image, we can see that it is dominated by Co, as shown in green color, in the overlap image in Figure 6.4a. The same information can also be observed from the EELS maps in Figure 6.5, where a shift in the color for the overlap image occurs with respect to the more dominant element.

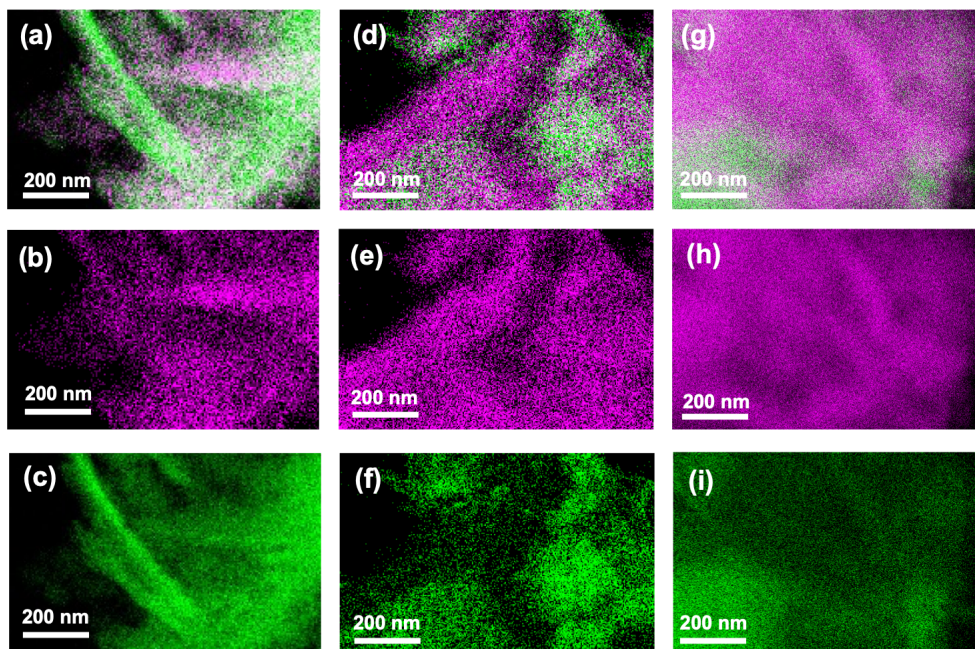


Figure 6.4: Chemical mapping results from STEM-EDS for (a-c) Ir_2Co_8 , (d-f) Ir_6Co_4 , and (g-i) Ir_8Co_2 . Ir signals are shown in purple while Co is in green. Overlap images for the two metals for each sample are shown in a, d and g.

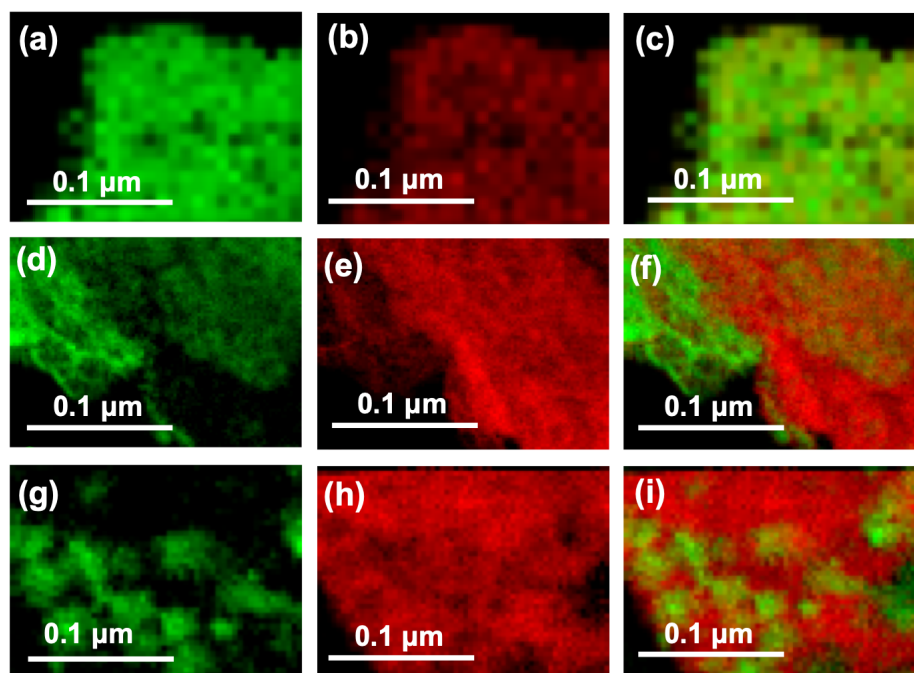


Figure 6.5: Chemical mapping results obtained from STEM-EELS experiments for (a,d,g) Ir_2Co_8 , (b,e,h) Ir_6Co_4 , and (c,f,i) Ir_{82} . Ir signals are shown in red while Co signals are colored green. The overlap images for the two metals are shown in g,h,and i.

After obtaining all relevant information from material characterization, the OER electrochemical activity of these catalysts was investigated in half-cell conditions using a rotating disk electrode in acidic and alkaline media. The raw data, as represented by the geometric current density from linear sweep voltammetry (LSV) in Figure 6.6 was further processed to get activity metrics such as mass activity based on Ir amount, overpotential, and Tafel slopes.

In general, from LSV in Figure 6.6a, it can be noted in acid media that there are only two major groups representing the best performing catalyst and another group that performs inferior to that of the former. Among the best-performing catalysts in acidic media are Ir_{82} and Ir_6Co_4 . In the alkaline media in Figure 6.6b, there are also two groups of catalyst performance but in this case, Ir black and IrO_2 belong to the best-performing catalysts joining Ir_3Co_2 and Ir_6Co_4 . This suggests a possible interaction of the Ir chemistry and the OER mechanism under different pH conditions.

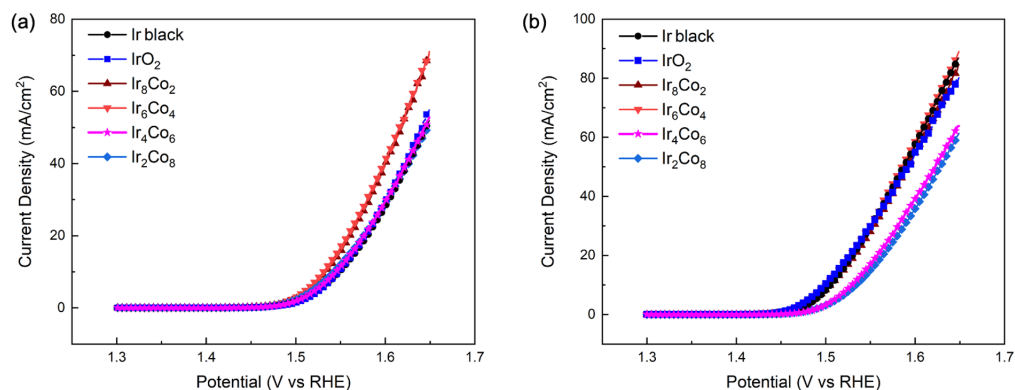


Figure 6.6: Linear sweep voltammetry (LSV) data collected in (a) 0.5 M H₂SO₄ and (b) 1.0 M KOH at 1 mV/s for samples with different Ir/Co ratios.

Mass activity is an important descriptor especially when it comes to cost consideration. The mass activity was calculated at 300 mV since this region is dominated by kinetics and normalized to the mass of Ir on the sample. Obtaining an accurate mass for Ir in the sample is difficult since the Ir-Co alloys are hard to fully digest for ICP-MS. Only a pinch of the material was digested for sample preparation in the ICP-MS which is not in the detection limit of the analytical balance. So, the calculations are mostly based on theoretical values and assuming that Ir forms IrO₂ and Co forms Co₃O₄ to estimate oxygen content in the material.

The results obtained for mass activity are then presented in Figure 6.7a for both acidic and alkaline media. It can be readily seen that the mass activities in alkaline media are significantly higher than that in acidic media for all samples. This discrepancy will not be covered in this work since there are a lot of differences in these two conditions such as the type and concentration of electrolyte used, the behavior of these two metals in different pH conditions, and the OER reaction mechanism. However, it is also very clear that the Ir-Co alloys have higher mass activity in acidic media compared to pure Ir catalysts, e.g., Ir black and IrO₂, with Ir₂Co₈ having the highest mass activity. This indicates an effective Ir utilization the synthesized Ir-Co alloys. In the alkaline media, Ir black and IrO₂ obtained higher mass activities than the Ir-Co alloys, except for Ir₆Co₄ which yielded a maximum mass activity of 117 mA/mg_{Ir} among all samples. This supports a possible synergistic effect between Ir and Co and is optimized at this condition.

Overpotential at 10 mA/cm², shown in Figure 6.7b was then taken for both acid and alkaline, with the same contention for the mass activity that this region is kinetically dominated. Conceptually, the overpotential represents how far the value is from 1.23 V for the theoretical OER potential. Similar to mass activity, acidic

media has higher overpotential than alkaline since the kinetics is much slower, thus, to achieve 10 mA/cm^2 , we need more overpotential to drive the reaction. However, major differences such as pH and electrolyte concentration need to be considered and a direct comparison between acidic and alkaline media in this work is avoided.

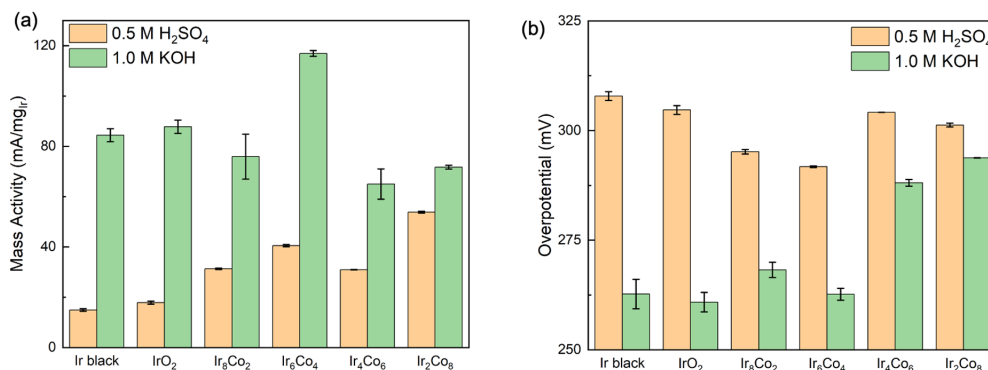


Figure 6.7: (a) Mass activity at 300 mV overpotential normalized to Ir mass estimated using stoichiometry for samples with different Ir/Co ratios. (b) Overpotential at 10 mA/cm^2 in both acidic and alkaline media.

The trend in acidic media OER overpotential is that it decreases from Ir black to Ir₆Co₄ at 292 mV, then increases again once the Co ratio is increased. In alkaline media, the lowest overpotential is obtained by IrO₂ at 261 mV, which is still comparable with Ir₆Co₄ at 263 mV. On the other hand, Co-rich samples Ir₄Co₆ and Ir₂Co₈ have the highest OER overpotential in alkaline media at 288 mV and 294 mV, respectively.

Tafel slopes were evaluated within the range of 0.3 to 3 mA/cm^2 to cover the kinetic region and the Tafel plots for acid and alkaline media are shown in Figure 6.8a and Figure 6.8b, respectively. The final Tafel slopes are then summarized in Figure 6.8c. For catalysts in the acidic media, the Tafel slopes generally fall within the range of 42.5 to 45 mV/dec, suggesting that the OER rate-determining step is not influenced by the Ir-Co composition. However, in the alkaline media, a minimum of 30 mV/dec was found with IrO₂ then shifting to a higher Tafel slope as the Co concentration increases. This indicates that the OER rate-determining step is influenced by the Ir/Co composition of the material in alkaline media. Almost all catalysts have much lower Tafel slopes in alkaline media, which means faster reaction rates, but the discrepancy between acidic and alkaline Tafel slopes diminishes with Co-rich samples like Ir₄Co₆ and Ir₂Co₈.

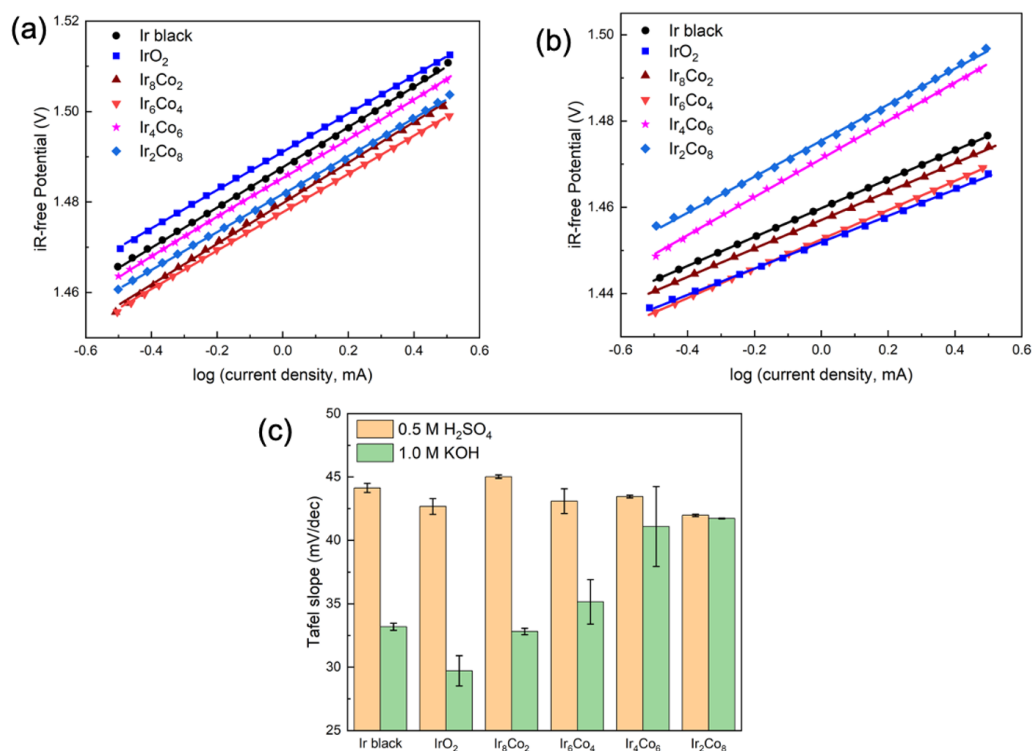


Figure 6.8: (a) Tafel plot derived from LSV in 0.5 M H₂SO₄ as well as in (b) 1.0 M KOH. (c) Summary of the Tafel slopes for all samples with different Ir/Co ratios.

Electrochemical impedance spectroscopy (EIS) is also another tool that can provide information related to the different sources of resistance in the system. The Nyquist plots for acid and alkaline media are presented in Figure 6.10a and Figure 6.10b, respectively. The experimental data are then fitted using an equivalent circuit in Figure 6.9 comprising different circuit elements that represent the physical phenomena in the system. These elements are the following: L for the inductance; R_{Ω} ohmic resistance from the bulk solution; R_{ct} from the charge transfer resistance between the reactant and the electrode surface; Q_1 is the constant phase element (CPE) for the electric double layer and the R_2Q_2 parallel is from diffusion/adsorption of reaction intermediate caused by slow diffusion through the reaction interphase.

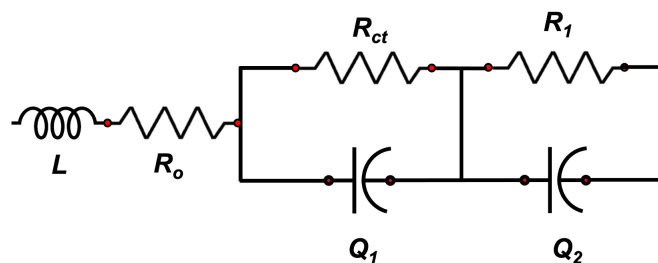


Figure 6.9: An equivalent circuit model used to fit the EIS data consisting of an inductor, L , solution resistance, R_{Ω} , charge transfer resistance, R_{ct} , double-layer capacitance, Q_1 , and resistance from diffusion/adsorption of intermediates coupled in R_1Q_2 .

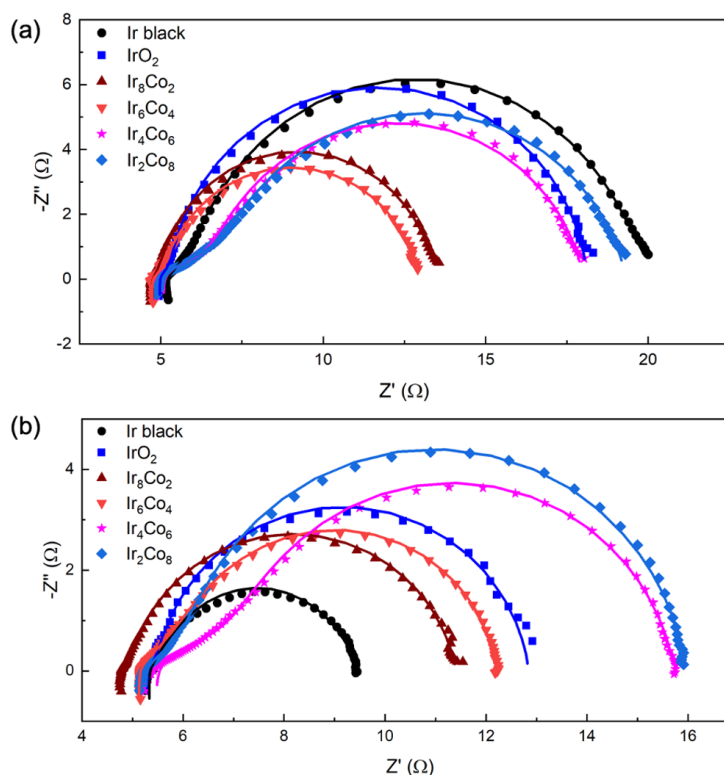


Figure 6.10: Electrochemical impedance spectra in (a) 0.5 M H_2SO_4 and (b) 1.0 M KOH for samples with different Ir/Co ratios.

The Nyquist plots in Figure 6.10 already reveal the correlation between the diameter of the loop, which is mostly related to R_{ct} [182], and the OER activity. This is further confirmed by taking the sum of R_{ct} and R_1 presented in Figure 6.11.

In the acidic media, the minimum for $R_{ct} + R_1$ is with Ir_6Co_4 at $1.61 \Omega \text{ cm}^2$ while in alkaline, Ir black has the minimum at $0.82 \Omega \text{ cm}^2$. When comparing the synthesized catalysts, the Ir_8Co_2 and Ir_6Co_4 yield the lowest total resistance values.

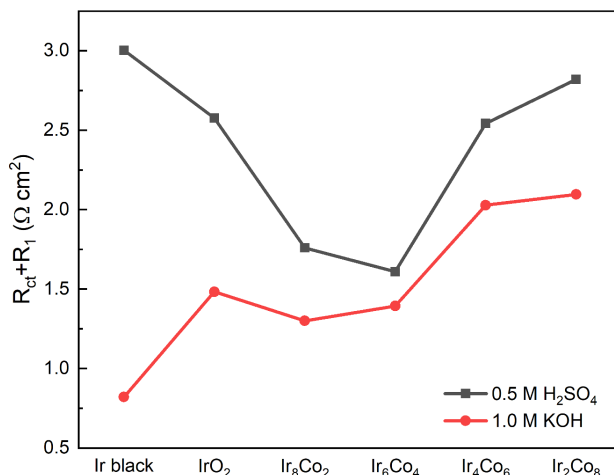


Figure 6.11: Total resistance ($R_{ct} + R_1$) extracted from EIS in 0.5 M H_2SO_4 and 1.0 M KOH for samples with different Ir/Co ratio.

Table 6.2: Values of the circuit elements for the fitted electrochemical impedance spectroscopy (EIS) data in 0.5 H_2SO_4 and the calculated ECSA from the EIS-based capacitance.

Catalyst	R_Ω	$R_{ct} + R_1$	C_1	n_1	C_2	n_2	C	ECSA @ $C_s = 1.3 \text{ F m}^{-2}$ m^2/g
	Ω	$\Omega \text{ cm}^2$	$\text{E}^{-3} \text{ F s}^{n-1}$		F s^{n-1}		mF	
Ir black	5.13	3.00	4.32	0.98	5.24E-02	0.47	3.93	154.27
IrO_2	4.97	2.58	5.90	0.95	1.26E-02	0.76	4.79	188.04
Ir_8Co_2	4.74	1.76	8.37	1.00	1.10E-01	0.56	8.37	328.41
Ir_6Co_4	4.71	1.61	8.57	0.94	1.28E-01	0.43	6.88	269.91
Ir_4Co_6	5.06	2.54	6.76	0.89	7.44E-03	0.59	4.28	168.10
Ir_2Co_8	4.97	2.82	6.05	0.88	1.20E-01	0.50	3.64	142.98

Table 6.3: Values of the circuit elements for the fitted electrochemical impedance spectroscopy (EIS) data in 1.0 M KOH and the calculated ECSA from the EIS-based capacitance.

Catalyst	R_{Ω}	$R_{ct} + R_1$	C_1	n_1	C_2	n_2	C	ECSA @
	Ω	$\Omega \text{ cm}^2$	$\text{E}^{-3} \text{ F s}^{n-1}$		F s^{n-1}		mF	$C_s = 1.3 \text{ F m}^{-2}$ m^2/g
Ir black	5.32	0.82	2.51	0.99	1.57E-02	0.64	2.39	93.97
IrO ₂	5.28	1.48	4.21	0.92	1.73E-02	0.69	2.90	113.77
Ir ₈ Co ₂	4.77	1.30	4.85	0.89	1.07E-02	0.75	2.83	110.95
Ir ₆ Co ₄	5.12	1.39	4.33	0.92	1.53E-02	0.61	3.04	119.38
Ir ₄ Co ₆	5.40	2.03	3.52	0.91	7.15E-03	0.54	2.22	87.15
Ir ₂ Co ₈	5.25	2.10	3.27	0.93	9.03E-03	0.64	2.28	89.62

On the other hand, cyclic voltammetry (CV) was employed to study the relevant redox pairs, shown in Figure 6.12. In the acidic media, the transition between Ir³⁺ to Ir⁴⁺ can be observed at around 0.75–0.78 V, as reported in the literature [194], which happens to increase with the best performing catalyst Ir₈Co₂ and Ir₆Co₄. It can be noted that the peak current density of IrO₂ is much smaller than the two catalysts previously mentioned. This signals the possible role of Co in making Ir more oxidizable in these binary systems.

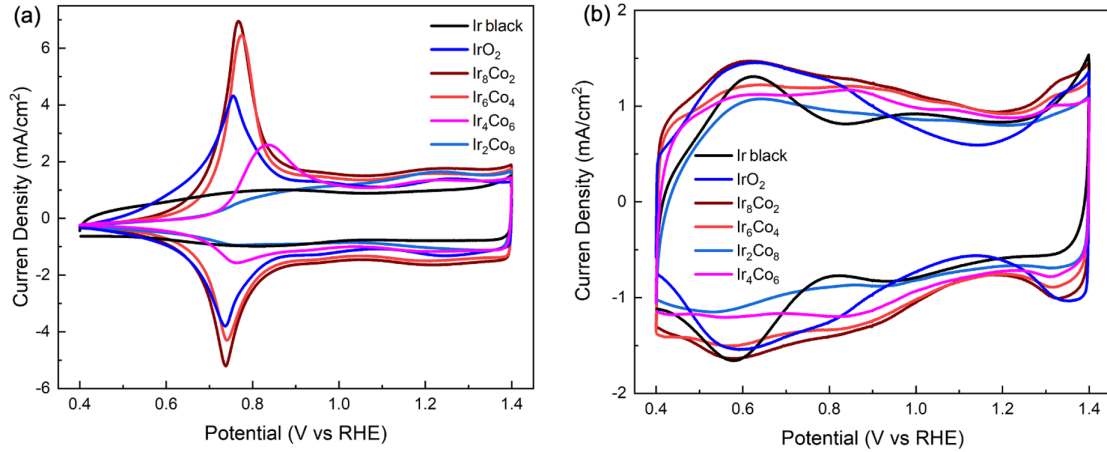


Figure 6.12: Cyclic voltammetry curves collected at 50 mV/s for samples with different Ir/Co ratios in (a) 0.5 M H₂SO₄ and (b) 1.0 M KOH

In the alkaline media, this peak is not as sharp compared to that in acidic media and shifts at a much lower potential at around 0.6 V, which is expected for the super-Nernstian behavior of Ir [179, 194]. The trend among the catalysts is also not so clear but it is evident that the less performing catalyst, Ir₄Co₆ and Ir₂Co₈,

do not have well-defined peaks compared to the others. Nevertheless, the further oxidation of Ir^{4+} to Ir^{5+} at around 1.3 V is much clearer than acidic CV results and is then proceeded by the OER reaction towards higher potential.

Another use of CV is the estimation of the double-layer capacitance (C_{dl}), which can then be related to the electrochemically active surface area (ECSA). By obtaining CV at different scan rates from 2 mV/s to 150 mV/s and plotting the current density at 0.9 V for each scan rate, a linear regression can be obtained with a slope related to the C_{dl} . This method has been described as well in the previous chapter. In both media, the optimum C_{dl} seems to occur between Ir_{82} and Ir_6Co_4 . Using an areal capacitance reference at 1.3 F/m² [183], ECSA values can be estimated as shown in Figure 6.14a.

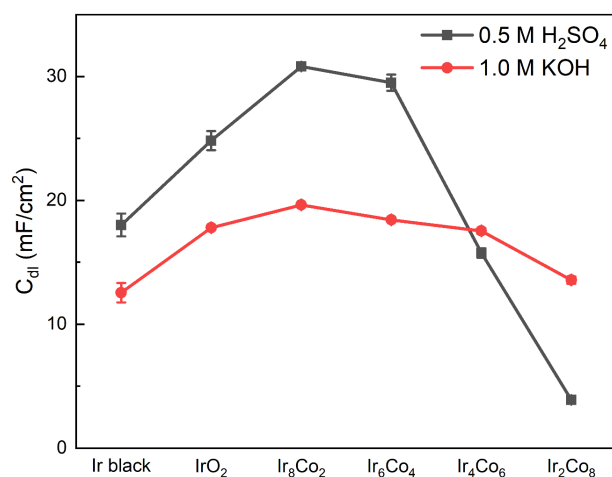


Figure 6.13: Double-layer capacitance (C_{dl}) estimated at 0.9 V using different CV scan rates from 2 mV/s to 150 mV/s.

Similarly, the effective capacitance can also be obtained from EIS as outlined by Li et al. [182] and then convert it to ECSA using the same areal reference. However, this ECSA represents the double-layer structure at 1.55 V, which is in the OER relevant region. It can be found in the acidic medium that an optimum exists for Ir_8Co_2 at 328 m²/g. In alkaline, the differences among the samples are very subtle with an observable decline for Ir_4Co_6 and Ir_2Co_8 . Although different approaches were applied to capture ECSA, both techniques yield almost similar trends and range of values and are even comparable to those obtained from BET surface area measurement as depicted in Figure 6.14b.

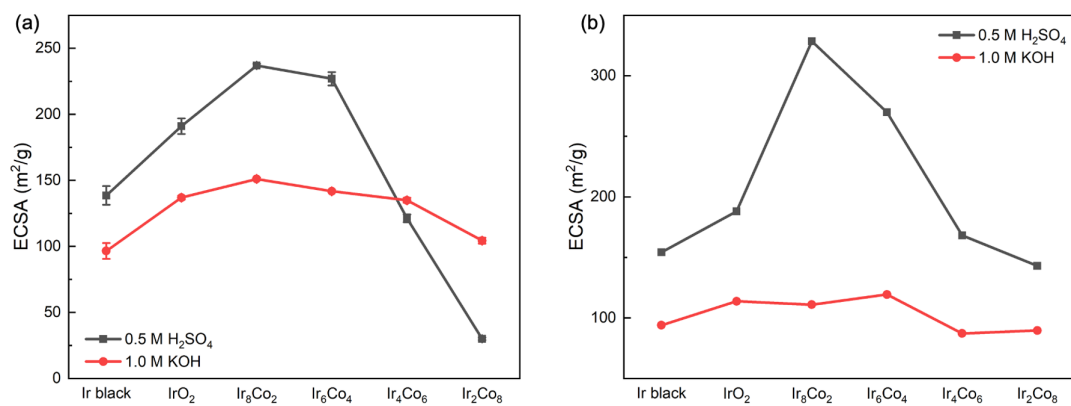


Figure 6.14: Comparison of electrochemically active surface areas (ECSA) obtained in acidic and alkaline media using (a) CV method and (b) EIS method.

6.5 Effect of Surfactant and Acid Etching

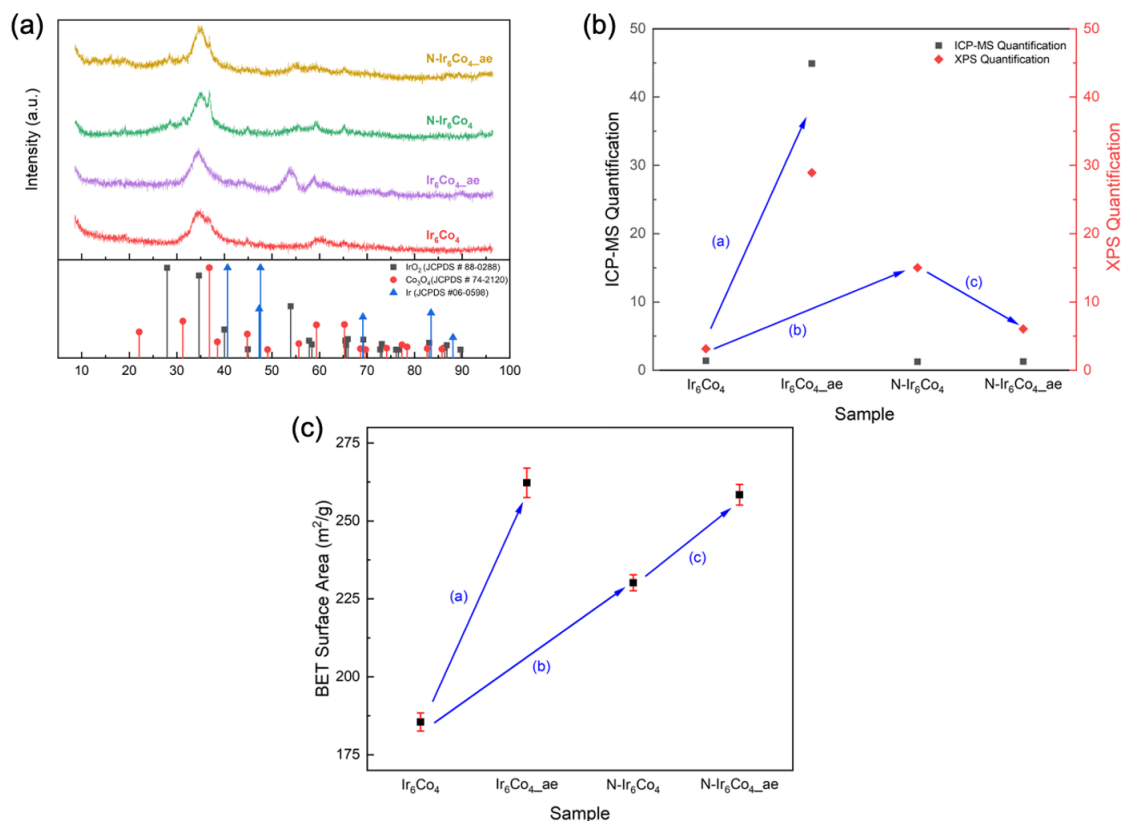


Figure 6.15: (a) X-ray diffractogram data for the Ir₆Co₄ samples prepared with and without surfactant and subjected to acid etching. (b) Quantification of the Ir/Co molar ratio on the bulk using ICP-MS and on the surface using XPS. (c) Surface area measurement implementing the BET model for N₂ gas adsorption experiment.

In the previous section, it has been identified that Ir₆Co₄ is one of the best catalysts for OER in both acidic and alkaline media. Thus, it is imperative to further probe additional synthesis variables that can potentially impact its performance. Here, two variables were investigated, specifically the effect of adding surfactant in the synthesis condition and post-processing with acid etching under similar conditions used in Chapter 5. The interaction between adding surfactant and acid etching was also studied. To sum up, four catalysts are studied here: Ir₆Co₄; Ir₆Co₄_ae for after acid etching; N-Ir₆Co₄ for without surfactant; and N-Ir₆Co₄_ae for without surfactant and after acid etching

The crystallographic information in XRD in Figure 6.15a shows that for N-Ir₆Co₄, the Co₃O₄ peaks for the (311) at ~37°, (400) at ~45°, (511) at ~59°, and (440) at ~65° planes become sharper compared to Ir₆Co₄. This could mean that the degree of separation between the Ir and Co phases is much stronger without the surfactant. In the case of Ir₆Co₄, more peaks from IrO₂ rutile appeared after acid etching, specifically (211) at ~ 54°, (220) at 57.8° and (002) at ~58.4° along with the disappearance of the characteristic Co₃O₄ (311) peak. This could indicate that upon removal of excess cobalt, these planes became more exposed. When acid etching was performed on the N-Ir₆Co₄, only a slight appearance of these additional peaks was observed coupled with reduction in Co₃O₄ (311) plane.

The surface Ir:Co ratio from XPS in Figure 6.15b indicate that N-Ir₆Co₄ is more Ir-enriched than Ir₆Co₄ (arrow ‘b’). This suggest that an even higher degree of surface segregation between Ir and Co, with Ir dominating the surface in N-Ir₆Co₄. For the acid etching effect, most of the cobalt has been leached out in Ir₆Co₄-ae where a significantly higher Ir:Co ratio is detected both from XPS and ICP compared to Ir₆Co₄ (arrow ‘a’). However, the reverse is happening for non-surfactant N-Ir₆Co₄-ae where the Ir: Co ratio decreased (arrow ‘c’), suggesting that both Ir and Co are leaching out, the Ir layer on the surface dissolves at a faster rate and minimizes the dissolution of Co. Regardless, the bulk composition of N-Ir₆Co₄ and N-Ir₆Co₄-ae remain similar and comparable to that of Ir₆Co₄ and the theoretical value.

The BET surface area measurements in Figure 6.15c suggest an enhancement due to the removal of Co in the material for acid etched samples, Ir₆Co₄-ae and N-Ir₆Co₄-ae. With most Co leached out in Ir₆Co₄-ae, the surface area increased by 41%. In N-Ir₆Co₄-ae, a significant amount of Co is retained, and the surface area enhancement was only 11%. Surprisingly, the surface area in N-Ir₆Co₄ is significantly higher than in Ir₆Co₄ which could possibly be driven by the morphological difference as revealed later by TEM imaging. More information from N₂ gas adsorption experiments is presented in Table 6.4.

Table 6.4: Porosity and surface area information for the different Ir/Co catalysts obtained from N₂ gas adsorption experiment.

Catalyst	BET surface area (m ² g ⁻¹)	BET desorption pore size diameter (nm)	Single point total pore volume (cm ³ g ⁻¹)	BJH desorption pore volume (cm ³ g ⁻¹)
Ir ₆ Co ₄	185.51 ± 2.92	0.2464	5.31	7.20
Ir ₆ Co ₄ -ae	262.21 ± 4.73	0.2752	4.20	7.34
N- ₆ Co ₄	230.17 ± 2.53	0.2413	4.19	5.78
N- ₆ Co ₄ -ae	258.39 ± 3.32	0.2750	4.26	5.49

In terms of the morphology and structure of the catalysts from TEM in Figure

6.16, the surfactant attains a more uniform structure, especially near the edge of the material comparing Figure 6.16a (Ir_6Co_4) and Figure 6.16c ($\text{N-Ir}_6\text{Co}_4$). Without the surfactant, the particle growth becomes heterogeneous with rod-like shapes. Rod structures coming from Adam's fusion method are also reported in the literature¹¹⁹. The extended structures near the edge for $\text{N-Ir}_6\text{Co}_4$ might also have contributed to its relatively larger surface area compared with Ir_6Co_4 BET measurements. For the acid etching effect in Figure 6.16b, the density of Ir nanoparticles that are visible increased compared to that in Figure 6.16a, where they might have been buried by the Co matrix. However, for $\text{N-Ir}_6\text{Co}_4\text{-ae}$ in Figure 6.16d, there is no clear difference before acid etching in $\text{N-Ir}_6\text{Co}_4$ (Figure 6.16c). This supports the idea that the Co component in the material is more preserved than with the surfactant.

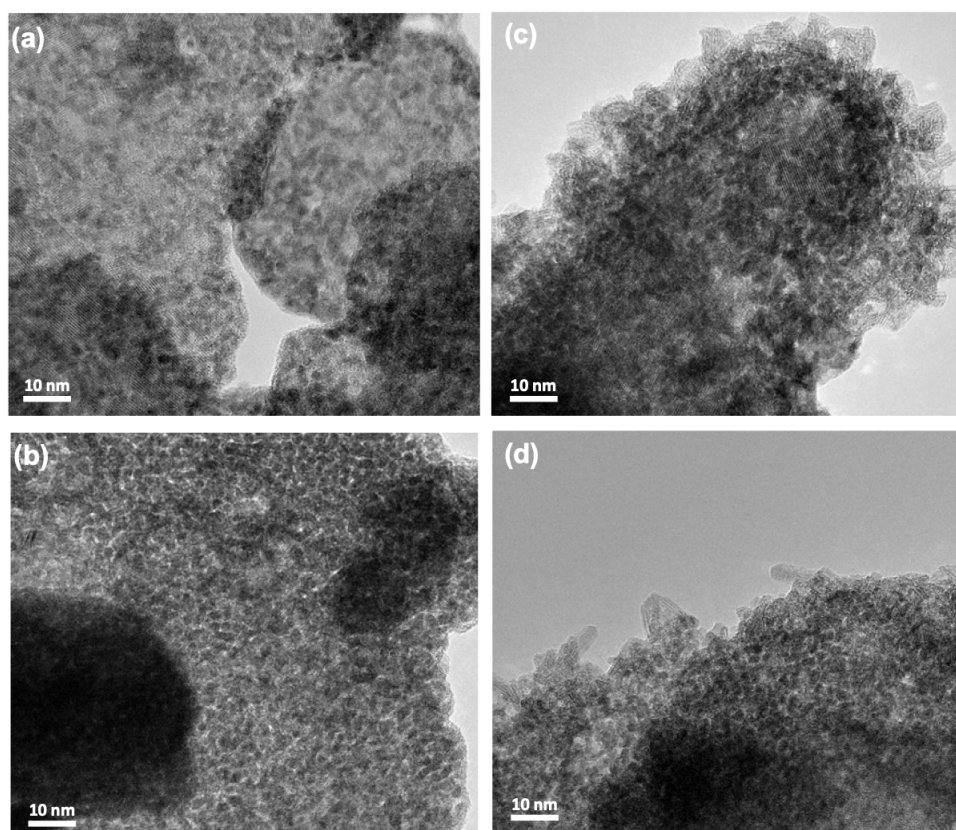


Figure 6.16: Transmission electron micrographs of (a) Ir_6Co_4 , (b) $\text{Ir}_6\text{Co}_4\text{-ae}$, (c) $\text{N-Ir}_6\text{Co}_4$ and (d) $\text{N-Ir}_6\text{Co}_4\text{-ae}$.

To understand the chemical distribution as a function of surfactant and acid etching process, EDS and EELS mapping are also performed. In Figure 6.17a and Figure 6.17d, the effect of acid etching can be visualized effectively where most of

Co are leached out. Comparing Ir_6Co_4 and $\text{N-Ir}_6\text{Co}_4$, in Figure 6.17g, the thick Ir layer on the surface forces the Co to aggregate in the middle, forming a core-shell structure. After applying acid etching on $\text{N-Ir}_6\text{Co}_4$, there is no significant difference in the chemical distribution for $\text{N-Ir}_6\text{Co}_4$ -ae. In the EELS maps, similar conclusions can be derived and even less Co signals are detected in Ir_6Co_4 -ae (Figure 6.18d). The chemical mapping aligns very well with the quantification results obtained from ICP-MS and XPS presented in Figure 6.2b and Figure 6.2c.

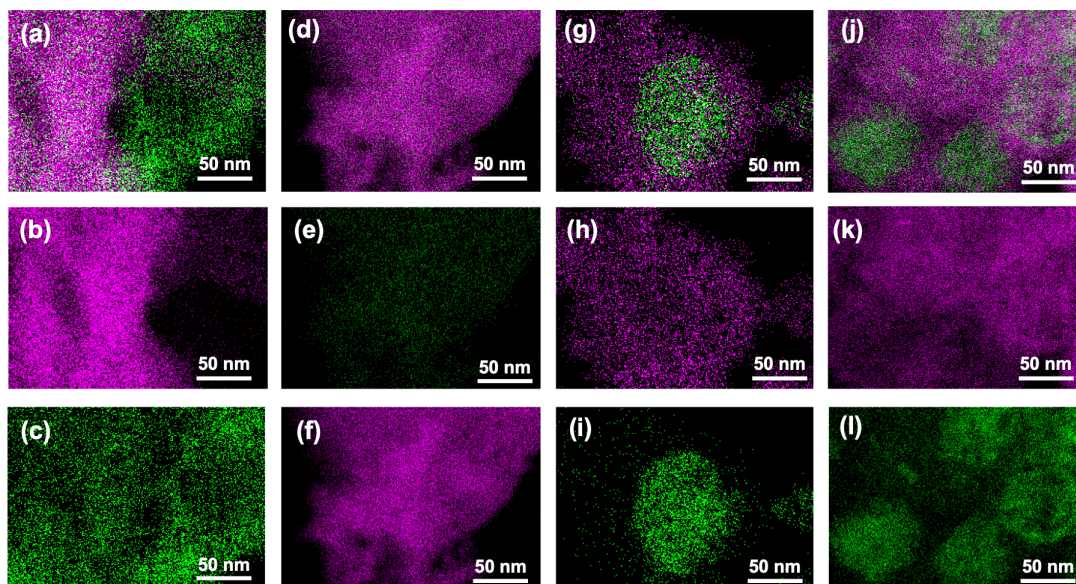


Figure 6.17: Chemical mapping results from STEM-EDS for (a-c) Ir_6Co_4 , (d-f) Ir_6Co_4 -ae, (g-i) $\text{N-Ir}_6\text{Co}_4$ and (j-l) $\text{N-Ir}_6\text{Co}_4$ -ae. Ir signals are shown in purple while Co is in green. Overlap images for the two metals for each sample are shown in a, d and g.

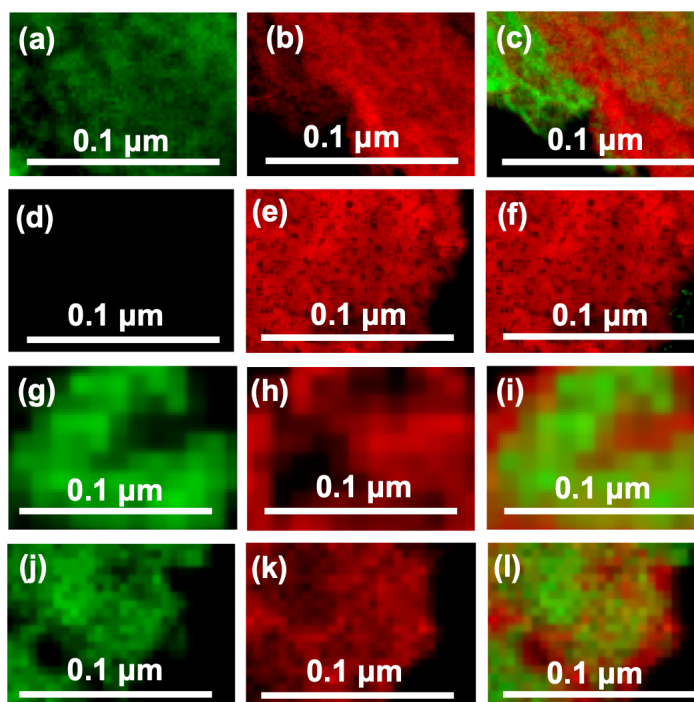


Figure 6.18: Chemical mapping results obtained from STEM-EELS experiments for (a-c) Ir_6Co_4 , (d-f) $\text{Ir}_6\text{Co}_4\text{-ae}$, (g-i) $\text{N-Ir}_6\text{Co}_4$, and (j-l) $\text{N-Ir}_6\text{Co}_4\text{-ae}$. Ir signals are shown in red while Co signals are colored green. The overlap images for the two metals are shown in g, h, and i.

For the OER activity, the geometric current density from LSV data is presented in Figure 6.19a and Figure 6.19b for acidic and alkaline media, respectively. The activity metrics for mass activity, overpotential, and Tafel slopes are also extracted from the LSV data and shown in Figure 6.20 and Figure 6.21.

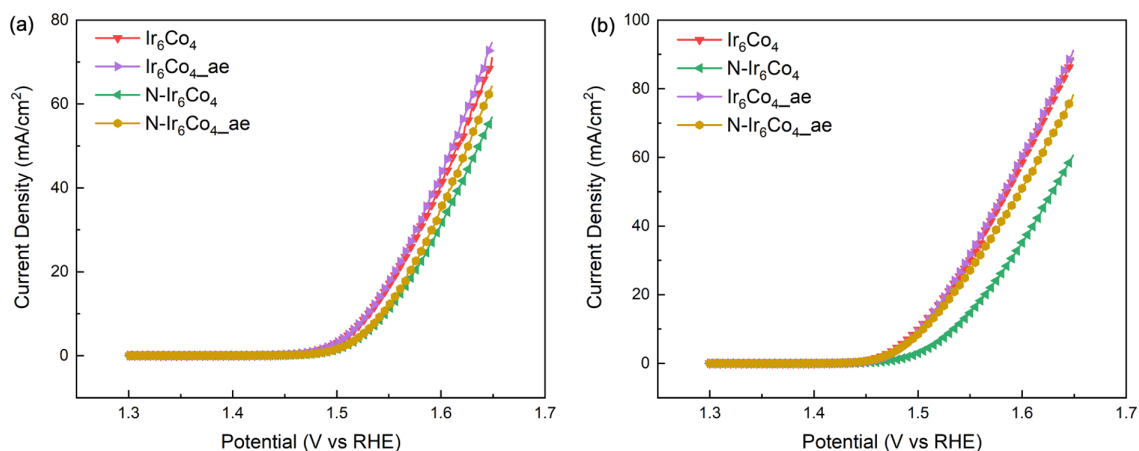


Figure 6.19: Linear sweep voltammetry (LSV) data collected at 1 mV/s in (a) 0.5 M H₂SO₄ and (b) 1.0 M KOH for Ir₆Co₄ samples prepared with and without surfactant and subjected to acid etching.

The effect of acid etching on mass activity is more evident in the alkaline media than in acidic media, especially for N-Ir₆Co₄-ae. The increased surface resulting from acid etching could have improved the mass activity area but is not reflected in the acidic media. The acid etching might have affected the surface Ir or Co chemistry, leading to altered reactivity towards OER that has more impact in the alkaline media. The role of cobalt and the possible change in Co chemistry in N-Ir₆Co₄ could also be attributed to the improved performance considering it is still present in significant amount for N-Ir₆Co₄-ae. The effect of surfactant on mass activity is also not very significant in the acidic media, comparing Ir₆Co₄ and N-Ir₆Co₄. However, the difference is much more significant in the alkaline media where Ir₆Co₄ attains 41 mA/mg_{Ir} compared to 28 mA/mg_{Ir} for N-Ir₆Co₄.

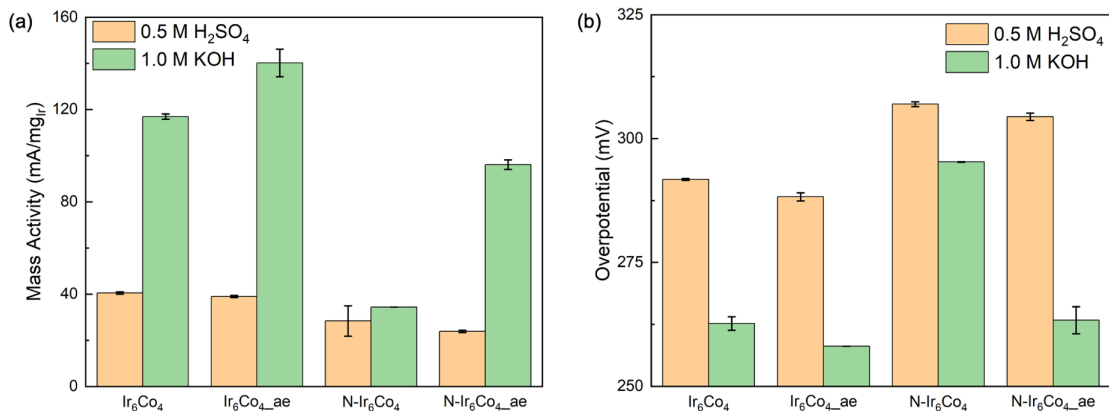


Figure 6.20: (a) Mass activity at 300 mV overpotential normalized to Ir mass estimated using stoichiometry for Ir₆Co₄ samples prepared with and without surfactant and subjected to acid etching. (b) Overpotential at 10 mA/cm² in both acidic and alkaline media.

A similar trend in mass activity is observed for the overpotential at 10 mA/cm². In acidic environment, the acid etching does not have any positive impact but in alkaline media, the overpotential is reduced, and more significant for N-Ir₆Co₄_ae. Nevertheless, significant reduction in overpotential can be obtained when surfactant is used, comparing Ir₆Co₄ with 292 mV while N-Ir₆Co₄ has 307 mV in the alkaline media.

While mass activity and overpotential are activity descriptors in the kinetic region, the mass transfer region must also be considered at high potential. In the LSV curves in Figure 6.19, the impact of mass transfer on N-Ir₆Co₄ in both acidic and alkaline media reveals the possibility of inefficient reactant transport due to the structure of this catalyst.

Information regarding the OER mechanism can be probed from the Tafel plots in Figure 6.21a and 6.21b, and the Tafel slope values are summarized in Figure 6.21c. The Tafel slope in acidic media remains almost the same at around 42-45 mV/dec across all catalysts, unaffected by the nature of the catalyst, similar to that in the Ir-Co ratio study in the previous section. However, a much lower Tafel slope is obtained in the alkaline media, with Ir₆Co₄ at 35 mV/dec against N-Ir₆Co₄ at 40 mV/dec. Applying acid etching in both samples reduced the Tafel slopes to 31 mV/dec and 33 mV/dec for Ir₆Co₄_ae and N-Ir₆Co₄_ae, respectively. The sensitivity of the Tafel slope in the alkaline media reveals the influence of the surface chemistry of the catalyst on the OER mechanism and rate-determining steps.

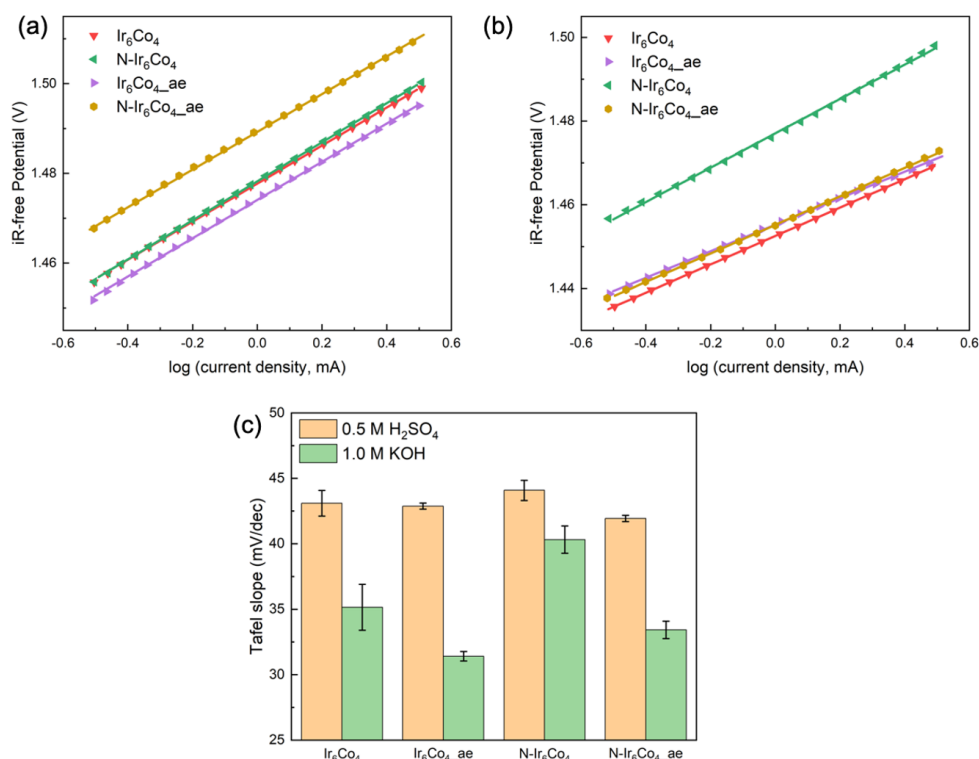


Figure 6.21: (a) Tafel plot derived from LSV in 0.5 M H₂SO₄ as well as in (b) 1.0 M KOH. (c) Summary of the Tafel slopes for Ir₆Co₄ samples prepared with and without surfactant and subjected to acid etching.

The resistances in the system are also analyzed using EIS technique and applying the equivalent circuit in Figure 6.9. The Nyquist plots for the raw and fitted data in acidic and alkaline media are shown in Figure 6.22a and 6.22b, respectively. The total resistance, $R_{ct} + R_1$, from the equivalent circuit is plotted in Figure 6.22 for all samples. Acid etching in both Ir₆Co₄ and N-Ir₆Co₄ resulted in reduced total resistance, as indicated in arrow (a) and arrow (c) in Figure 6.22. Without the surfactant, the total resistance is much higher comparing Ir₆Co₄ and N-Ir₆Co₄. The total resistances in alkaline media are all lower than in acidic media and this difference is more pronounced in N-Ir₆Co₄-ae.

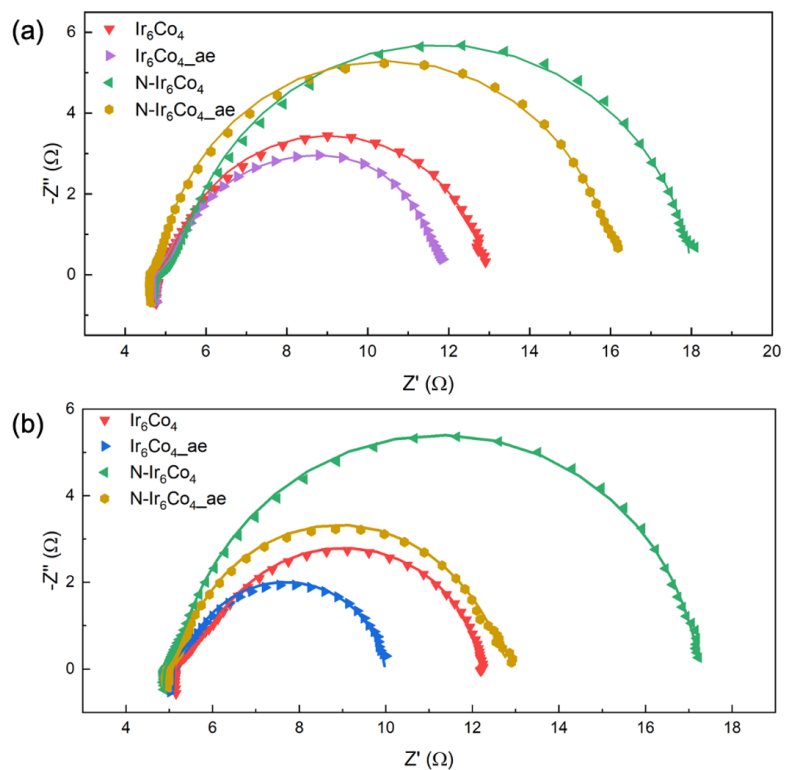


Figure 6.22: Electrochemical impedance spectra in (a) 0.5 M H_2SO_4 and (b) 1.0 M KOH

Table 6.5: Values of the circuit elements for the fitted electrochemical impedance spectroscopy (EIS) data in 0.5 H_2SO_4 and the calculated ECSA from the EIS-based capacitance for Ir_6Co_4 samples subjected to different conditions.

Catalyst	R_Ω	$R_{ct} + R_1$	C_1	n_1	C_2	n_2	C	ECSA @
	Ω	$\Omega \text{ cm}^2$	$\text{E}^{-3} \text{ F s}^{n-1}$		F s^{n-1}		mF	$C_s = 1.3 \text{ F m}^{-2}$ m^2/g
Ir_6Co_4	4.71	1.61	8.57	0.94	1.28E-01	0.43	6.88	269.91
$\text{Ir}_6\text{Co}_4\text{-ae}$	4.75	2.56	10.3	0.94	3.90E-02	0.57	8.32	326.52
N- Ir_6Co_4	4.78	2.35	5.37	0.94	4.18E-02	0.51	4.17	163.82
N- $\text{Ir}_6\text{Co}_4\text{-ae}$	4.61	1.38	6.31	0.99	2.57E-01	0.41	6.03	236.59

Table 6.6: Values of the circuit elements for the fitted electrochemical impedance spectroscopy (EIS) data in 1.0 M KOH and the calculated ECSA from the EIS-based capacitance for Ir₆Co₄ samples subjected to different conditions.

Catalyst	R_{Ω}	$R_{ct} + R_1$	C_1	n_1	C_2	n_2	C	ECSA @
	Ω	$\Omega \text{ cm}^2$	$\text{E}^{-3} \text{ F s}^{n-1}$		F s^{n-1}		mF	$C_s = 1.3 \text{ F m}^{-2}$ m^2/g
Ir ₆ Co ₄	4.71	1.61	8.57	0.94	1.28E-01	0.43	6.88	269.91
Ir ₆ Co ₄ -ae	4.75	2.56	10.3	0.94	3.90E-02	0.57	8.32	326.52
N-Ir ₆ Co ₄	4.78	2.35	5.37	0.94	4.18E-02	0.51	4.17	163.82
N-Ir ₆ Co ₄ -ae	4.61	1.38	6.31	0.99	2.57E-01	0.41	6.03	236.59

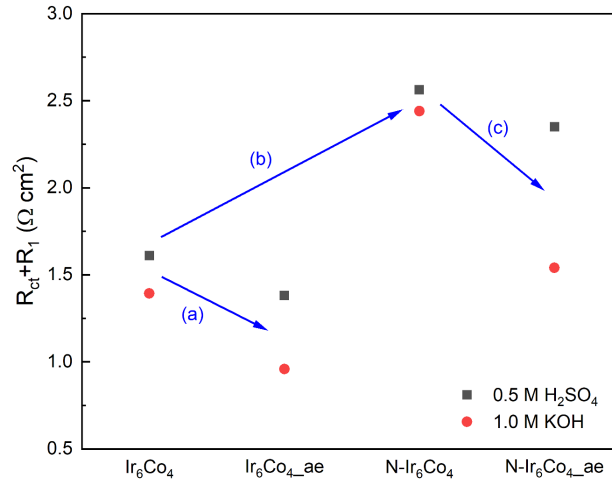


Figure 6.23: Total resistance ($R_{ct} + R_1$) extracted from EIS in 0.5 M H₂SO₄ and 1.0 M KOH for Ir₆Co₄ samples subjected to different conditions.

For the CV results, the redox couple at around 0.77 V for Ir³⁺/Ir⁴⁺ pair shifts to a lower potential after acid etching in the acidic media, shown in Figure 6.24a. Although, the peak current density remains almost the same. For N-Ir₆Co₄ and N-Ir₆Co₄-ae, the peak current density for this redox pair is significantly less, possibly indicating less amount of Ir³⁺ on the surface. Similar to the analysis in the previous section, it is difficult to obtain a clear trend for the Ir³⁺/Ir⁴⁺ peak in the alkaline media which shifted at around 0.58-0.59 V from that in acidic media. However, the peak for Ir₆Co₄-ae stands out as it has a significantly higher peak current density.

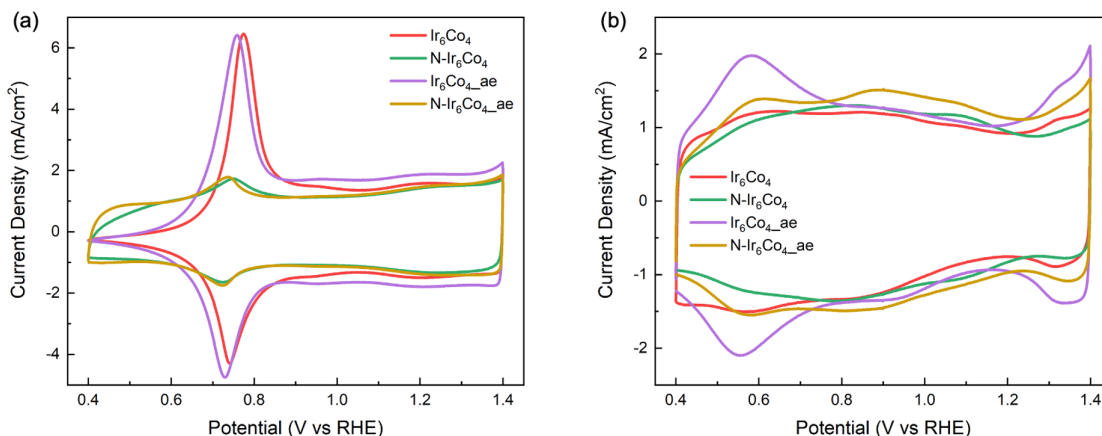


Figure 6.24: Cyclic voltammograms collected at 50 mV/s in (a) 0.5 M H_2SO_4 and (b) 1.0 M KOH for Ir_6Co_4 samples subjected to different conditions.

The ECSA of the samples for this section are also estimated from the capacitance obtained from CV with different scan rates, as illustrated in Figure 6.25, and the effective capacitance from EIS method. Regardless of the differences in the techniques, a similar conclusion can be derived in both Figure 6.26a and Figures 6.26b. After acid etching, the ECSA increased for both $\text{Ir}_6\text{Co}_4\text{-ae}$ (arrow ‘a’ and ‘b’) and $\text{N-Ir}_6\text{Co}_4\text{-ae}$ (arrow ‘d’) in acidic and alkaline media.

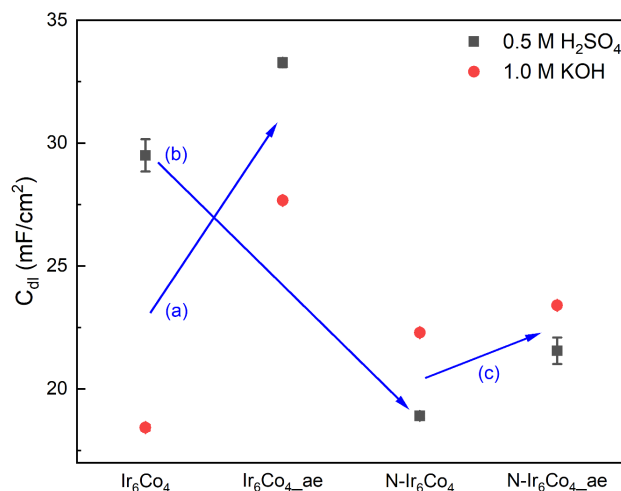


Figure 6.25: Double-layer capacitance (C_{dl}) estimated at 0.9 V using different CV scan rates from 2 mV/s to 150 mV/s for Ir_6Co_4 samples subjected to different conditions.

The impact of adding surfactant to the ECSA enhancement is more pronounced in the alkaline media (arrow ‘c’) than in acidic media. These observations connect back to the mass activity, overpotential, and the Tafel slope where the effect of surfactant is more pronounced in the alkaline media compared to acidic media. This gives rise to the possibility of the interrelationship between the pH and ions involved in the electrolyte and the surface chemistry of the catalyst, and how the interact with each other affects the OER mechanism.

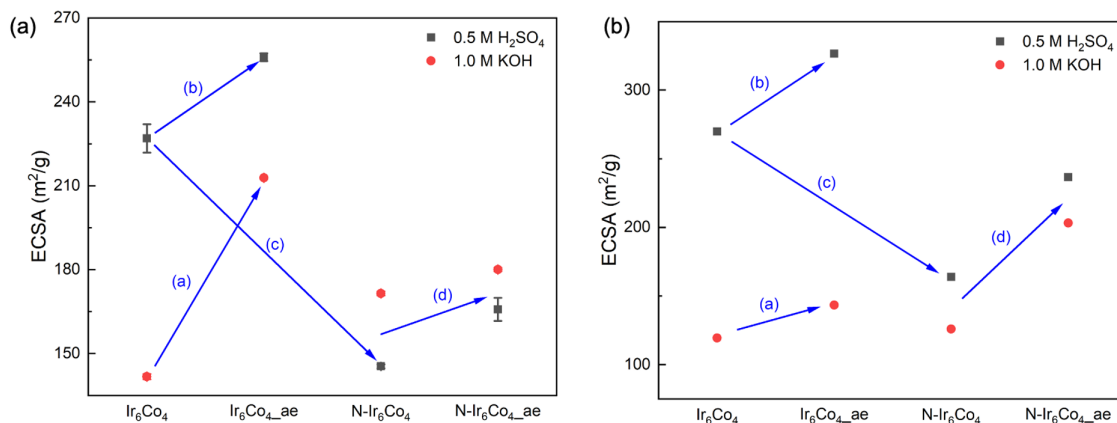


Figure 6.26: Comparison of electrochemically active surface areas (ECSA) obtained in acidic and alkaline media using (a) CV method and (B) EIS method for Ir_6Co_4 samples subjected to different conditions.

6.6 Catalyst Stability Under Half-Cell and Full-Cell Conditions

A critical aspect in catalyst development is the stability of the material, especially at highly oxidizing conditions. In this work, stability was investigated in both half-cell and full-cell tests. For the half-cell conditions, 2,000 potential cycles were performed in the range of 0.4 V to 1.4 V and the LSV performance are collected before and after the stability testing. In the case of full-cell condition, a constant current density of 50 mA/cm^2 was held for 100 hours and the cell voltage was tracked.

The stability test in the half-cell condition shows that the highest degradation occurred in Ir black for both acidic and alkaline media, shown in Figure 6.27. In acidic media, the synthesized catalysts with high Ir content, IrO_2 and Ir_8Co_2 , has an improved activity after the potential cycling. This has been observed in other works¹⁵⁸ as well where an improved activity occurs after the potential cycling, possibly due to the increased surface area. However, as the Co content increases, the stability of the material also decreases. In the alkaline media, the same trend is observed with decreasing catalyst stability as Co content increases but instead of

improved performance, Ir-rich catalysts also suffered from activity reduction. In all synthesized samples, alkaline media degradation seems to be higher than in acidic media, except for Ir_2Co_8 where a comparable degradation is observed in both pH conditions.

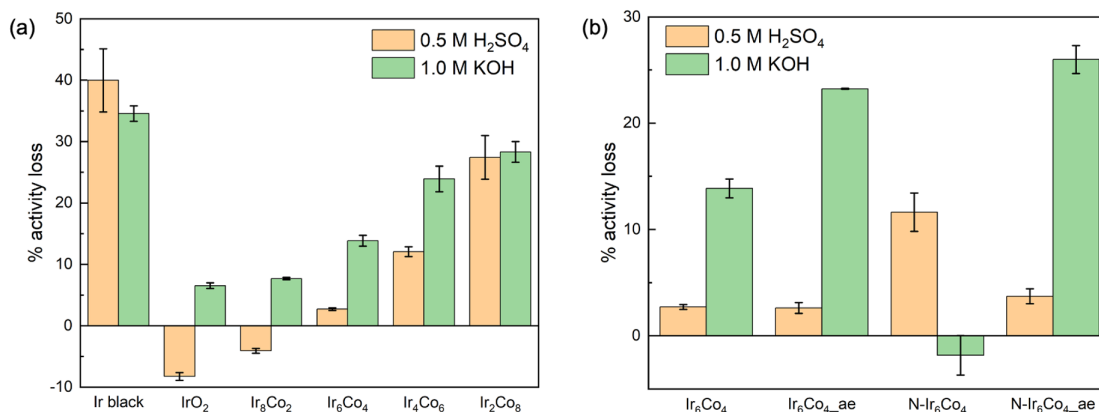


Figure 6.27: Stability of the catalyst tracked as the change in the area of the LSV curve after performing 2,000 CV cycles between 0.4 to 1.4 V for (a) samples with different Ir/Co ratios and (b) Ir_6Co_4 samples prepared with different conditions.

In evaluating the effect of acid etching, there is no significant difference on catalyst stability comparing Ir_6Co_4 and Ir_6Co_4 _ae but in alkaline media, the Ir_6Co_4 _ae sample obtained a much higher degradation rate than Ir_6Co_4 as represented in Figure 6.27b. Without the surfactant, the degradation in acidic media is much higher for N- Ir_6Co_4 than that of Ir_6Co_4 . But this trend is reversed for N- Ir_6Co_4 in the alkaline media where an enhanced activity was found. After acid etching, a different response was obtained. For N- Ir_6Co_4 _ae, the acid stability was improved, comparable to N- Ir_6Co_4 but the alkaline degradation is the worst, with 26% activity loss among the four samples compared in Figure 6.26b.

A scaled-up and longer degradation study was conducted in full-cell conditions with similar electrolytes, 0.5 M H_2SO_4 and 1.0 M KOH for acidic and alkaline media, respectively. The same electrode conditions were used as described in Chapter 5. Due to time constraints, only selected catalysts were tested to understand the trend in stability. In Figure 6.28a and Figure 6.28b, it is obvious that the degradation in the catalyst in terms of increasing cell voltage overtime is more drastic in the alkaline media than in acidic media, which agrees with the results obtained in half-cell test conditions. For acid-etched samples in Figure 6.28c, the Co-rich Ir_2Co_8 _ae obtained the highest degradation in cell voltage with 4.14% increase in the acidic media. However, in the alkaline media, the Ir-rich material Ir_{82} _ae had the

highest voltage change with 20% increase. Regardless, the trend is still consistent that alkaline degradation results to much higher increase in cell voltage.

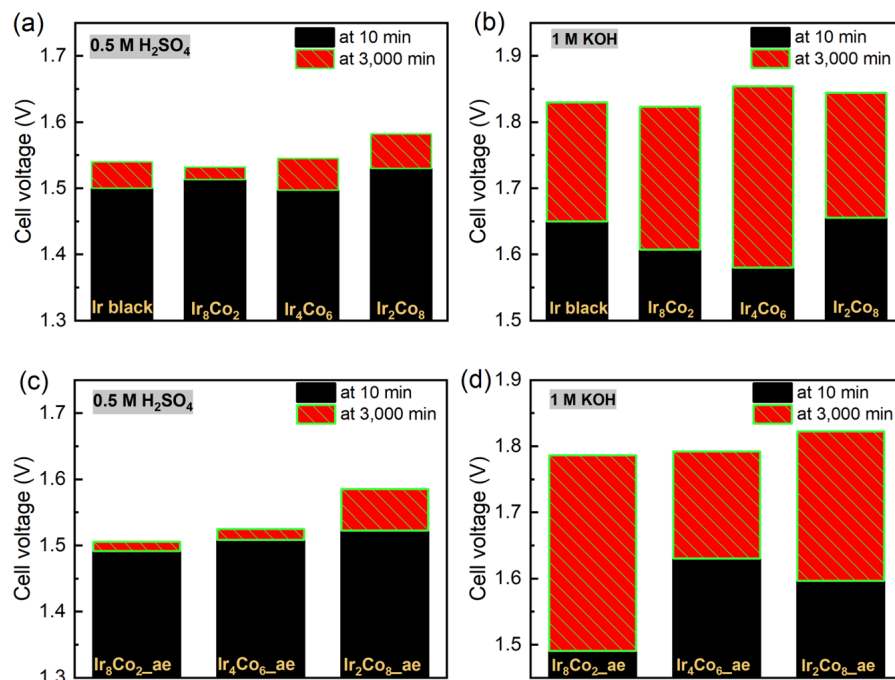


Figure 6.28: Full-cell stability tests in (a,c) 0.5 M H_2SO_4 and (b,d) 1.0 M KOH at a fixed current density of $50 \text{ mA}/\text{cm}^2$ for synthesized Ir-Co catalysts and acid etched counterparts.

The full-cell set-up allows the collection of electrolytes after the test and detection of dissolved metals using ICP-MS, as shown in Figure 6.28. Overall, the consistently high degradation of cell voltage in the alkaline media can be explained by the high dissolution of Ir from the catalyst, depicted in Figure 6.29a and Figure 6.29c. The high Ir dissolution can also explain the trend found in the half-cell tests in Figure 6.28. Similarly, it has been reported in earlier studies [195] that Ir tend to be less stable in the alkaline media than in acidic media. Ir black tends to have the highest Ir dissolution in both acidic and alkaline media, suggesting that the Ir chemical state might play a role in the dissolution behavior. For Co dissolution, it can only be detected in the acidic media and not in alkaline media, shown in Figure 6.29b and Figure 6.29d. The behavior of Co in both acidic and alkaline media can be explained from the Pourbaix diagram, as cited in Chapter 5.

In both non-acid etched and acid-etched samples, the degree of Co dissolution increases with increasing Co content, demonstrated in Figure 6.28b and 6.28d. Also,

for the acid etched $\text{Ir}_2\text{Co}_8\text{-ae}$, the high Ir dissolution observed in Figure 6.29c can be tied up to the high Co dissolution for the same sample in Figure 6.29d. However, this trend is reversed in the alkaline media where $\text{Ir}_8\text{Co}_2\text{-ae}$ has the highest Ir dissolution coinciding with the increase in cell voltage illustrated in Figure 6.29d. In general, acid-etched samples have much higher dissolution in both acidic and alkaline media compared to non-acid etched counterparts.

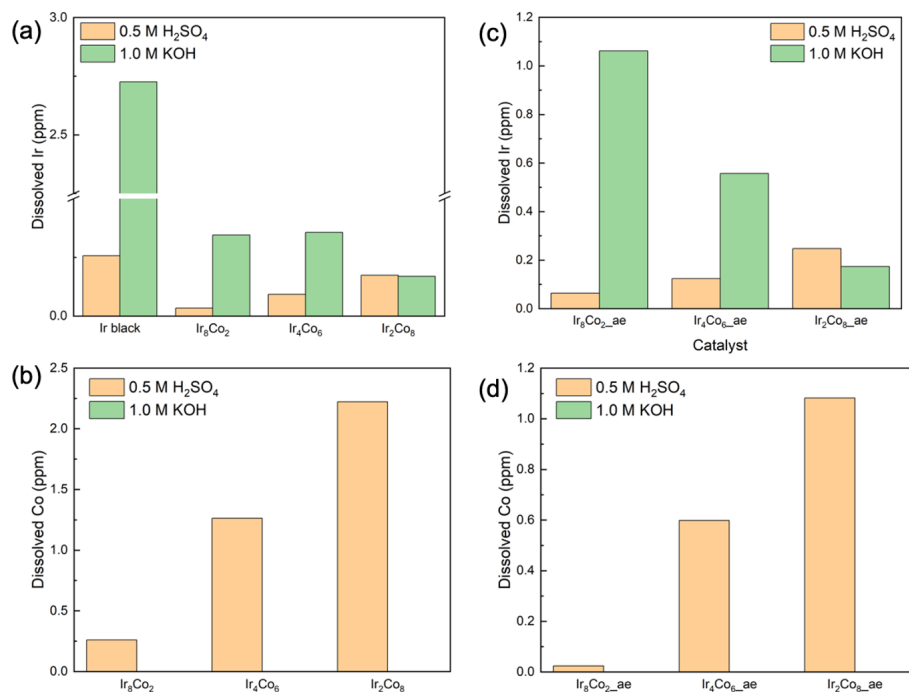


Figure 6.29: Dissolved metals in the electrolyte after the full cell tests for (a,c) Ir and (b,d) Co in both 0.5 M H₂SO₄ and 1.0 M KOH.

6.7 Possible Influence of Iridium Oxidation State on OER Activity

It is highly debated in the literature whether the Ir oxidation state is a critical parameter for OER activity. Some works^{110,191} suggest that an Ir³⁺ rich surface is beneficial, forming Ir(OOH), while others claim that an Ir⁴⁺ surface is more preferred¹⁹⁰. On one hand, another paper⁹⁸ concludes that the Ir oxidation state is not a relevant parameter to determine OER activity since all Ir catalyst, regardless of the initial oxidation states attain a similar Ir oxidation state during OER, which is much higher than Ir⁴⁺.

Here, the Ir *4f* XPS spectra for different catalysts are deconvoluted into three major oxidation states, namely Ir⁰, Ir³⁺ and Ir⁴⁺. The deconvoluted peaks are shown

in Figure 6.30 for the different Ir-Co ratio study and Figure 6.31 for understanding the effects of acid etching and surfactant. The areas under these individual peaks are then converted to relative amounts in Figure 6.32. For Ir black on the surface, it is dominated by Ir^0 at around 56% and some oxidized Ir at smaller quantities. In the pure IrO_2 synthesized catalyst, a comparable amount of Ir^{4+} and Ir^{3+} exists at around 55% and 45%, respectively.

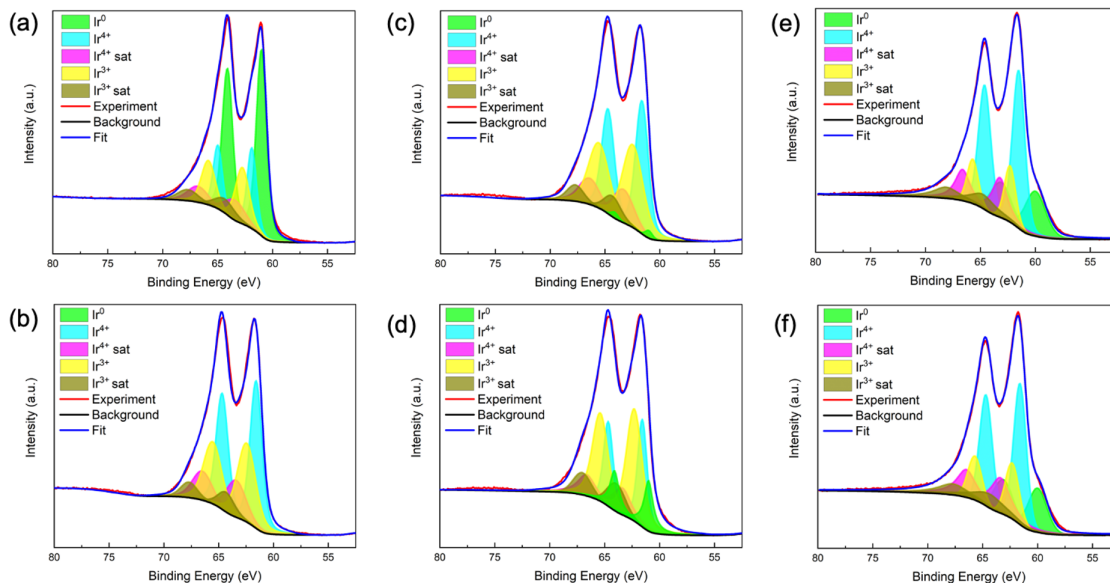


Figure 6.30: Deconvolution of Ir $4f$ XPS peaks into three Ir chemical states: Ir^0 , Ir^{3+} and Ir^{4+} . The analysis was performed for (a) Ir black, (b) IrO_2 , (c) Ir_{82} , (d) Ir_6Co_4 , (e) Ir_4Co_6 and (f) Ir_2Co_8 .

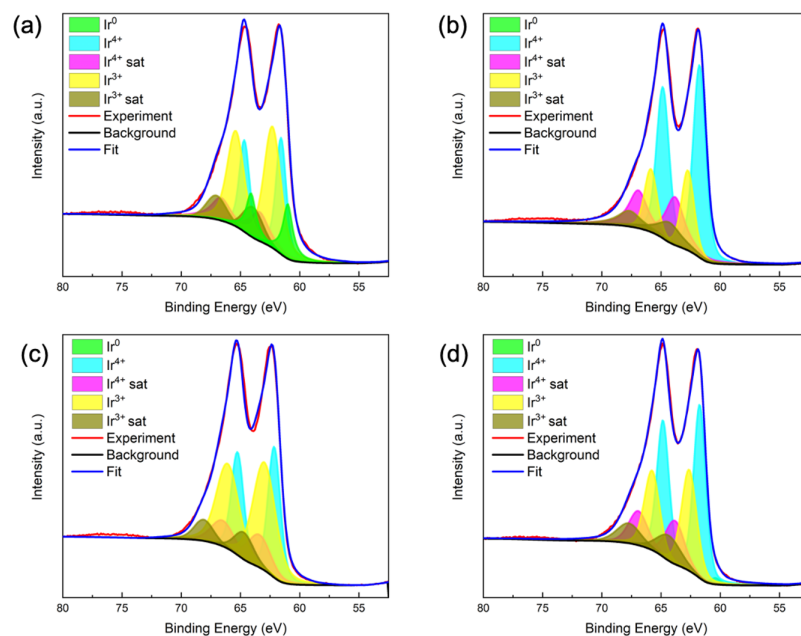


Figure 6.31: Deconvolution of Ir $4f$ XPS peaks into three Ir chemical states: Ir^0 , Ir^{3+} and Ir^{4+} . The analysis was performed for (a) Ir_6Co_4 , (b) Ir_6Co_4 -ae, (c) N- Ir_6Co_4 , and (d) N- Ir_6Co_4 -ae.

Upon the addition of Co in the material, a metallic Ir^0 begins to form, and its quantity increases with more Co concentration. Coinciding this increase in metallic composition is the preference for Ir^{4+} as well over Ir^{3+} . With Ir_6Co_4 , the amount of Ir^{3+} on the surface is much higher at 52% compared to Ir^0 at 17% and Ir^{4+} at 31%. From the CV peaks for $\text{Ir}^{3+}/\text{Ir}^{4+}$ redox peak in Figure 6.12a, a correlation can be drawn from its Ir^{3+} surface composition.

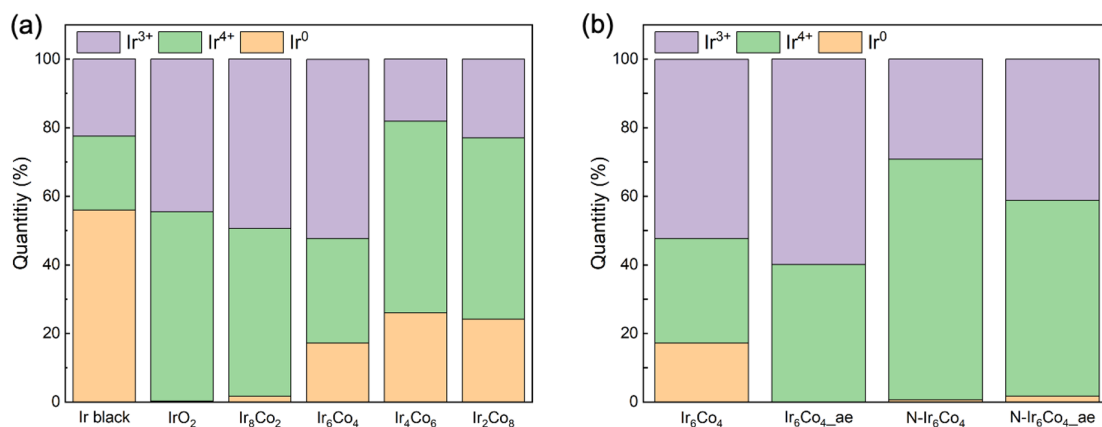


Figure 6.32: Quantification of the different Ir chemical states for samples with (a) different Ir/Co molar ratio and (b) Ir₆Co₄ samples prepared under different conditions.

The formation of the of Ir⁰ is also confirmed using energy electron loss spectroscopy (EELS). Willinger et al. [111] established the linear relationship between the energy shift in the second derivative of the Ir O_{2,3} edge and the oxidation state of the material. The shift in the maxima of the EELS plot in Figure 6.33 suggest the differences in the oxidation states of the materials being probed. The standard materials, IrCl₃ and calcined IrO_x-C, served as reference for Ir³⁺ and Ir⁴⁺, respectively. The peak for Ir₈₂ falls between Ir³⁺ and Ir⁴⁺, but leans closer to the Ir⁴⁺ peak, suggesting a higher fraction of Ir⁴⁺ in the sample. However, for Ir₆Co₄, the peak shifts further to the left of Ir³⁺ reference and Ir₂Co₈ shifts even further. These peak shifts for Ir₆Co₄ and Ir₂Co₈ supports that Ir⁰ is formed as more Co is added in the material.

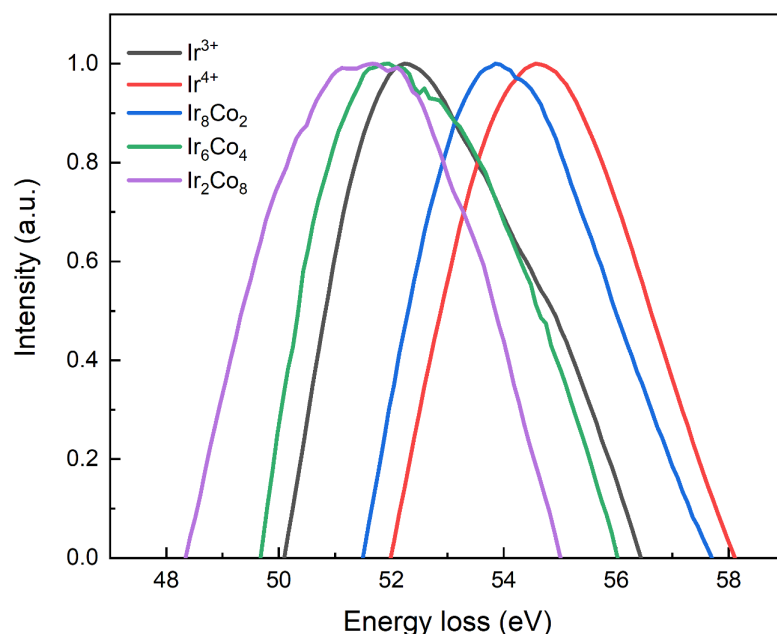


Figure 6.33: Second derivative EELS spectra of Ir samples from the Ir O_{2,3} edge. Peak shifts correlate with the oxidation state, as indicated by the reference materials IrCl₃ for Ir³⁺ and calcined IrOx_C for Ir⁴⁺.

To understand how the Ir⁰ formation is driven by the addition of Co in the material, the oxidation states of Co in the samples were also assessed using XPS. Figure 6.34a shows how the phase fractions of Co change as a function of Ir/Co ratio and the quantification is presented in Table 6.7. As more Co is added in the sample, the preferred phase is Co₃O₄ with 86.61% in Ir₂Co₈, which agrees with the well-defined XRD peaks for the Co₃O₄ pattern in Ir₂Co₈. However, with less Co such as in Ir₈, the Co₃O₄ phase reduced to 47.44% but the amount of Co⁰ and CoO both increased. The formation of Co₃O₄ comes from the conversion of a Co²⁺ precursor to a mixed valency of Co²⁺ and Co³⁺. This oxidation reaction possibly pairs with the reduction of an Ir⁴⁺ precursor to Ir⁰. Thus, as more Co is added, formation metallic Ir is promoted.

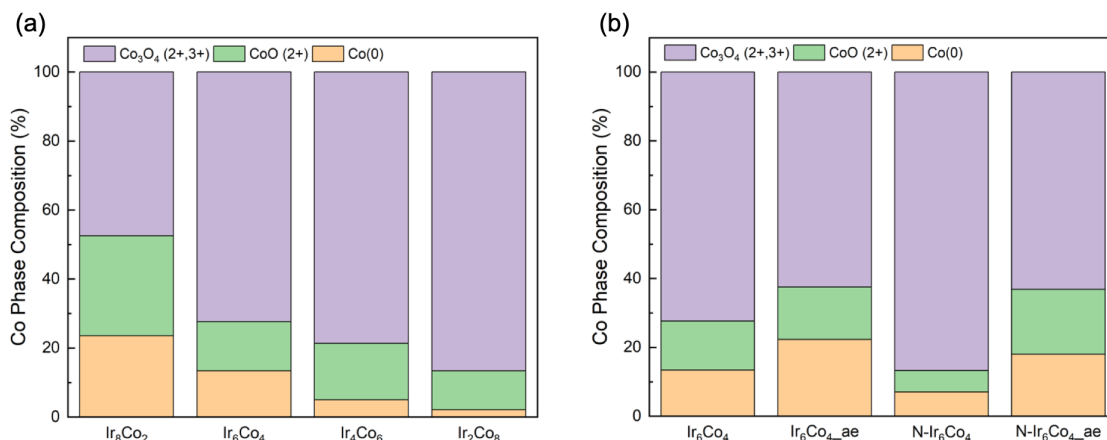


Figure 6.34: Quantification of the different Co phases for samples with (a) different Ir/Co molar ratio and (b) Ir_6Co_4 samples prepared under different conditions.

Table 6.7: Relative fractions of Co phases determined from XPS as a function of Ir:Co ratios.

Sample	Co(0)	CoO	Co ₃ O ₄
Ir_2Co_8	2.16%	11.23%	86.61%
Ir_4Co_6	4.98%	16.40%	78.62%
Ir_6Co_4	13.37%	14.28%	72.35%
Ir_8Co_2	23.52 %	29.04 %	47.44%

Table 6.8: Relative fractions of Co phases from XPS as influenced by the presence of surfactant in the synthesis and acid etching process.

Sample	Co(0)	CoO	Co ₃ O ₄
Ir_6Co_4	13.37%	14.28%	72.35%
N- Ir_6Co_4	7.03%	6.24%	86.74%
Ir_6Co_4 _ae	22.28%	15.25%	62.46%
N- Ir_6Co_4 _ae	18.01%	18.85%	63.14%

Meanwhile, without the surfactant, N- Ir_6Co_4 has a much lower Ir^0 content compared to Ir_6Co_4 but has a much higher Ir^{4+} over Ir^{3+} fraction. The difference in Ir^{3+} surface composition between Ir_6Co_4 and N- Ir_6Co_4 is well observed in the acidic media CV in Figure 6.24a. The Co phase fractions are also influenced by the presence of the surfactant. In Figure 6.34b and Table 6.8, there is much higher

Co_3O_4 phase formed at 86.74% for N- Ir_6Co_4 against 72.35% for Ir_6Co_4 . A lower Co^0 phase was also found in N- Ir_6Co_4 . With both Ir^0 and Co^0 reduced in N- Ir_6Co_4 , without the surfactant the formation of oxide phases is preferred for both Ir and Co and the dependence of their oxidation states are not clearly observed. From the chemical maps in Figure 6.17 and Figure 6.18, the strong segregation between Ir and Co phases hinders metallic formation of both Ir^0 and Co^0 .

For the effect of acid etching on Ir_6Co_4 , the amount of Ir^0 significantly reduced to undetectable amount in Ir_6Co_4 -ae but with an increase in Ir^{3+} surface concentration. After performing acid etching, N- Ir_6Co_4 -ae obtained an increase in Ir^{3+} concentration but also enhanced the concentration of Ir^0 . This is probably due to some metallic Ir^0 being exposed when Ir and Co are released from the material. As for Co oxidation phase, both with and without surfactant had an increase amount of Co^0 and CoO but a decreased amount of Co_3O_4 after acid etching. The Co_3O_4 phase can be easily removed by the acid etching process while leaving the more stable and resistant Co^0 and CoO phases.

In general, the high OER activity is correlated to a higher fraction of Ir^{3+} over Ir^{4+} , especially in the in acidic media where the overpotential is reduced for catalysts with high Ir^{3+} concentration, e.g., Ir_8Co_2 and Ir_6Co_4 . Similarly, without the surfactant, the overpotential increased for N- Ir_6Co_4 , which has a much lower Ir^{3+} surface concentration than Ir_6Co_4 . The influence of Ir^{3+} can also be related to the fact that Tafel slopes of all catalyst are almost comparable in the acidic media, indicating that the same OER reaction mechanism holds for all of them.

However, there is no clear evidence in the alkaline media whether Ir^{3+} has an influence since Ir black is also one of the best catalysts, where Ir^{3+} surface concentration is not dominating. This might be due to the changing Tafel slopes with different catalysts and that the OER reaction mechanism adapts to different surface chemistry, with some proceeding at much faster rate not necessarily dependent on high Ir^{3+} concentration.

6.8 Conclusions

The synthesized Ir-Co catalyst using the modified Adam's fusion method was further studied to investigate the effects of different material processing conditions, in particular the effect of Ir-Co molar ratio, surfactant, and acid etching. A pure IrO_2 catalyst was also prepared along with a commercial Ir black as baselines. For Ir-rich samples, the IrO_2 (101) peak from XRD is the only main peak visible. As more Co is added to the material, Co_3O_4 (311) peak becomes more visible until most of Co_3O_4 peaks appear in Ir_2Co_8 . The proper control of the Ir and Co content in the sample is confirmed by the ICP-MS results, however, an Ir-enriched surface for all samples is suggested by XPS data. Chemical mapping from both STEM-EDS and

STEM-EELS allows the visualization of the distribution of Ir and Co. In terms of their electrochemical performance, Ir-Co samples have much higher mass activities in the acidic media compared to pure Ir samples, IrO₂ and Ir black. This signifies the advantage of adding Co in the material. With overpotential at 10 mA/cm² and total resistance from charge transfer and diffusion/adsorption of intermediates ($R_{ct} + R_1$), Ir₆Co₄ demonstrates the best possible option in both acidic and alkaline media for OER. Hence, Ir₆Co₄ was further analyzed to study the effects of surfactant and acid etching on this material.

The presence of surfactant in Ir₆Co₄ allows better interaction between Ir and Co atoms, with less segregation compared to the non-surfactant sample, N-Ir₆Co₄ as illustrated in XRD, XPS, and chemical maps obtained from STEM-EDS and STEM-EELS. In N-Ir₆Co₄, a Co core and Ir shell were formed and in terms of particle morphology, heterogeneous structures are found from TEM imaging for N-Ir₆Co₄ with rod-shaped structures near the edge which are not found in Ir₆Co₄. These extended might also explain the relatively higher BET surface-area of N-Ir₆Co₄ at 230 m²/g compared to Ir₆Co₄ at 186 m²/g.

After subjecting the samples to acid etching, the presence of Co in Ir₆Co₄ almost diminished, as detected from both XPS and ICP-MS. However, acid etching has no significant effect for the bulk composition of N-Ir₆Co₄ from ICP-MS but XPS shows a reduced Ir composition on the surface. In any case, acid etching resulted in an increased surface area for both Ir₆Co₄ and N-Ir₆Co₄. In terms of their OER activity, the surfactant can boost the mass activity especially in the alkaline media. On the other hand, acid etching leads to improvement for both with and without surfactant but has much drastic effect on N-Ir₆Co₄. This trend agrees well with other metrics such as the overpotential at 10 mA/cm² and the $R_{ct} + R_1$ from EIS. To sum up, surfactant promotes a better distribution and interaction of Ir and Co and is further improved by acid etching, although most Co is leached out from Ir₆Co₄.

Aside from OER activity, the stability of the samples is also critical, thus was tested in this work using both half-cell and full-cell conditions. In the half-cell test, the stability of the catalyst is evaluated using 2,000 potential cycles between 0.4 to 1.4 V. The stability decreases as more Co is added to the sample for the Ir-Co alloy. In the acidic media, Ir-rich samples IrO₂ and Ir₈₂ tend to have an improved activity possibly due to the creation of new surface area induced by the cycling condition. The non-surfactant N-Ir₆Co₄ suffered a much higher activity loss in the acidic media than Ir₆Co₄ but had an activity enhancement in the alkaline media. In either catalyst, acid etching caused a much higher activity loss in both Ir₆Co₄ and N-Ir₆Co₄.

In the full-cell tests performed for 100 hours at 50 mA/cm², the alkaline media caused a much higher increase in the overpotential. This aligns well with the

half-cell results wherein higher activity degradation is observed in the alkaline media for most catalysts. Using ICP-MS, a high amount of Ir dissolved in the electrolyte was detected in the alkaline media which explains the high activity degradation. On the other hand, the amount of Co in the alkaline media is below the detection limit of the instrument but significant Co dissolution exists in the acidic media. This observation agrees with the established stability behavior of Co in the Pourbaix diagrams.

The oxidation state of Ir which has been debated in the literature as a critical parameter for OER activity was also studied here. Using XPS, Ir $4f$ peaks were deconvoluted to quantify Ir⁰, Ir³⁺ and Ir⁴⁺ surface concentrations. The surface concentration of Ir³⁺ increases from IrO₂ to Ir₆Co₄ but as more Co is added to the material, the Ir³⁺ quantity decreases followed by an increase in both Ir⁴⁺ and Ir⁰. Without the surfactant, there is also a preference to form more Ir⁴⁺ on the surface. When surfactant and non-surfactant catalysts were subjected to acid etching, the concentration of Ir³⁺ also increased. The catalysts with high Ir³⁺ concentration achieve a much lower overpotential in the acidic media, suggesting a positive correlation. However, this trend is not clear in the alkaline media. This might be related to the Tafel slopes where in acidic media, it remains almost similar for all catalysts at around 42-45 mV/dec, indicating a similar OER mechanism where the role of Ir³⁺ is critical. In the alkaline media, the Tafel slope vary significantly in all catalysts, which becomes higher as more Co is added into the material. A high Tafel slope was also obtained without the surfactant in alkaline media which translates to lower OER activity. The critical role and presence of Ir³⁺ in the catalysts can be confirmed from the CV curves, where the peak current density in acidic media for Ir³⁺/Ir⁴⁺ redox transition is much higher for Ir³⁺-rich catalysts. However, the trend in Ir³⁺/Ir⁴⁺ redox is not visible in the alkaline media.

In this work, it has been concluded that surface area is not the most critical predictor of catalyst activity, as well as a high Ir surface content comparing both N-Ir₆Co₄ and Ir₆Co₄. The results from this study support a possible influence of Ir³⁺ oxidation state in the acidic media towards a better OER activity. Overall, alkaline OER activities are much higher than in acidic media, but this major difference was not explored in this work since there are several differences in the experimental conditions, such as pH and electrolyte concentration, that can alter the surface chemistry of the catalyst and in turn dictate the OER mechanism. Nevertheless, this study provides an alternative catalyst design using Ir and Co and enhance the efficiency of future water electrolyzers.

6.9 Appendix

6.9.1 XPS Fitting Details

The fitting parameters used to deconvolute the Ir $4f$ spectra are shown in Table 6.9 with an asymmetric line shape detailed by Povia et al. [108] and Freakley et al. [177]. Relaxation of the constraints in the binding energy (BE) and full width half maximum (FWHM) are applied within the range specified in the table below. Height ratios for the Ir $4f7/2$ and Ir $4f5/2$ were constrained by the software database at 0.787 while main peak to satellite was set at 4:1 height ratio. Convergence was achieved with a minimum residual as determined by the Avantage XPS software.

Table 6.9: XPS fitting parameters for the deconvolution of Ir $4f$ spectra.

Reference	Peak	Binding Energy (eV)	Height Ratio	FWHM (eV)
A	Ir ⁰ $4f7/2$	60.5:61.00		0.5:1
B	Ir ⁰ $4f5/2$	A + 3.20 (+0.2 - 0.1)	A*0.787	A*1
C	Ir ⁴⁺ $4f7/2$	61.5:62.20		1:2
D	Ir ⁴⁺ $4f5/2$	C + 3.20 (+0.2 - 0.1)	C*0.787	C*1
E	Ir ⁴⁺ $4f7/2$ (satellite)	63.00:63.40	C*0.25	1.94:2.74
F	Ir ⁴⁺ $4f5/2$ (satellite)	E + 3.20 (+0.2 - 0.1)	E*0.787	E*1
G	Ir ³⁺ $4f7/2$	62.30:63.00		1:2
H	Ir ³⁺ $4f5/2$	G + 3.20 (+0.2 - 0.1)	G*0.787	G*1
I	Ir ³⁺ $4f7/2$ (satellite)	63.90:64.60	G*0.25	1.94:2.74
J	Ir ³⁺ $4f5/2$ (satellite)	I + 3.20 (+0.2 - 0.1)	I*0.787	0.5:3.5

For the Co $2p$ XPS, the constraints established by Biesinger et al. [196] identified five different phases for Co. However, in this study only the major Co phases were considered that would clearly indicate the oxidation phase changes from Co⁰ to a Co²⁺ in the form of CoO and to a mixed valency of Co²⁺ and Co³⁺ in Co₃O₄, shown in Table 6.10. Similar to fitting the Ir $4f$ spectra, relaxations in the peak BE and FWHM were applied to allow some flexibility in the fitting until convergence has been reached.

Table 6.10: XPS fitting parameters for the deconvolution of Co $2p$ spectra.

Reference	Peak	Binding Energy (eV)	FWHM (eV)
A	Co ₃ O ₄	779.30 : 779.90	1.11: 2.11
B	Co ₃ O ₄	780.60 : 781.20	0.82 : 1.82
C	Co ₃ O ₄	781.90: 782.50	1.38 : 2.38
D	Co ₃ O ₄	784.90 :785.50	3.64 : 4.64
E	Co ₃ O ₄	789.20 : 789.80	2.49 : 3.49
F	Co ⁰	777.80 : 778.40	0.55 : 1.55
G	Co ⁰	780.80 : 781.40	2.56 : 1.55
H	Co ⁰	782.80 : 783.40	2.2 : 3.2
I	CoO	779.90 : 780.10	2.5 : 3.5
J	CoO	782.00 : 782.20	1.8 : 2.8
K	CoO	785.40 : 785.60	2.5 : 3.5
L	CoO	786.40 : 786.60	3.7 : 4.7

6.9.2 Error Propagation for Oxidation State from XPS

To assess the error involved in estimating the oxidation states from XPS, three data sets were compared for two samples, Ir₆Co₄ in Table 6.11 and Ir₆Co₄-ae in Table Table 6.12, and the standard deviation was calculated. However, the data sets were taken a year a part and the sample could have changed. Nevertheless, oxidation states with larger fractions seem consistent, and the overall trend can still be captured well.

Table 6.11: Comparison of the Ir fractions obtained for three data sets from Ir₆Co₄.

Data Collected	Ir ⁰ (%)	Ir ³⁺ (%)	Ir ⁴⁺ (%)
2020_1016	17.23	52.33	30.44
2021_1110_P1	2.6	60.61	36.79
2021_1110_P2	1.52	70.35	28.13
Average	7.11 ± 7.16	61.10 ± 7.36	31.79 ± 3.67

A relative standard deviation of around 10–12% for the major components were obtained. Caution should be taken for oxidation states comprising less than 10% in the quantification. From this analysis, it is assumed that variations in the measurement would arise from the instrument and a 10–12% error for oxidation states comprising more than 10% in the material can be assumed.

Table 6.12: Comparison of the Ir fractions obtained for three data sets from Ir₆Co₄.ae.

Data Collected	Ir⁰ (%)	Ir³⁺ (%)	Ir⁴⁺ (%)
2020_1016	0.00	59.91	40.09
2021_1110_P1	0.00	56.05	43.95
2021_1110_P2	0.53	46.18	53.32
Average	0.18 ± 0.25	54.05 ± 5.78	45.79 ± 5.56

Chapter 7

CONCLUSIONS

The climate crisis that has been impacting the lives of many people around the globe demands new technologies that can curtail our greenhouse gas emissions. Among these options are fuel cells, that can generate electricity without any harmful gases if hydrogen is used as a fuel, and water electrolyzers, which can generate green hydrogen if coupled with renewable wind or solar energy. However, technical advancements and fundamental understanding of some of the phenomena happening in these devices are still lacking. In this dissertation, the degradation mechanism of the platinum-carbon catalyst (Pt/C) used in fuel cells is studied in both acidic and alkaline environments and the results are presented in Chapter 4. On the other hand, the development of a less expensive electrocatalyst for water electrolyzers was pursued to reduce the use of expensive and rare metal, iridium, by alloying with cobalt. Preliminary results as well as the effect of material processing are presented in Chapters 5 and 6, respectively.

For the degradation study on fuel cells catalyst, deactivation of some surface sites occurs when carbon was corroded with high potential cycling conditions in acidic environment. This protocol leads to the generation of carbon surface oxides predominantly O-C=O functional groups, which can enhance the wettability of the carbon support, but the consequence is poisoning of the Pt active sites when the same functional groups adsorb onto the catalyst surface and impede the ORR activity. The carbon corrosion mechanism can also influence the mobility of Pt. In the alkaline media, larger chain-like Pt agglomerations are formed. Meanwhile, the presence of O-C=O in high-potential cycling samples in acid strengthened the interaction and bonding between the Pt nanoparticles and the carbon support. These findings can help in the development of more durable ORR catalysts, especially for heavy-duty transport where fuel cells have a niche market.

The other half of this dissertation focused on OER catalyst development using a surfactant-assisted Adam's fusion method developed in-house. It has been found that an optimal ratio between Ir and Co is with Ir₆Co₄. The benefit of adding surfactant was highlighted, where it promotes a much better interaction and distribution of Ir and Co metals. Without surfactant, the segregation between Ir and Co is much stronger and although it led to a much higher Ir concentration on

the surface, the OER performance is inferior. Acid etching was also implemented to enhance the surface area and activity, where majority of Co leached out in the surfactant-assisted Ir_6Co_4 catalyst. By analyzing the surface chemical states of Ir using XPS, a correlation is found between the Ir^{3+} concentration and OER activity, especially in the acidic media. However, the stability remains a concern for the synthesized catalyst especially in the alkaline media where significant Ir dissolution occurs.

The works summarized in these papers, although conducted at the fundamental and laboratory conditions, can still provide new directions for fuel cell and electrolyzer development. Nevertheless, the significance of these electrochemical technologies as part of the climate solution are emphasized. Fuel cells and electrolyzers have the potential to transform our energy system, leveraging the declining cost of wind and solar energies. With the advancement in clean technology and collaboration between government and industry, we can fully transition to a decarbonized society and achieve net-zero emission by 2050.

Chapter 8

FUTURE WORKS

In this work, the analysis of precious-metal catalysts for ORR and OER used in fuel cells and water electrolyzers has been successfully studied in the half-cell environment. But, the development of these technologies rely on the scaling up of the laboratory investigations. Thus, it is desirable that component integration with the ionomer and catalyst should be well understood. The interaction of these two materials controls the final structure of the catalyst layer, which in turn influences the performance and durability of the device. In the device level, the polymer electrolyte membrane technologies are more mature, but a lot of research opportunity can still be done with alkaline membrane counterparts.

In terms of the fundamental study, modeling approach based on first principles can guide the catalyst discovery and lead to more understanding of reaction mechanisms and degradation modes of the catalyst. Advanced characterization, especially *in situ* methods at the nanoscale, are also essential to be able to identify the active sites and degradation behaviors. With both computational and characterization tools, the material synthesis approach can be tailored to create a more durable and efficient electrocatalysts. To accurately predict the performance of the new materials, multiphysics simulation should also be improved with the right input parameters at the desired length scale.

Aside from fuel cells and electrolyzers, there are also other emerging electrochemical devices that can be used to combat the climate crisis. One that our group has worked on before is the urea oxidation reaction (UOR) where instead of simply using water, urea or urea-rich waste streams like human urine can be used. In theory, UOR has a lower reversible potential, thus less energy needed for the reaction to proceed but the challenge is still finding the right catalyst for this application. UOR-assisted hydrogen production could be a promising technology in regions where urea contamination from excessive fertilizer use happens. Another application of electrochemistry in the nitrogen cycle is the production of ammonia through nitrogen reduction reaction as an alternative to the Haber-Bosch process. Lastly, carbon dioxide reduction to valuable chemicals is also a viable research path where electrochemical devices can be beneficial to the environment. However, the selectivity is crucial to be able to direct the conversion of CO₂ to desired products.

All these promising technologies are still in the early stages of research and development. But policies and government funding are continuously evolving in response to the urgency of the climate crisis. In the coming decades, as soon as fuel cells and water electrolyzers are fully commercialized with wide-scale deployment, these emerging electrochemical technologies can follow the path and further strengthen the vision of a decarbonized society.

Bibliography

- [1] *The Warming Effects of the Industrial Revolution - Global Temperatures*. URL: <https://www.climate-policy-watcher.org/global-temperatures/the-warming-effects-of-the-industrial-revolution.html> (visited on 04/15/2022).
- [2] *The Keeling Curve*. URL: <https://keelingcurve.ucsd.edu/> (visited on 04/14/2022).
- [3] *Scientific Consensus — Facts - Climate Change: Vital Signs of the Planet*. URL: <https://climate.nasa.gov/scientific-consensus/> (visited on 04/15/2022).
- [4] *Secretary-General Calls Latest IPCC Climate Report ‘Code Red for Humanity’, Stressing ‘Irrefutable’ Evidence of Human Influence — Meetings Coverage and Press Releases*. URL: <https://www.un.org/press/en/2021/sgsm20847.doc.htm> (visited on 04/15/2022).
- [5] *The Paris Agreement — UNFCCC*. URL: <https://unfccc.int/process-and-meetings/the-paris-agreement/the-paris-agreement> (visited on 11/06/2019).
- [6] Matthew R Smith and Samuel S Myers. “Impact of anthropogenic CO₂ emissions on global human nutrition”. In: *Nature Climate Change* 8.9 (2018), pp. 834–839.
- [7] Detlef P Van Vuuren et al. “The representative concentration pathways: an overview”. In: *Climatic change* 109.1 (2011), pp. 5–31.
- [8] *Rising CO₂ levels could push ‘hundreds of millions’ into malnutrition by 2050*. URL: <https://www.carbonbrief.org/rising-co2-levels-could-push-hundreds-of-millions-into-malnutrition-by-2050> (visited on 04/15/2022).
- [9] *Falling Renewable Power Costs Open Door to Greater Climate Ambition*. URL: <https://www.irena.org/newsroom/pressreleases/2019/May/Falling-Renewable-Power-Costs-Open-Door-to-Greater-Climate-Ambition> (visited on 04/14/2022).
- [10] *Inventory of U.S. Greenhouse Gas Emissions and Sinks — US EPA*. URL: <https://www.epa.gov/ghgemissions/inventory-us-greenhouse-gas-emissions-and-sinks> (visited on 04/15/2022).

- [11] *Transportation and Climate Change*. URL: https://www.biologicaldiversity.org/programs/climate_law_institute/transportation_and_global_warming/ (visited on 04/15/2022).
- [12] *Climate change: Should you fly, drive or take the train? - BBC News*. URL: <https://www.bbc.com/news/science-environment-49349566> (visited on 04/15/2022).
- [13] *Zero carbon by 2050 is possible. Here's what we need to do — World Economic Forum*. URL: <https://www.weforum.org/agenda/2019/09/cutting-emissions-to-net-zero-carbon-possible-what-we-need-to-do/> (visited on 04/14/2022).
- [14] *H2@Scale — Department of Energy*. URL: <https://www.energy.gov/eere/fuelcells/h2scale> (visited on 04/14/2022).
- [15] *Hydrogen Shot — Department of Energy*. URL: <https://www.energy.gov/eere/fuelcells/hydrogen-shot> (visited on 04/15/2022).
- [16] *Fuel Cells — Department of Energy*. URL: <https://www.energy.gov/eere/fuelcells/fuel-cells> (visited on 04/15/2022).
- [17] *What is a Hydrogen Fuel Cell?* URL: <https://www.setra.com/blog/what-is-a-hydrogen-fuel-cell-and-how-does-it-work> (visited on 04/14/2022).
- [18] *Parts of a Fuel Cell — Department of Energy*. URL: <https://www.energy.gov/eere/fuelcells/parts-fuel-cell> (visited on 04/15/2022).
- [19] *Hydrogen Production: Electrolysis — Department of Energy*. URL: <https://www.energy.gov/eere/fuelcells/hydrogen-production-electrolysis> (visited on 04/15/2022).
- [20] *Introduction to Electrolyzers*. URL: <https://www.fuelcellstore.com/blog-section/introduction-to-electrolyzers> (visited on 04/15/2022).
- [21] James Larminie and Andrew Dicks. “Introduction”. In: *Fuel Cell Systems Explained*. Wiley Online Books. West Sussex, England: John Wiley & Sons, Ltd., Dec. 2013, pp. 1–24. ISBN: 9781118878330. DOI: 10.1002/9781118878330.ch1. URL: <https://doi.org/10.1002/9781118878330.ch1> %20http://doi.wiley.com/10.1002/9781118878330.ch1.
- [22] Sharon Thomas and Marcia Zalbowitz. *Fuel cells-green power*. Los Alamos National Laboratory, 1999.
- [23] Ryan O’hayre et al. *Fuel cell fundamentals*. John Wiley & Sons, 2016.

- [24] *Toyota Ushers in the Future with Launch of 'Mirai' Fuel Cell Sedan* — Toyota Motor Corporation Official Global Website. URL: <https://global.toyota/en/detail/4198334/> (visited on 08/29/2019).
- [25] *Southern California Customers Take Delivery of New 2017 Honda Clarity Fuel Cell Sedan - Press Releases - Honda News*. URL: <https://hondanews.com/honda-automobiles/channels/clarity-fuel-cell-press-releases/releases/southern-california-customers-take-delivery-of-new-2017-honda-clarity-fuel-cell-sedan> (visited on 08/29/2019).
- [26] Felix N. Büchi, Thomas J. Schmidt, and Minoru Inaba. *Polymer electrolyte fuel cell durability*. English. New York: Springer, 2009, pp. 1–507. ISBN: 9780387855349. DOI: 10.1007/978-0-387-85536-3.
- [27] Ulrich Eberle, Bernd Müller, and Rittmar Von Helmolt. “Fuel cell electric vehicles and hydrogen infrastructure: status 2012”. In: *Energy & Environmental Science* 5.10 (2012), pp. 8780–8798.
- [28] Oliver Gröger, Hubert A Gasteiger, and Jens-Peter Suchsland. “Electromobility: Batteries or fuel cells?” In: *Journal of The Electrochemical Society* 162.14 (2015), A2605.
- [29] Natalia Macauley et al. “Carbon corrosion in PEM fuel cells and the development of accelerated stress tests”. In: *Journal of The Electrochemical Society* 165.6 (2018), F3148.
- [30] US DOE. *The Fuel Cell Technologies Office Multi-Year Research, Development, and Demonstration Plan*. Tech. rep. Technical report: US Department of Energy, 2016.
- [31] Farhana S Saleh and E Bradley Easton. “Diagnosing degradation within PEM fuel cell catalyst layers using electrochemical impedance spectroscopy”. In: *Journal of the Electrochemical Society* 159.5 (2012), B546.
- [32] Shanna D Knights et al. “Aging mechanisms and lifetime of PEFC and DMFC”. In: *Journal of power sources* 127.1-2 (2004), pp. 127–134.
- [33] Elodie Guilminot et al. “Membrane and active layer degradation upon PEMFC steady-state operation: I. platinum dissolution and redistribution within the MEA”. In: *Journal of The Electrochemical Society* 154.11 (2007), B1106.
- [34] Luis Castanheira et al. “Carbon corrosion in proton-exchange membrane fuel cells: effect of the carbon structure, the degradation protocol, and the gas atmosphere”. In: *Acs Catalysis* 5.4 (2015), pp. 2184–2194.
- [35] Rod Borup et al. “Scientific aspects of polymer electrolyte fuel cell durability and degradation”. In: *Chemical reviews* 107.10 (2007), pp. 3904–3951.

- [36] Y Shao-Horn et al. “Instability of supported platinum nanoparticles in low-temperature fuel cells”. In: *Topics in Catalysis* 46.3-4 (2007), pp. 285–305.
- [37] Robert M Darling and Jeremy P Meyers. “Kinetic model of platinum dissolution in PEM fuel cells”. In: *ECS Proceedings Volumes* 2002.1 (2002), p. 44.
- [38] György Inzelt. “Electrode potentials”. In: *Handbook of reference electrodes*. Springer, 2013, pp. 1–24.
- [39] T Yu Paul et al. “The impact of carbon stability on PEM fuel cell startup and shutdown voltage degradation”. In: *Ecs Transactions* 3.1 (2006), p. 797.
- [40] Wenbin Gu et al. “Start/stop and local H₂ starvation mechanisms of carbon corrosion: model vs. experiment”. In: *ECS transactions* 11.1 (2007), p. 963.
- [41] Paul T Yu et al. “Carbon-support requirements for highly durable fuel cell operation”. In: *Polymer electrolyte fuel cell durability*. Springer, 2009, pp. 29–53.
- [42] Arun Pandey et al. “A carbon corrosion model to evaluate the effect of steady state and transient operation of a polymer electrolyte membrane fuel cell”. In: *Journal of the Electrochemical Society* 160.9 (2013), F972.
- [43] Norimitsu Takeuchi, Emily Jennings, and Thomas F Fuller. “Investigation and modeling of carbon oxidation of Pt/C under dynamic potential condition”. In: *ECS Transactions* 25.1 (2009), p. 1045.
- [44] Jeremy P Meyers and Robert M Darling. “Model of carbon corrosion in PEM fuel cells”. In: *Journal of the Electrochemical Society* 153.8 (2006), A1432.
- [45] Oran Lori and Lior Elbaz. “Advances in ceramic supports for polymer electrolyte fuel cells”. In: *Catalysts* 5.3 (2015), pp. 1445–1464.
- [46] Haifeng Lv and Shichun Mu. “Nano-ceramic support materials for low temperature fuel cell catalysts”. In: *Nanoscale* 6.10 (2014), pp. 5063–5074.
- [47] Yan-Jie Wang, David P Wilkinson, and Jiujun Zhang. “Noncarbon support materials for polymer electrolyte membrane fuel cell electrocatalysts”. In: *Chemical reviews* 111.12 (2011), pp. 7625–7651.
- [48] Bing-Jen Hsieh et al. “Platinum loaded on dual-doped TiO₂ as an active and durable oxygen reduction reaction catalyst”. In: *Npg Asia Materials* 9.7 (2017), e403–e403.
- [49] Abha Bharti and Gouri Cheruvally. “V-doped TiO₂ supported Pt as a promising oxygen reduction reaction catalyst: Synthesis, characterization and in-situ evaluation in proton exchange membrane fuel cell”. In: *Journal of Power Sources* 363 (2017), pp. 413–421.

- [50] Jun-Hyuk Kim et al. “Effects of transition metal doping in Pt/M-TiO₂ (M= V, Cr, and Nb) on oxygen reduction reaction activity”. In: *Journal of Power Sources* 320 (2016), pp. 188–195.
- [51] Noramalina Mansor et al. “Graphitic carbon nitride as a catalyst support in fuel cells and electrolyzers”. In: *Electrochimica Acta* 222 (2016), pp. 44–57.
- [52] Dana Schonvogel et al. “Stability of Pt nanoparticles on alternative carbon supports for oxygen reduction reaction”. In: *Journal of the Electrochemical Society* 164.9 (2017), F995.
- [53] Zeyu Li et al. “Low content Pt nanoparticles anchored on N-doped reduced graphene oxide with high and stable electrocatalytic activity for oxygen reduction reaction”. In: *Scientific reports* 7.1 (2017), pp. 1–9.
- [54] Jiemei Yu et al. “Reduced graphene oxide supported TiO₂ as high performance catalysts for oxygen reduction reaction”. In: *International Journal of Hydrogen Energy* 41.5 (2016), pp. 3436–3445.
- [55] Md Ariful Hoque et al. “Optimization of sulfur-doped graphene as an emerging platinum nanowires support for oxygen reduction reaction”. In: *Nano Energy* 19 (2016), pp. 27–38.
- [56] Lei Du et al. “Advanced catalyst supports for PEM fuel cell cathodes”. In: *Nano Energy* 29 (2016), pp. 314–322.
- [57] Shuaiba Samad et al. “Carbon and non-carbon support materials for platinum-based catalysts in fuel cells”. In: *international journal of hydrogen energy* 43.16 (2018), pp. 7823–7854.
- [58] Philipp Weber et al. “Fundamental insights in degradation mechanisms of Pt/C nanoparticles for the ORR”. In: *ECS Transactions* 86.13 (2018), p. 433.
- [59] Enrico Pizzutilo et al. “On the need of improved accelerated degradation protocols (ADPs): examination of platinum dissolution and carbon corrosion in half-cell tests”. In: *Journal of the electrochemical society* 163.14 (2016), F1510.
- [60] B Merzougui and S Swathirajan. “Rotating disk electrode investigation of fuel cell catalyst degradation due to potential cycling in acid electrode’J”. In: *Electrochem. Soc* 153 ().
- [61] Adam Riese et al. “Accelerated stress testing by rotating disk electrode for carbon corrosion in fuel cell catalyst supports”. In: *Journal of The Electrochemical Society* 162.7 (2015), F783.
- [62] Jan N Schwämmlein et al. “Activity and stability of carbon supported Pt_xY alloys for the ORR determined by RDE and single-cell PEMFC measurements”. In: *Journal of The Electrochemical Society* 165.15 (2018), J3173.

- [63] Yuanliang Zhang et al. “Study of the degradation mechanisms of carbon-supported platinum fuel cells catalyst via different accelerated stress test”. In: *Journal of Power Sources* 273 (2015), pp. 62–69.
- [64] SS Kocha, Y Garsany, and D Myers. “Testing Oxygen Reduction Reaction Activity with the Rotating Disc Electrode Technique”. In: *DOE Webinar* (2013).
- [65] Raghunandan Sharma and Shuang Ma Andersen. “An opinion on catalyst degradation mechanisms during catalyst support focused accelerated stress test (AST) for proton exchange membrane fuel cells (PEMFCs)”. In: *Applied Catalysis B: Environmental* 239 (2018), pp. 636–643.
- [66] SR Dhanushkodi et al. “Carbon corrosion fingerprint development and deconvolution of performance loss according to degradation mechanism in PEM fuel cells”. In: *Journal of Power Sources* 240 (2013), pp. 114–121.
- [67] Luis Castanheira et al. “Carbon corrosion in proton-exchange membrane fuel cells: from model experiments to real-life operation in membrane electrode assemblies”. In: *Acs Catalysis* 4.7 (2014), pp. 2258–2267.
- [68] Clémence Lafforgue et al. “Selected Review of the Degradation of Pt and Pd-based Carbon-supported Electrocatalysts for Alkaline Fuel Cells: Towards Mechanisms of Degradation”. In: *Fuel Cells* 18.3 (2018), pp. 229–238.
- [69] Clémence Lafforgue et al. “Degradation of carbon-supported platinum-group-metal electrocatalysts in alkaline media studied by in situ Fourier transform infrared spectroscopy and identical-location transmission electron microscopy”. In: *ACS Catalysis* 9.6 (2019), pp. 5613–5622.
- [70] Anicet Zadick et al. “Huge instability of Pt/C catalysts in alkaline medium”. In: *Acs Catalysis* 5.8 (2015), pp. 4819–4824.
- [71] Youngmi Yi et al. “Electrochemical corrosion of a glassy carbon electrode”. In: *Catalysis Today* 295 (2017), pp. 32–40.
- [72] Hydrogen Council. “How hydrogen empowers the energy transition”. In: January (2017), p. 28. ISSN: 0018-926X. DOI: 10.1109/TAP.2009.2035997. URL: <http://hydrogencouncil.com/wp-content/uploads/2017/11/Hydrogen-scaling-up-Hydrogen-Council.pdf>.
- [73] Bryan Pivovar, Neha Rustagi, and Sunita Satyapal. “Hydrogen at scale (H2@Scale): key to a clean, economic, and sustainable energy system”. In: *The Electrochemical Society Interface* 27.1 (2018), p. 47.
- [74] IEA. “The Future of Hydrogen: Seizing today’s opportunities”. In: June (2019), p. 203. URL: <https://webstore.iea.org/the-future-of-hydrogen>.

- [75] Jing Gao et al. “Solar water splitting with perovskite/silicon tandem cell and TiC-supported Pt nanocluster electrocatalyst”. In: *Joule* 3.12 (2019), pp. 2930–2941.
- [76] Nien-Chu Lai et al. “A highly active oxygen evolution catalyst for lithium-oxygen batteries enabled by high-surface-energy facets”. In: *Joule* 2.8 (2018), pp. 1511–1521.
- [77] Nathan S Lewis and Daniel G Nocera. “Powering the planet: Chemical challenges in solar energy utilization”. In: *Proceedings of the National Academy of Sciences* 103.43 (2006), pp. 15729–15735.
- [78] Richard L Doyle and Michael EG Lyons. “The oxygen evolution reaction: mechanistic concepts and catalyst design”. In: *Photoelectrochemical solar fuel production*. Springer, 2016, pp. 41–104.
- [79] Emiliana Fabbri and Thomas J Schmidt. *Oxygen evolution reaction—the enigma in water electrolysis*. 2018.
- [80] Wei Zhou et al. “Stable hierarchical bimetal–organic nanostructures as high-performance electrocatalysts for the oxygen evolution reaction”. In: *Angewandte Chemie International Edition* 58.13 (2019), pp. 4227–4231.
- [81] Xuesi Wang et al. “Electronic and structural engineering of carbon-based metal-free electrocatalysts for water splitting”. In: *Advanced Materials* 31.13 (2019), p. 1803625.
- [82] Qiurong Shi et al. “Robust noble metal-based electrocatalysts for oxygen evolution reaction”. In: *Chemical Society Reviews* 48.12 (2019), pp. 3181–3192.
- [83] Kaiyue Zhu, Xuefeng Zhu, and Weishen Yang. “Application of in situ techniques for the characterization of NiFe-based oxygen evolution reaction (OER) electrocatalysts”. In: *Angewandte Chemie International Edition* 58.5 (2019), pp. 1252–1265.
- [84] Hannah Osgood et al. “Transition metal (Fe, Co, Ni, and Mn) oxides for oxygen reduction and evolution bifunctional catalysts in alkaline media”. In: *Nano Today* 11.5 (2016), pp. 601–625.
- [85] Emiliana Fabbri et al. “Developments and perspectives of oxide-based catalysts for the oxygen evolution reaction”. In: *Catalysis Science & Technology* 4.11 (2014), pp. 3800–3821.
- [86] Charles CL McCrory et al. “Benchmarking heterogeneous electrocatalysts for the oxygen evolution reaction”. In: *Journal of the American Chemical Society* 135.45 (2013), pp. 16977–16987.

- [87] Camillo Spöri et al. “The stability challenges of oxygen evolving catalysts: towards a common fundamental understanding and mitigation of catalyst degradation”. In: *Angewandte Chemie International Edition* 56.22 (2017), pp. 5994–6021.
- [88] Liaona She et al. “On the Durability of Iridium-Based Electrocatalysts toward the Oxygen Evolution Reaction under Acid Environment”. In: *Advanced Functional Materials* 32.5 (2022), p. 2108465.
- [89] Shaun M Alia et al. “Activity and durability of iridium nanoparticles in the oxygen evolution reaction”. In: *Journal of The Electrochemical Society* 163.11 (2016), F3105.
- [90] Shaun M Alia and Grace C Anderson. “Iridium oxygen evolution activity and durability baselines in rotating disk electrode half-cells”. In: *Journal of The Electrochemical Society* 166.4 (2019), F282.
- [91] Christine Minke et al. “Is iridium demand a potential bottleneck in the realization of large-scale PEM water electrolysis?” In: *international journal of hydrogen energy* 46.46 (2021), pp. 23581–23590.
- [92] Zachary Taie et al. “Pathway to complete energy sector decarbonization with available iridium resources using ultralow loaded water electrolyzers”. In: *ACS applied materials & interfaces* 12.47 (2020), pp. 52701–52712.
- [93] Alaina L Strickler et al. “Systematic investigation of iridium-based bimetallic thin film catalysts for the oxygen evolution reaction in acidic media”. In: *ACS applied materials & interfaces* 11.37 (2019), pp. 34059–34066.
- [94] Isabela C Man et al. “Universality in oxygen evolution electrocatalysis on oxide surfaces”. In: *ChemCatChem* 3.7 (2011), pp. 1159–1165.
- [95] Shaun M Alia et al. “Iridium-based nanowires as highly active, oxygen evolution reaction electrocatalysts”. In: *ACS Catalysis* 8.3 (2018), pp. 2111–2120.
- [96] Marine Elmaalouf et al. “The origin of the high electrochemical activity of pseudo-amorphous iridium oxides”. In: *Nature Communications* 12.1 (2021), pp. 1–10.
- [97] Dmitry Lebedev et al. “Highly active and stable iridium pyrochlores for oxygen evolution reaction”. In: *Chemistry of materials* 29.12 (2017), pp. 5182–5191.
- [98] Yong-Tae Kim et al. “Balancing activity, stability and conductivity of nanoporous core-shell iridium/iridium oxide oxygen evolution catalysts”. In: *Nature communications* 8.1 (2017), pp. 1–8.

- [99] Xueqiang Zhang et al. “Probing interfacial electrochemistry on a Co_3O_4 water oxidation catalyst using lab-based ambient pressure X-ray photoelectron spectroscopy”. In: *The Journal of Physical Chemistry C* 122.25 (2018), pp. 13894–13901.
- [100] Zhao Cai et al. “Single-crystalline ultrathin Co_3O_4 nanosheets with massive vacancy defects for enhanced electrocatalysis”. In: *Advanced Energy Materials* 8.3 (2018), p. 1701694.
- [101] Xiao Wang et al. “Metal–organic framework hybrid-assisted formation of $\text{Co}_3\text{O}_4/\text{Co-Fe}$ oxide double-shelled nanoboxes for enhanced oxygen evolution”. In: *Advanced materials* 30.29 (2018), p. 1801211.
- [102] Wei Hu et al. “Ir-surface enriched porous Ir–Co oxide hierarchical architecture for high performance water oxidation in acidic media”. In: *ACS applied materials & interfaces* 6.15 (2014), pp. 12729–12736.
- [103] Toshihiko Yoshida and Koichi Kojima. “Toyota MIRAI fuel cell vehicle and progress toward a future hydrogen society”. In: *The Electrochemical Society Interface* 24.2 (2015), p. 45.
- [104] Chenyu Wang and Jacob S Spendelow. “Recent developments in Pt–Co catalysts for proton-exchange membrane fuel cells”. In: *Current Opinion in Electrochemistry* 28 (2021), p. 100715.
- [105] Yuanfang Ying et al. “Hydrous cobalt–iridium oxide two-dimensional nanoframes: insights into activity and stability of bimetallic acidic oxygen evolution electrocatalysts”. In: *Nanoscale Advances* 3.7 (2021), pp. 1976–1996.
- [106] Dickson D Babu et al. “Atomic iridium@ cobalt nanosheets for dinuclear tandem water oxidation”. In: *Journal of Materials Chemistry A* 7.14 (2019), pp. 8376–8383.
- [107] Areum Yu et al. “Nanotubular iridium–cobalt mixed oxide crystalline architectures inherited from cobalt oxide for highly efficient oxygen evolution reaction catalysis”. In: *ACS applied materials & interfaces* 9.40 (2017), pp. 35057–35066.
- [108] Mauro Povia et al. “Operando X-ray characterization of high surface area iridium oxides to decouple their activity losses for the oxygen evolution reaction”. In: *Energy & Environmental Science* 12.10 (2019), pp. 3038–3052.
- [109] Camillo Spöri et al. “Experimental activity descriptors for iridium-based catalysts for the electrochemical oxygen evolution reaction (OER)”. In: *ACS Catalysis* 9.8 (2019), pp. 6653–6663.

- [110] Raghunandan Sharma et al. “Crystalline disorder, surface chemistry, and their effects on the oxygen evolution reaction (OER) activity of mass-produced nanostructured iridium oxides”. In: *ACS Applied Energy Materials* 4.3 (2021), pp. 2552–2562.
- [111] Elena Willinger et al. “Identifying key structural features of IrO_x water splitting catalysts”. In: *Journal of the American Chemical Society* 139.34 (2017), pp. 12093–12101.
- [112] Roger Adams and RL Shriner. “Platinum oxide as a catalyst in the reduction of organic compounds. III. Preparation and properties of the oxide of platinum obtained by the fusion of chloroplatinic acid with sodium nitrate¹”. In: *Journal of the American Chemical Society* 45.9 (1923), pp. 2171–2179.
- [113] Himanshi Dhawan, Natalia Semagina, and Marc Secanell. “State-of-the-art iridium-based catalysts for acidic water electrolysis: a minireview of wet-chemistry synthesis methods”. In: (2020).
- [114] Yadi Liu et al. “Investigation of high-performance IrO₂ electrocatalysts prepared by Adams method”. In: *International Journal of Hydrogen Energy* 43.42 (2018), pp. 19460–19467.
- [115] Cecil Felix et al. “Ex-situ electrochemical characterization of IrO₂ synthesized by a modified Adams fusion method for the oxygen evolution reaction”. In: *Catalysts* 9.4 (2019), p. 318.
- [116] Emma Oakton et al. “A simple one-pot Adams method route to conductive high surface area IrO₂-TiO₂ materials”. In: *New Journal of Chemistry* 40.2 (2016), pp. 1834–1838.
- [117] Daniel F Abbott et al. “Iridium oxide for the oxygen evolution reaction: correlation between particle size, morphology, and the surface hydroxo layer from operando XAS”. In: *Chemistry of Materials* 28.18 (2016), pp. 6591–6604.
- [118] Guangfu Li et al. “A Hard-Template Method for the Preparation of IrO₂, and Its Performance in a Solid-Polymer-Electrolyte Water Electrolyzer”. In: *ChemSusChem* 5.5 (2012), pp. 858–861.
- [119] Guangfu Li et al. “Highly effective Ir_xSn_{1-x}O₂ electrocatalysts for oxygen evolution reaction in the solid polymer electrolyte water electrolyser”. In: *Physical Chemistry Chemical Physics* 15.8 (2013), pp. 2858–2866.
- [120] Wenbo Wei, Feng Bai, and Hongyou Fan. “Surfactant-assisted cooperative self-assembly of nanoparticles into active nanostructures”. In: *IScience* 11 (2019), pp. 272–293.

- [121] Chunyu Du et al. “Rotating Disk Electrode Method”. In: *Rotating Electrode Methods and Oxygen Reduction Electrocatalysts* (Jan. 2014), pp. 171–198. DOI: 10.1016/B978-0-444-63278-4.00005-7.
- [122] Z Jia, G Yin, and J Zhang. “Rotating Ring-Disk Electrode Method. Rotating Electrode Methods and Oxygen Reduction Electrocatalysts”. In: *Elsevier BV* (2014), pp. 171–198.
- [123] Allen J Bard, Larry R Faulkner, et al. “Fundamentals and applications”. In: *Electrochemical Methods* 2.482 (2001), pp. 580–632.
- [124] *Linear Sweep and Cyclic Voltammetry: The Principles — Department of Chemical Engineering and Biotechnology*. URL: <https://www.ceb.cam.ac.uk/research/groups/rg-eme/Edu/linear-sweep-and-cyclic-voltammetry-the-principles> (visited on 06/25/2022).
- [125] G Bontempelli, N Dossi, and R Toniolo. “Polarography/Voltammetry”. In: *Reference Module in Chemistry, Molecular Sciences and Chemical Engineering* 218 (2018).
- [126] Noémie Elgrishi et al. “A practical beginner’s guide to cyclic voltammetry”. In: *Journal of chemical education* 95.2 (2018), pp. 197–206.
- [127] Yannick Garsany et al. *Experimental methods for quantifying the activity of platinum electrocatalysts for the oxygen reduction reaction*. 2010.
- [128] *What is Electrochemical Impedance Spectroscopy (EIS)? (Electrochemistry Basics Series) - Biologic*. URL: <https://www.biologic.net/topics/what-is-eis/> (visited on 04/16/2022).
- [129] *Basics of EIS: Electrochemical Research-Impedance Gamry Instruments*. URL: <https://www.gamry.com/application-notes/EIS/basics-of-electrochemical-impedance-spectroscopy/> (visited on 06/24/2022).
- [130] *Electrochemical Impedance Spectroscopy (EIS) Basics – Pine Research Instrumentation Store*. URL: <https://pineresearch.com/shop/kb/theory/eis-theory/eis-basics/> (visited on 06/24/2022).
- [131] Xiao-Zi Yuan et al. “Electrochemical impedance spectroscopy in PEM fuel cells: fundamentals and applications”. In: (2010).
- [132] PS Liu et al. “Characterization methods: basic factors”. In: *Porous Materials; Liu, PS, Chen, GF, Eds.; Butterworth-Heinemann: Boston, UK* (2014).
- [133] *Electrochemical Impedance Spectroscopy (EIS) Basics – Pine Research Instrumentation Store*. URL: <https://pineresearch.com/shop/kb/theory/eis-theory/eis-basics/> (visited on 06/24/2022).

- [134] *A Beginner's Guide to ICP-MS, Mass Spectrometry basics — Agilent*. URL: <https://www.agilent.com/en/support/atomic-spectroscopy/inductively-coupled-plasma-mass-spectrometry-icp-ms/icp-ms-instruments/what-is-icp-ms-icp-ms-faqs> (visited on 06/21/2022).
- [135] *ICP-MS as a Technique — OHSU*. URL: <https://www.ohsu.edu/elemental-analysis-core/icp-ms-technique> (visited on 06/21/2022).
- [136] *ICP-MS — Analysis for elemental impurities — EAG Laboratories*. URL: <https://www.eag.com/techniques/mass-spec/inductively-coupled-plasma-icp-ms/> (visited on 06/21/2022).
- [137] “Effect of Polymer-Based Nanoparticles on the Assay of Antimicrobial Drug Delivery Systems”. In: *Multifunctional Systems for Combined Delivery, Biosensing and Diagnostics* (Jan. 2017), pp. 67–108. DOI: 10.1016/B978-0-323-52725-5.00005-8.
- [138] *Omega-scan - Freiberg Instruments - lifetime, single crystal orientation, PID, automation and more*. URL: <https://www.freiberginstruments.com/x-ray-diffraction/technology/omega-scan.html> (visited on 06/21/2022).
- [139] *What are Electron Microscopes?* URL: <https://www.unl.edu/ncmn-cfem/xzli/em/em.htm> (visited on 06/22/2022).
- [140] *Electron Interactions*. URL: https://serc.carleton.edu/research_education/geochemsheets/electroninteractions.html (visited on 06/22/2022).
- [141] *Scanning Electron Microscope — Scratching the Surface*. URL: <https://rockymountainlaboratory.wordpress.com/tag/scanning-electron-microscope/> (visited on 06/23/2022).
- [142] Beverley J Inkson. “Scanning electron microscopy (SEM) and transmission electron microscopy (TEM) for materials characterization”. In: *Materials characterization using nondestructive evaluation (NDE) methods*. Elsevier, 2016, pp. 17–43.
- [143] *An Introduction to Electron Microscopy - SEM*. URL: <https://www.fei.com/introduction-to-electron-microscopy/sem/#gsc.tab=0> (visited on 06/22/2022).
- [144] *An Introduction to Electron Microscopy - TEM — Thermo Fisher Scientific*. URL: <https://www.fei.com/introduction-to-electron-microscopy/tem/#gsc.tab=0> (visited on 06/22/2022).

- [145] *electron microscopy home*. URL: <https://www.microscopy.ethz.ch/> (visited on 06/22/2022).
- [146] *An Introduction to Electron Microscopy - STEM — Thermo Fisher Scientific*. URL: <https://www.fei.com/introduction-to-electron-microscopy/stem/#gsc.tab=0> (visited on 06/22/2022).
- [147] *Keywords "objective lens" — Keywords — Glossary of TEM Terms — JEOL*. URL: https://www.jeol.co.jp/en/words/emterms/search_result.html?keyword=objective%20lens (visited on 06/23/2022).
- [148] *Spectroscopy — PASCO*. URL: <https://www.pasco.com/products/guides/what-is-spectroscopy> (visited on 06/23/2022).
- [149] *spectroscopy — Definition, Types, Facts — Britannica*. URL: <https://www.britannica.com/science/spectroscopy> (visited on 06/23/2022).
- [150] *EDS Analysis — Energy Dispersive Spectroscopy — Thermo Fisher Scientific - US*. URL: <https://www.thermofisher.com/us/en/home/materials-science/eds-technology.html> (visited on 06/23/2022).
- [151] *Energy-dispersive detector (EDS)*. URL: https://serc.carleton.edu/research_education/geochemsheets/eds.html (visited on 06/23/2022).
- [152] *What is EELS? — EELS.info*. URL: <https://eels.info/about/overview> (visited on 06/23/2022).
- [153] *X-ray Photoelectron Spectroscopy*. URL: https://serc.carleton.edu/msu_nanotech/methods/xps.html (visited on 06/22/2022).
- [154] *X-Ray Photoelectron Spectroscopy (XPS) Surface Analysis Technique*. URL: <https://www.phl.com/surface-analysis-techniques/xps-esca.html> (visited on 06/22/2022).
- [155] Marc Francis Labata et al. "Insights on platinum-carbon catalyst degradation mechanism for oxygen reduction reaction in acidic and alkaline media". In: *Journal of Power Sources* 487 (2021), p. 229356.
- [156] Guangfu Li and Po-Ya Abel Chuang. "Identifying the forefront of electrocatalytic oxygen evolution reaction: Electronic double layer". In: *Applied Catalysis B: Environmental* 239 (2018), pp. 425–432.
- [157] Frederic Maillard et al. "Size effects on reactivity of Pt nanoparticles in CO monolayer oxidation: The role of surface mobility". In: *Faraday discussions* 125 (2004), pp. 357–377.

- [158] Raghunandan Sharma and Shuang Ma Andersen. “Quantification on degradation mechanisms of polymer electrolyte membrane fuel cell catalyst layers during an accelerated stress test”. In: *Acs Catalysis* 8.4 (2018), pp. 3424–3434.
- [159] Guangyu Chen et al. “Evaluation of oxygen reduction activity by the thin-film rotating disk electrode methodology: The effects of potentiodynamic parameters”. In: *Electrocatalysis* 7.4 (2016), pp. 305–316.
- [160] Quentin Meyer, Yachao Zeng, and Chuan Zhao. “Electrochemical impedance spectroscopy of catalyst and carbon degradations in proton exchange membrane fuel cells”. In: *Journal of Power Sources* 437 (2019), p. 226922.
- [161] Ramesh Kumar Singh et al. “Electrochemical impedance spectroscopy of oxygen reduction reaction (ORR) in a rotating disk electrode configuration: effect of ionomer content and carbon-support”. In: *Journal of The Electrochemical Society* 162.6 (2015), F489.
- [162] Francisco J Vidal-Iglesias et al. “Electrochemical characterization of shape-controlled Pt nanoparticles in different supporting electrolytes”. In: *ACS Catalysis* 2.5 (2012), pp. 901–910.
- [163] Nagappan Ramaswamy and Sanjeev Mukerjee. “Fundamental mechanistic understanding of electrocatalysis of oxygen reduction on Pt and non-Pt surfaces: acid versus alkaline media”. In: *Advances in Physical Chemistry* 2012 (2012).
- [164] Kazuma Shinozaki et al. “Oxygen reduction reaction measurements on platinum electrocatalysts utilizing rotating disk electrode technique: I. Impact of impurities, measurement protocols and applied corrections”. In: *Journal of The Electrochemical Society* 162.10 (2015), F1144.
- [165] Hany A El-Sayed et al. “OER catalyst stability investigation using RDE technique: a stability measure or an artifact?” In: *Journal of The Electrochemical Society* 166.8 (2019), F458.
- [166] Kim Henrik Kangasniemi, DA Condit, and TD Jarvi. “Characterization of vulcan electrochemically oxidized under simulated PEM fuel cell conditions”. In: *Journal of the Electrochemical Society* 151.4 (2004), E125.
- [167] Yitao He et al. “Capacitive mechanism of oxygen functional groups on carbon surface in supercapacitors”. In: *Electrochimica Acta* 282 (2018), pp. 618–625.
- [168] Bharat Avasarala, Richard Moore, and Pradeep Haldar. “Surface oxidation of carbon supports due to potential cycling under PEM fuel cell conditions”. In: *Electrochimica Acta* 55.16 (2010), pp. 4765–4771.
- [169] XPS Thermo Scientific. *XPS Interpretation of Carbon*. 2016.

- [170] Songfeng Pei et al. “Green synthesis of graphene oxide by seconds timescale water electrolytic oxidation”. In: *Nature communications* 9.1 (2018), pp. 1–9.
- [171] Jon Ustarroz et al. “Mobility and poisoning of mass-selected platinum nanoclusters during the oxygen reduction reaction”. In: *ACS Catalysis* 8.8 (2018), pp. 6775–6790.
- [172] Paran Jyoti Sarma et al. “Strategic implementation of pulsed oxidation for mitigation of CO poisoning in polymer electrolyte fuel cells”. In: *Journal of Power Sources* 468 (2020), p. 228352.
- [173] Serhiy Cherevko et al. “Dissolution of platinum in the operational range of fuel cells”. In: *ChemElectroChem* 2.10 (2015), p. 1471.
- [174] Jong Hun Kim et al. “Nanoscale adhesion between Pt nanoparticles and carbon support and its influence on the durability of fuel cells”. In: *Current Applied Physics* 15 (2015), S108–S114.
- [175] Xiaomei Chang et al. “Construction of carboxyl functional groups and their enhancement effect for methanol electrocatalytic oxidation reaction”. In: *International Journal of Hydrogen Energy* 44.50 (2019), pp. 27445–27454.
- [176] Mark E. Davis and Robert J Davis. “Chapter 5- Heterogenous Catalysis”. Undetermined. In: *Fundamentals of chemical reaction engineering*. New York, NY: McGraw-Hill Higher Education, 2003. Chap. Chapter 5, pp. 144–145. ISBN: 007245007X.
- [177] Simon J Freakley, Jonathan Ruiz-Esquiús, and David John Morgan. “The X-ray photoelectron spectra of Ir, IrO₂ and IrCl₃ revisited”. In: *Surface and Interface Analysis* 49.8 (2017), pp. 794–799.
- [178] Jiajian Gao et al. “Breaking long-range order in iridium oxide by alkali ion for efficient water oxidation”. In: *Journal of the American Chemical Society* 141.7 (2019), pp. 3014–3023.
- [179] Patrick Steegstra et al. “Revisiting the redox properties of hydrous iridium oxide films in the context of oxygen evolution”. In: *The Journal of Physical Chemistry C* 117.40 (2013), pp. 20975–20981.
- [180] Serhiy Cherevko et al. “Oxygen evolution activity and stability of iridium in acidic media. Part 2.—Electrochemically grown hydrous iridium oxide”. In: *Journal of Electroanalytical Chemistry* 774 (2016), pp. 102–110.
- [181] Sengen Anantharaj, Pitchiah Esakki Karthik, and Suguru Noda. “The significance of properly reporting turnover frequency in electrocatalysis research”. In: *Angewandte Chemie International Edition* 60.43 (2021), pp. 23051–23067.

- [182] Guangfu Li et al. “New insights into evaluating catalyst activity and stability for oxygen evolution reactions in alkaline media”. In: *Sustainable Energy & Fuels* 2.1 (2018), pp. 237–251.
- [183] Chao Wei et al. “Approaches for measuring the surface areas of metal oxide electrocatalysts for determining their intrinsic electrocatalytic activity”. In: *Chemical Society Reviews* 48.9 (2019), pp. 2518–2534.
- [184] Haoran Yu et al. “Nano-size IrO_x catalyst of high activity and stability in PEM water electrolyzer with ultra-low iridium loading”. In: *Applied Catalysis B: Environmental* 239 (2018), pp. 133–146.
- [185] Olga Kasian et al. “Degradation of iridium oxides via oxygen evolution from the lattice: correlating atomic scale structure with reaction mechanisms”. In: *Energy & Environmental Science* 12.12 (2019), pp. 3548–3555.
- [186] Wei Sun et al. “Effect of lattice strain on the electro-catalytic activity of IrO₂ for water splitting”. In: *Chemical Communications* 54.8 (2018), pp. 996–999.
- [187] M Pourbaix, H Zhang, and A Pourbaix. “Presentation of an Atlas of Chemical and Electrochemical Equilibria in the Presence of a Gaseous Phase”. In: *Materials science forum*. Vol. 251. Trans Tech Publ. 1997, pp. 143–148.
- [188] Scott A Speakman. “Estimating crystallite size using XRD”. In: *MIT Center for Materials Science and Engineering* 2 (2014), p. 14.
- [189] Marina Sokolsky-Papkov and Alexander Kabanov. “Synthesis of well-defined gold nanoparticles using pluronic: The role of radicals and surfactants in nanoparticles formation”. In: *Polymers* 11.10 (2019), p. 1553.
- [190] Stef Kerkhofs et al. “Self-Assembly of Pluronic F127 Silica Spherical Core–Shell Nanoparticles in Cubic Close-Packed Structures”. In: *Chemistry of Materials* 27.15 (2015), pp. 5161–5169.
- [191] Daniel G Angelescu et al. “Synthesis and association of Ag (0) nanoparticles in aqueous Pluronic F127 triblock copolymer solutions”. In: *Colloids and Surfaces A: Physicochemical and Engineering Aspects* 394 (2012), pp. 57–66.
- [192] *Pluronic F-127 — C₇H₁₆O₄ - PubChem*. URL: <https://pubchem.ncbi.nlm.nih.gov/compound/Pluronic-F-127> (visited on 06/16/2022).
- [193] Shaun M Alia et al. “Mercury underpotential deposition to determine iridium and iridium oxide electrochemical surface areas”. In: *Journal of The Electrochemical Society* 163.11 (2016), F3051.
- [194] Jurga Juodkazytė et al. “Iridium anodic oxidation to Ir (III) and Ir (IV) hydrous oxides”. In: *Electroanalysis: An International Journal Devoted to Fundamental and Practical Aspects of Electroanalysis* 17.11 (2005), pp. 947–952.

- [195] Serhiy Cherevko et al. “Oxygen and hydrogen evolution reactions on Ru, RuO₂, Ir, and IrO₂ thin film electrodes in acidic and alkaline electrolytes: A comparative study on activity and stability”. In: *Catalysis Today* 262 (2016), pp. 170–180.
- [196] Mark C Biesinger et al. “Resolving surface chemical states in XPS analysis of first row transition metals, oxides and hydroxides: Cr, Mn, Fe, Co and Ni”. In: *Applied Surface Science* 257.7 (2011), pp. 2717–2730.